



LAWRENCE
LIVERMORE
NATIONAL
LABORATORY

UCRL-LR-155288

Technical Basis Document No. 6: Waste Package and Drip Shield Corrosion

J. Farmer, V. Pasupathi, P. Nair, G. Gordon, D. McCright, G. Gdowski, S. Carroll, T. Steinborn, T. Summers, F. Wong, R. Rebak, R. Lian, G. Ilievbare, J. Lee, F. Hua, J. Payer

August 1, 2003

This document was prepared as an account of work sponsored by an agency of the United States Government. Neither the United States Government nor the University of California nor any of their employees, makes any warranty, express or implied, or assumes any legal liability or responsibility for the accuracy, completeness, or usefulness of any information, apparatus, product, or process disclosed, or represents that its use would not infringe privately owned rights. Reference herein to any specific commercial product, process, or service by trade name, trademark, manufacturer, or otherwise, does not necessarily constitute or imply its endorsement, recommendation, or favoring by the United States Government or the University of California. The views and opinions of authors expressed herein do not necessarily state or reflect those of the United States Government or the University of California, and shall not be used for advertising or product endorsement purposes.

This work was performed under the auspices of the U.S. Department of Energy by University of California, Lawrence Livermore National Laboratory under Contract W-7405-Eng-48.



TECHNICAL BASIS REPORT: WASTE PACKAGE AND DRIP SHIELD PERFORMANCE

**Prepared by
Dr. Joseph Farmer**

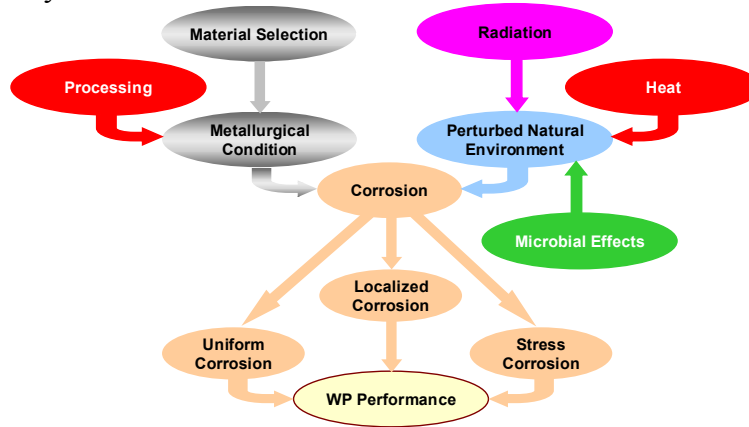
**Contributions by
Dr. Gerald Gordon, Dr. Terry Steinborn and Prof. Joseph Payer**

August 5, 2003

Revision 1.

Executive Summary

The waste package and drip shield will experience a wide range of interactive environmental conditions and degradation modes that will determine the overall performance of the waste package and repository.



The operable modes of degradation are determined by the temperature regime of operation (region), and are summarized here. *Dry-Out Region* ($T \geq 120^\circ\text{C}$; 50 to 400 Years): During the pre-closure period, the waste package will be kept dry by ventilation air. During the thermal pulse, heat generated by radioactive decay will eventually increase the temperature of the waste package, drip shield and drift wall to a level above the boiling point, where the probability of seepage into drifts will become insignificant. Further heating will push the waste package surface temperature above the deliquescence point of expected salt mixtures, thereby preventing the formation of deliquescence brines from dust deposits and humid air. Phase and time-temperature-transformation diagrams predicted for Alloy 22, and validated with experimental data, indicates no significant phase instabilities (LRO and TCP precipitation) at temperatures below 300°C for 10,000 years. Neither will dry oxidation at these elevated temperatures limit waste package life. After the peak temperature is reached, the waste package will begin to cool, eventually reaching a point where deliquescence brine formation may occur. However, corrosion testing of Alloy 22 underneath such films has shown no evidence of life-limiting localized corrosion. *Transition Region* ($120^\circ\text{C} \geq T \geq 100^\circ\text{C}$; 400 to 1,000 Years): During continued cooling, the temperature of the drift wall will drop to a level close to the boiling point of the seepage brine, thus permitting the onset of seepage. Corrosion in a concentrated, possibly aggressive, liquid-phase brine, evolved through evaporative concentration, is possible while in this region. However, based upon chemical divide theory, most ($\geq 99\%$) of the seepage water entering the drift is predicted to evolve as benign chloride-sulfate or bicarbonate brines. Less than one percent will evolve to aggressive calcium chloride brines, and these brines will have significant levels of nitrate inhibitor present. Thus, waste package life will not be limited by localized corrosion while in this region of operation. Rates of uniform general corrosion are relatively insignificant, and stress corrosion cracking is prevented by stress mitigation, and physical isolation of welded regions from corrosive environments. *Low Temperature Region* ($100^\circ\text{C} \leq T$; 1,000-10,000 Years) Continued cooling will eventually lower the temperature below the boiling point of the seepage brine, thus minimizing the extent of evaporative concentration. Once the waste package temperature drops below the critical temperature for crevice corrosion, corrosion will no longer limit waste package performance.

Chapter 1. Expected In-Drift Environment

The objective of this Technical Basis Report (TBR) is to describe the logic for the safety case for the high-level waste repository at Yucca Mountain as it pertains to the performance of the waste package and drip shield. Since any selection of an engineering material depends upon the service environment, Chapter 1 is dedicated to a thorough description of the waste package surface environment. The evolution of this local “in-drift” environment depends upon the interaction between hot waste packages, rocks in the drift wall, and seepage water. Chapter 1 will describe these interactions in sufficient detail to set the stage for subsequent chapters, which describe the time-dependent performance of the waste package and drip shield.

The time-temperature profile taken from the Supplemental Science and Performance Assessment (SSPA) Analysis is shown in Figure 1-1 and illustrates the thermal pulse, as well as the three operational regions: dry-out; transition; and low-temperature. These predictions are for those waste packages located at the center of repository (hottest). This analysis assumes that all of the waste packages are emplaced instantaneously. A more realistic sequential emplacement process will lower waste package temperatures by approximately 30°C. An additional 30°C drop would result from only 20-30 years of additional ventilation. The corresponding RH-time profile is shown in Figure 1-2, and shows a minimum in relative humidity corresponding to the maximum in temperature. The current repository design will enable the repository to operate in three distinct temperature regions: dry-out; transition; and low-temperature.

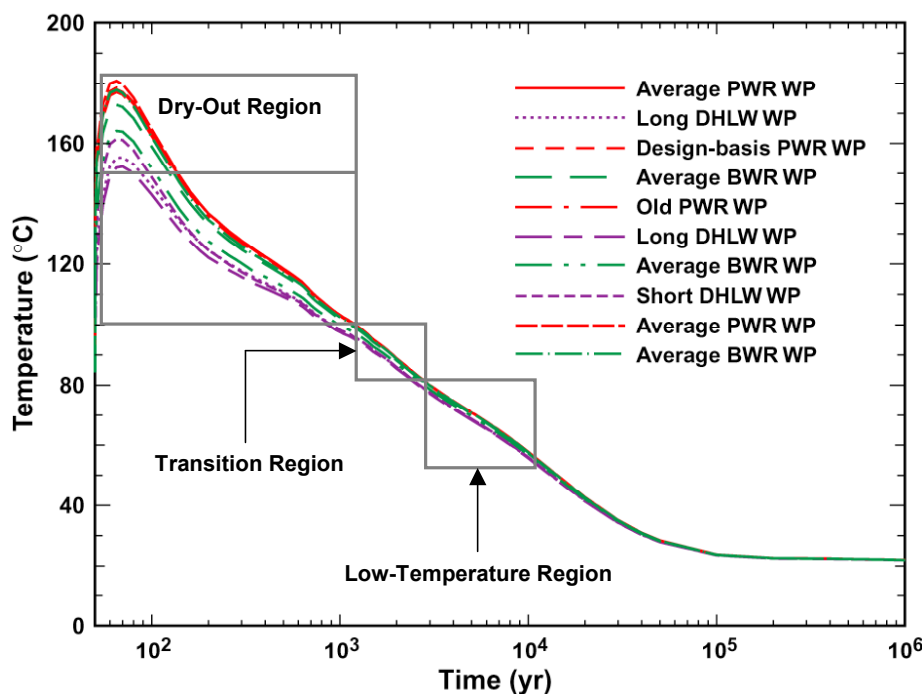


Figure 1-1. SSPA temperature-time profiles for waste packages at the center of the repository. The three characteristic temperature regions of operation are illustrated.

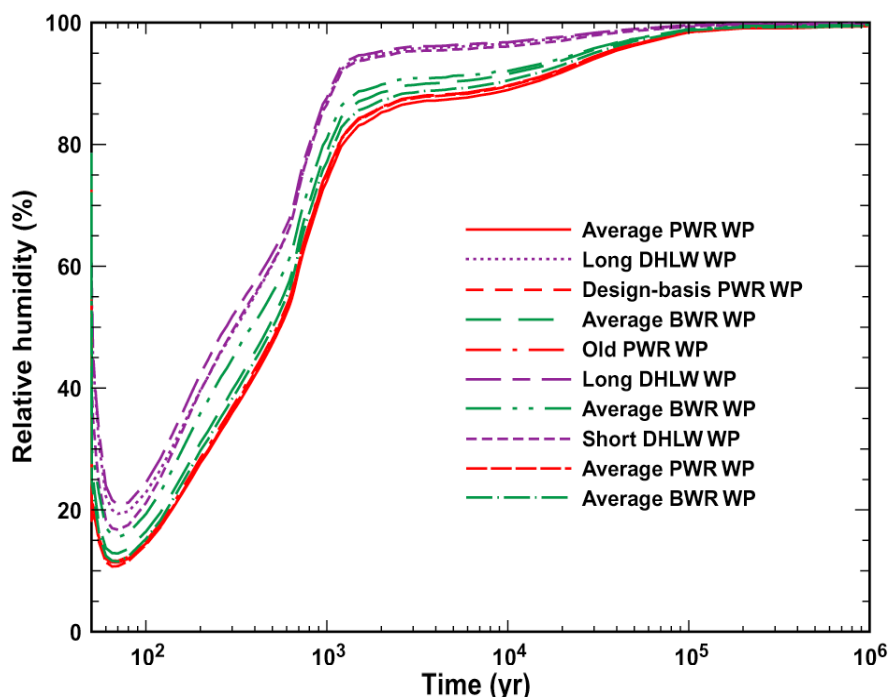


Figure 1-2. SSPA RH-time profiles for waste packages at the center of the repository. The three characteristic temperature regions of operation are illustrated.

Dry-Out Region ($T \geq 120^\circ\text{C}$; 50 to 400 Years) – Drift walls will first be dried by ventilation air. Eventually, heat generated by radioactive decay will increase the temperature of waste packages above the boiling point of seepage water, and at or above the point where deliquescence brine formation is possible. Since no significant seepage is expected at temperatures above the boiling point (100°C), no aqueous phase corrosion due to seepage is expected. While the formation of deliquescence brines may be possible at temperatures that lie between the boiling and deliquescence points, no corrosion of Alloy 22 has been observed beneath films of CaCl_2 deliquescence brines at $160\text{--}165^\circ\text{C}$. This is close to maximum calculated deliquescence point.

Transition Region ($120^\circ\text{C} \geq T \geq 100^\circ\text{C}$; 400 to 1,000 Years) – Seepage into the drifts will become possible as the waste package cools, and as the temperature drops below the boiling point (100°C). At the point where the drip shield seepage diversion function is lost, such water can undergo evaporative concentration on the waste package surface, thereby evolving into either benign (bicarbonate- or sulfate-type brines) or aggressive electrolytes (CaCl_2 -type brines). Localized attack is possible in CaCl_2 -type brines at temperatures above the threshold temperature for crevice corrosion. Such attack is unlikely as the temperature cools below the threshold temperature.

Low Temperature Region ($100^\circ\text{C} \leq T$; 1,000-10,000 Years) – As the waste package cools to a temperature below the threshold for crevice corrosion in CaCl_2 -type brines (believed to represent a worst-case scenario), waste package performance becomes insensitive to the chemistry of any water entering the drifts. The Alloy 22 will provide protection for the spent nuclear fuel and high-level waste under, even in such worst-than-expected environments.

Dry-Out Region ($T \geq 120^\circ\text{C}$; 50 to 400 Years)

Drift walls will first be dried by ventilation air. Eventually, heat generated by radioactive decay will increase the temperature of waste packages above the boiling point of seepage water (100°C). Since no significant seepage is expected at temperatures above the boiling point, no aqueous phase corrosion due to seepage is expected. At the highest temperature ($150\text{--}180^\circ\text{C}$), only dry oxidation is expected. As the waste packages cool below the deliquescence point of the dust deposits (150°C), the formation of thin films of deliquescence brines is possible. While the formation of deliquescence brines may be possible at temperatures that lie between the boiling and deliquescence points, no corrosion of Alloy 22 has been observed beneath films of CaCl_2 deliquescence brines. This is close to maximum calculated deliquescence point.

Detailed knowledge of the Dry-Out Region requires detailed Thermal Hydrology (TH) modeling, which has been done by the Project (LBNL, LLNL, etc.). The modeling results for water content (saturation level) of the drift wall at 100 and 500 years indicate that the dry-out zone extends into the rock and fractures for a distance of approximately 5 meters during this period. Further, the water content (saturation level) model predictions of the drift wall at 1000 and 2000 years indicate the shrinking of the dry-out zone as the repository cools with the onset of seepage at 2000 years, as the rock drops below the boiling point. From this prediction, it is also evident that very little water enters the drift until the temperature drops below the boiling point.

A variety of realistic studies of the in-drift environment have been conducted that provides substantial insight into the Dry-Out Region. The Exploratory Studies Facility (ESF) is an 8-km tunnel that provides direct access to layers of rock in the proposed repository horizon. The Exploratory Cross Drift is a 3-km drift, oriented east-to-west, that enables access to rock layers above and below repository horizon. There are also several alcoves and niches. Seven (7) alcoves enable experiments in the rock layer at repository horizon, while four (4) niches are used for a variety of hydrology tests. Experimental work being conducted in Alcove 5 provides data of particular relevance. The Drift-Scale Test (DST) is being conducted in this alcove, and heated a full-scale simulated waste package to 197°C to explore thermal effects on seepage and dry-out [Lin et al.]. The corresponding temperatures in the air and rock were 200°C and 195°C , respectively. The time required to achieve this temperature was 26,396 hours (December 20, 2000). The DST in Alcove 5 is shown in Figure 1-3.

Dry-out has been observed experimentally [Carlson et al.]. The effect of borehole temperature on the volumetric water content was determined experimentally in Borehole 79 with neutron measurements, and is shown in Figure 1-4. These measurements were made during the drift scale test (DST), over a 2-year period during heating. This borehole is almost level over an instrumented 40-m section, almost parallel and 9.5-m offset from the center of the drift, and about 3.5-m above the wing heaters that simulate the heat from a waste package. The test was conducted from February 1998 to May 2000.



Figure 1-3. The Drift Scale Test is conducted in Alcove 5 with full-scale heated waste package model, and has been used to experimentally simulate the expected thermal effects on the drift walls and seepage.

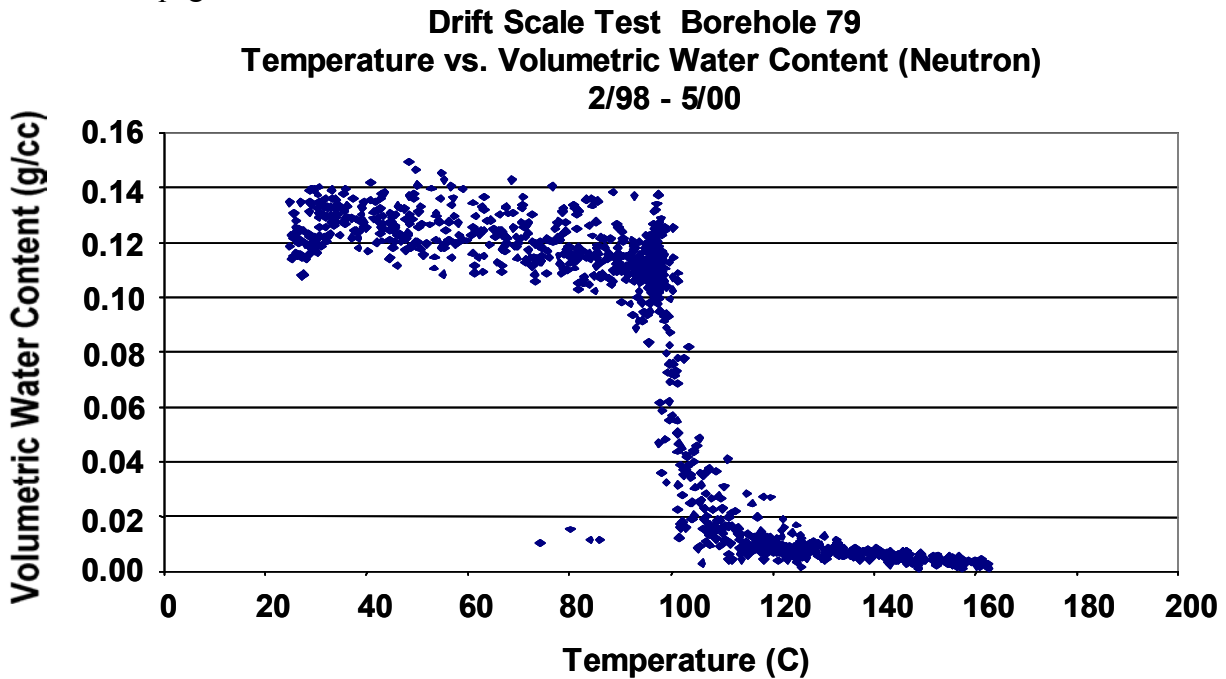


Figure 1-4. The effect of borehole temperature on the volumetric water content was determined experimentally in Borehole 79 with neutron measurements.

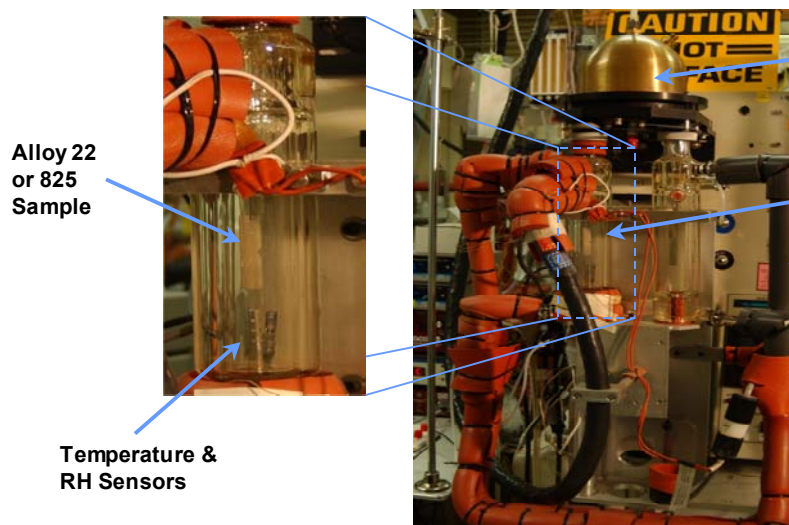
Formation of Deliquescence Brines in Dry-Out Region

As discussed by Gdowski (CRWMS M&O 2000i), hygroscopic salts may be deposited from aerosols and dust introduced with the backfill and ventilation air. They will be contained in seepage water that enters the drifts and the episodic water that flows through the drifts. Such hygroscopic salts enable aqueous solutions to exist as thin surface films at a relative humidity below 100%. The threshold relative humidity ($RH_{critical}$) at which an aqueous solution can exist is defined as the deliquescence point. This threshold defines the condition necessary at a given temperature for aqueous-phase electrochemical corrosion reactions to occur at the metal substrate/salt deposit interface. As pointed out by Gdowski (CRWMS M&O 2000i), observed deliquescence points cover a very broad range of RH. For example, the deliquescence point of NaOH is 1.63% RH at 75°C, while that of K_2SO_4 is 97.59% RH at 20°C.

Deliquescence brines can be formed from dry salt deposits and moisture in the air (humidity) in the dry-out region. Depending on the surface temperature/relative humidity conditions, the existence of liquid-phase water on the waste package is effected by the presence of a salt deposit. In the presence of such a deposit, a thin-film liquid phase can be established at a higher temperature and lower relative humidity (RH) than otherwise possible. The process of deliquescence has been studied in detail by the Project (Gdowski et al. 2003) with thermal gravimetric analysis (TGA). The Environmental TGA is shown in Figure 1.5.

TGA data shown in Figure 1-6 illustrates the formation of a deliquescence brine from a salt deposit and humidity from the air. The substrate was Alloy 22 and the salt deposit was pure $CaCl_2$. The moisture in the air flowing over the sample was maintained constant at 22.5% RH. Conclusions are summarized as follows:

1. At 100°C, deliquescence brines of $CaCl_2$ are stable for the duration for test.
2. At 125°C, the brine evolves slowly, forming insoluble precipitates.
3. At 150°C, the brine evolves rapidly, forming insoluble precipitates & HCl gas.
4. Precipitates from 150°C and 125°C tests are similar.
5. No degradation of Alloy 22 was detected.



Sensitive to weight changes as small as “tens of micrograms”
Operation at temperatures up to 150°C

Figure 1-5. The Environmental Thermal Gravimetric Analyzer (TGA) was used to study the deliquescence of deposited films of CaCl_2 salt.

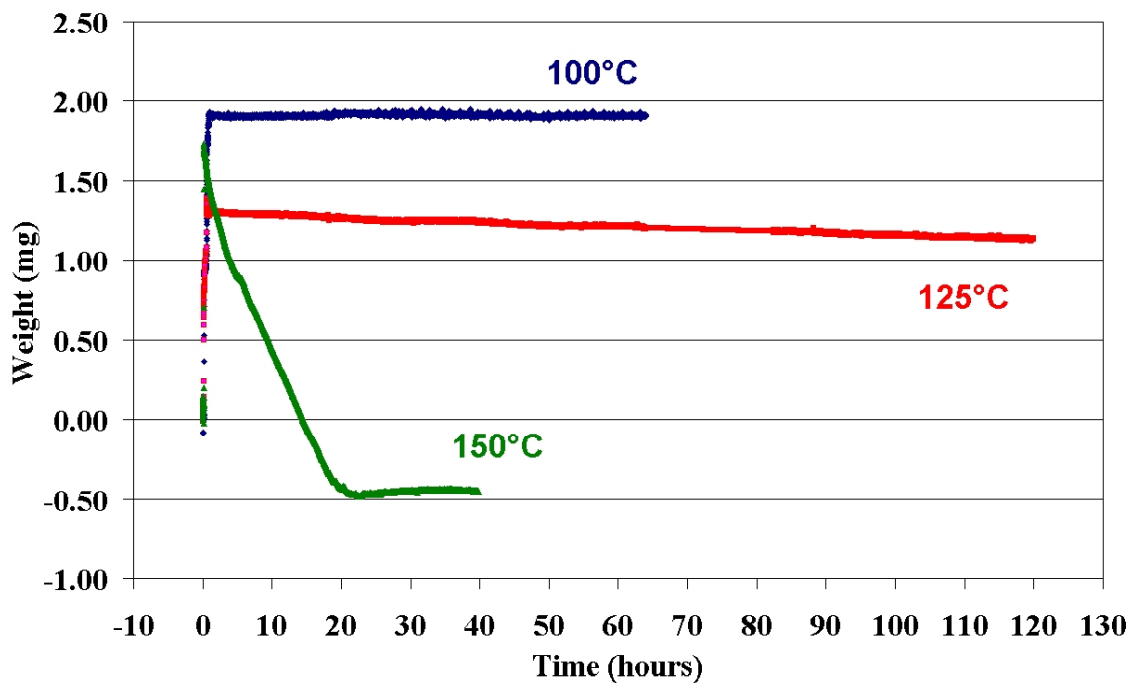


Figure 1-6. TGA data showing the formation of CaCl_2 deliquescence brines on Alloy 22 in flowing air streams with 22.5% RH at three temperature levels (100, 125 & 150°C).

Dry-Out Region – Acid-Gas from Decomposition of CaCl_2

Scenarios have been postulated where the hydrogen chloride (HCl) formed during the thermal decomposition of CaCl_2 deliquescent brines is condensed in a closed system, and continuously contacted with Alloy 22 during refluxing. Assessment of this scenario based on simple preliminary calculations indicates that the maximum possible impact of the hydrogen chloride on a waste package constructed of a nickel-based alloy (or pure nickel) is limited by the availability of chloride in the repository. The following assumptions are made for this simple bounding calculation and are believed to be extremely conservative:

1. The drift diameter is 18 ft
2. The waste package diameter is 6 ft
3. The sum of all waste package lengths is 90% of the drift length
4. Ambient seepage flux through 4000 years
5. Seepage entering repository proportional to footprint seepage flux
6. Chloride entering repository proportional to seepage Cl concentration
7. The Cl concentration in the seepage remains constant at 10 mg/liter
8. All chloride entering the repository is converted to HCl
9. All HCl remains in drifts and reacts with waste package outer layers
10. The primary corrosion product is NiCl_2

Assuming that all incident ambient seepage enters the repository, corrosion of the waste package outer layer by volatilized HCl would be mass-limited to less than 5% (3.47%) of the total wall thickness (Tables 1-1 and 1-2). The impact is smaller in the case of thermal seepage.

Table 1-1. Limiting Mass of Chloride Entering Repository per Mile of Tunnel

Time	Assumed Temp.	Air Density	Air Mass in Drift	Ambient Seepage	Ambient Seepage	Chloride in Seepage	HCl ~ Cl	HCl ~ Cl
Years	°C	moles/liter	moles	mm/yr	moles/yr	mg/liter	moles/yr	moles
0-600	180	0.026888	1.0227×10^6	60	29,431,683	10	149	8.967×10^4
600-2000	100	0.032655	1.2424×10^6	160	78,484,488	10	398	6.476×10^5
2000-4000	25	0.040873	1.5551×10^6	250	122,632,012	10	623	1.893×10^6

Table 1-2. Limiting Mass of Hypothetical Nickel Waste Package Reacted

Assumed Characteristics of Hypothetical Drift	Quantity	Assumed Characteristics of Hypothetical Ni Waste Package	Quantity
Length of Drift	5280 ft	Total Combined Length of Hypothetical Waste Packages	$0.9 \times 5280 \text{ ft} = 4752 \text{ ft}$
Diameter of Drift	18 ft	Diameter of Hypothetical Waste Package	6 ft
Volume of Air Inside Drift	$1,343,596 \text{ ft}^3$	Volume of Hypothetical Waste Package Outer Layer	$166,432,247 \text{ cm}^3$
Foot Print of Drift	$88,295,049 \text{ cm}^2$	Area of Hypothetical Waste Package Outer Layer	$83,216,123 \text{ cm}^2$
Maximum Possible HCl Mass in Drift After 4000 Years	1.893×10^6 moles	Mass of Hypothetical Waste Package Outer Layer	2.535×10^7 moles
Maximum Possible NiCl_2 Mass Formed from HCl After 4000 Years	9.465×10^5 moles	Waste Package Outer Layer Converted to Corrosion Product	3.73%

Dry-Out Region – Dispersion of Acid Gas in Drifts

In addition to bounding the extent of the acid gas issue with a simple mass balance, more detailed modeling is being conducted by Sandia National Laboratory to enable the Project to understand the dispersion of any acid gas in the repository, which would further bound the problem. The modeling now being used to elucidate the dispersion of evolved hydrogen chloride is summarized below:

1. Computational fluid dynamics (CFD) approach using FLUENT
2. Three-dimensional (3D) turbulent-flow model inside the drift
3. Drift segment with fourteen (14) waste packages modeled (70 meters)
4. Conduction, natural convection, thermal radiation heat transfer included in model
5. Mass concentration gradient along drift
6. No temperature gradient along drift
7. Run at various post-closure times
8. Model validated for heat transfer, not mass \transfer
9. Intended to quantify water vapor movement in the drift
10. Applicable to general vapor movement in the drift

Predictions indicate high flow velocities and strong mixing within drift. For example, the maximum flow velocity of air along the drift is predicted to be 0.26 meters per second at 1000 years. The overall maximum velocity is predicted to be 0.30 meters per second. The predicted dispersion coefficients are very high. For example, the axial transport by convection is expected to be three to four orders-of-magnitude higher than that due to molecular diffusion alone. Thus, significant mixing (and dilution) would be expected to occur along the drift. Additional work is needed to account for the distribution of local acid gas sources and sinks along the drift. It is recognized that these predictions require further validation. The Vapor Dispersion Test (VDT) has been planned for late FY03 to FY04.

Transition Region ($120^{\circ}\text{C} \geq T \geq 100^{\circ}\text{C}$; 400 to 1,000 Years)

Seepage into the drifts will become possible as the waste package cools, and as the temperature drops below the boiling point (100°C). At the point where the drip shield seepage diversion function is lost, such water can undergo evaporative concentration on the waste package surface, thereby evolving into either benign (bicarbonate- or sulfate-type brines) or aggressive electrolytes (CaCl_2 -type brines). Localized attack is possible in CaCl_2 -type brines at temperatures above the threshold temperature for crevice corrosion. Such attack is unlikely as the temperature cools below the threshold temperature.

The Chemical Divide Theory (Gdowski et al. 2003) provides substantial insight into the evolution of seepage that may enter the actual repository, as well as into the evolution waters collected during the Drift-Scale Heater Test. This concept is most easily understood in terms of the pseudo ternary diagram shown in Figure 1-7, with Ca^{+2} , SO_4^{-2} , and HCO_3^{-} at the three vertices. The three colored regions represent broad ranges (categories) of possible water chemistries. Any water chemistry falling into a particular category will evolve like other water chemistries falling into the same category. This conceptual representation of the Chemical Divide Theory shows the evolution of broad categories of natural waters to common end-point compositions (Gdowski et al.).

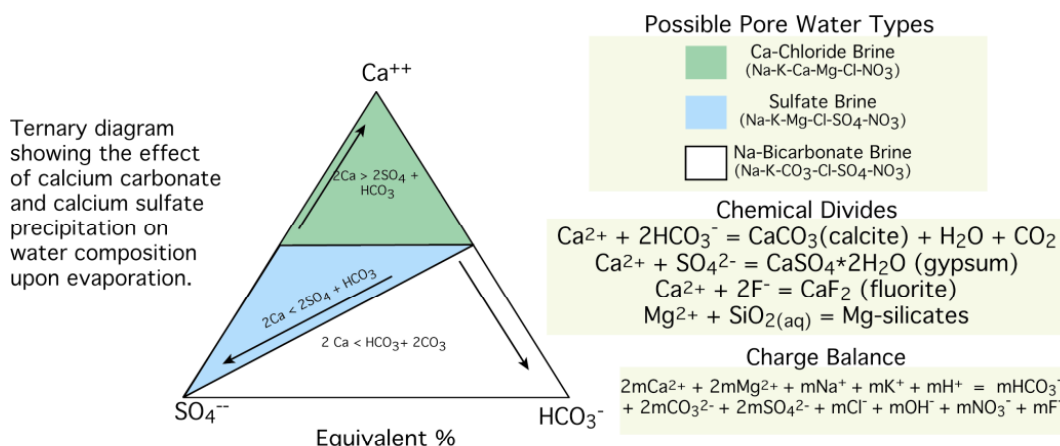


Figure 1-7. This conceptual representation of the Chemical Divide Theory shows the evolution of broad categories of natural waters to common end-point compositions.

Due to the disproportionate precipitation of bicarbonate in calcite, the disproportionate precipitation of sulfate in gypsum and the disproportionate precipitation of fluoride in fluorite, any water falling into the CaCl_2 Region (green) should follow a trajectory towards the Ca^{+2} vertex during evaporation, thereby rendering a concentrated CaCl_2 -type brine. Similarly, due to the disproportionate precipitation of calcium in calcite, any water falling into the Bicarbonate Region (white) will follow a trajectory towards the HCO_3^{-} vertex during evaporation. Due to the disproportionate precipitation of calcium in gypsum, any water falling into the Sulfate Region (blue) will follow a trajectory towards the SO_4^{-2} vertex during evaporation. The boundaries shown in this diagram are highly idealized, and may not be obeyed exactly since fluoride and other ions that can form precipitates are not accounted for. The boundaries provide a general

heuristic guidance on the evolution of seepage waters due to evaporative concentration, but are not absolute.

While appreciating the limitations of the chemical divide theory, it still provides beneficial understanding when used to categorize observed water chemistries. For example, Figure 1-8 shows a number of observed water chemistries plotted on the pseudo ternary diagram, with Ca^{+2} , SO_4^{-2} , and HCO_3^- at the three vertices. Data plotted on this ternary diagram include: actual Drift-Scale Test (DST) water chemistries; pore water chemistries determined by the United States Geological Survey (Peterman et al. 2002); pore water chemistries for both the Paintbrush and the Topopah formations (Yang et al.); and water chemistries used in the Project's Long Term Corrosion Test Facility (LTCTF), as well as water chemistries used for accelerated electrochemical testing. The distribution of these observed water chemistries into the three categories is summarized in Figure 1-9. The pie chart shows the distribution of all observed waters, and the column chart shows the breakdown for each data set. Most of the observed waters fall in the bicarbonate and sulfate categories, and would be expected to evolve into relatively benign environments.

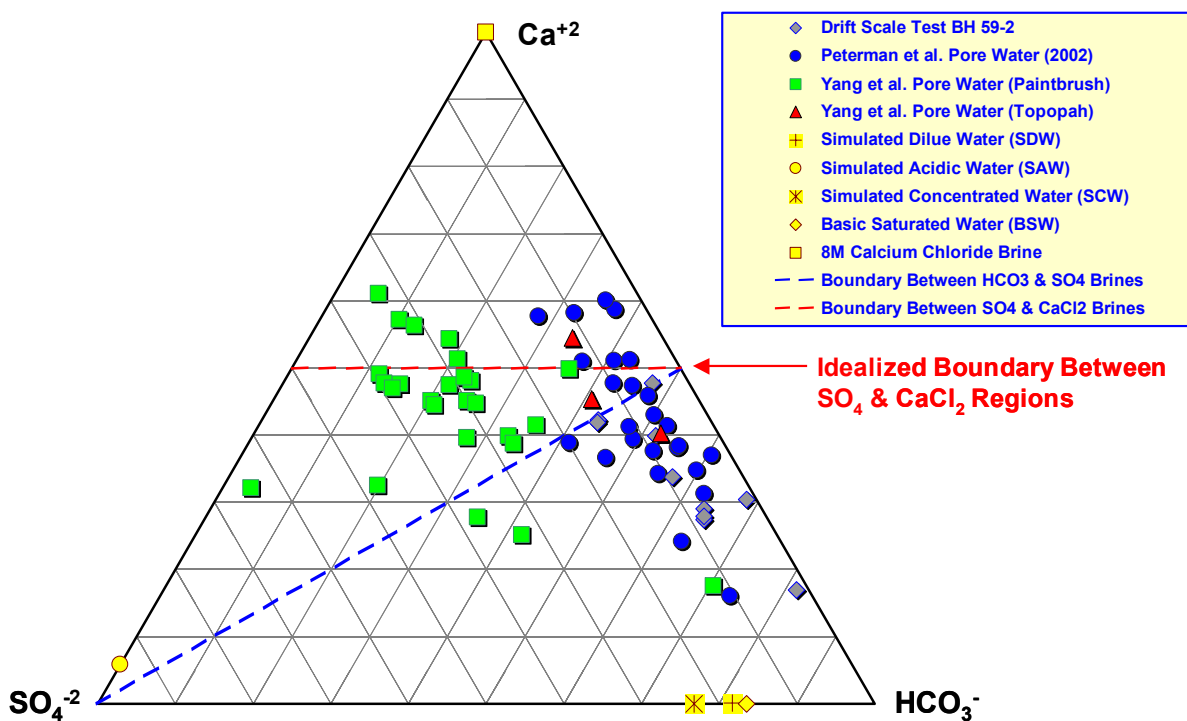
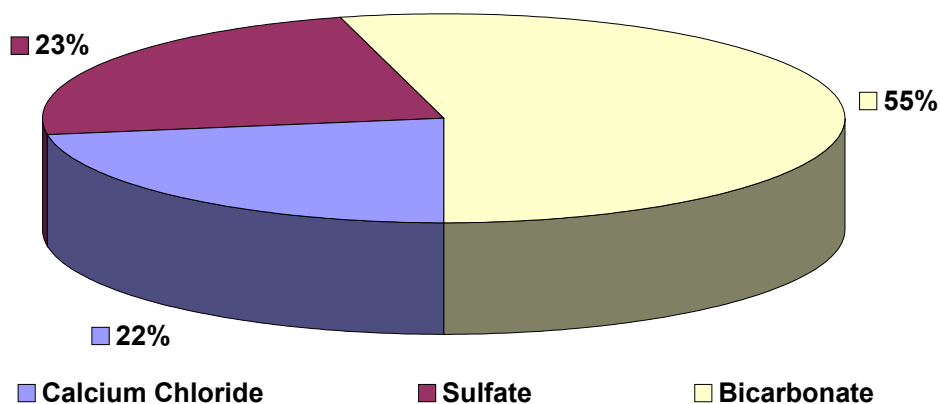


Figure 1-8. Observed water chemistries plotted on the pseudo ternary diagram, with Ca^{+2} , SO_4^{-2} , and HCO_3^- at the three vertices.

Distribution of Water Chemistries Observed at Yucca Mountain



Distribution of Water Chemistries Observed at Yucca Mountain

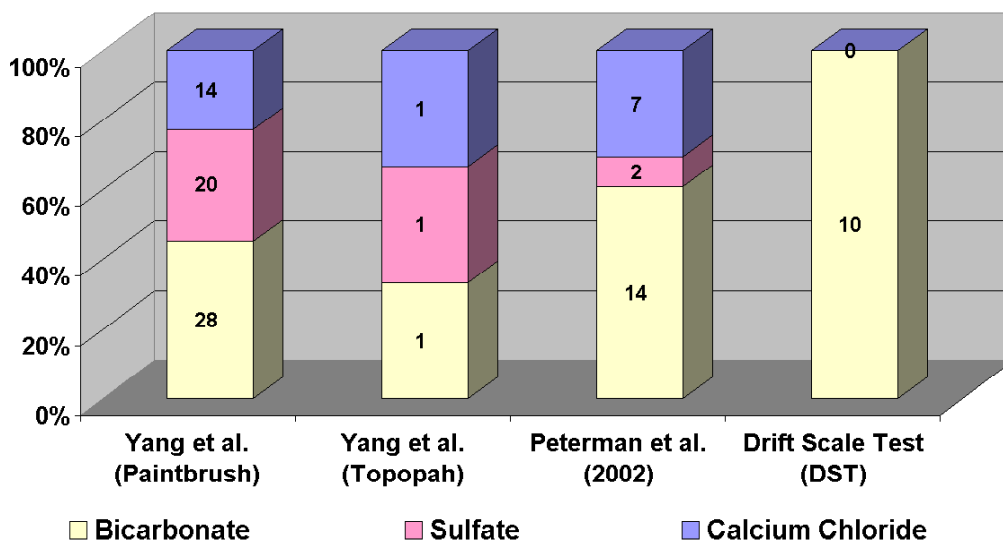


Figure 1-9. Distribution of observed water chemistries plotted in Figure 1-8. The pie chart shows the distribution of all observed waters, and the column chart shows the breakdown for each data set. Most of the observed waters fall in the bicarbonate and sulfate categories, and would be expected to evolve into relatively benign environments.

A geo-chemical model has been developed by the Project to more fully characterize the Engineered Barrier System (EBS) environment and is summarized in Figure 1-10 (BSC 2003a, ANL-EBS-MD-000033 REV 02 ICN 00; Peters 2003). This model uses five (5) experimentally determined pore-water chemistries as inputs to the Thermal Hydrology Chemistry (THC) Seepage Model, and generates approximately 3,700,000 water chemistries, representing 2000 spatial nodes, 370 increments in time, and 5 possible initial pore water chemistries. Of these, only those water chemistries in closes proximity to the drifts, and in a position to actually effect seepage into the drifts are carried forward for down-stream performance assessment calculations. Eventually, the evaporative concentration of 368 of these selected water chemistries is simulated with EQ3/6, with the output used to characterize the waters into 11 representative bins. Waters falling into a particular bin are expected to evolve in a similar way, approaching to various degrees on of the three vertices of the pseudo ternary discussed in the foregoing section. After establishment of the 11 bins of representative water chemistry, which corresponds to ambient seepage water before evaporative concentration, a second round of EQ3/6 simulations is performed. This series of predictions simulates the evaporation-to-dryness of the 11 bins of representative water chemistries. Evaporative concentrations are conducted for 9 different sensitivity cases, representing 3 levels of carbon dioxide partial pressure, and 3 levels of temperature. The output is in the form of ion concentrations and pH as a function of relative humidity (RH). These results serve as set of look-up tables for total system performance assessment (TSPA), where the index (look-up) variable is relative humidity.

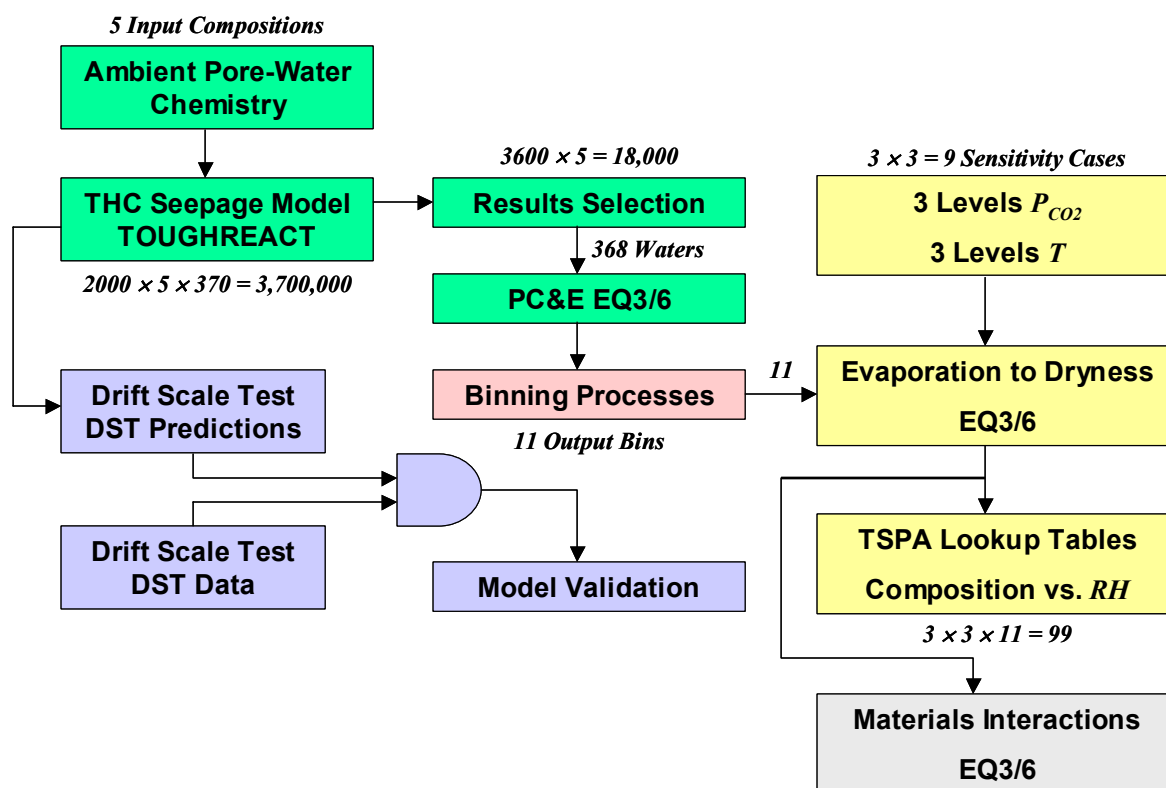


Figure 1-10. EBS Chemistry Model used to explore a broad and comprehensive range of evolved water chemistries inside the repository, based upon simulations of evaporation.

Insight can be gained from the characterization of input and output water compositions for the EBS Chemistry Model in terms of the Chemical Divide Theory, as shown in Figure 1-11 (Gdowski, Carroll, and Farmer 2003). The blue circles show the five input pore water chemistries, selected from pore water chemistries determined by Peterman et al. (2002) at the USGS. Since these five input pore water chemistries all fall below the boundary between the CaCl_2 -type and sulfate-type brines, in either the sulfate or bicarbonate regions, they would be expected to evolve to benign water chemistries. However, by accounting for mixing with fracture flow within matrices, and evaporation and transport within the rock, it is possible to evolve binned waters that fall within the CaCl_2 region. The 11 bins of representative water chemistries are shown as green squares, with the red triangles showing the eventual position of these binned water chemistries after evaporative concentration. Most of the binned water chemistries evolve to relatively benign sulfate- or bicarbonate-type brines, with relatively few evolving to CaCl_2 -type brines. For simplicity, results for the evaporative concentration of only one level of carbon dioxide partial pressure, and one level of temperature are shown. The yellow circles represent those water chemistries used thus far by the Project for corrosion testing, and are located close to the three vertices of this pseudo ternary diagram. These corrosion test solutions are therefore considered valid bounding environments. The use of EQ3/6 to simulate the evolution of representative bins of water chemistry is shown in Figures 1-12 through 1-14 (BSC 2003a, ANL-EBS-MD-000033 REV 02 ICN 00), with the corresponding evolution trajectories plotted in Figure 1-15 (Gdowski, Carroll, and Farmer 2003).

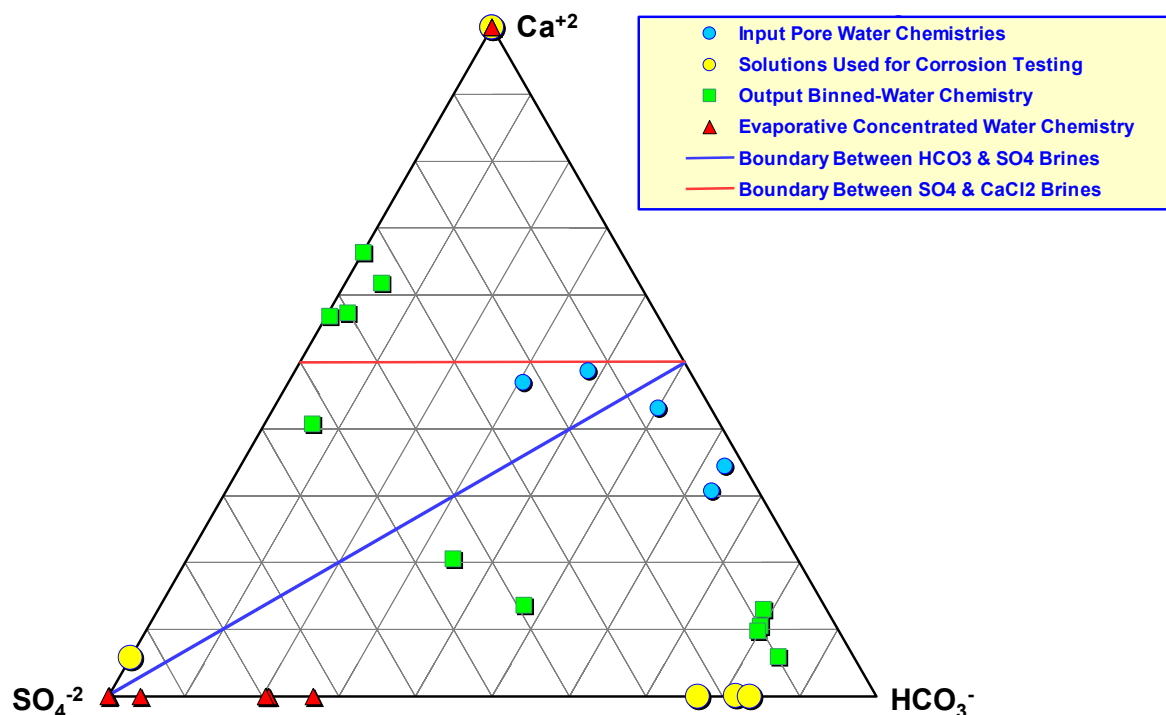


Figure 1-11. Characterization EBS Chemistry Model input and output water compositions in terms of the Chemical Divide Theory.

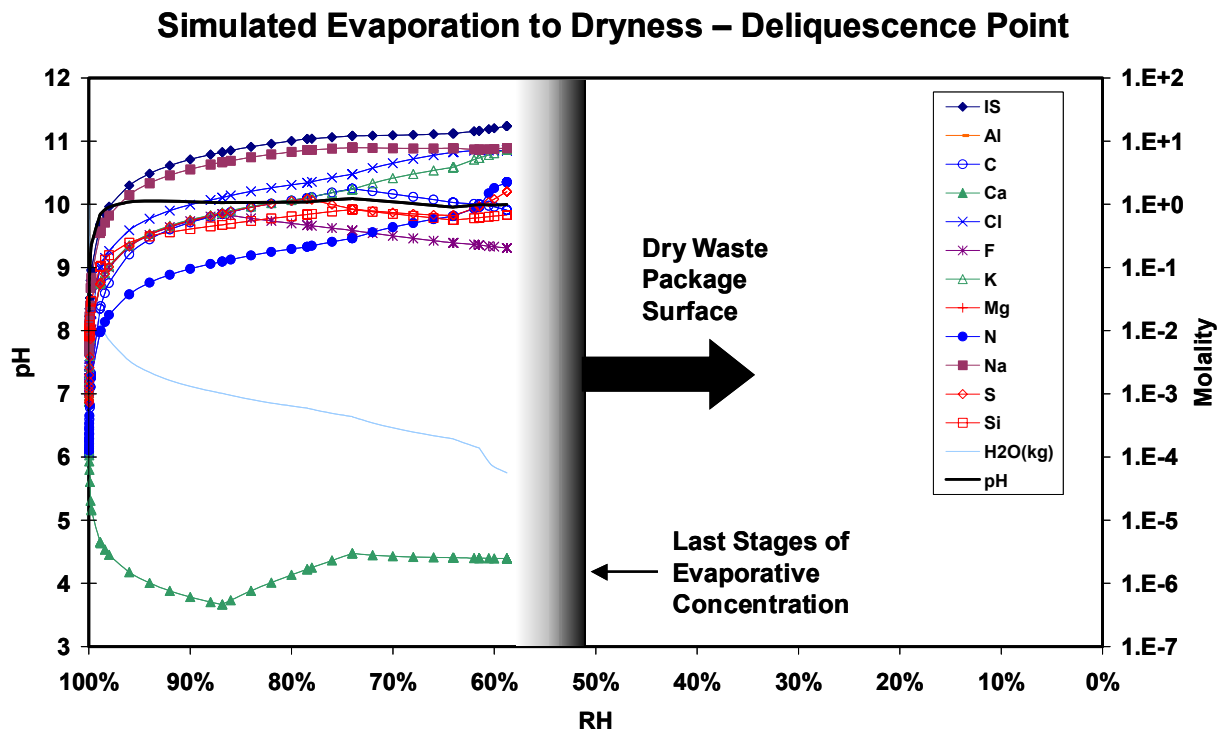


Figure 1-12. Evaporative concentration of Bin 11 water simulated with EQ3/6 code.

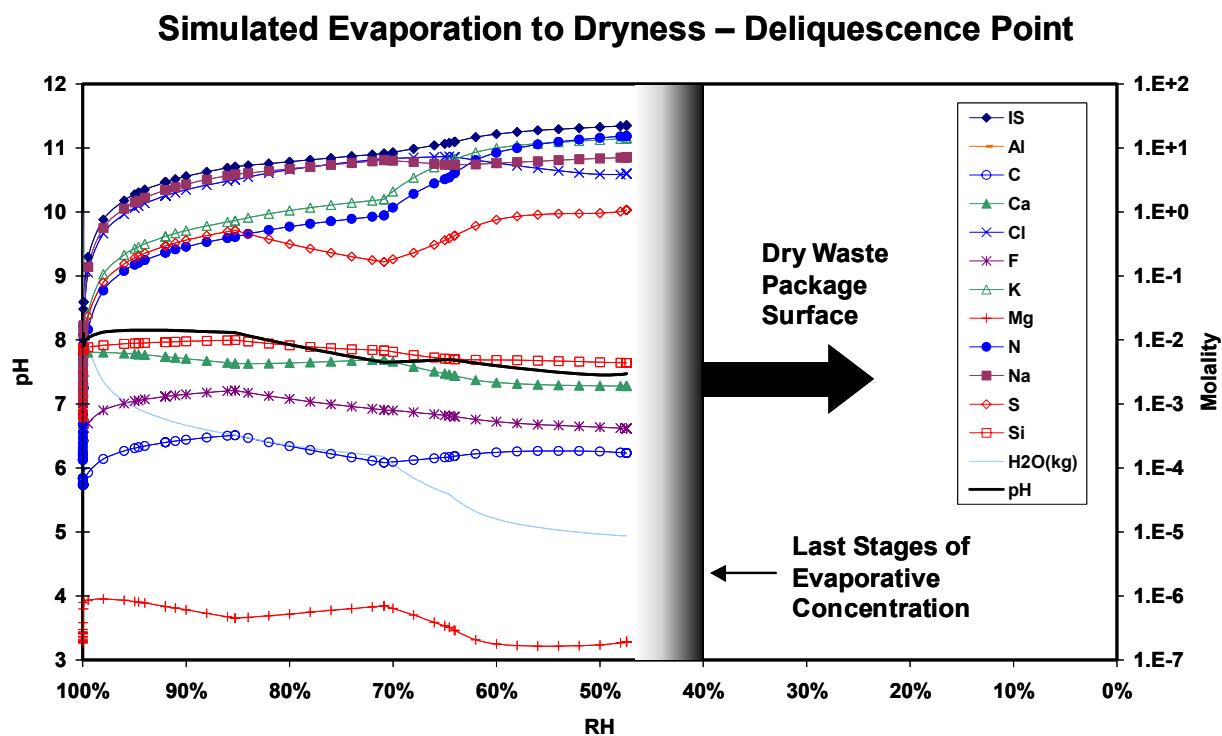


Figure 1-13. Evaporative concentration of Bin 4 water simulated with EQ3/6 code.

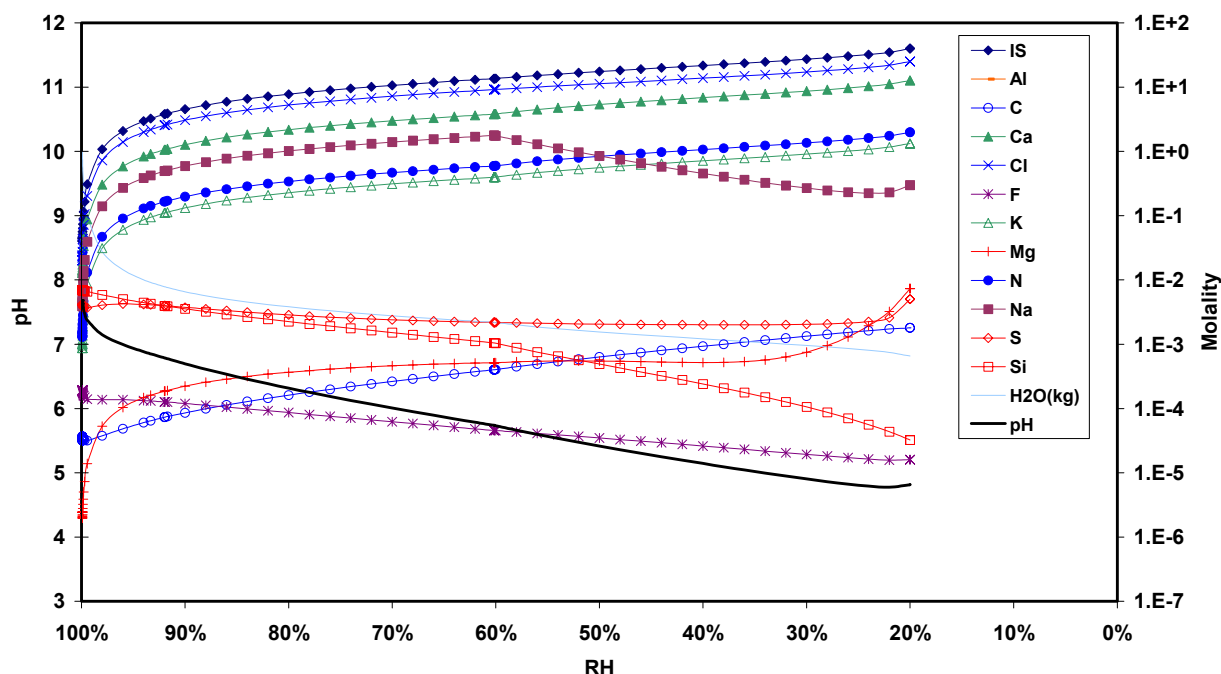


Figure 1-14. Evaporative concentration of Bin 1 water simulated with EQ3/6 code.

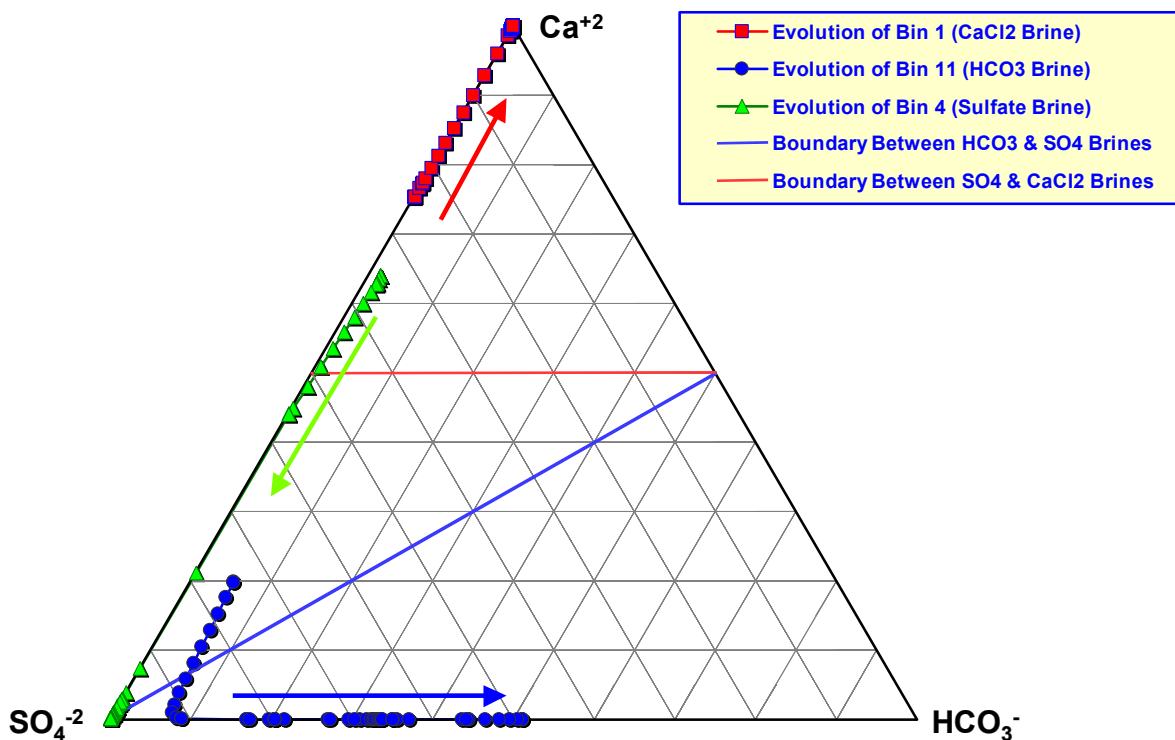


Figure 1-15. Evolution of water compositions predicted with EBS Chemistry Model shown in terms of the Chemical Divide Theory.

Bin 1 waters evolve to CaCl_2 -type brines, as expected. However, even though Bin 4 waters lie in the CaCl_2 region (very close to the CaCl_2 -sulfate boundary), they evolve to sulfate-type brines. Even though Bin 11 waters lie in the sulfate region, they evolve to bicarbonate-type brines. This shows that the idealized boundaries based on the simple Chemical Divide Theory (CDT) are idealized, and highly conservative. The simple CDT does not fully account for the complexities of real electrolytes, which contain many more species than can be accounted for in a simple ternary diagram. For example, in these diagrams, the precipitation of fluoride as calcite accounts for the difference between actual and idealized boundaries.

The evolved water chemistries predicted with the EBS Chemistry Model have been interpreted in terms of “time-integrated relative frequencies for crown waters” as shown in Table 1-3. While these frequencies may not be rigorous estimates of probability, they are quantitative measures of the number of thermally evolved crown-seepage brines that are predicted to fall into each of the eleven (11) representative bins. These frequencies should therefore reflect the distribution of thermally evolved waste package surface environments. It is noteworthy that less than 1% of the crown seepage waters fall into Bins 1 through 3, which would be expected to be CaCl_2 -type brines. Most of the waters ($\geq 99\%$) fall into Bins 4 through 11, which evolve to more benign electrolytes. The standard solutions used for corrosion testing by the Project have also been categorized in terms of the representative bins, and seem to cover the range of expected conditions. It should be noted that no localized corrosion or stress corrosion cracking of Alloy 22 or Ti Grade 7 have been observed after more than five-years exposure to solutions that include SDW, SCW and SAW in the Long Term Corrosion Test Facility (LTCTF). These tests cover Bins 4 through 11, with a combined time integrated frequency of $\geq 99\%$.

Table 1-3. The probability of occurrence of waters evolved during the evaporative concentration of representative bins of (crown seepage) water chemistry.

Bin	Time Integrated Relative Frequency for Crown Waters	Average End-Point RH	98% RH Bin	End Point Brine	Representative Corrosion Test Solution
1	~ 0%	20%	Ca-Cl	Ca-Cl	5-8 M CaCl_2 + Nitrate
2	~ 0%	24%	Na-Cl	Ca-Cl	5-8 M CaCl_2 + Nitrate
3	~ 1%	40%	Na-Cl	K-Ca-Cl- NO_3	5-8 M CaCl_2 + Nitrate
4	~ 15%	50%	Na-Cl	Na-K-Cl- NO_3	SSW, SAW
5	~ 10%	60%	Na-Cl	Na-K-Cl	SSW, SAW
6	~ 1%	60%	Na-Cl	Na-K-Cl- NO_3	SSW, SAW
7	~ 1%	60%	Na-Cl	Na-K-Cl- NO_3	SSW, SAW
8	~ 1%	60%	Na- CO_3	Na-K-Cl	SDW, SCW, BSW
9	~ 20%	60%	Na- CO_3	Na-K- NO_3 -Cl	SDW, SCW, BSW
10	~ 1%	60%	Na- CO_3	Na-K- CO_3 -Cl	SDW, SCW, BSW
11	~ 50%	60%	Na- CO_3 -Cl	Na-K- CO_3 -Cl	SDW, SCW, BSW

Note: “Crown Waters” are those waters in fractures above drift > 10% liquid saturation

As shown in Figures 1-16 and 1-17, even those waters that appear to be CaCl_2 -type brines have significant levels of nitrate ion, which serves as a strong corrosion inhibitor. The important role of this naturally occurring nitrate will be discussed in the following section.

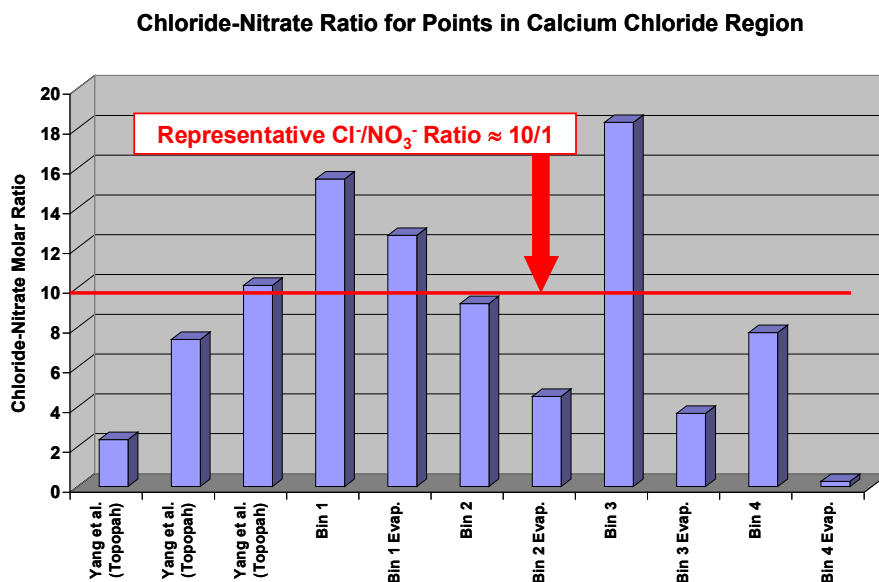


Figure 1-16. Chloride-nitrate ratios ($[\text{Cl}^-]/[\text{NO}_3^-]$) for Bins 1, 2, 3 and 4. The starting compositions of these representative solutions are within the CaCl_2 region of the ternary diagram. The ratios for three pore-water samples taken from Topopah Springs formation are shown for comparison.

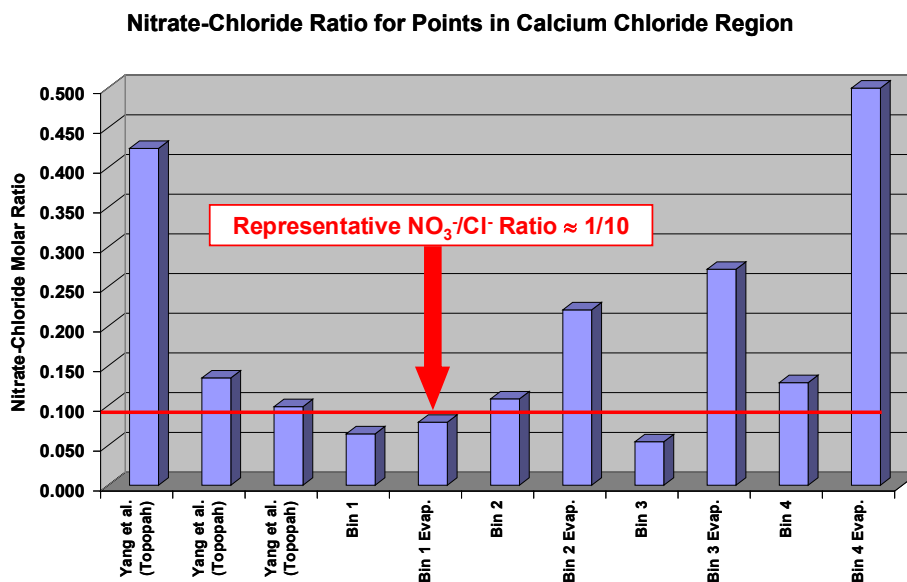


Figure 1-17. Nitrate-chloride ratios ($[\text{NO}_3^-]/[\text{Cl}^-]$) for Bins 1, 2, 3 and 4. The starting compositions of these representative solutions are within the CaCl_2 region of the ternary diagram. The ratios for three pore-water samples taken from Topopah Springs formation are shown for comparison.

Based upon the foregoing analyses, standardized solutions developed by the Project are believed to be relevant test environments. These solutions include simulated dilute water (SDW), simulated concentrated water (SCW), and simulated acidified water (SAW) at 30, 60, and 90°C, as well as simulated saturated water (SSW) at 100 and 120°C. The SSW used for testing is an abstract embodiment of this observation. The SSW formulation is based upon the assumption that evaporation of J-13 eventually leads to a sodium-potassium-chloride-nitrate solution. The absence of sulfate and carbonate in this test medium is believed to be conservative, in that carbonate would help buffer pH in any occluded geometry such as a crevice. It is well known that polyprotic acids serve as buffers. The compositions of these environments are given in the following table (Table 1-4) (BSC 2003d, ANL-EBS-MD-000003 REV 01 ICN 00).

Table 1-4. Target Composition of Standard Test Media Based Upon J-13 Well Water

	Concentration (mg/L)		
Ion	Simulated Dilute Water (SDW)	Simulated Concentrated Water (SCW)	Simulated Acidified Water (SAW)
	60 & 90 °C	60 & 90 °C	60 & 90 °C
K	34	3400	3400
Na	409	40,900	37,690
Mg	1	<1	1000
Ca	0.5	<1	1000
F	14	1400	0
Cl	67	6700	24,250
NO ₃	64	6400	23,000
SO ₄	167	16,700	38,600
HCO ₃	947	70,000	0
Si (aq)	27 (60 °C) 49 (90 °C)	27 (60 °C) 49 (90 °C)	27 (60 °C) 49 (90 °C)
PH	9.8 – 10.2	9.8 – 10.2	2.7

Source: DTN LL000320405924.146

Recently, another relevant test environment has been postulated. Basic Saturated Water (BSW) has a pH between 11 and 13, and a boiling point near 110°C. This test medium was established on the basis of results from a distillation experiment (Wang 1999). The total concentration of dissolved salts in the starting liquid was approximately five-times (5×) more concentrated than that in the standard SCW solution. It was prepared by using five-times the amount of each chemical that is specified for the preparation of SCW. After evaporation of approximately ninety percent (~90%) of the water from the starting solution, the residual solution reaches a maximum

chloride concentration and has a boiling point of ~111°C. The resultant BSW solution contains (sampled at 111°C) 9% chloride, 9% nitrate, 0.6% sulfate, 0.1% fluoride, 0.1% metasilicate, 1% TIC (total inorganic carbon from carbonate and bicarbonate), 5% potassium ion and 11% sodium ion. A recipe for preparing synthetic BSW with an alkaline pH of ~11 is shown in the following table (Table 1-5) (CRWMS M&O 2000d, ANL-EBS-MD-000003 REV 00 ICN 00).

Table 1-5. Initial BSW Solution Recipe

Chemical	Quantity (g)
Na ₂ CO ₃ (anhydrous)	10.6
KCl	9.7
NaCl	8.8
NaF	0.2
NaNO ₃	13.6
Na ₂ SO ₄ (anhydrous)	1.4
H ₂ O	55.7
PH	11.3 (measured at room temperature)

The synthetic BSW solution represented by Table 1-5 has been slightly modified for these and other corrosion tests, yielding BSW-13, BSW-12, and BSW-11. These recipes are summarized below in Table 1-6 (CRWMS M&O 2000d, ANL-EBS-MD-000003 REV 00 ICN 00). The three solutions have pH values of approximately 13, 12, and 11 respectively. All BSW-type solutions contain 9% chloride, 9% nitrate, 0.6% sulfate, and 0.1% fluoride. Sodium and potassium ions are used to balance the charge. More specifically, each testing solution contains 8.7 g KCl, 7.9 g NaCl, 0.2 g NaF, 13.6 g NaNO₃, and 1.4 g Na₂SO₄ (anhydrous). The pH 13 solution (BSW-13) was prepared by adding 65 mL of water and 2.0 mL of the 10 N NaOH to the chemicals (total weight = 100 g). The measured pH was 13. The pH 12 solution (BSW-12) was prepared by adding 66 mL of water and 2.0 mL of the 1 N NaOH to the chemicals. The measured pH was 12.25. The pH 11 solution (BSW-11) was prepared by adding 66 mL of water and 2.0 mL of the 0.1 N NaOH to the chemicals. The measured pH was 11. It should be pointed that the modified BSW solutions are not buffered. In order to add some soluble silica to the solution, the BSW solution recipe was later revised to contain 4.0 g (~1% metasilicate) by adding sodium metasilicate (Na₂SiO₃·9H₂O). With the addition of the metasilicate the pH was increased from 11 to 13 as measured at room temperature.

Table 1-6. Modified BSW Solution Recipes

	BSW-13	BSW-12	BSW-11
Chemical	Quantity	Quantity (g)	Quantity (g)
KCl	8.7 g	8.7 g	8.7 g
NaCl	7.9 g	7.9 g	7.9 g
NaF	0.2 g	0.2 g	0.2 g
NaNO ₃	13.0 g	13.0 g	13.0 g
Na ₂ SO ₄ (anhydrous)	1.4 g	1.4 g	1.4 g
H ₂ O (deionized)	66 ml	66 ml	66 ml
10N NaOH	2 ml		
1N NaOH		2 ml	
0.1N NaOH			2 ml
CO ₂ partial pressure	0	0	0
pH (at room temperature)	13.13	12.25	11.11

It has been noted that the pH of aqueous solutions is dependent on the partial pressure of gaseous CO₂. The implication of this is that unless many constraints are taken to control the pH of the BSW solution, the pH may vary with test conditions. The partial pressure of CO₂ that is in equilibrium with the revised BSW solution is unknown. In order to conduct a long-term test (few months to a year), the test environment should be stable. It was decided that to make a stable test solution, carbonate and silicates should not be added since both species can affect solution pH. Sodium hydroxide is used instead to maintain higher pH values. Gaseous CO₂ must be removed from the air passing above the solution since it affects the solution pH. With no gaseous CO₂ in contact with the solution, and without carbonate, bicarbonate and silicates in solution, the test environment is relatively stable.

Low Temperature Region ($100^{\circ}\text{C} \leq T$; 1,000-10,000 Years)

As the waste package cools to a temperature below the threshold for crevice corrosion in CaCl₂-type brines (believed to represent a worst-case scenario), waste package performance becomes insensitive to the chemistry of any water entering the drifts. The Alloy 22 will provide protection for the spent nuclear fuel and high-level waste under, even in such worst-than-expected environments.

The waste package is protected by different mechanisms in each of the three temperature regions. The Dry-out Region effectively provides an additional barrier, and additional protection for the waste package. The Project's overall strategy is consistent with conceptual models generated by other experts in the field. Please refer to the acknowledgements for a detailed list of contributors to the work presented here.

Chapter 2. Description of the Integrated Degradation-Mode Model

Systematic interactions between the in-drift environment and various degradation modes will influence the performance of the waste-package and drip-shield, and are shown schematically in Figure 2-1. This schematic accounts for a wide range of degradation modes, each operable to varying degrees, depending upon the temperature regime [Farmer 1991, 2000a, 2000b, 2003]. In the Pre-Closure Region (0-50 Years), the walls of the drifts will be kept dry by ventilation air, and no significant degradation of the waste packages or drip shields is expected. In the Dry-Out Region ($T \geq 120^{\circ}\text{C}$, 50 to 400 Years), degradation phenomena of importance at the relatively high temperature includes thermal aging and phase stability, dry oxidation, and corrosion underneath deliquescence brines (formed by the absorption of air-borne water by dust deposits). In the Transition Region ($120^{\circ}\text{C} \geq T \geq 100^{\circ}\text{C}$, 400 to 1000 Years), the waste package is above the boiling point, and can concentrate seepage brines through evaporation. The modes of attack in these concentrated, potentially aggressive brines include: uniform general corrosion (GC); localized corrosion (LC); stress corrosion cracking (SCC), and hydrogen induced cracking. In the Low Temperature Region ($100^{\circ}\text{C} \leq T$; 1,000-10,000 Years), seepage brines can enter the drift, but the driving force for evaporative concentration would be less. The water chemistry would be expected to be more benign than that encountered in the transition region. Here too the possible modes of attack include GC, LC, SCC and HIC. Microbial influenced corrosion (MIC) may also occur. These modes of failure are dealt with in this TBR, and are illustrated in Figure 2-1. In addition to these scenarios, other possible events that could lead to failure include earthquakes, volcanic activity, and human intrusion. However, these scenarios are not dealt with in this TBR.

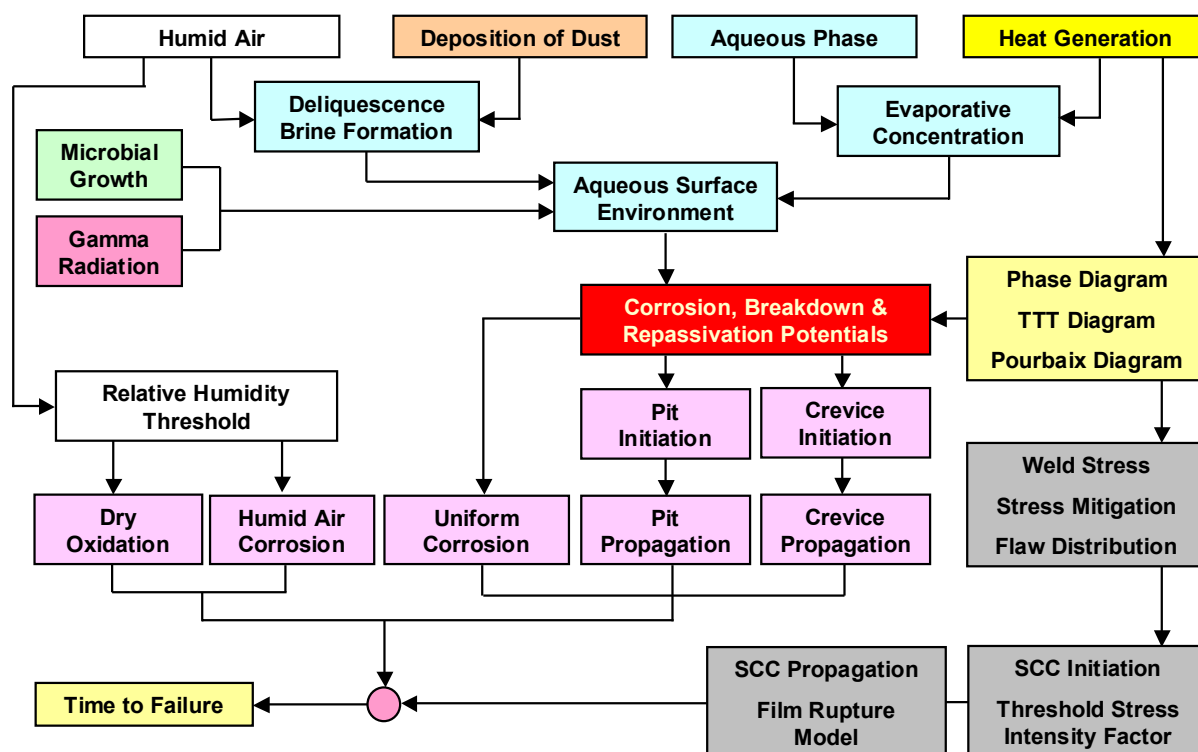


Figure 2-1. Systematic interactions between the in-drift environment and various degradation modes will influence overall waste-package and drip-shield performance.

Alloy 22 is a metastable austenitic alloy, where intermetallic phases can be precipitated at high temperature (BSC 2003c, ANL-EBS-MD-000002 REV 01 ICN 00). These intermetallic phases (P, σ and μ) are rich in those elements responsible for the exceptional corrosion resistance of Alloy 22, and can therefore cause depletion of the passivating elements in close proximity to the precipitates. Such depleted, localized areas may be more susceptible to corrosion than areas where no precipitation has occurred. Furthermore, these precipitates may cause degradation of the mechanical properties. Predictions of multi-component phase diagrams have enabled the Project to predict the phases that are possible, as a function of elemental composition and temperature. Time-temperature-transformation (TTT) diagrams have been predicted, and are used to calculate the rate at which allowable phases (precipitates and long range ordering) can occur. As will be discussed in a subsequent section, such predictions indicate insignificant precipitation and long-range ordering (LRO) during the 10,000-year service life of the repository, as long as the temperature is kept below 300°C.

Dry oxidation is another high-temperature degradation mode (BSC 2003d, ANL-EBS-MD-000003 REV 01 ICN 00; CRWMS M&O 2000d, ANL-EBS-MD-000003 REV 00 ICN 00). The reaction of oxygen with Alloy 22, or Ti Grade 7, can cause a uniform thickening of the oxide layer on the surface. The surface oxide can consist of any of the alloying elements/constituents, through a chromium oxide layer has been assumed as the basis of approximate calculations. The rate of dry oxidation at the highest temperature in the repository is insignificant compared to other modes of attack.

As the temperature begins to decrease during cooling, the possibility of aqueous phase electrolytes exists, first through the formation of deliquescence brines, and then through the evaporative concentration of seepage brines. Modes of attack experienced in aqueous electrolytes include general uniform corrosion, localized corrosion, and environmental fracture. In the case of general corrosion, the rate of dissolution is uniform over all surfaces, and is due to the transport of cations from the metal-oxide interface to the oxide-electrolyte interface, where the formation of soluble metal-containing corrosion products can occur. The transport of cations and/or anions through the passive oxide film is controlled by the diffusion and electric field-driven electromigration.

Localized corrosion is any type of distributed, non-uniform corrosive attack of the surface, and is due to the localized failure of the passive film. Such localized failure may be due to surface inclusions of relatively soluble species, the precipitation of small soluble halide crystallites on the passive film, destabilization of the passive film within occluded areas such as crevices, due to the lowering of pH, which results from the combined effects of differential aeration, the hydrolysis of dissolved metal cations within the crevice, and the electric field-driven electromigration of aggressive halide anions into the crevice. Localized attack may also occur at sites where intermetallic precipitation has occurred, which includes exposed grain boundaries.

Crevices may be formed between the waste package and supports, beneath mineral precipitates, corrosion products, dust, rocks, cement, and bio-films, and between layers of the containers. In the absence of inhibitor and buffer ions, the hydrolysis of dissolved metal can lead to the accumulation of H^+ and a corresponding decrease in pH. Electromigration of Cl^- (and other

anions) into the crevice must occur to balance cationic charge associated with H^+ ions (Gartland 1997; Walton et al. 1996; Farmer et al. 1998). These exacerbated conditions can set the stage for subsequent attack of the corrosion resistant material by passive corrosion, pitting (initiation and propagation), stress corrosion cracking (SCC), or other mechanisms (Farmer et al. 1998, 2000a, 2000b). Gamma radiolysis may produce hydrogen peroxide, thereby increasing the open circuit corrosion potential (Glass et al. 1986; Kim 1987, 1988, 1999a, 1999b).

This TBR documents the analyses and models for general and localized corrosion of the waste package outer barrier (WPOB). An overview of the model, as it is used in TSPA, is presented in Figure 2-2 (BSC 2003d, ANL-EBS-MD-000003 REV 01 ICN 00). The general and localized corrosion models have been used to analyze the degradation of the Alloy 22 outer barrier of the waste package by general and localized corrosion, under the expected repository exposure condition, and over the repository performance period. The general and localized corrosion models include several sub-models, which account for dry oxidation (DOX), aqueous general corrosion (GC), localized corrosion (LC), which includes crevice corrosion initiation and propagation, and microbial-influenced corrosion (MIC).

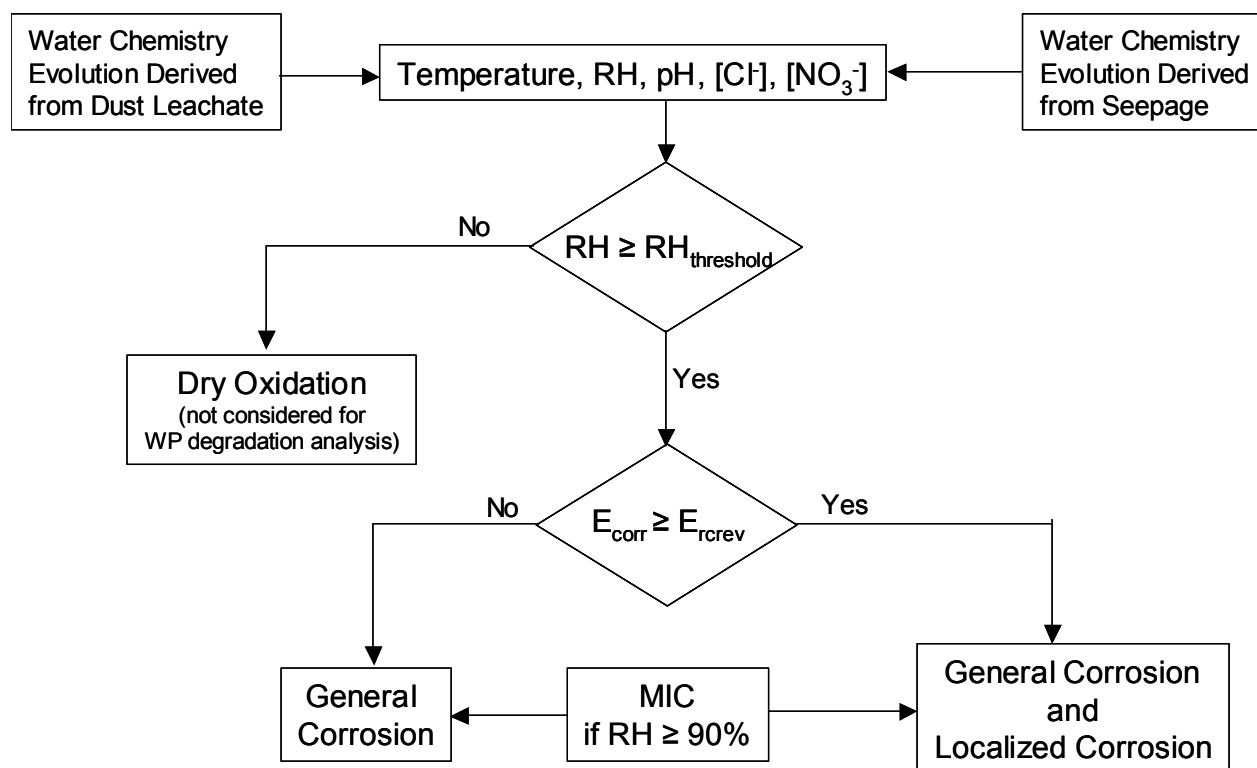


Figure 2-2. Corrosion model used to predict degradation of Alloy 22 WPOB.

The passivity of Alloy 22 was evaluated by examining the oxide layers formed in a mixed-salt environment at 95°C. The surface analysis data indicated that the oxide layers responsible for passivity of Alloy 22 consist of chromium oxide (Cr_2O_3) containing Ni. The collected data indicated that (1) the passive films become very protective and stable, (2) contributions from metal corrosion become extremely small, and (3) redox reactions from the species in solution are stable (BSC 2003d, ANL-EBS-MD-000003 REV 01 ICN 00).

Dry oxidation is not a performance limiting process of the WPOB under the exposure condition expected in the repository and not considered for the waste package performance analysis in the repository. Thermal aging and phase instability of the WPOB is expected to be insignificant for the thermal conditions expected in the repository, and this process is therefore not considered in the waste package performance analysis. General corrosion of the WPOB occurs when the RH at the waste package surface is equal to or greater than the RH threshold ($RH_{threshold}$) for corrosion initiation. The general corrosion rate of the WPOB is a function of temperature, expressed with an activation energy using a modified Arrhenius relation. Because of very low general corrosion rates of the WPOB for the conditions expected in the repository, the waste package performance is not limited by the general corrosion during the regulatory time period (BSC 2003d, ANL-EBS-MD-000003 REV 01 ICN 00).

The WPOB is subject to MIC when the relative humidity at the waste package surface is equal to or greater than 90 %. The MIC effect is represented by an enhancement to the abiotic general corrosion rate of the WPOB (BSC 2003d, ANL-EBS-MD-000003 REV 01 ICN 00).

Crevice corrosion of the WPOB is modeled with the crevice corrosion initiation model and propagation model. The initiation model assumes that crevice corrosion of the WPOB occurs when the steady-state corrosion potential (E_{corr}) is equal to or greater than the crevice repassivation potential (E_{rcrev}). This criterion is expressed mathematically as: $\Delta E \leq 0$ where $\Delta E = E_{rcrev} - E_{corr}$. The WPOB is not subject to crevice corrosion if the solution contacting the waste package has a neutral to alkaline pH or contains significant concentrations of inhibitive ions such as nitrate. The WPOB is potentially susceptible to crevice corrosion if an acidic chloride-containing solution with relatively lower concentrations of inhibitive ions contacts the waste package while it is at elevated temperatures. However, once the waste package cools to temperatures that are lower than a minimum temperature for crevice corrosion initiation in such chloride-containing solutions, the waste packages is completely immune to crevice corrosion. Such threshold temperatures depend on pH, chloride concentration and nitrate concentration of the contacting solutions. Additional details of the model summary are given in the following subsections (BSC 2003d, ANL-EBS-MD-000003 REV 01 ICN 00).

Recall that the waste package is affected by different degradation modes (mechanisms) in each of the Three Temperature Regions previously discussed. The Dry-Out Region effectively provides an additional barrier, and thus additional protection for the waste package.

Chapter 3. Waste Package and Drip Shield Materials Selection, Design, and Fabrication

Spent nuclear fuel and high-level waste (70,000 MTHM) will be placed in approximately 11,000 waste containers (Figure 3-1). The License Application (LA) Design for the waste package (WP) is based upon double-wall construction. The inner wall serves as a structural support and is constructed from Type 316 stainless steel with controls on carbon and nitrogen levels making it equivalent to so-called 316 Nuclear Grade (316NG) stainless steel (Figure 3-1). The corrosion-resistant waste package outer barrier (WPOB) is constructed from Alloy 22, a high-performance nickel based alloy. The structural support (316NG) cylinder is inserted into the WPOB (Alloy 22) using a thermal fit operation. Solution heat treatment of the as-fabricated waste package is used to remove fabrication-related residual tensile stress. After the container is filled with high-level waste (HLW) or spent nuclear fuel (SNF), at the site hot cell facility, two lids made of Alloy 22 will be joined to the container by gas tungsten arc welding (GTAW). Other advanced joining methods are also under investigation by OCRWM, which include reduced pressure electron beam and friction stir welding. Since residual weld stress at the closure might drive SCC or HIC, a post-weld stress mitigation process will be used to removing the tensile stress from the outer surface, thereby precluding the possibility of environmental fracture. In the past, localized induction annealing was considered for stress mitigation, but has now been replaced with a non-thermal stress mitigation process. The baseline stress mitigation process for LA is LSP, though CPB is also being explored as a less expensive alternative. These waste containers will be placed horizontally in drifts, underneath drip shields (Figure 3-2). The current Exploratory Studies Facility (ESF) shown in Figure 3-3 is expected to serve as the starting point for the repository. The titanium alloy drip shield (DS) is used to prevent dripping water, as well as rocks, from directly impinging the waste package.

Materials Selection for the Waste Package

Alloy 22 (UNS N06022) will be used for construction of the outer barrier of the waste package, and has already been used for the construction of prototypes (Figure 3-4). As shown in Table 3-1, it consists of 20.0-22.5% Cr, 12.5-14.5% Mo, 2.0-6.0% Fe, 2.5-3.5% W, 2.5% (max.) Co, 0.015% (max.) C, and balance Ni (ASTM 1997a). Other impurity elements include P, Si, S, and Mn (Treseder et al. 1991). Alloy 22 is less susceptible to localized corrosion (LC) in environments that contain Cl⁻ than Alloys 825 and 625, materials of choice in earlier designs. The unusual LC resistance of Alloy 22 is apparently due to the additions of Mo and W, both of which are believed to stabilize the passive film at very low pH (Hack 1983). The oxides of these elements are very insoluble at low pH. Consequently, Alloy 22 exhibits relatively high thresholds for localized attack. Very high repassivation potentials have been observed by some (Gruss et al. 1998), while others have found very low corrosion rates in simulated crevice solutions containing 10 wt. % FeCl₃ (Haynes 1987, 1988). Furthermore, no significant localized attack of Alloy 22 has been seen in crevices exposed to water compositions representative of those expected in the repository. Such tests have been conducted in the Yucca Mountain Project's Long Term Corrosion Test Facility (LTCTF).

Alloy 22 is one of the most corrosion resistant commercially available metallic alloys suitable for the full range of environments that could potentially exist on the waste package surfaces. Alloy 22 is believed to have better corrosion resistance than Alloy C, which is similar in composition but with lower Cr (Table 1). The mirror finish on the Alloy C sample shown in Figure 4 was unharmed after more than fifty-years exposure to the Atlantic seacoast environment at Kure Beach, North Carolina (courtesy of the Nickel Development Institute). A direct comparison of the general corrosion rates of several nickel based alloys and Type 316L stainless steel exposed in an oxidizing acidic chloride solution known as the 'Green Death' solution, Figure 3-6 show that Alloy 22 has significantly greater resistance to localized corrosion, Figure 3-6 (courtesy of Haynes Alloy). Alloy 22 has also demonstrated far greater resistance to pitting attack during anodic polarization in 10% NaCl solutions at 90°C than Alloy 825, Figure 3-7 (Roy et al.).

The Engineered Barrier System (EBS) design is very robust in that it provides for defense in depth through the use of a protective drip shield that will be made from a second corrosion-resistant material, Titanium Grade 7. Like Alloy 22, this material is also very resistant to localized corrosion in chloride media, although it appears to be somewhat more susceptible to stress corrosion and hydrogen induced cracking. The composition of several titanium alloys, including Grade 7, are shown in Table 3-2.

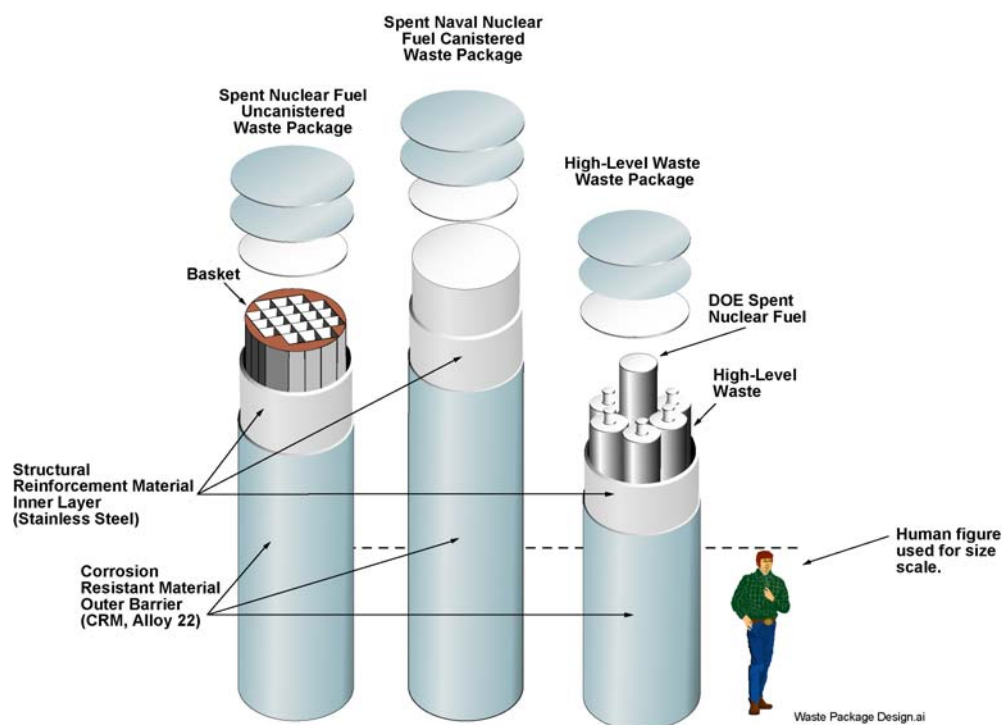


Figure 3-1. Three types of waste packages that will be used for the storage of spent nuclear fuel and high-level waste.

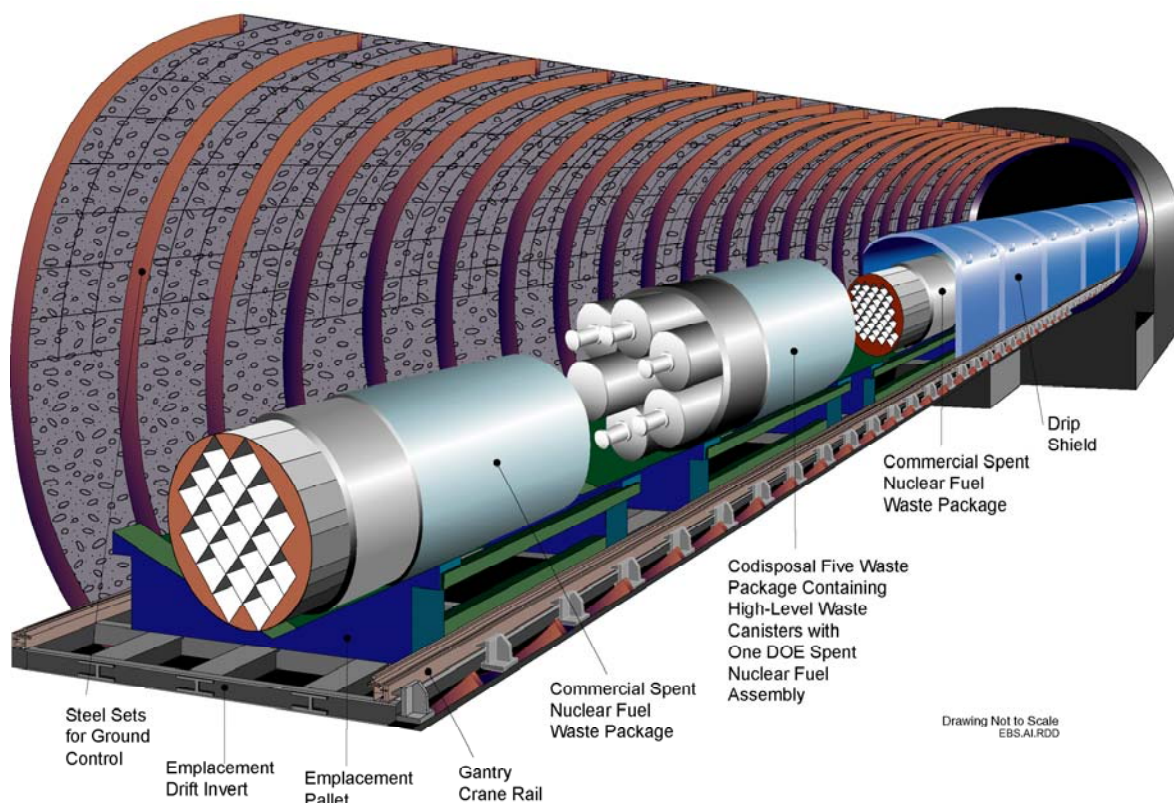


Figure 3-2. Conceptual drawing of the Engineered Barrier System (EBS) at Yucca Mountain, with horizontally-emplaced waste packages underneath drip shields.



Figure 3-3. Existing Exploratory Studies Facility (ESF) with the entrance at the North Portal.



Figure 3-4. Quarter-length full-diameter SR configuration waste package mockup with a corrosion-resistant outer layer made of nickel-based Alloy 22, and an inner structural support made of Type 316L stainless steel.

Table 3-1. Composition of Ni-Cr-Mo Alloys

UNS No.	Alloy Name	Cr	Mo	W	Fe	Co	Mn	Si	C	P	S	Ni	Other
N06022	Hastelloy C-22	20.0-22.5	12.5-14.5	2.5-3.5	2.0-6.0	2.5 max	0.50 max	0.08 max	0.015 max	0.02 max	0.02 max	Rem	V: 0.35 max
N06455	Hastelloy C-4	14.0-18.0	14.0-17.0		3.0 max	2.0 max	1.0 max	0.08 max	0.015 max	0.04 max	0.03 max	Rem	Ti: 0.70 max
N10276	Hastelloy C-276	14.5-16.5	15.0-17.0	3.0-4.5	4.0-7.0	2.5 max	1.0 max	0.08 max	0.02 max	0.030 max	0.030 max	Rem	V: 0.35 max
N10002	Hastelloy C	14.5-16.5	15.0-17.0	3.0-4.5	4.0-7.0	2.5 max	1.00 max	1.00 max	0.08 max	0.040 max	0.030 max	Rem	V: 0.35 max
N06059	Nicofer 59	22.0-24.0	15.0-16.5		1.5 max	0.3 max	0.5 max	0.010 max	0.010 max	0.015 max	0.010 max	Rem	Al: 0.1-0.4
N06686	Inconel 686	19.0-23.0	15.0-17.0	3.0-4.4	5.0 max		0.75 max	0.08 max	0.010 max	0.04 max	0.02 max	Rem	
N06200	Hastelloy C-2000	22.0-24.0	15.0-17.0		3.0 max	2.0 max	0.50 max	0.08 max	0.010 max	0.025 max	0.010 max	Rem	Cu: 1.3-1.9

Table 3-2. Composition of Titanium Alloys

UNS No.	Grade	Intentional Elements	Residual Elements	Other
R52400	Grade 7	Pd: 0.12-0.25	C: 0.03 max; Fe: 0.30 max; H: 0.015 max; N: 0.03 max; O: 0.25 max	
R52402	Grade 16	Pd: 0.04-0.08	C: 0.10 max; Fe: 0.30 max; H: 0.010 max; N: 0.03 max; O: 0.25 max	Other residuals: each 0.1 max; total 0.4 max
R56403 R56405	Grade 24	Al: 5.5-6.5; V: 3.5-4.5; Pd: 0.04-0.08	C: 0.10 max; Fe: 0.40 max; H: 0.015 max; N: 0.05 max; O: 0.20 max	Other residuals: each 0.1 max; total 0.4 max
R53400	Grade 12	Mo: 0.2-0.4; Ni: 0.6-0.9	C: 0.08 max; Fe: 0.30 max; H: 0.010 max; N: 0.03 max; N: 0.020 max; O: 0.25 max	



Figure 3-5. The mirror finish on this Alloy C specimen was unharmed after more than fifty-years exposure to the Atlantic seacoast environment at Kure Beach, North Carolina. Alloy 22 is believed to have better corrosion resistance than Alloy C.

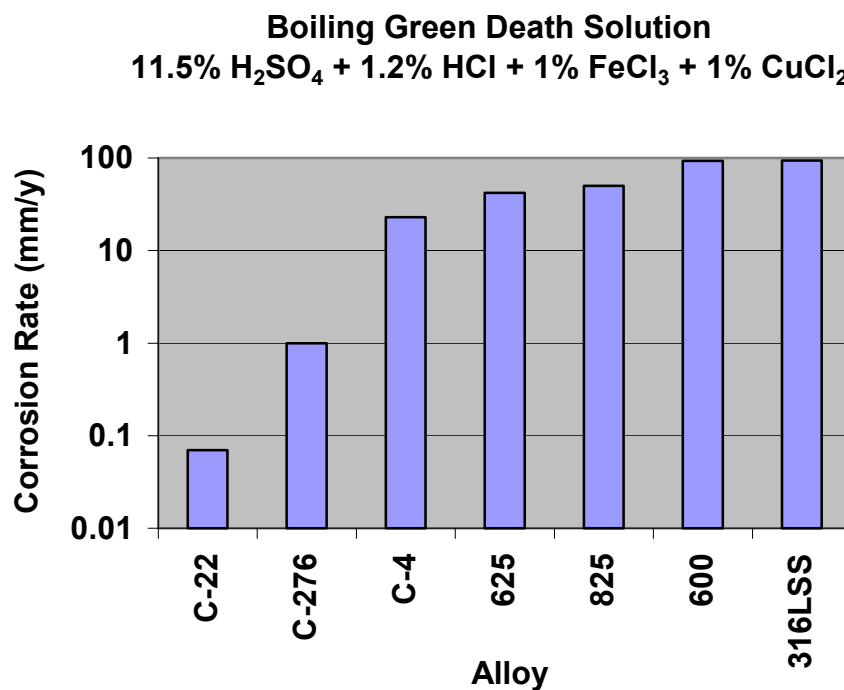


Figure 3-6. A direct comparison of the corrosion rates of several nickel-based alloys (and Type 316L stainless steel) after exposure to boiling green death solution.

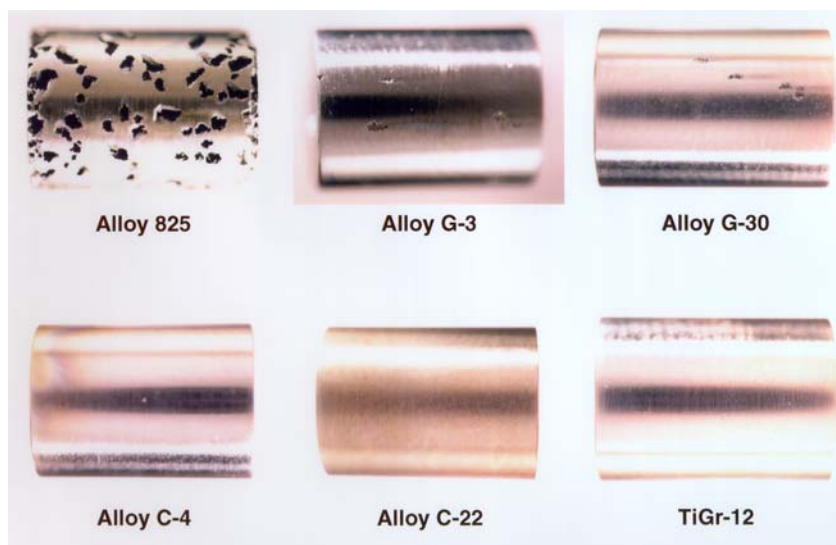


Figure 3-7. The susceptibility of Alloy 22 to localized corrosion in acidified 10% NaCl solution experienced during potentiodynamic polarization.

Chapter 4. Long-Term Thermal Aging of Alloy 22 in Dry-Out Region

Aside from the final waste package (WP) lid closure welding thermal cycle, the WP Alloy 22 barrier temperature must be kept below 350°C to prevent degradation of cladding on spent nuclear fuel. In fact, the LA drift emplaced WP surface temperature will remain significantly below 300°C as indicated in Figure 1-1. With these constraints, the impact of thermal aging and phase instability on the corrosion of Alloy 22 are expected to be minimal. Early work by Summers (CRWMS M&O 2000h, ANL-EBS-MD-000002 REV 00 ICN 00) indicated that the phase stability of Alloy 22 base metal will not be a problem at less than about 300°C. More recently, the precipitation kinetics has been modeled based on fundamental thermodynamics and kinetic concepts and principles (BSC 2003c, ANL-EBS-MD-000002 REV 01). This model is being used to provide predictive insight into the long-term metallurgical stability of Alloy 22 under repository relevant conditions.

Prediction of Phase Diagrams

Kinetic and thermodynamic modeling are combined and applied to the study of diffusion-controlled transformations [ANL-EBS-MD-000002 REV 01]. These kinetic studies were focused on the time-dependent formation of complex tetrahedrally close-packed (TCP) phases (also called topologically close packed) and long range ordering (LRO) in terms of phase evolution from the fcc matrix for times up to 10,000 years. The approach used in the kinetic and thermodynamic modeling involved simulating the Ni-Cr-Mo-W alloy system with a series of increasingly more complex calculations. A quantitative analysis of the phase formation in samples annealed at various temperatures and for several aging times is being performed to reduce uncertainties in this study's conclusions. In these simulations, grain boundary formation is not considered. Precipitation on grain boundaries, which is observed, occurs at a faster rate than bulk precipitation, which was treated here.

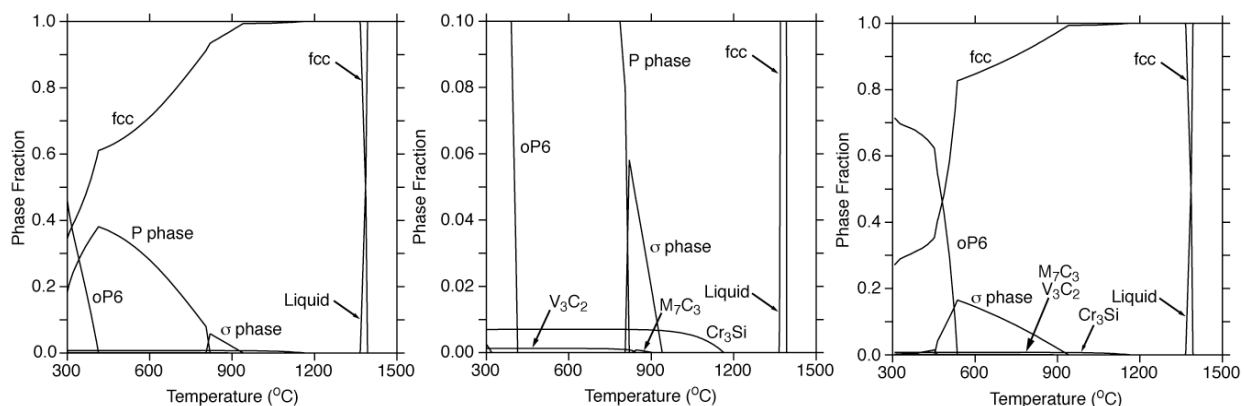
Starting with the thermo-chemical database provided by the SGTE (Scientific Group Thermodata Europe) data group, a detailed analysis of the stability of the binary alloys Ni-Cr, Ni-Mo, and Mo-Cr, and of the ternary Ni-Cr-Mo alloys was undertaken, since the databases included with the software were not optimally configured for Ni-Cr-Mo-W alloy studies. The study then focused on the role of additional solutes such as Si, C, Co, Nb, Ta, and W on stability, ordering, and precipitation in Ni-Cr-Mo-based alloys. Finally, kinetic and thermodynamic modeling have been combined and applied to the study of diffusion-controlled transformations with the use of the DICTRA software linked to Thermo-Calc (1998).

In the case of Alloy 22, the Thermo-Calc results shown in Figure 4-1 (left and central panels) confirms, that at equilibrium and low temperature, a three-phase field that includes the Ni₂Cr-type of ordered phase (or oP6), a complex tetrahedrally closed-packed (TCP) structure (P phase, or similar μ phase), and the fcc matrix should exist. It is interesting to note in Figure 4-1 (right panel) that if the P phase is suspended during the calculation of the property (phase) diagram (suspending a phase is analogous to assuming that the phase is not kinetically favored), the domain of stability of the σ phase extends in a broader range of temperatures, towards low temperatures from 930°C to 448°C (instead of 802°C). Also, it is interesting to note that the ordered phase of Ni₂Cr-type (oP6) competes with the P phase, as illustrated in Figure 4-1.

Whereas oP6 is itself stable up to 566°C (all phases suspended except fcc and oP6), the complete property diagram indicates a maximum temperature of stability at about 408°C. Finally, at low phase fraction, a number of carbides and silicides are stable, namely: M_7C_3 , V_3C_2 , and Cr_3Si . It is likely that these precipitate phases will preferably form in the proximity of the grain boundaries, where C and Si are usually observed.

By retaining the liquid phase and the fcc matrix, and σ phase, P phase, or oP6 ordered phase during the calculation of the property diagram, the domain of existence of σ , P or oP6 with respect to fcc can be easily evaluated, as shown in Figure 4-2. For example with no other competing phases than the fcc, the σ phase exhibits a broad domain of stability that is limited at low temperature when the oP6 is reintroduced in the calculations (see Figure 4-1, right panel), and even more so when the P phase is allowed (see Figure 4-2, left panel). Hence it can be concluded that under particular circumstances where metastability can be promoted, the σ phase can be found at temperature lower than the one predicted at equilibrium.

In Figure 4-3, the analysis in terms of weight fraction as a function of temperature of each major element (Ni, Cr, or Mo), and W and Fe (when present) for each individual phase, namely the fcc matrix, the oP6 ordered phase, and the two TCP phases, P and σ , confirms the expectation. Indeed, in the TCP phases, a noticeable depletion in Ni and an enhancement in Cr in the P phase or Mo in the σ phase in their temperature range of stability (indicated by the horizontal line with arrows on both ends) are observed in Figure 4-3 (bottom panels). In the case of the oP6 ordered phase, a depletion in Ni and a noticeable departure from the nominal Cr and Mo compositions is observed (see Figure 4-3, top right panel). These predictions should be revisited in the case of welding where alloy stability can be affected by the presence of TCP phases and of the oP6 ordered phase at compositions that strongly depart from the nominal composition of Alloy 22.



DTN: LL030106312251.013

Figure 4-1. Calculated property diagrams of Alloy 22. In the left panel, the diagram in the whole range of phase fraction is displayed whereas in the central panel a detailed description of the diagram clearly shows the phases that occur at low phase fraction. The right panel is the property diagram of Alloy 22 in the case the P phase is not considered in (i.e., suspended during) the calculations.

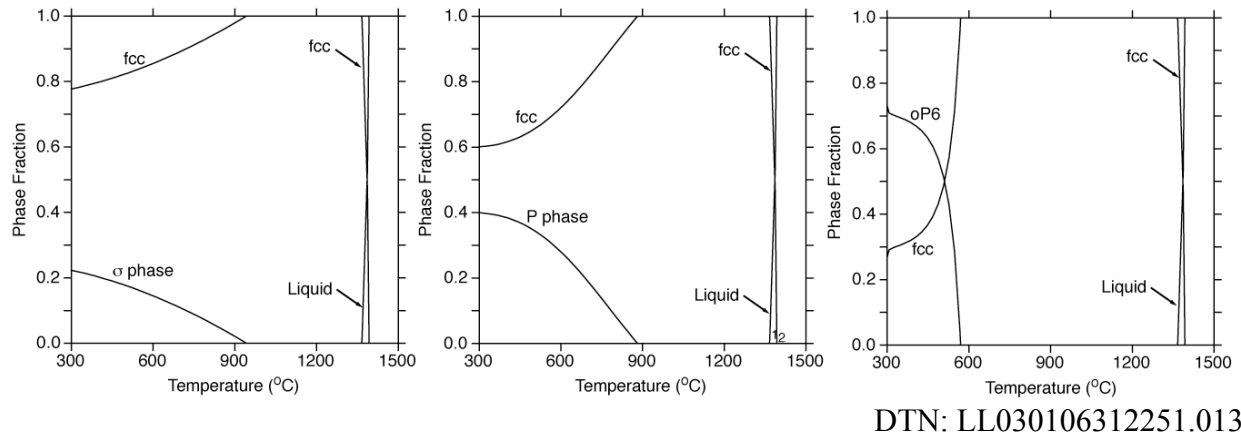


Figure 4-2. Calculated property diagrams of Alloy 22 with the liquid, the fcc matrix, and the σ phase (left panel), the P phase (central panel), and the oP6-ordered phase (right panel) considered in the calculations.

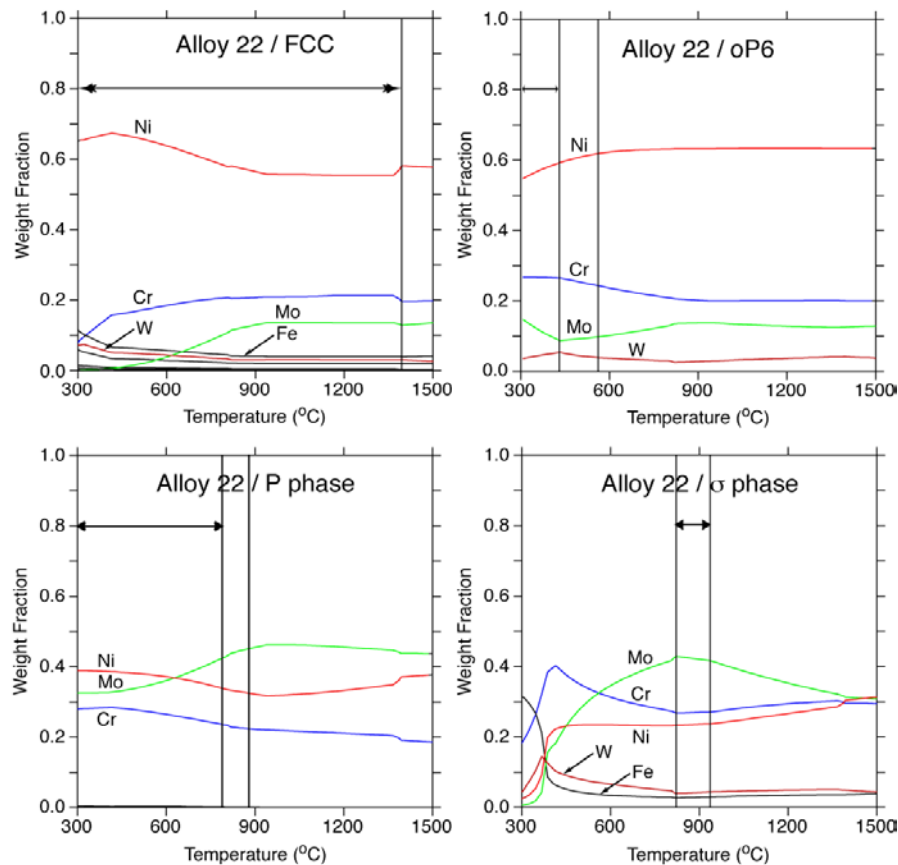


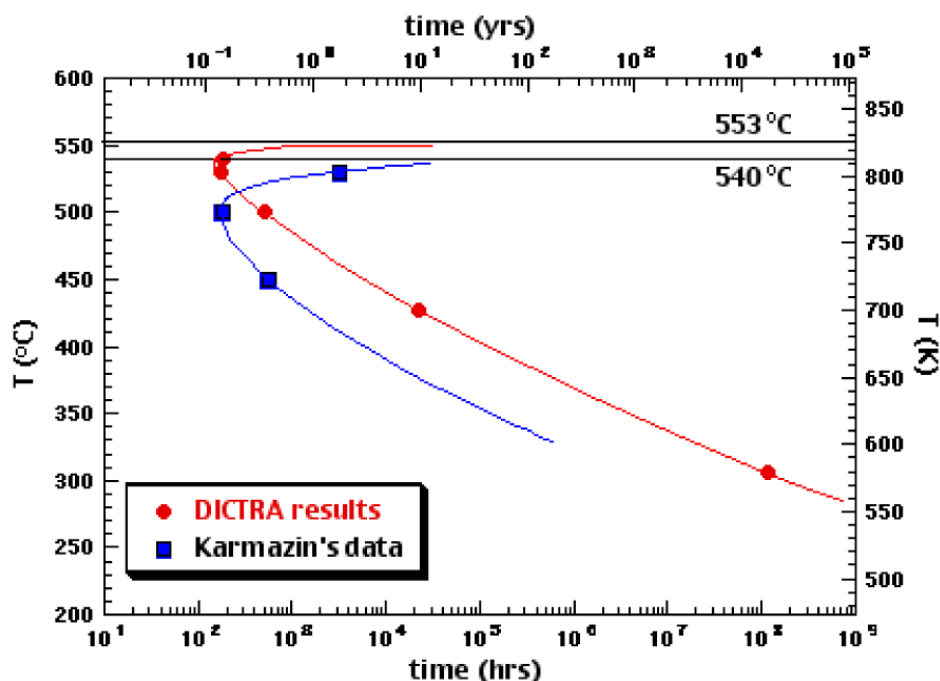
Figure 4-3. Weight fraction of Ni (red), Cr (blue), Mo (green), W (brown), and Fe (black), versus temperature in the fcc matrix, the oP6, the P and σ phases for Alloy 22 at its nominal composition (see text). The horizontal line with arrows on both ends indicates the domain of stability of the phase whereas the stand-alone vertical line indicates the temperature at which the phase starts occurring.

Time Temperature Transformation (TTT) Diagrams

The DICTRA code fulfills the need to provide critical modeling and analysis of data by solving the diffusion equations, calculating thermodynamic equilibrium (with Thermo-Calc), solving the flux-balance equations, and finally predicting the displacement of phase-interface positions. This application is used to analyze the kinetics of phase evolution in alloys selected for the barriers of the waste package by predicting time-temperature-transformation (TTT) diagrams for relevant phases forming as functions of time. This application also will help determine the solidification path and the effect of welding, and eventually post-annealing, on the stability and long-term aging of alloys selected for the waste package. Kinetics studies are focusing on the time-dependent formation of complex Frank–Kasper phases (such as P and σ phases), and the long-range ordering in terms of phase evolution from the fcc matrix with times up to 10,000 years. The DICTRA application can also be applied to the study of grain boundary formation of carbides, silicides, and TCP phases and phase evolution under non-isothermal conditions as is the case during welding.

TTT Diagram for the fcc to Ni₂Cr-type (oP6) Ordered Phase in Ni₂Cr

A first series of calculations have been performed to predict the TTT diagram in the case of a 10% transformation of an fcc-based Ni–Cr solid solution to the ordered Ni₂Cr (oP6) phase for which case experimental results were available (Karmazin 1982 [DIRS 154881]). The results are displayed In Figure 4-4. The MOB database that contains the mobility and the diffusion coefficient of the Cr species in a fcc-Ni matrix has been adjusted to account for the kinetics of transformation studied experimentally by Karmazin 1982 [DIRS 154881]. It was assumed that the variation of the fcc lattice parameter as a function of time at various annealing temperatures is directly proportional to the amount of ordered phase formed in the disordered fcc matrix. Based on this relation, three points of the TTT diagram have been obtained at 450, 500, and 530°C from (Karmazin 1982, Figure 6 [DIRS 154881]) in the case of a 10% transformation from fcc to oP6 of the Ni-rich solid solution with 33.3 atomic % Cr. The location of the nose of the experimental TTT curve has been used to determine the kinetic parameters that are defined in the MOB database for subsequent DICTRA calculations. The DICTRA results for the same rate of transformation (10 %) are also displayed in Figure 4-4, and the shape of the C curve compares very favorably with the experimentally deduced one. From the stability studies, the value of the critical order-disorder temperature (that positions the asymptote in the TTT diagram), 553°C, compares very well to the experimentally assessed value of 540°C. Note that the transformation is rather sluggish and is initiated after about 200 hours. Extrapolation of the TTT curve to lower temperatures clearly indicates that in this binary alloy, the oP6 ordered phase cannot form out of the fcc solid solution at less than 200°C for as long as 10,000 years.



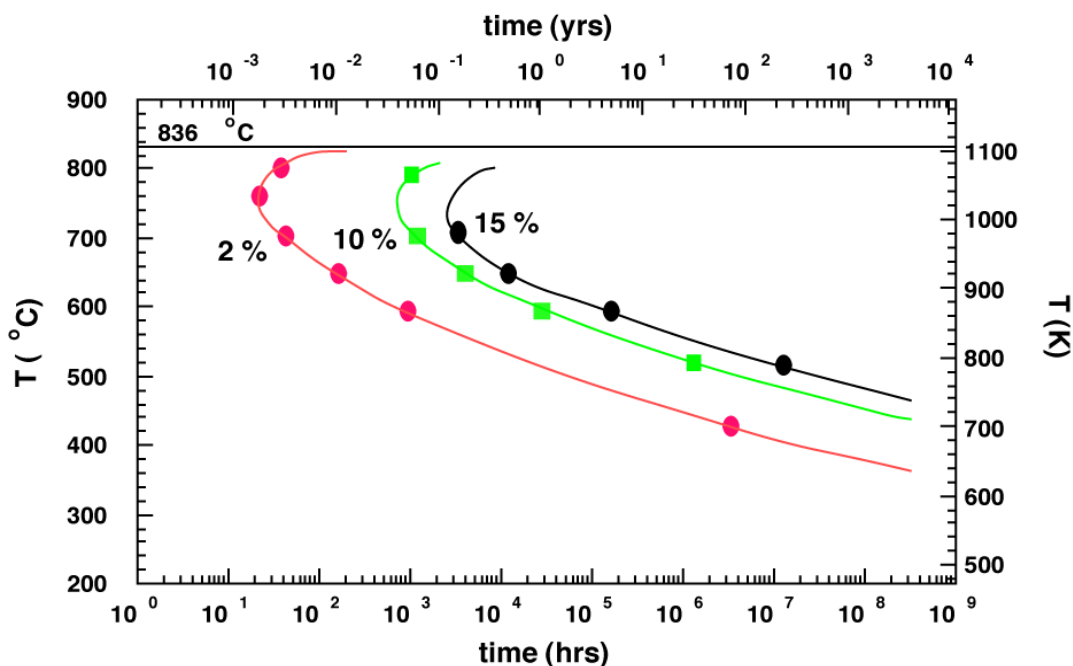
DTN: LL030106312251.013

Figure 4-4. Calculated Isothermal TTT diagrams (red solid circles) for a fcc-based matrix of a binary Ni_2Cr alloy transforming into the oP6 ordered phase, with transformation rate of 10%.

TTT Diagrams for Formation of Tetrahedrally Close-Packed (TCP) Phases

The transformation from the fcc-based matrix to the P phase with 2, 10, and 15% transformation rates was considered (from left to right in Figure 4-5) as a function of time and temperature. The experimentally deduced TTT diagram (blue solid squares) (Karmazin 1982 [DIRS 154881]) for the same transformation rate is also shown for comparison. In contrast to the formation from the fcc-matrix to the oP6 ordered phase that is rather slow, the incipient formation of the P phase is quite fast (a few hours in the bulk)

Similar to P phase formation, the transformation from the fcc-based matrix to the σ phase with 2, 5, and 10% transformation rates was simulated (from left to right in Figure 4-6) as a function of time and temperature. However, as was concluded previously for oP6 formation, the extrapolation of these TTT curves to lower temperatures clearly indicates that both P phase and σ phase formation out of the fcc-solid solution at less than 200°C will not occur for as long as 10,000 years.



DTN: LL030106312251.013

Figure 4-5. Calculated isothermal TTT diagram for an fcc-based matrix of a ternary Ni-21.1Cr-13.5Mo (in wt %) alloy (surrogate for Alloy 22) transforming into the P phase, with transformation rates of 2, 10, and 15%.

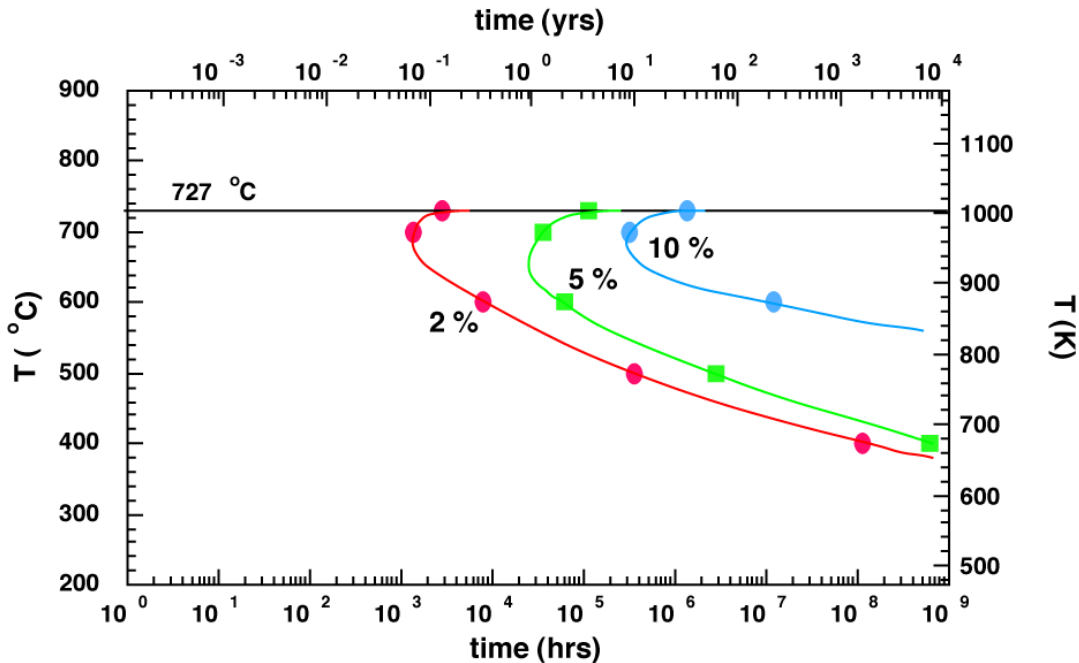


Figure 4-6. Calculated isothermal TTT diagrams for an fcc-based matrix of a ternary Ni-21.1Cr-13.5Mo (in wt %) alloy (surrogate for Alloy 22) transforming into the σ phase, with transformation rates of 2, 5, and 10%.

However, it is worth noting that before any conclusion can be drawn from this study, validation of the predictions by additional quantitative analysis of phase formation in samples annealed at various temperatures and for several aging times will be required. Note also, that in these calculations, grain boundary formation is not considered; that is, the results only apply to bulk formation and homogeneous phase evolution. Also, for WP closure weld regions where stress mitigation techniques are used, these techniques can result in the increase in dislocation density and may result in faster diffusion rates for phase precipitation. Thus, the waste package materials degradation models need to address the potential for thermal aging to increase corrosion degradation rates.

Volume-Fraction Measurements in Alloy 22

In order to measure the amount of TCP phase precipitation in Alloy 22 base metal and welds, area-fraction measurements have been made, using SEM image analyses, as a function of aging time and temperature. Using standard methods of quantitative stereology, it has been shown that area-fraction measurements (and correspondingly, linear-fraction measurements on grain boundaries) are mathematically equivalent to volume-fraction measurements (Vander Voort 1999 [DIRS 161300]; Hilliard et al. [DIRS 161454]). Thus, the area-fraction measurements presented in this AMR are equivalent to the volume-fraction values in Alloy 22 as a function of time and temperature. The SEM image analyses that were performed measured gross TCP phase precipitation in the samples as a function of time and temperature. No TCP phase extraction was conducted to differentiate the types of TCP phases that may be present (e.g., μ or P phases) in these measurements.

Volume-Fraction Measurements in Base Metal

The measurements of area-fraction TCP precipitation for base metal, as a function of time and temperature, are presented in Figure 4-7. A trend line is included for the results at 760°C, where more than two measurements were made. The trends of the results shown in Figure 4-7 are consistent with SEM observations and the TTT diagram of Figure 4-6. TCP phases are seen to readily form at higher temperatures (760 to 800°C) in less than 1000 hr. In general, as the temperature is decreased, the onset of TCP phase precipitation is delayed, and it also appears that the slopes of trend lines at lower temperatures may become shallower, indicating a slower rate of phase precipitation. While more measurements over longer periods of time are needed to formulate conclusions on long-term behavior, the measurements presented here are similar to the results of the TTT diagram (Figure 4-6), in that forming TCP phases from the fcc-solid solution at less than 300°C within 10,000 years is unlikely.

Area-Coverage Measurements on Grain Boundaries

Area-coverage measurements (linear-fraction measurements) on grain boundaries have been performed using SEM image analyses, and are shown in Figure 4-8. These measurements are similar to the area-fraction measurements on base metal samples discussed in the previous section. Using standard methods of quantitative stereology, these linear-fraction measurements of TCP phase precipitation on grain boundaries are mathematically equivalent to volume-fraction measurements (Vander Voort 1999 [DIRS 161300]; Hilliard et al. [DIRS 161454]).

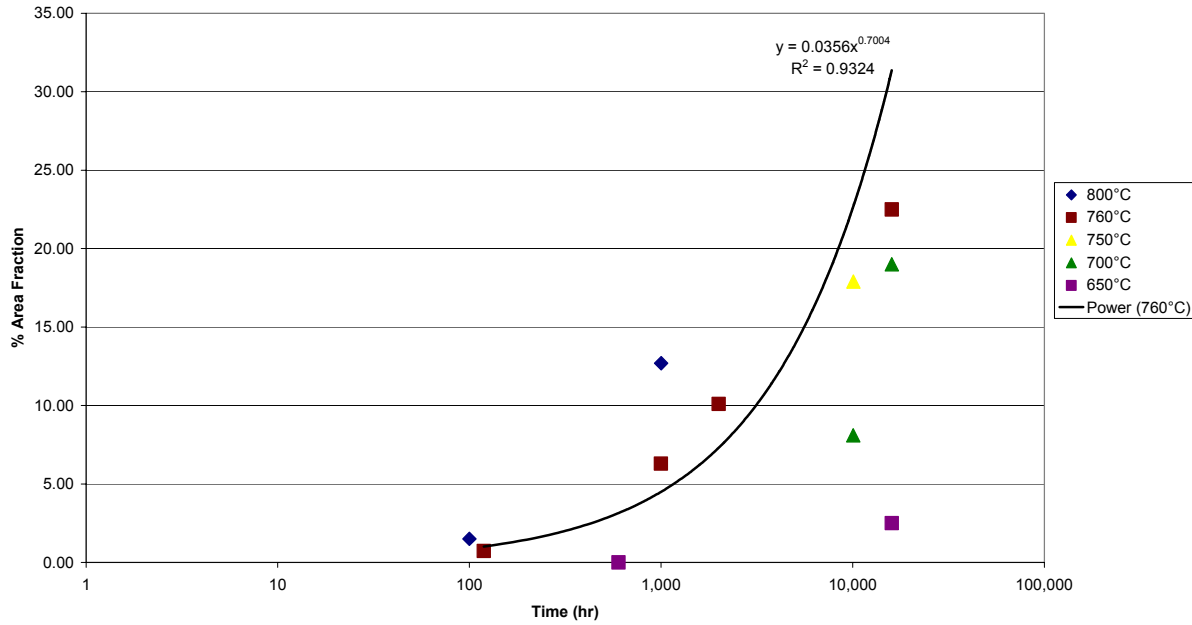
Due to the paucity of grain boundary coverage data (Figure 4-8), only a few observations regarding TCP phase precipitation on grain boundaries are noted. Similar to TCP phase precipitation in base metal, TCP phase precipitation on grain boundaries is dependent on temperature. The onset of TCP phase precipitation on grain boundaries appears to be delayed with decreasing temperature. More measurements over longer time periods, as well as computational modeling, are needed before any conclusions can be made.

Long Range Ordering

The kinetics of LRO are treated in a manner similar to that discussed for TCP phase precipitation. However, very little kinetic data exists for LRO in Alloy 22. A very fine dispersion of ordered domains was seen after aging for 30,000 and 40,000 hr at 427°C in Alloy 22 base metal and in a weld similarly aged. The ordering in these cases is so fine that it would be difficult to measure the volume fraction of the ordered domains. LRO was also observed in Alloy 22 base metal aged at 593°C for 16,000 hr and at 538 and 593°C for 1000 hr. The volume fraction of ordered domains has not been measured in these samples. Alloy 22 base metal samples aged for 40,000 hr at 260 and 343°C and for 1000 hr at 482°C were also examined in TEM, but no LRO was observed.

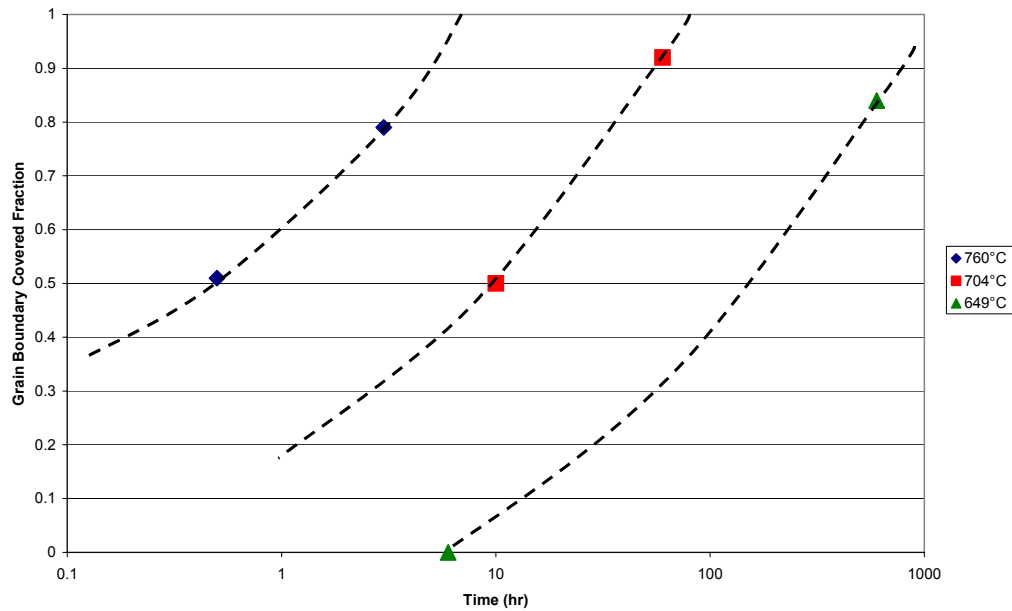
Unlike TCP phase precipitates, LRO results in very small and finely dispersed precipitates. As a result, SEM image analysis is not well suited to determine the extent of LRO kinetics. However, due to the uniformly and finely dispersed nature of LRO, micro-hardness measurements are indicative of LRO, because analogous to precipitation age-hardened alloys, hardness increases with the amount of precipitation (Reed-Hill 1973 [DIRS 162684]).

Figure 4-9 shows such micro-hardness (Hv) measurements made on Alloy 22 as a function of time and temperature. Trend lines have been included for the results at 500 and 550°C. The micro-hardness of “as-received” material was 217 Hv. The micro-hardness measurements indicate that LRO has occurred at temperatures in approximately the 500 to 550°C range up to 40,000 hr. In addition, for results up to 40,000 hr, no LRO is evident for temperatures below 400°C, and little LRO is seen at temperatures around 600°C. The observation of very little LRO near 600°C corroborates well with the critical order-disorder temperature of about 596°C of the computational model. These micro-hardness measurements add confidence to the observation from the computational TTT diagrams that forming the oP6 ordered phase from the fcc-solid solution at less than 200°C within 10,000 years is unlikely.



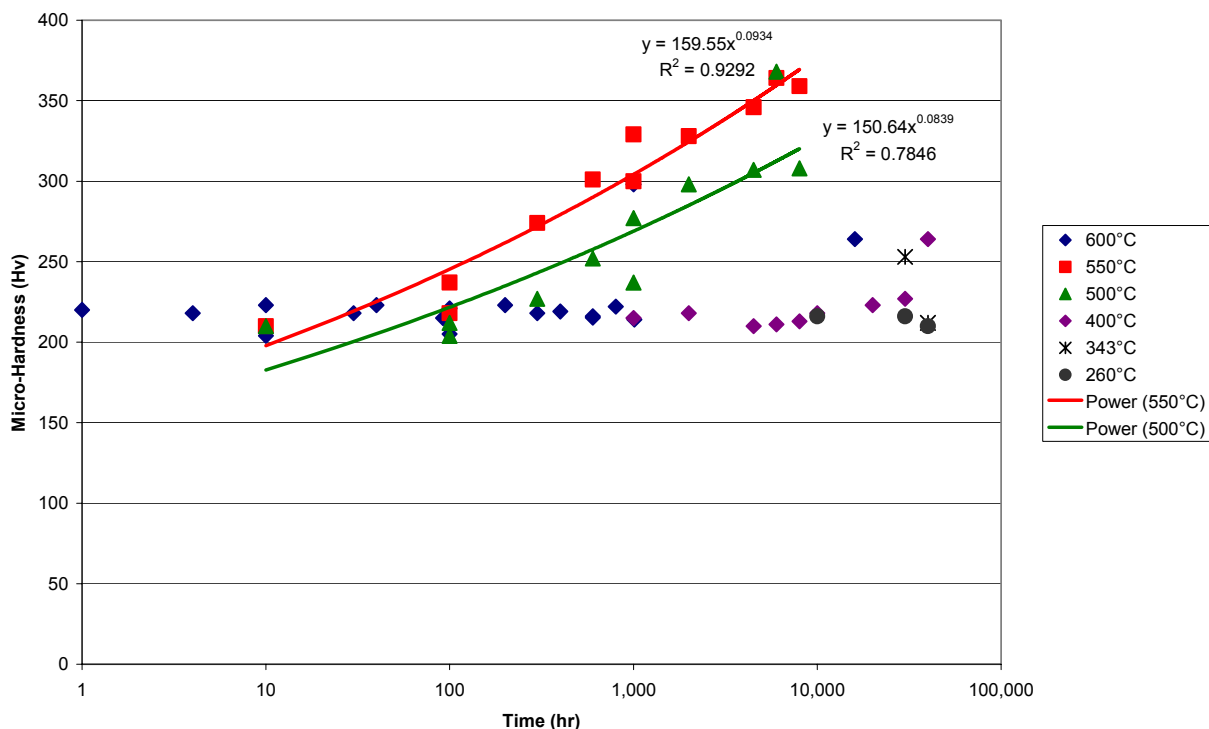
DTN: LL030106512251.015

Figure 4-7. Precipitation of TCP phases in Alloy 22 “base metal” as a function of time and temperature.



DTN: LL030106512251.015

Figure 4-8. Precipitation of TCP phases at Alloy 22 “grain boundaries” as a function of time and temperature.



DTN: LL030106512251.015

Figure 4-9. Micro-hardness (Hv) measurements on aged Alloy 22 base metal are shown as a function of time and temperature, and are indicative of LRO. Micro-hardness of “as-received” base metal is 217 Hv.

Phase Stability in Welds

The long-term phase stability data for Alloy 22 is also relevant to the understanding of fabrication and welding metallurgy, and the impact that those processes may have in corrosion resistance. The heat-affected zone (HAZ) of a weld is the region of the base metal near the weld that is subjected to a significant thermal pulse during the welding process. TCP precipitation kinetics in the HAZ will be similar to those in the base metal, but the actual rates of precipitation may be different. The high temperatures, approaching the melting point, seen in the HAZ of welds may trigger nucleation of TCP and/or carbide precipitates. If nuclei are already present, precipitation will proceed much faster than in the base metal where they are not present.

Very few precipitates have been observed in the HAZ of weld samples thus far, but only two weld samples have been examined: one in the as-welded condition and one after aging at 427°C for 40,000 hr. These precipitates may simply be carbides that were present in the mill-annealed (i.e., as-received) condition. Carbides are known to be present in Ni-base alloys similar to Alloy 22, but they are usually within the grains and are generally called primary carbides to distinguish them from other secondary phases that form, often on grain boundaries, after an aging treatment (Tawancy et al. 1983 [DIRS 104991]).

Welding causes melting of the alloy and the development of an as-cast structure upon cooling. The dendritic structure of typical of welds is visible in micrographs [ANL-EBS-MD-000002]. As an Alloy 22 weld solidifies, Mo and Cr are rejected from the solid phase, causing their concentration to increase in the liquid. Therefore, the interdendritic regions, which are the last solids to form in a weld, tend to have high concentrations of these elements relative to typical values for Alloy 22 (Cieslak et al. 1986 [DIRS 104966]). TCP phases are enriched in Mo and/or Cr, are therefore favored at higher Mo and Cr concentrations, and are present in the interdendritic regions of Alloy 22 welds. P phase is primarily seen in the as-welded condition of Alloy 22 welds, but σ and μ phases are also seen (Cieslak et al. 1986 [DIRS 104966]). Only one particle was seen in TEM in an Alloy 22 weld; this particle could be indexed as either P or σ phase.

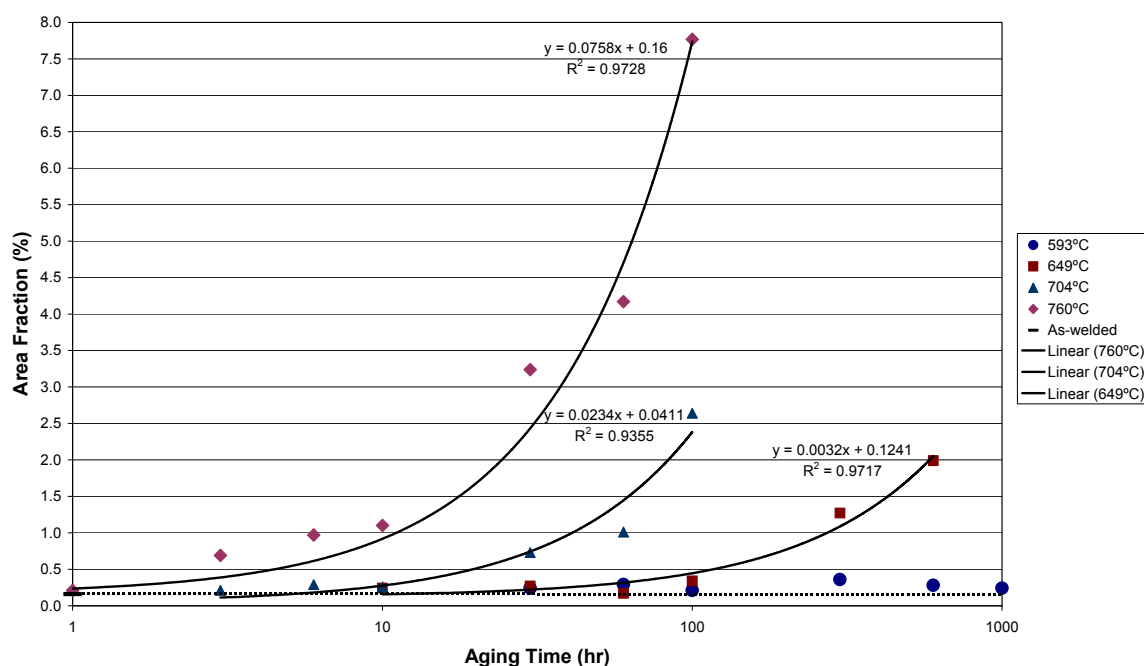
Because precipitates are present in Alloy 22 welds from the beginning, kinetics of precipitation is not an issue as it is in the base metal and HAZ. Instead, it must be verified that the weld's mechanical and corrosion properties are not degraded by this precipitation. Whether these precipitates are stable and grow or unstable and dissolve with aging at repository-relevant temperatures must also be determined.

Volume-Fraction Measurements in Weld Metal

Gas-tungsten-arc welds (GTAWs) were made from 0.5-in. thick Alloy 22 base metal in a single V groove configuration using nine passes. These welds were produced and aged at 593, 649, 704, and 760°C for times up to 1000 hours at Haynes International, Inc. in Kokomo, Indiana (Summers et al. 2000 [DIRS 154854]). Volume fraction measurements were also made. The amount and size of precipitates in the welds vary with position in the weld. For example, relatively few and smaller precipitates tend to be present near weld pass boundaries, while many larger precipitates tend to be present at the top of the last weld pass. The measurements presented here represent averages over several positions in the weld. Future studies will correlate precipitate amount with location in the weld. These welds are also much thinner than those called out in the current waste package design. Welding conditions, such as heat input, that may affect the starting weld structure and the subsequent precipitation kinetics will be different for thicker welds. A study of precipitation kinetics in thicker welds is currently planned. Also, several phases are expected in Alloy 22 welds (σ , μ , and P) have been observed (Cieslak et al. 1986 [DIRS 104966]). The growth kinetics for each of these phases may be different. In the base metal, it is likely that the amount of σ phase precipitating is small at temperatures below about 750°C and that μ and P phases are similar. In the weld, however, the amount of σ phase may be quite high due to chemical segregation. More refined studies that take these factors into account must be done to reduce uncertainties associated with conclusions drawn about weld stability.

Tetrahedrally Close-Packed (TCP) Phase Kinetics in Alloy 22 Welds

As observed by Cieslak et al. (1986 [DIRS 104966]), TCP phases are present in the interdendritic regions of the as-welded structure. After aging, the amount and size of TCP precipitates increases with both time and temperature up to 760°C. Nucleation of precipitation was also observed to form possibly along grain boundaries in some areas of these samples. The volume fraction of precipitates is shown as a function of time in Figure 4-10. Each of the data points in Figure 4-10 represents the average of 20–40 measurements. In the as-welded condition, there is approximately 0.02 volume-percent TCP phase. The average activation energy calculated from the slopes of these plots is 241 kJ/mol, which is comparable to but lower than the values of 250 and 260 kJ/mol reported previously for base metal (Rebak et al. 2000 [DIRS 155013]). Extrapolations of these data do not indicate that precipitate nucleation and growth in the welds will occur to a significant extent at temperatures below approximately 300°C.



DTN: LL030106512251.015

Figure 4-10. TCP-phase precipitation kinetics for Alloy 22 gas tungsten arc weld (GTAW) as a function of temperature.

Chapter 5. Oxidation and Corrosion in Dry-Out Region

While in the dry-out region, Alloy 22 may undergo some degree of dry oxidation at temperatures above the deliquescence point or equivalently, at relative humidities below the critical value for humid air or aqueous corrosion (CRWMS M&O 2000d, ANL-EBS-MD-000003 REV 00 ICN 00, Section 6.4.2). However, the extent of dry oxidation is believed to be insignificant.

Dry Oxidation Above Deliquescence Point

A simple bounding analysis has been performed that assumes the protective oxide film is primarily Cr₂O₃ (other oxides may also be present). The rate of dry oxidation is assumed to be limited by mass transport through this growing metal oxide film. Fick's first law is applied, assuming a linear concentration gradient across the oxide film of thickness x . Integration shows that the oxide thickness should obey the following parabolic growth law, also known as Wagner's Law (Welsch et al. 1996), where the film thickness is proportional to the square root of time. This is represented by the following equation.

$$x = \sqrt{x_0^2 + k \times t}$$

where x_0 is the initial oxide thickness, x is the oxide thickness at time t , and k is a temperature-dependent parabolic rate constant. The rate constant in the above equation is defined as follows:

$$\log[k(m^2 s^{-1})] = -12.5 \left(\frac{10^3}{T(K)} \right) - 3.5$$

where T is defined as the absolute temperature. The highest Alloy 22 temperature is expected to be less than 200°C which is well below 350°C (623 K), which corresponds to the limit for the fuel cladding. The value of k corresponding to this very conservative upper limit of 350°C is $2.73 \times 10^{-24} \text{ m}^2 \text{ s}^{-1}$ (8.61×10^{-5} square μm per year). After one year, this corresponds to a growth of $0.0093 \text{ } \mu\text{m}$ (about 9.3 nm y^{-1}). As will be seen in a subsequent discussion, this estimated rate is comparable to that expected for aqueous phase corrosion at lower temperatures. It is, therefore, assumed that dry oxidation of the Alloy 22 can be accounted for through application of the parabolic law. The above expression represents a conservative upper bound, based upon published data. The logarithmic growth law may be more appropriate for use at low temperature than the parabolic law. However, such a logarithmic expression predicts that the oxide thickness (penetration) will asymptotically approach a small maximum level. In contrast, the parabolic law predicts continuous growth of the oxide, which is much more conservative. Since such conservative estimates of the rate of dry oxidation do not appear to be life limiting and since reliable data for determining the maximum oxide thickness for Alloy 22 do not appear to be available, the parabolic growth law will be used for the waste package outer barrier. The upper bound conservative estimate above is $0.0093 \text{ } \mu\text{m}$ (about 9.3 nm y^{-1}) for exposure at 350°C. Recent measurements (CRWMS M&O 2000d, ANL-EBS-MD-000003 REV 00 ICN 00, Section 6.4.2, Section 6.4.2) of the thickness of the Alloy 22 oxide film exposed to air at 550°C showed the oxide film approaches a limiting thickness of about 0.025 to 0.050 microns after about 333 days exposure which corresponds to a penetration rate of 0.027 to 0.054 microns/year (TBD). Therefore, the upper bound conservative rate of $0.0093 \text{ microns/year}$ is consistent with the

measurement data considering the higher test temperature. The dry oxidation model presented here assumes uniform oxidation of the Alloy 22 surface.

Corrosion Underneath Deliquescence Brines

The Dry-Out Region, the Environmental TGA has also been used to study the corrosion of waste package materials underneath those brines, and the evolution of acid gas due to the thermal decomposition of those brines. Weight change data for two materials (Alloy 825 and Alloy 22) at 150°C and 22.5% RH are shown in Figure 5-1 (Gdowski et al. 2003).

Initial weight gains shown in Figure 5-1 are due to the formation of films of deliquescence brine from the deposited CaCl_2 and humidity. The subsequent weight loss is due to the thermal-driven decomposition of the deliquescence brine, with the volatilization of hydrogen chloride. No further change in weight occurs after loss of chlorine from the surface. No sustained oxidation of Alloy 22, usually indicated by an increase in weight due to the addition of oxygen to the surface, is evident from the TGA data.

Figure 5-2 (need a reference for this and the next figure) shows photographs of the samples after such testing in the TGA. There is no evidence of localized corrosion of Alloy 22 (UNS # N06022, 55.5 Ni 22 Cr 13 Mo 3 W 4 Fe 2.5 Co) due to deliquescence. However, substantial attack of a less corrosion resistant material, Alloy 825 (UNS # N08825, 42Ni 22Cr 3Mo 0.9Ti 2.2Cu 1Mn 28.9Fe) is evident. Thus, Alloy 22 has been shown to be resistant to localized attack under aggressive CaCl_2 -type deliquescence brines at 150°C and 22.5%. Because of its lower corrosion resistance, Alloy 825 was tested in parallel to provide insight into localized modes of attack that might occur under deliquescence brine films.

Figure 5-3 shows a scanning electron micrograph of the white precipitates on the Alloy 22 surface, which are formed from the deliquescence brine and are evident in the photographs of Figure 5-2. Elemental analysis of the deposit was done with energy dispersive spectroscopy (EDS) and indicated that these precipitates contain calcium, chlorine and oxygen. Raman spectroscopy indicates that precipitates are not $\text{Ca}(\text{OH})_2$ or CaCO_3 , but may be CaOHCl (calcium hydroxy chloride). Furthermore, EDS and wet-chemical analyses indicate a loss of chlorine relative to calcium, which is believed to be due to the formation of volatile hydrogen chloride gas.

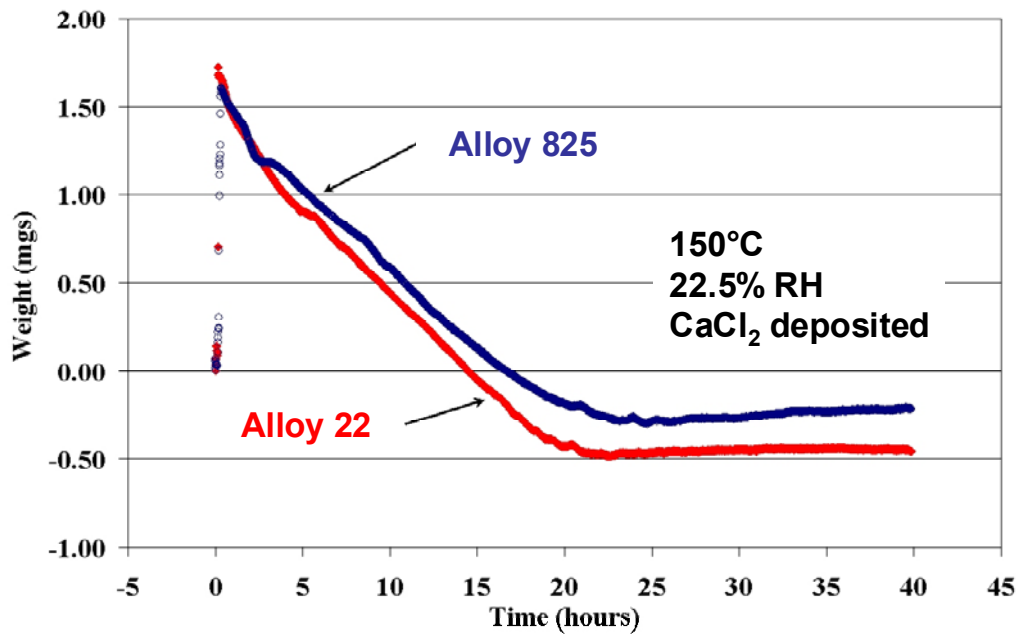


Figure 5-1. TGA data comparing the weight gains of Alloy 825 and Alloy 22 at 150°C and 22.5% relative humidity (RH).

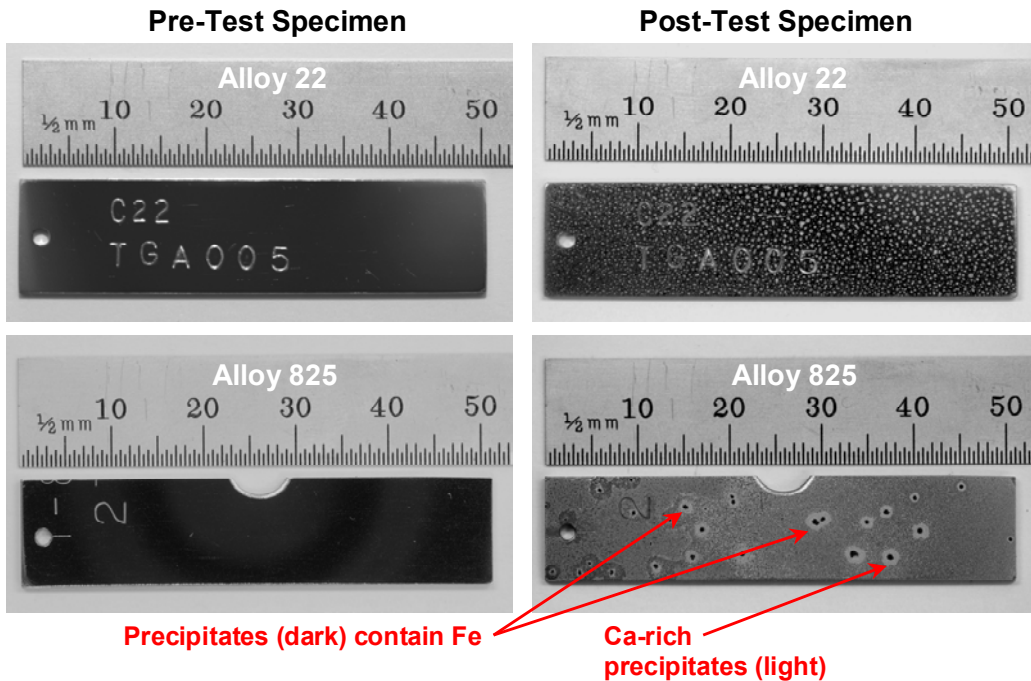


Figure 5-2. Photographs showing localized corrosion of Alloy 825 underneath a deliquescence brine. No such localized corrosion of Alloy 22 was observed under identical conditions.

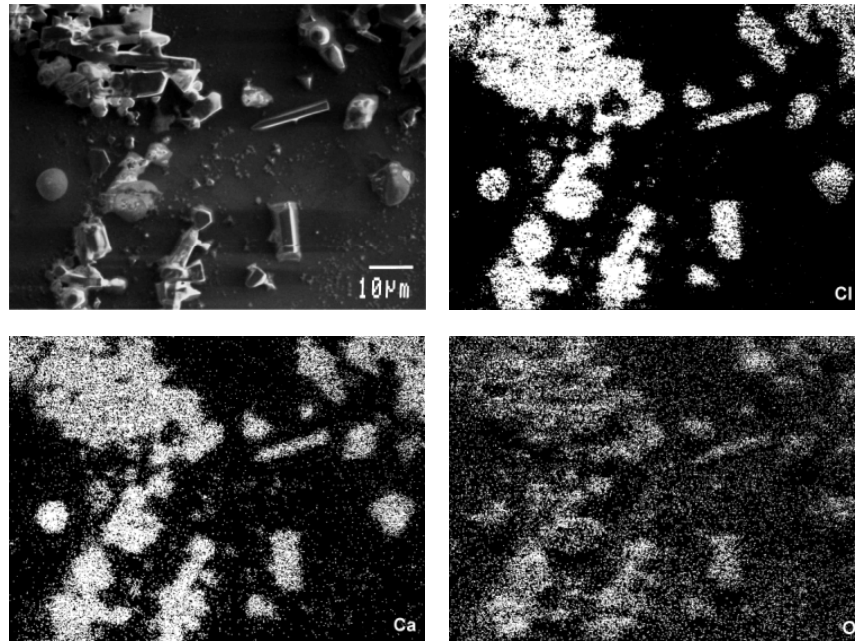


Figure 5-3. SEM of the white precipitates on the Alloy 22 surface, which are formed from the deliquescence brine and evident in the photographs of Figure 5-2. Elemental analysis with EDS indicates that the precipitates are probably CaOHCl .

At a given surface temperature, the existence of liquid water on the waste package surface depends upon the hygroscopic nature of any salt and mineral deposits on the surface. In the presence of such deposits, a liquid-phase can be established at a higher temperature and lower RH than otherwise possible. General corrosion of the WPOB is assumed to occur at any RH above the corrosion initiation threshold RH ($RH_{critical}$). Rates are estimated with the data presented in Chapter 6.

Chapter 6. Rates of General and Crevice Corrosion Based Upon Five-Year Exposure Data

In this Chapter, it will be shown that the life of the waste package is not limited by the rate of uniform, general corrosion. General corrosion (or passive corrosion) is the uniform thinning of the WPOB at its open-circuit corrosion potential (E_{corr}). General corrosion is assumed to progress uniformly over a large surface at a (time-independent) constant rate. Therefore the depth of penetration or thinning of the WPOB by general corrosion is equal to the general corrosion rate multiplied by the time that the waste package is exposed to an environment under which general corrosion occurs. This assumption is considered conservative because the general corrosion rate of metals and alloys tends to decrease with time. As discussed in the following sections, general corrosion rates of the WPOB have been estimated based on the descaled weight-loss data of Alloy 22 samples after 5-year exposure in the Long Term Corrosion Testing Facility (LTCTF). The LTCTF provides a comprehensive source of corrosion data for Alloy 22 in environments relevant to the proposed repository (BSC 2003d, ANL-EBS-MD-000003 REV 01).

Long-Term Weight Loss Measurements

The LTCTF is equipped with an array of fiberglass tanks. Each tank has a total volume of ~2000 L and is filled with ~1000 L of aqueous test solution. The solution in a particular tank is controlled at either 60 or 90°C, covered with a blanket of air flowing at approximately 150 cm³/min, and agitated. Four generic types of samples, U-bends, crevices, weight loss samples, and galvanic couples, are mounted on insulating racks and placed in the tanks. Approximately half of the samples are submersed, half are in the saturated vapor above the aqueous phase, and a limited number are at the water line. It is important to note that condensed water is present on specimens located in the saturated vapor (BSC 2003d, ANL-EBS-MD-000003 REV 01).

The weight loss measurement testing includes a wide range of plausible generic test media, including SDW, SCW, Simulated Cement-Modified Water, and SAW. The compositions of three of these solutions are summarized in Table 6-1 and these data along with a detailed discussion of corrosion rate measurement and analysis results are presented in [ANL-EBS-MD-000003 REV 01]. The corrosion rate of Alloy 22 was determined using immersion tests according to ASTM G 1 (ASTM G 1-90 1990). Two types of coupons were used. These were labeled weight loss coupons and crevice coupons (BSC 2003d, ANL-EBS-MD-000003 REV 01).

The SCW test medium is about three orders-of-magnitude (1000×) more concentrated than J-13 well water and is slightly alkaline (pH~8-10). The SAW test medium is about three orders-of-magnitude (1000×) more concentrated than J-13 well water and is acidic (pH~2.7). These concentrated solutions are intended to mimic the evaporative concentration of the various potential electrolytes on the hot WP surface. Two temperature levels (60 and 90°C) are included (BSC 2003d, ANL-EBS-MD-000003 REV 01).

Table 6-1. Target Chemical Compositions of the Electrolyte Solutions (mg/L) Employed in the Long-Term Weight Loss Measurement.

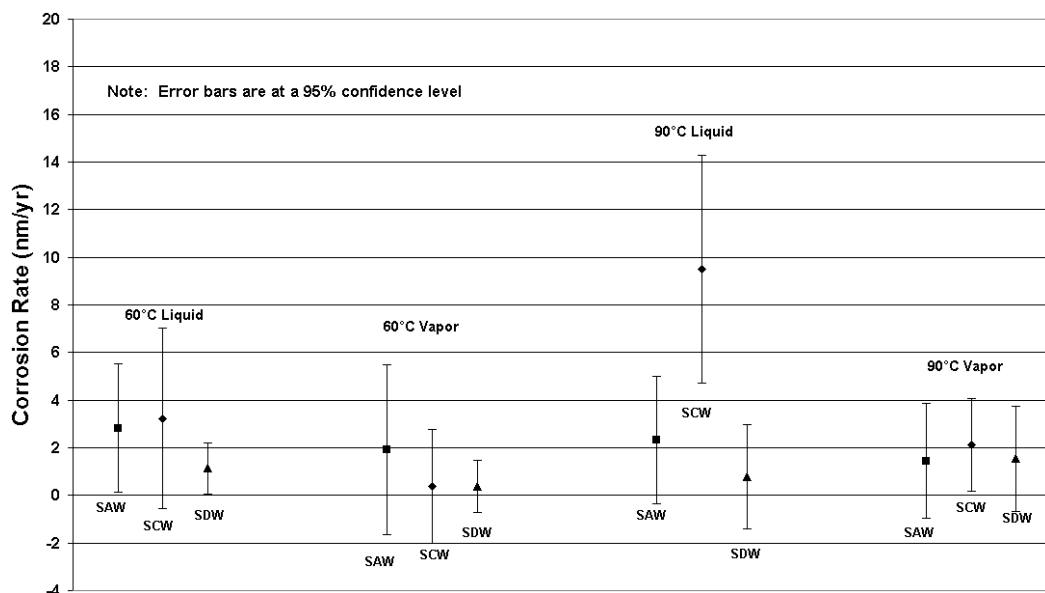
	Concentration (mg/L)		
Ion	Simulated Dilute Water (SDW)	Simulated Concentrated Water (SCW)	Simulated Acidified Water (SAW)
	60 & 90 °C	60 & 90 °C	60 & 90 °C
K	34	3400	3400
Na	409	40,900	37,690
Mg	1	<1	1000
Ca	0.5	<1	1000
F	14	1400	0
Cl	67	6700	24,250
NO ₃	64	6400	23,000
SO ₄	167	16,700	38,600
HCO ₃	947	70,000	0
Si (aq)	27 (60 °C) 49 (90 °C)	27 (60 °C) 49 (90 °C)	27 (60 °C) 49 (90 °C)
pH	9.8 – 10.2	9.8 – 10.2	2.7

Source: DTN LL000320405924.146

Approximately half of the specimens were exposed to the liquid phase of the solution (complete immersion) and the other half were exposed to the vapor phase (suspended over the liquid surface). The simulated electrolyte solutions were naturally aerated. After an approximate five years exposure to each solution/environmental condition, the specimens were removed from their respective test vessel to determine the corrosion rate by mass loss. In all of the tested conditions, the coupons were covered with deposits. Therefore, the coupons were cleaned prior to final weighing. Cleaning was carried out using ASTM standard G 1 (ASTM G 1-90 1990).

A detailed analysis of these results based on weight loss coupons exposed to the SAW, SCW and SDW solutions at 60°C and 90°C for over 5 years is reported in the AMR on the general and localized corrosion of the Alloy 22 WPOB (BSC 2003d, ANL-EBS-MD-000003 REV 01), and a summary of these Alloy 22 corrosion rate results is presented here. The average corrosion rates and 2 σ ranges are presented for the un-creviced (designated weight loss specimens) and the creviced specimens in Figures 6-1 and 6-2 respectively.

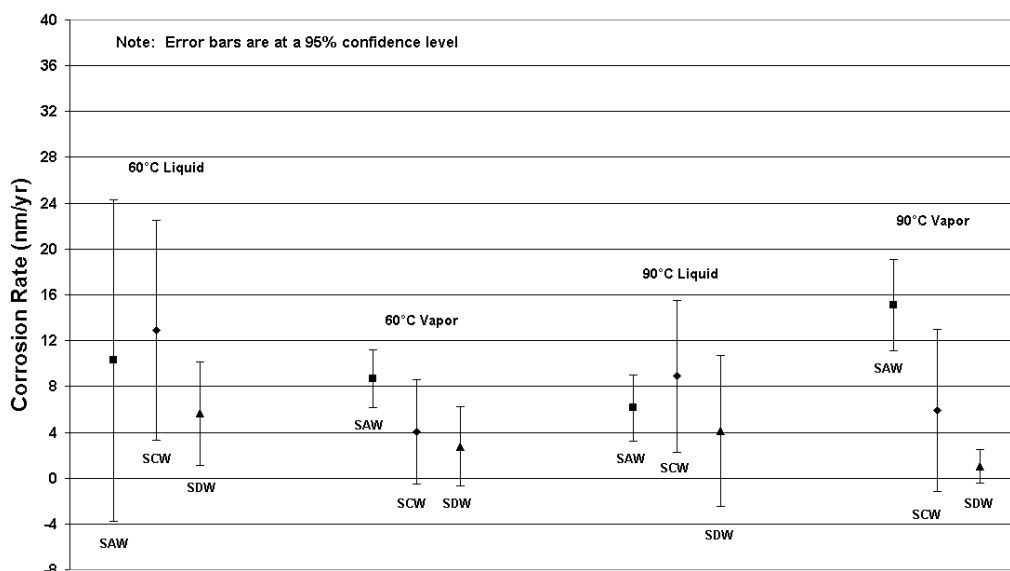
Corrosion Rate for 5+ Year LTCTF Samples - Alloy 22 Weight Loss Coupons



Output DTN: SN0306T0506303.002

Figure 6-1. Corrosion rates for Alloy 22 weight-loss coupons in SAW, SCW and SDW.

Corrosion Rate for 5+ Year LTCTF Samples - Alloy 22 Crevice Coupons



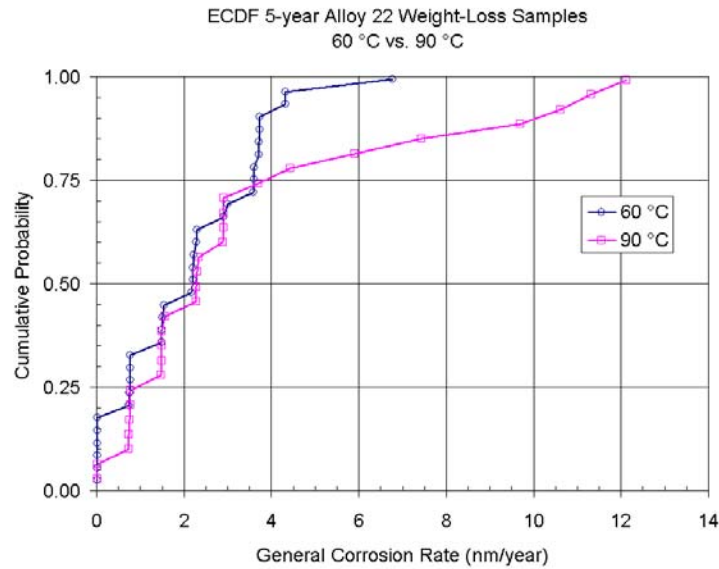
Output DTN: SN0306T0506303.002

Figure 6-2. Corrosion rates for Alloy 22 crevice coupons in SAW, SCW and SDW.

The 2σ range represents a 95% confidence level. As can be seen in Figure 6-1, the individual corrosion rates for the weight loss coupons ranged from 0-12 nm/yr with the lowest rates observed for the coupons in the SDW solution. The individual corrosion rates for the crevice coupons, shown in Figure 6-2, ranged from 0-23 nm/yr with the highest rates observed in the SAW solution vessels and, again, the lowest rates observed in the SDW solution vessels. In most cases, the crevice coupons exhibited corrosion rates 2-5 times higher than the weight loss coupons in the same solutions. Stereomicroscopic, scanning electron microscope (SEM) and atomic force microscopy (AFM) observations of both weight loss and crevice specimens indicated little or no corrosion for Alloy 22. The machining grooves remained uniform and sharp throughout each coupon. It is not yet clear why the corrosion rates of the crevice coupons were higher than those of the weight loss coupons because crevice corrosion was not observed in any of the tested coupons. However, it is noteworthy that among all test specimens, a maximum measured corrosion rate of only 23 nm/yr was observed (BSC 2003d, ANL-EBS-MD-000003 REV 01).

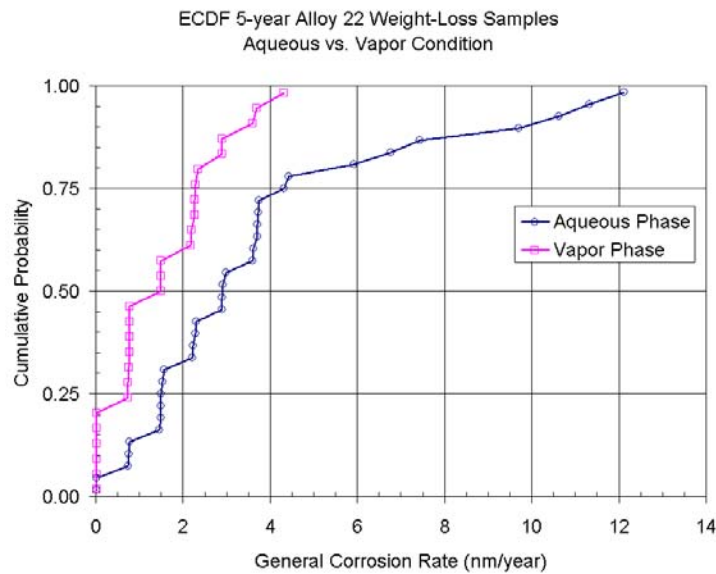
For both the weight loss and crevice coupons, the corrosion rates were generally lower for those specimens exposed to vapor than immersed in liquid, regardless of the test temperature or electrolyte solution. For the weight loss coupons exposed to liquid, the corrosion rates were generally lower at 90°C than at 60°C. For the weight loss coupons exposed to vapor, the corrosion rates were generally higher at 90°C than at 60°C. Overall, coupons in the SAW solution vessels exhibited slightly lower corrosion rates at the higher temperature. This was also previously observed for the 2-year specimens. Similar to the weight loss coupons, the corrosion rates for the crevice coupons exposed to liquid were lower at 90°C than at 60°C, while the corrosion rates were generally higher at 90°C than at 60°C for the crevice coupons exposed to vapor. In general, for corrosion processes, the corrosion rate increases with temperature. However, since in this study the corrosion rates were so low and the temperature range studied (60 to 90 °C) is small, a clear dependence with the temperature cannot be established for any set of coupons. Finally, for the weight loss coupons, there appeared to be no weld effect on the corrosion rate, however, the non-welded crevice coupons exhibited slightly higher rates than their welded counterparts (BSC 2003d, ANL-EBS-MD-000003 REV 01).

The empirical cumulative distribution functions (ECDFs) for the general corrosion rates of Alloy 22 weight-loss and crevice samples are presented in the AMR on the general and localized corrosion of the Alloy 22 WPOB (BSC 2003d, ANL-EBS-MD-000003 REV 01). In this report, the ECDFs for the general corrosion of the Alloy 22 weight-loss samples are shown in Figures 6-3 through 6-7, while the ECDFs for the general corrosion rates of the Alloy 22 crevice samples are shown in Figures 6-8 through 6-13. These figures (6-3 through 6-7, and 6-8 through 6-13) provide a comparison of the effect of various experimental factors on the general corrosion rate, such as for the solution chemistry, temperature, and metallurgical condition. For the weight-loss samples, the mean corrosion rate is 2.75 nm/year and the standard deviation is 2.74 nm/year. For the crevice samples, the mean corrosion rate is 7.24 nm/year, and the standard deviation is 4.95 nm/year. The corrosion-rate distribution for the crevice coupons used as the base case general corrosion rate of the WPOB (BSC 2003d, ANL-EBS-MD-000003 REV 01).



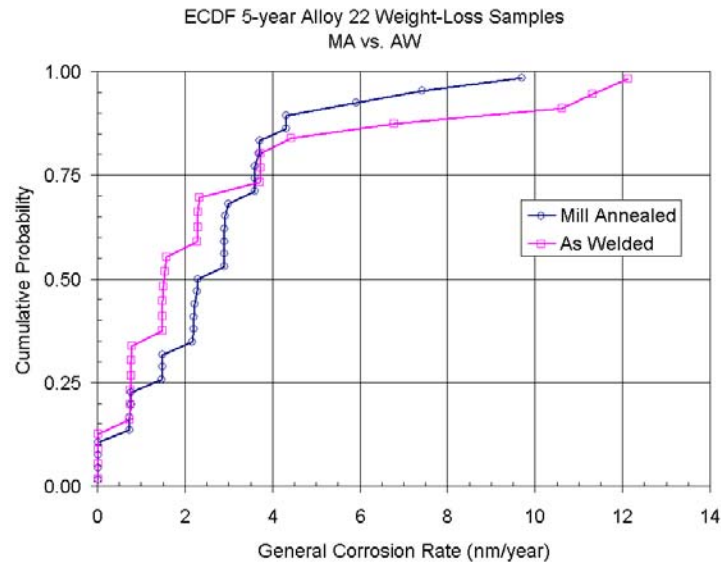
DTN: SN0306T0506303.002

Figure 6-3. Empirical cumulative distributions of general corrosion (GC) rate data for Alloy 22 weight-loss samples at 60 and 90°C after 5-years exposure in the LTCTF.



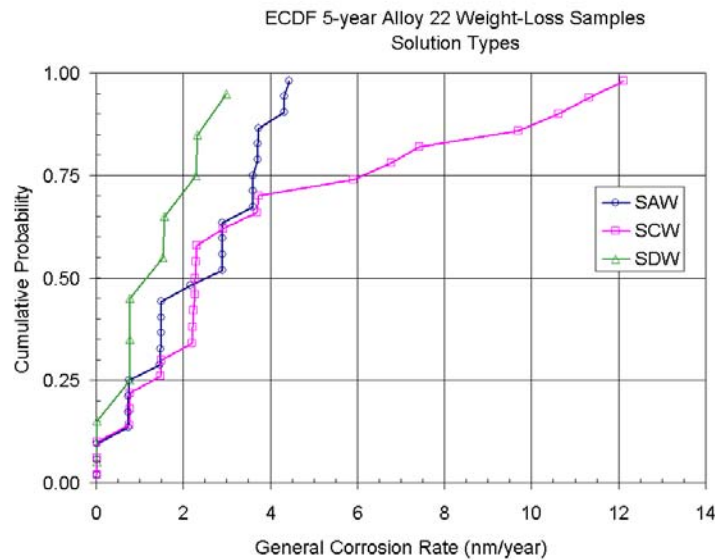
DTN: SN0306T0506303.002

Figure 6-4. Empirical cumulative distributions for general corrosion (GC) rate data for Alloy 22 weight-loss samples exposed in the vapor and aqueous phase for 5 years in the LTCTF.



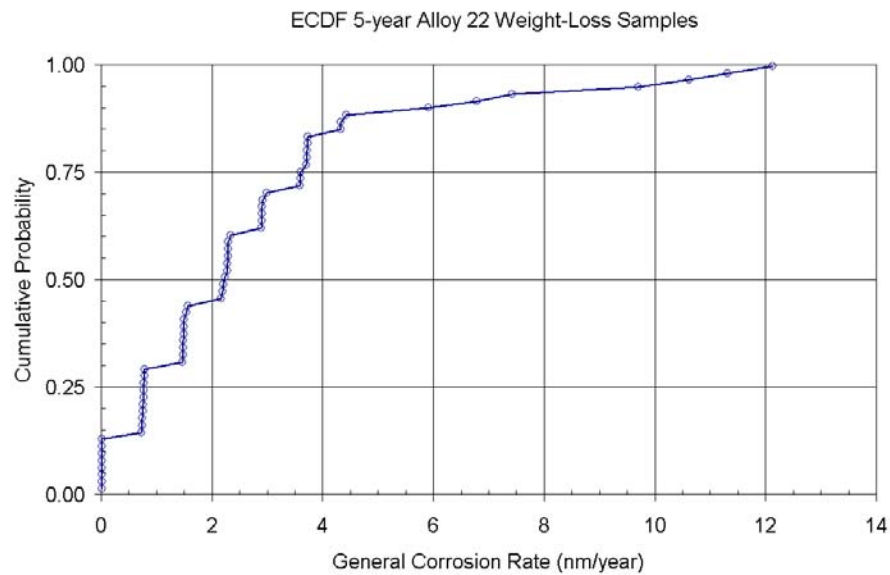
DTN: SN0306T0506303.002

Figure 6-5 Empirical cumulative distributions for general corrosion (GC) rate data for mill-annealed and as-welded Alloy 22 weight-loss samples after exposure for 5 in the LTCTF.



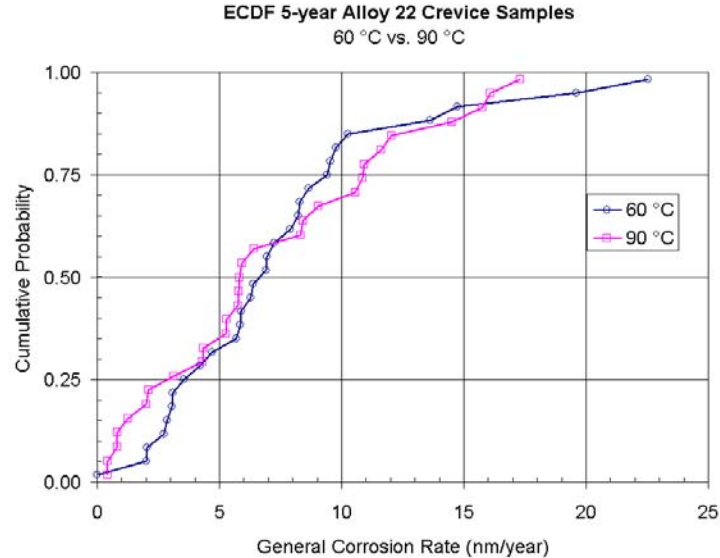
DTN: SN0306T0506303.002

Figure 6-6 Empirical cumulative distributions for general corrosion (GC) rate data for Alloy 22 weight-loss samples tested in three types of solutions after exposure for 5 years in the LTCTF.



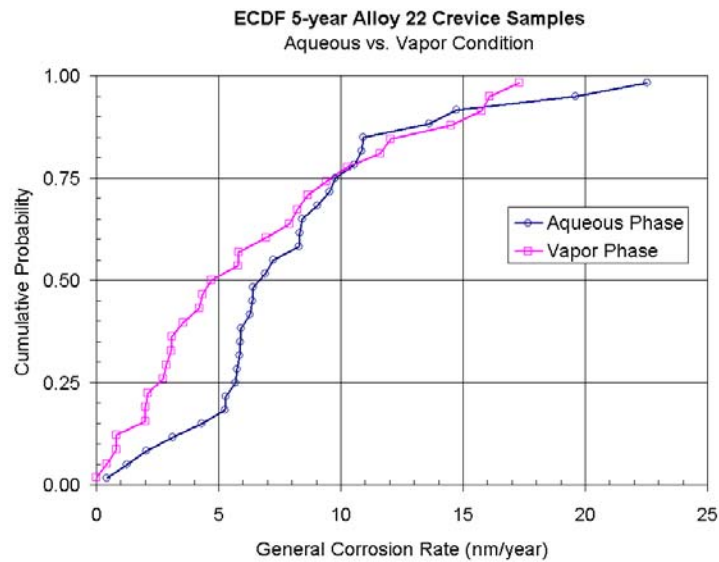
DTN: SN0306T0506303.002

Figure 6-7. Empirical cumulative distributions for general corrosion (GC) rate data for all Alloy 22 weight-loss samples after exposure for 5 years in the LTCTF.



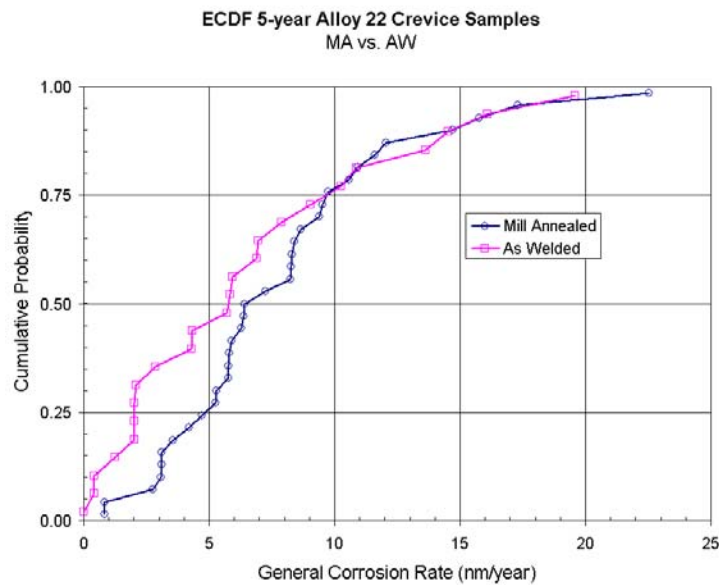
DTN: SN0306T0506303.002

Figure 6-8. Empirical cumulative distributions for general corrosion (GC) rate data for Alloy 22 crevice samples at 60 and 90°C after exposure for 5 years in the LTCTF.



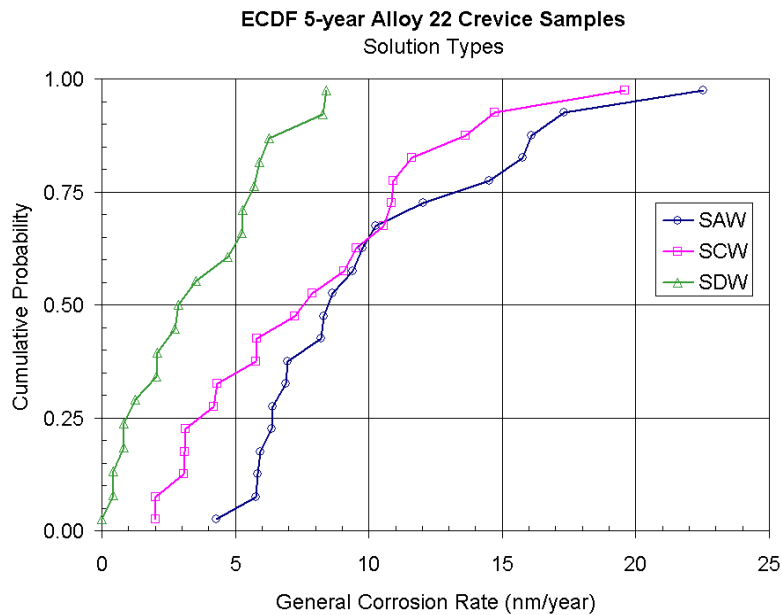
DTN: SN0306T0506303.002

Figure 6-9 Empirical cumulative distributions for general corrosion (GC) rate data for Alloy 22 crevice samples Exposed in the vapor and aqueous phases for 5 years in the LTCTF.



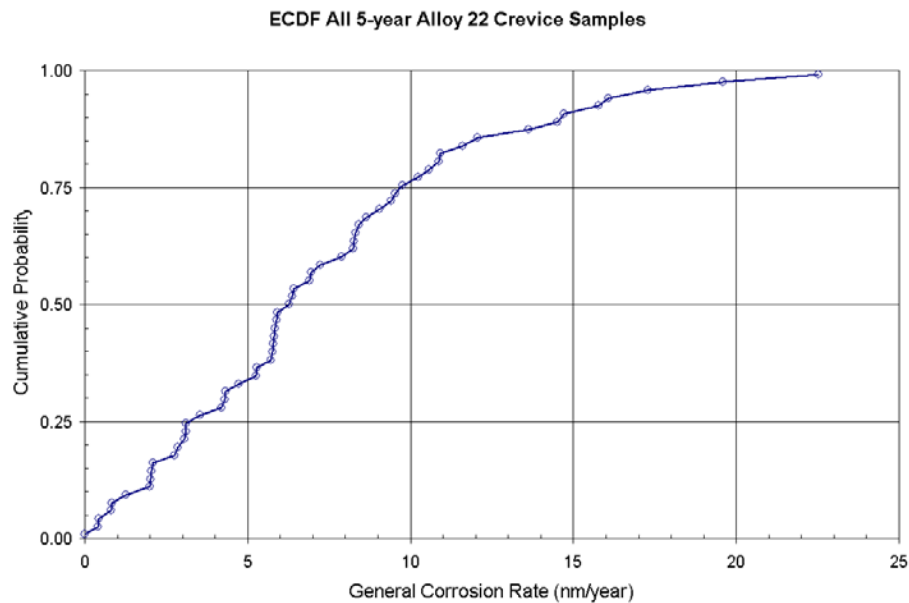
DTN: SN0306T0506303.002

Figure 6-10. Empirical cumulative distributions for general corrosion (GC) rate data for mill-annealed and as-welded Alloy 22 crevice samples after exposure for 5 years in the LTCTF.



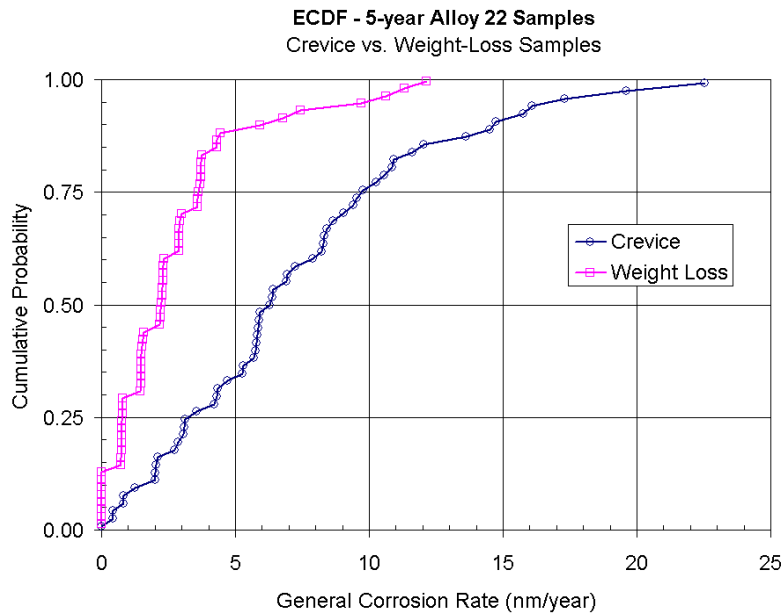
DTN: SN0306T0506303.002

Figure 6-11. Empirical cumulative distributions for general corrosion (GC) rate data for Alloy 22 crevice samples tested in three types of solutions after exposure for 5 years in the LTCTF.



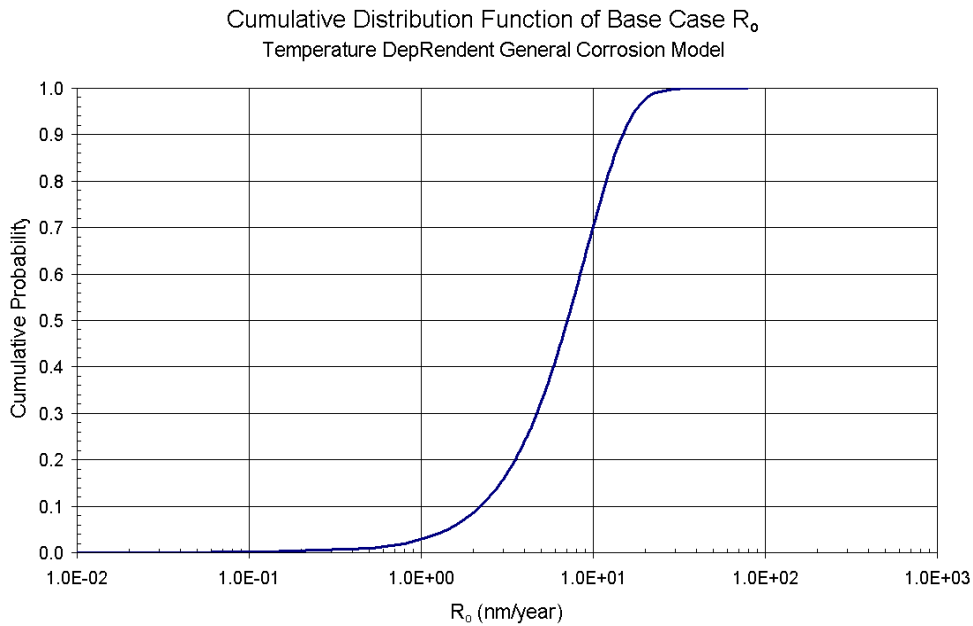
DTN: SN0306T0506303.002

Figure 6-12. Empirical cumulative distributions for general corrosion (GC) rate data for all Alloy 22 crevice samples after exposure for 5 years in the LTCTF.



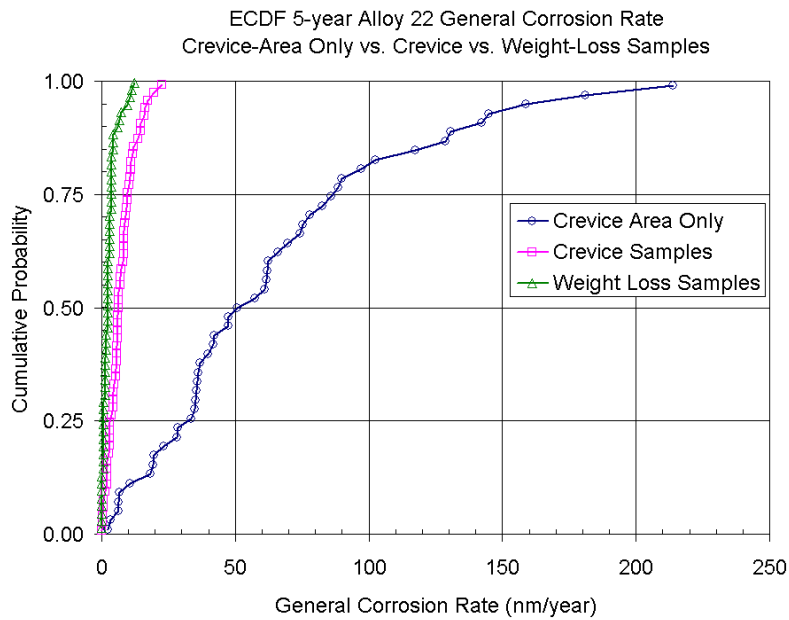
DTN: SN0306T0506303.002

Figure 6-13. Empirical cumulative distributions for general corrosion (GC) rate data for Alloy 22 weight-loss and crevice samples after exposure for 5 years in the LTCTF.



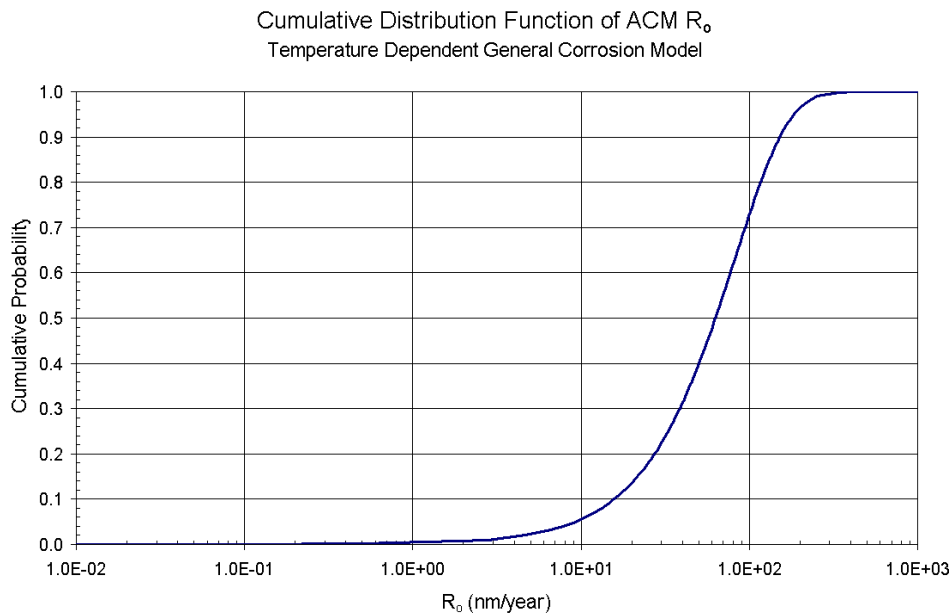
DTN: SN0306T0506303.002

Figure 6-14. Cumulative distribution function (CDF) of $\log(R_0)$, for the base-case, temperature-dependent, general-corrosion (GC) model for the Alloy 22 WPOB.



DTN: SN0306T0506303.002

Figure 6-15. Empirical cumulative distributions for general corrosion (GC) rate data for Alloy 22 crevice and weight-loss samples after exposure for 5 years in the LTCTF. The GC rates for creviced areas are compared to the rates for areas lying outside of the crevice.



DTN: SN0306T0506303.002

Figure 6-16. Cumulative distribution function (CDF) for R_o , determined for crevice areas alone, for the temperature-dependent, general-corrosion model for the Alloy 22 WPOB.

From Figures 6-3 through 6-13, it is evident that the general corrosion rate can be represented by an appropriate statistical distribution. The general corrosion rate at 60°C (R_o), based upon the weight loss of 5-year crevice samples, has been found to obey a Weibull distribution with a scale factor of (8.88), a shape factor of (1.62), and location factor of (0). This distribution, for uniform general corrosion, is shown in Figure 6-14. Similarly, Figures 6-15 and 6-16 show the distributions of crevice corrosion rates (R_o) at 60°C. Thus, distributions for both general and localized corrosion rates of Alloy 22 have been deduced from the LTCTF five-year data.

General Corrosion Model

The temperature dependence of general corrosion rate can be represented by the Arrhenius relationship.

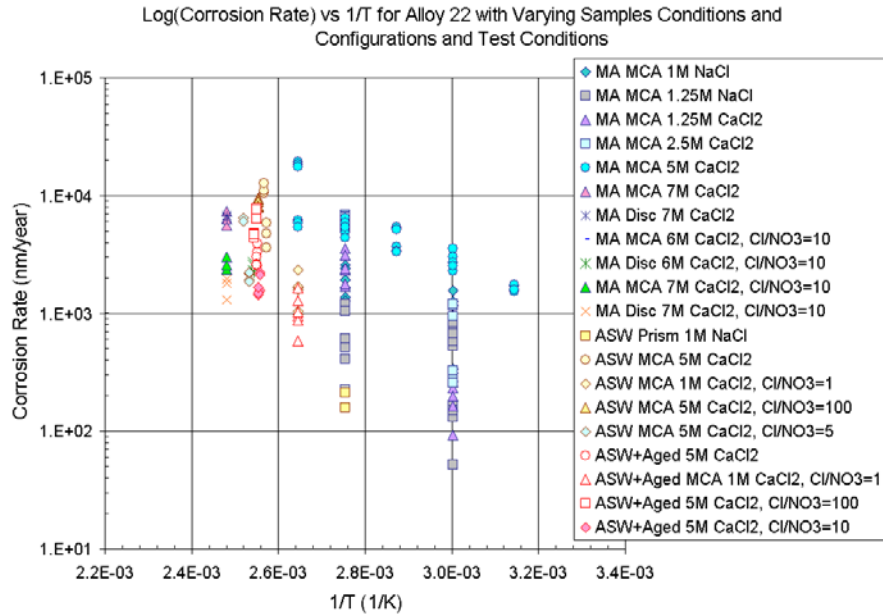
$$\ln(R_T) = C_o + \frac{C_1}{T}$$

The temperature-dependent general corrosion rate in nanometers per year is (R_T), the absolute temperature in Kelvin is (T), and (C_o) and (C_1) are constants. The activation energy term (C_1) is determined from short-term polarization resistance data for Alloy 22 specimens tested for a range of sample configurations, metallurgical conditions, and exposure conditions (temperature and water chemistry). Figure 6-17 shows the temperature dependence of Alloy 22 corrosion rates measured by the polarization resistance technique over the temperature range from 45 to 130°C. From fitting the data to the Arrhenius relationship, the activation energy term (C_1) was found to obey a normal distribution with a mean of -3374.98 and a standard deviation of 397.81. This temperature dependence is characterized by the activation energy of 28 kJ/mol. Sample configuration (crevice, disk or rod), metallurgical conditions (mill annealed or weld), and water chemistry within the range expected in the repository are assumed to have no significant effect on the temperature dependence of general corrosion rate.

The Arrhenius relationship is used to predict the temperature-dependent general corrosion rate (R_T) from the general corrosion rate at 60°C (R_o) and the activation energy term.

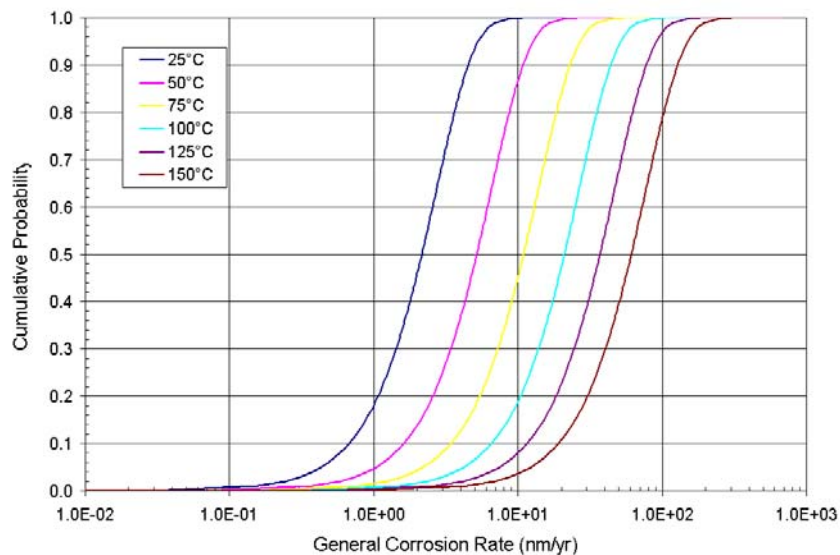
$$\ln(R_T) = \ln(R_o) + C_1 \left(\frac{1}{T} - \frac{1}{333.15} \right)$$

Predictions of the distribution of the temperature-dependent general corrosion rate (R_T) at 25, 50, 75, 100, 125 and 150 °C are shown in Figure 6-18.



DTN: SN0306T0506303.002

Figure 6-17. Temperature dependence of corrosion rates for Alloy 22, for various metallurgical conditions and sample configurations, and in a wide range of test solutions.



DTN: SN0306T0506303.002

Figure 6-18. Simulated model outputs of the base-case temperature-dependent general-corrosion (GC) model, based on the crevice-sample data at temperatures of 25, 50, 75, 100, 125 and 150°C. Note that the simulation was performed using the mean value (-3374.98) of the temperature-dependency term (C_1), and the predicted general corrosion rate range represents the variability of the rate.

Uncertainty Analysis of General Corrosion Rate Data

The general corrosion rate of Alloy 22 based on the weight-loss measurements has large uncertainties. Most of the uncertainties have resulted from insufficient resolution of the weight-loss measurements of the samples due to the extremely low corrosion rates of the alloy in the test media. It was concluded that measurement uncertainty was the main source of uncertainty. The combined standard uncertainty is estimated to be approximately 0.185 nm/year in the case of crevice samples and 0.314 nm/year in the case of weight loss samples. These estimates correspond to one standard deviation (1σ). Therefore, for the crevice samples, about 3 percent of the variation in the measured general corrosion rate is due to the measurement uncertainty, and 97 percent of it is from the variations of the corrosion rate among the specimens. For the weight loss samples, most of the variation (about 89 percent) in the measured corrosion rate is due to variations among the specimens, and the rest is from measurement uncertainty.

Time-Dependent General Corrosion Behaviour of the WPOB

The general corrosion model implemented in the TSPA assumes that general corrosion of the WPOB progresses uniformly over a large surface at a (time-independent) constant rate. Therefore the depth of penetration or thinning of the WPOB by general corrosion is equal to the general corrosion rate multiplied by the time that the waste package is exposed to an environment under which general corrosion undergoes. However general corrosion rates of metals and alloys tend to decrease with time. This is shown in Figure 6-19 for the mean general corrosion rates of Alloy 22 for up to more than 2-year exposure at the LTCTF. The mean general corrosion rate after 5-year exposure at the LTCTF is 0.007 $\mu\text{m}/\text{year}$. Each data point in the figure is the mean of the measurements on at least 144 samples. The trend of decreasing general corrosion rate with time is consistent with the expected corrosion behavior of passive alloys such as Alloy 22 under repository-type aqueous conditions. The time-dependent general corrosion behavior of the WPOB was not included in the TSPA because the constant (time-independent) rate model is more conservative and should bound the general corrosion behavior of the WPOB over the repository time period. The 5-year corrosion rates were conservatively selected for extrapolation over the repository time scale.

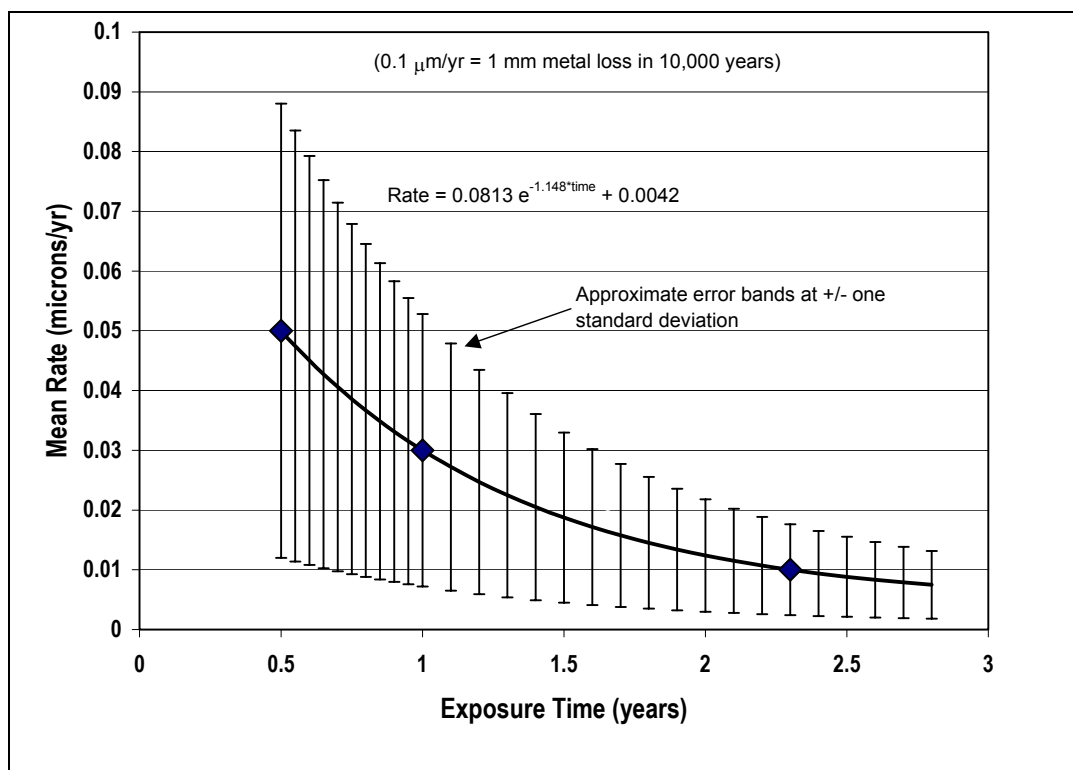


Figure 6-19. The mean general corrosion rate after 5-year exposure at the LTCTF is 0.007 $\mu\text{m/year}$. Each data point is the mean of the measurements on at least 144 samples.

Chapter 7. Electrochemical Determination of the Threshold for Localized Corrosion of Alloy 22 in Aggressive Brines Evolved in the Transition Region (Frequency $\leq 1\%$)

Chapter 7 describes the localized corrosion of the corrosion-resistant outer barrier of the waste package, which is made of Alloy 22. The threshold temperature is the level at which spontaneous localized corrosion can occur, and determines the operating temperature of the waste package, below which no localized attack will occur. The threshold temperature for localized corrosion can be determined from measurements of the open-circuit corrosion potential (E_{corr}) and the critical potential ($E_{critical}$) as functions of temperature. Spontaneous breakdown of the passive film and localized corrosion require that the open circuit corrosion potential exceed the critical potential (CRWMS M&O 2000d, ANL-EBS-MD-000003 REV 00 ICN 00; Farmer et al. 2000a):

$$E_{corr} \geq E_{critical} \quad (\text{Eqn. 7-1})$$

In the published scientific literature, different bases exist for determining the critical potential from electrochemical measurements. For example, Scully et al. (1999) define the critical potential for crevice corrosion of Alloy 22 as the point where the current density increases to 1 to 10 $\mu\text{A}/\text{cm}^2$ (10^{-6} to 10^{-5} A/cm^2) during the forward (anodic) scan. Gruss et al. (1998) define the repassivation potential as the point where the current density drops to 0.1 to 1 $\mu\text{A}/\text{cm}^2$ (10^{-6} to 10^{-7} A/cm^2), and use the repassivation potential as a conservative estimate of the critical value.

Cyclic Potentiodynamic Polarization (CPP) is used as a means of measuring the critical potential of the corrosion-resistant outer layer of waste package ($E_{critical}$), relative to the open-circuit corrosion potential (E_{corr}). Hypothetical cyclic potentiodynamic polarization curves for Type 316L stainless steel, Alloy 22, and titanium are shown in Figure 7-1, and illustrate the beneficial effects of molybdenum additions on the corrosion resistance of Alloy 22.

In regard to its resistance to localized corrosion in chloride medium, titanium alloys are superior to 316L and Alloy 22. However, titanium alloys tend to be more susceptible to stress corrosion cracking, and much more prone to hydrogen absorption in crevices, and the associated hydrogen induced cracking.

The Project has used cyclic potentiodynamic polarization (CPP) to determine threshold potentials for Alloy 22 in test media relevant to the environment expected in the repository. Figure 7-2 shows one of the potentiostats used to measure critical potentials for, as well as time-dependent corrosion potential. The temperature-controlled electrochemical cell is also shown. The cell is equipped with three electrodes, a working electrode (test specimen), the reference electrode, and the counter electrode. The electrochemical cell is equipped with coolers and condensers to maintain reference electrodes at ambient temperature, and to prevent the loss of volatile species.

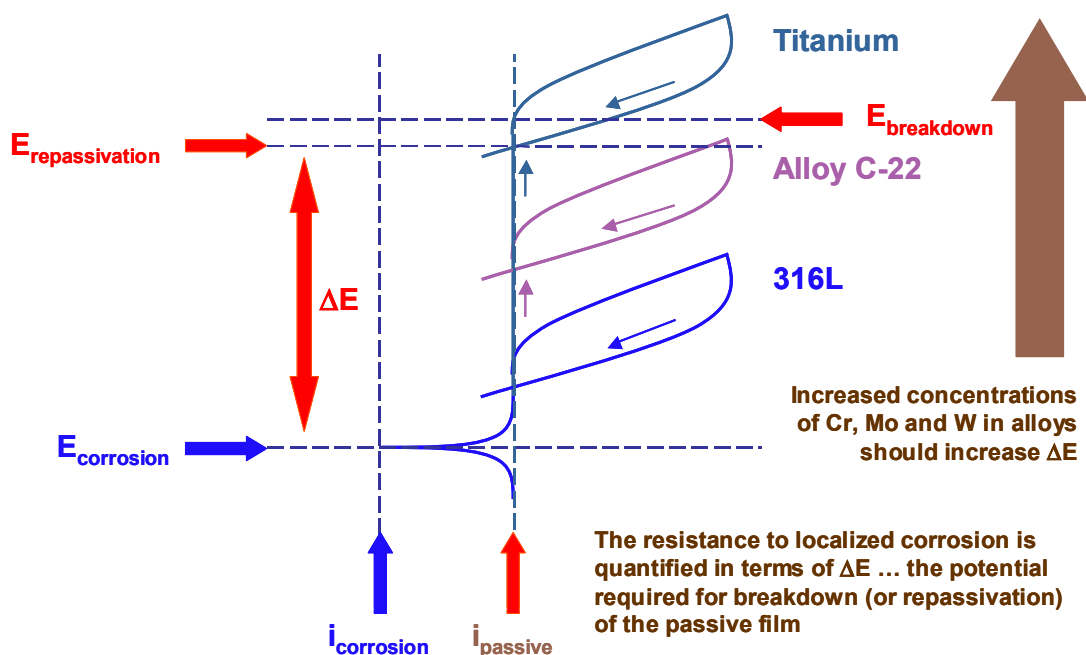


Figure 7-1. Hypothetical cyclic potentiodynamic polarization (CPP) curves for 316L, Alloy 22 and titanium. The critical potential can be defined as either the breakdown potential, which corresponds to the onset of passive film destabilization, or the repassivation potential evident during the reverse scan.

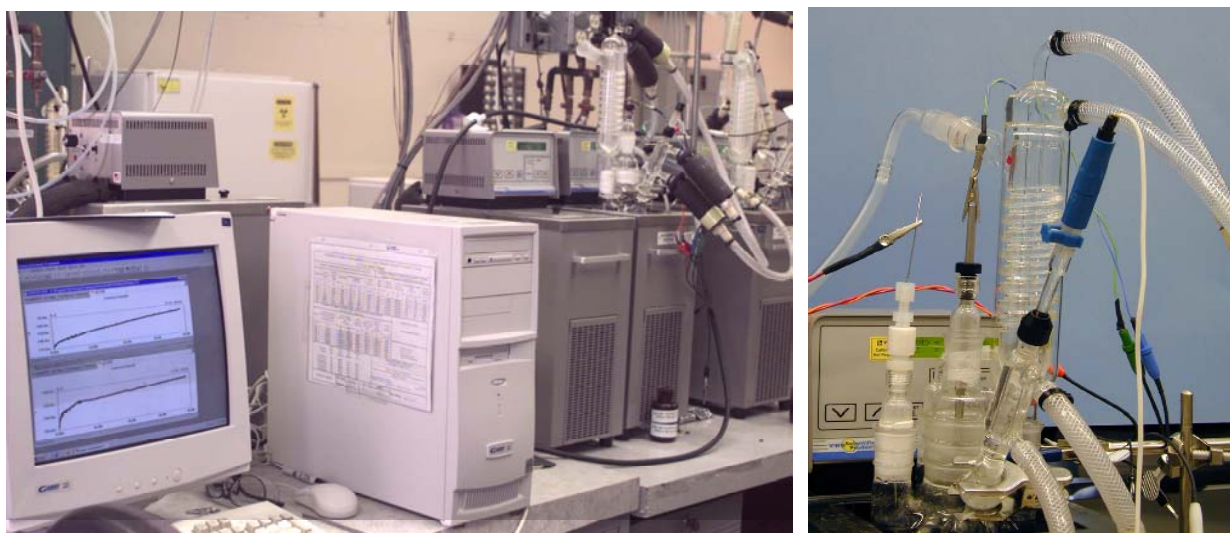


Figure 7-2. Potentiostat and temperature-controlled three-electrode electrode cell with a condenser to prevent loss of condensable volatiles, and a cooler to control the temperature of the reference electrode.

CPP measurements have been based on a procedure similar to ASTM G 5-94 (ASTM 1994), with slight modification. For example, ASTM G 5-94 calls for an electrolyte of 1N H₂SO₄, whereas SDW, SCW, SAW, SSW, BSW and near-saturation CaCl₂ solutions with various levels of nitrate are used here. Furthermore, aerated solutions were used here, unlike the procedure that calls for de-aerated solutions. It has been found that the CPP curves for Alloy 22 and Type 316L stainless steel can be categorized as Type 1, 2 or 3.

Type 1 Cyclic Potentiodynamic Polarization Curves. A generic Type 1 curve exhibits complete passivity (no passive film breakdown) between the open circuit corrosion potential and the breakdown potential, or the potential where oxygen evolution begins if no breakdown is observed. Type 1 behavior is observed in the standardized SSW test medium near its ambient-pressure boiling point of approximately 120°C. This saturated sodium-potassium-chloride-nitrate electrolyte was formulated to represent the type of concentrated electrolyte that might evolve on a hot WP surface. It is evident from Figure 7-3 that Alloy 22 maintains passivity at potentials up to the reversal potential (1200 mV versus Ag/AgCl), even under these relatively hostile conditions.

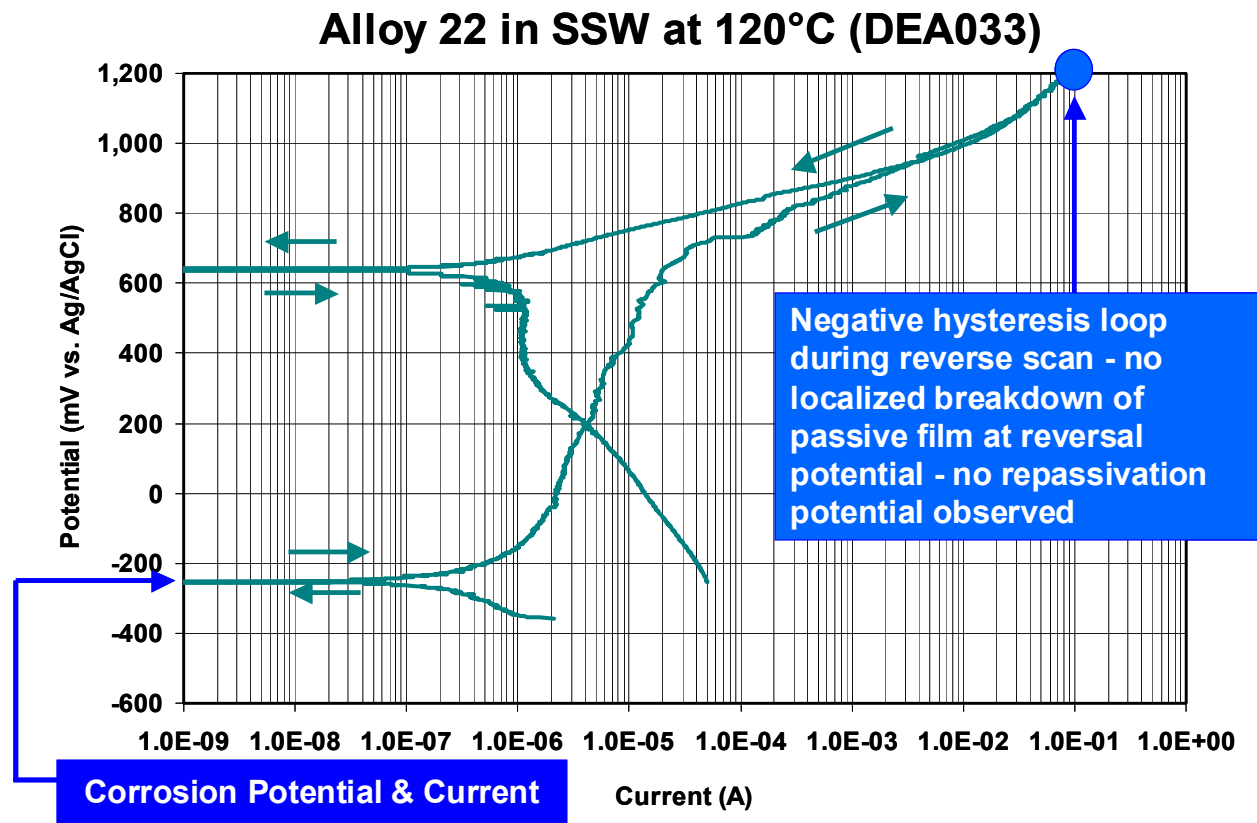


Figure 7-3. Cyclic potentiodynamic polarization (CPP) data for Alloy 22 in SSW at 120°C shows no loss of passivity, even with a voltage reversal of 1200 mV vs. Ag/AgCl, and exhibits Type 1 behavior.

Type 2 Cyclic Potentiodynamic Polarization Curves. A generic Type 2 curve exhibits a well-defined oxidation peak between the open circuit corrosion potential and the breakdown potential, or the potential where oxygen evolution begins if no breakdown is observed. The anodic oxidation peak (process) is believed to be due to the conversion metals in the passive film to higher, perhaps more soluble, oxidation states. This oxidation processes is accompanied by dramatic changes in XPS and surface morphology, both of which have been well documented by the Project.

Type 3 Cyclic Potentiodynamic Polarization Curves. A generic Type 3 curve exhibits a complete breakdown of the passive film and active pitting at potentials relatively close to the open-circuit corrosion potential. The critical pitting potential is clearly evident in Figure 7-4. Type 3 behavior has only been observed with Type 316L stainless steel.

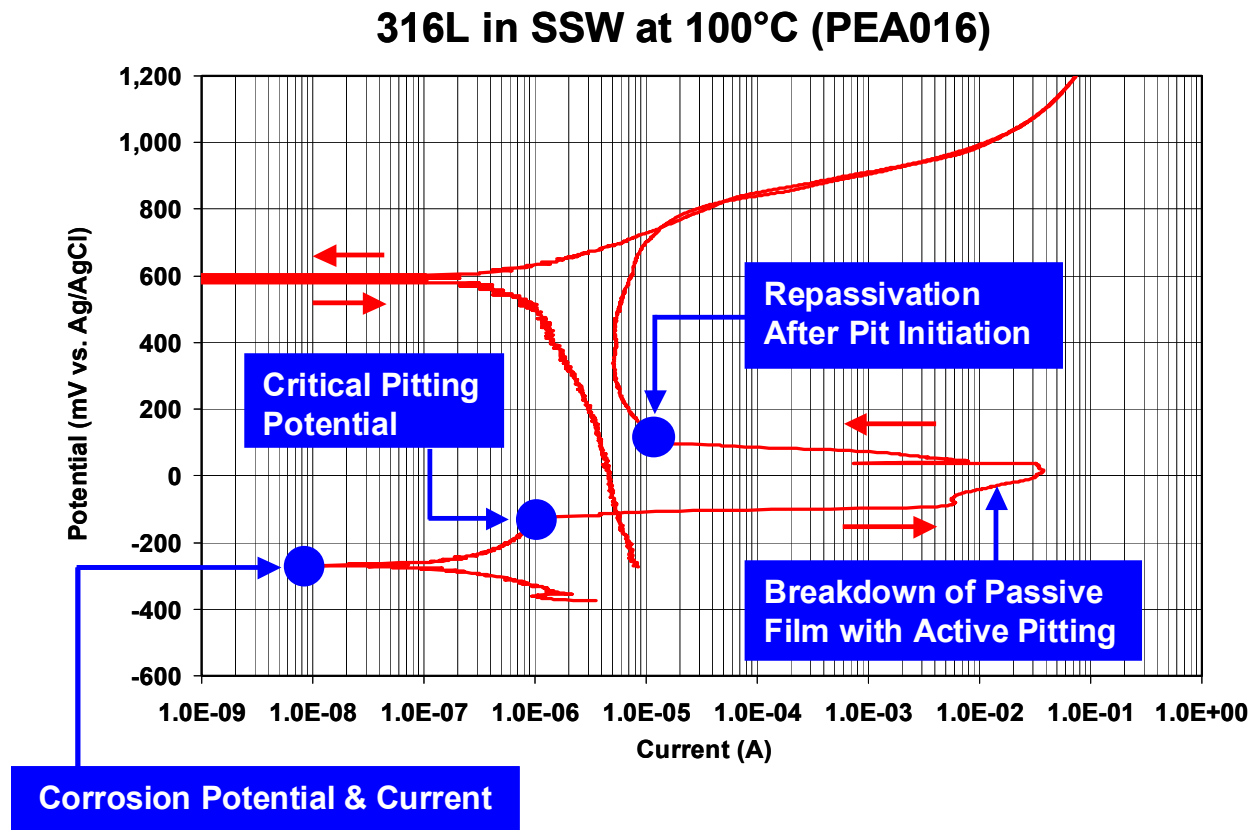


Figure 7-4. Cyclic potentiodynamic polarization (CPP) data for Type 316L stainless steel in SSW at 120°C shows pitting potential very close to the open circuit corrosion potential, and exhibits Type 3 behavior.

*Cyclic Potentiodynamic Polarization (CPP) Measurements in Aggressive CaCl₂-Type Brines
(Frequency $\leq 1\%$)*

The test conditions for the most severe tests are given below, along with other details pertaining to the sample configurations and measurements:

- Test Conditions
 - Chloride Concentrations: 10 to 18 M
 - Inhibitor Level: $\text{NO}_3^-/\text{Cl}^- = 0.0 \text{ \& } 0.1$
 - Temperature Range: 45 to 160°C
- Sample Configurations and Measurement Details
 - CPP measurements in temperature controlled electrochemical cell
 - Alloy 22 samples: disks & multiple crevice assemblies
 - Surface analysis of specimens after exposure

In regard to the most severe tests, multiple crevice assembly (MCA) samples like the one shown in Figure 7-5 are used to create the types of severe occluded geometries experienced with crevices. The hydrolysis reactions that occur in such occluded regions, which involved dissolved metals, cause the disproportionate production of hydrogen ion, and the lowering of local pH. Charge balance in the crevice is maintained by the transport of halide anions such as chloride, through both diffusion and electro-migration. The surface finish of the as-received MCA-type sample is established with 600-grit SiC paper. The edges of the sample are ground to remove metallurgy damaged by cutting processes such as electrical discharge machining (EDM). The exposed area is typically 7.43 cm². The scalloped crevice-forming washer is held tightly to the metal surface with a nut and bolt, tightened to a precisely measured torque of 70 in-lb. Teflon inserts into the MCA to fill micro voids. The bolts used to hold the MCA together are wrapped with Teflon that serves as electrical insulation. Welded samples were produced with narrow-groove gas tungsten arch welding (NG-GTAW).



Figure 7-5. Multiple-crevice assembly (MCA) used for cyclic potentiodynamic polarization (CPP) studies of artificially creviced samples.

At the present time, three competing methodologies exist for the interpretation of experimental data, and are summarized as follows. Method A strives to identify the potential where the passive film disappears during the forward (anodic) potential scan. The loss of passivity is indicated by a sudden, dramatic increase in the measured current density. The current density corresponding to a complete loss of passivity is assumed to be approximately $20 \mu\text{A}/\text{cm}^2$. The breakdown potential may be the best estimate of the true critical potential, since it corresponds to the onset of passive film destabilization. Methods B and C strive to identify the potential where the passive film reappears during the negative (cathodic) potential scan. Repassivation is indicated by a sudden, precipitous decrease in the measured current density, to levels indicative of an in-tact passive film.

- Method A – Initial Breakdown of Passive Film
 - Critical Potential (E_{crit}) = Breakdown Potential (E_{20})
 - Based Threshold Current Density of $20 \mu\text{A}/\text{cm}^2$
- Method B – Repassivation of Surface
 - Critical Potential (E_{crit}) = Repassivation Potential (ER_1)
 - Based Threshold Current Density of $1 \mu\text{A}/\text{cm}^2$
- Method C – Repassivation of Surface
 - Critical Potential (E_{crit}) = Repassivation Potential (ERP)
 - Intersection of Forward Scan with Hysteresis Loop (Cross-Over Point)

CPP curves are shown for Alloy 22 multiple crevice assembly (MCA) samples in 5M CaCl₂ without nitrate in Figures 7-6 through 7-8, for temperatures ranging from 45 to 120°C. Since there is no breakdown of the passive film at 45°C, the breakdown and repassivation potentials cannot be determined. However, there are well-defined breakdown and repassivation potentials at 90 and 120°C, with a large potential margin (ΔE) evident. The repassivation potentials at 90 and 120°C can be determined with either Methods B or C (similar results are obtained in both cases). The ennoblement of Alloy 22 in 5M CaCl₂ without nitrate is shown in Figure 7-9. After 18 months, the open-circuit corrosion potential increased to a steady-state value of approximately -150 to -125 mV vs. Ag/AgCl. The critical potentials determined by Method C, which are based upon the crossover point, is shown in Figure 7-10. These data indicate that the criterion for crevice corrosion in pure, concentrated CaCl₂ will probably be met at temperatures above approximately 75°C, which is the apparent threshold temperature for crevice corrosion in the absence of nitrate inhibitor. However, it is noted that significant levels of nitrate will probably be present, even in the most aggressive CaCl₂-type brines that could be evolved from seepage.

CPP curves are shown for Alloy 22 multiple crevice assembly (MCA) samples in 5M CaCl₂ with nitrate inhibitor ($[\text{NO}_3^-]/[\text{Cl}^-] \sim 0.1$) at 45 and 120°C are shown in Figures 7-11 and 7-12. There are well-defined breakdown and repassivation potentials at these temperatures, and a large potential margin (ΔE) at both temperatures. As previously discussed, repassivation potentials can be determined with either Methods B or C. Both methods yield similar results. The ennoblement of Alloy 22 in 5M CaCl₂ with nitrate is shown in Figure 7-13. After 12 months, the open-circuit corrosion potential increased to a steady-state value of approximately 0 to 200 mV vs. Ag/AgCl for base metal, and approximately 200 to 300 mV vs. Ag/AgCl for weld metal. As shown in Figures 7-14 and 7-15, this indicates that the criterion for crevice corrosion may be met at temperatures above 90°C for base metal, and at a slightly lower temperature for the weld metal.

From these data, we therefore conclude that localized corrosion of Alloy 22 may occur in pure, concentrated, liquid, aqueous-phase CaCl₂ electrolytes at temperatures below the boiling point of ~100°C (below which seepage is possible), and above the apparent threshold temperature for crevice corrosion of ~75°C (above which crevice corrosion is possible). There is a 25°C range of vulnerability in the absence of nitrate. In the presence of nitrate, there is only a 10°C range of vulnerability, extending from 100 to 90°C during cool-down.

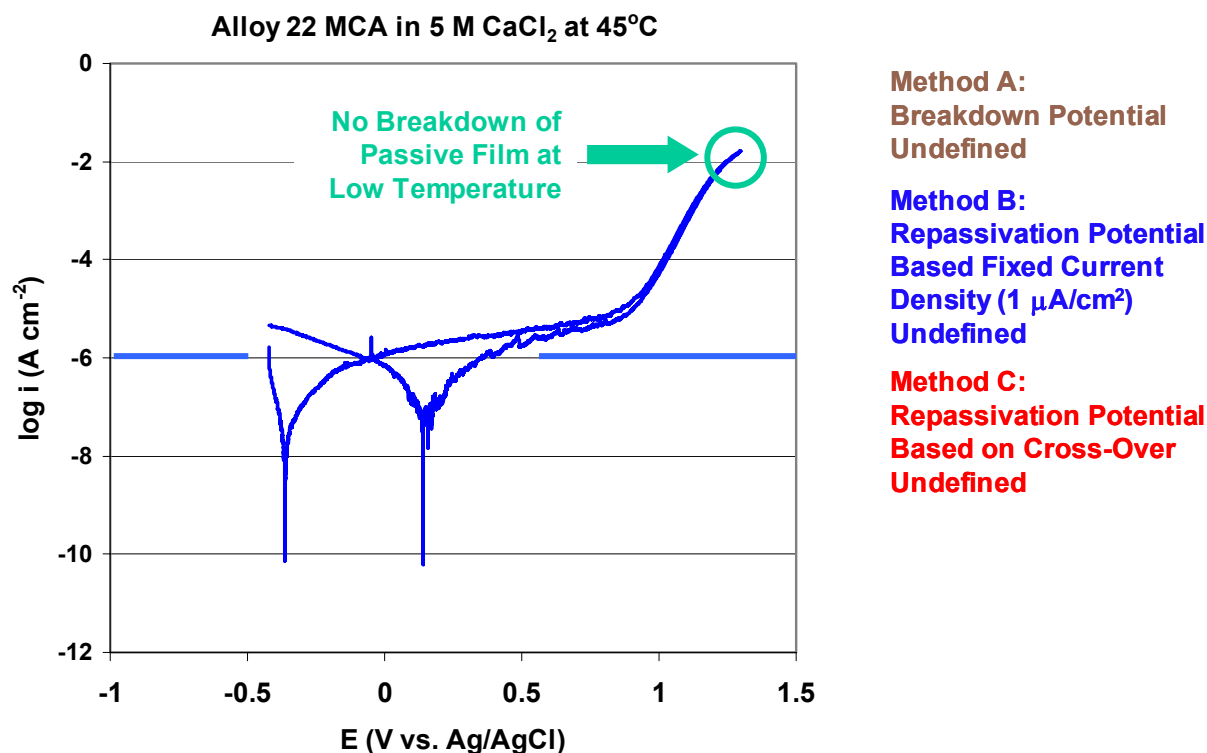


Figure 7-6. CPP data for creviced Alloy 22 in 45°C CaCl₂ brine without NO₃⁻ Inhibitor.

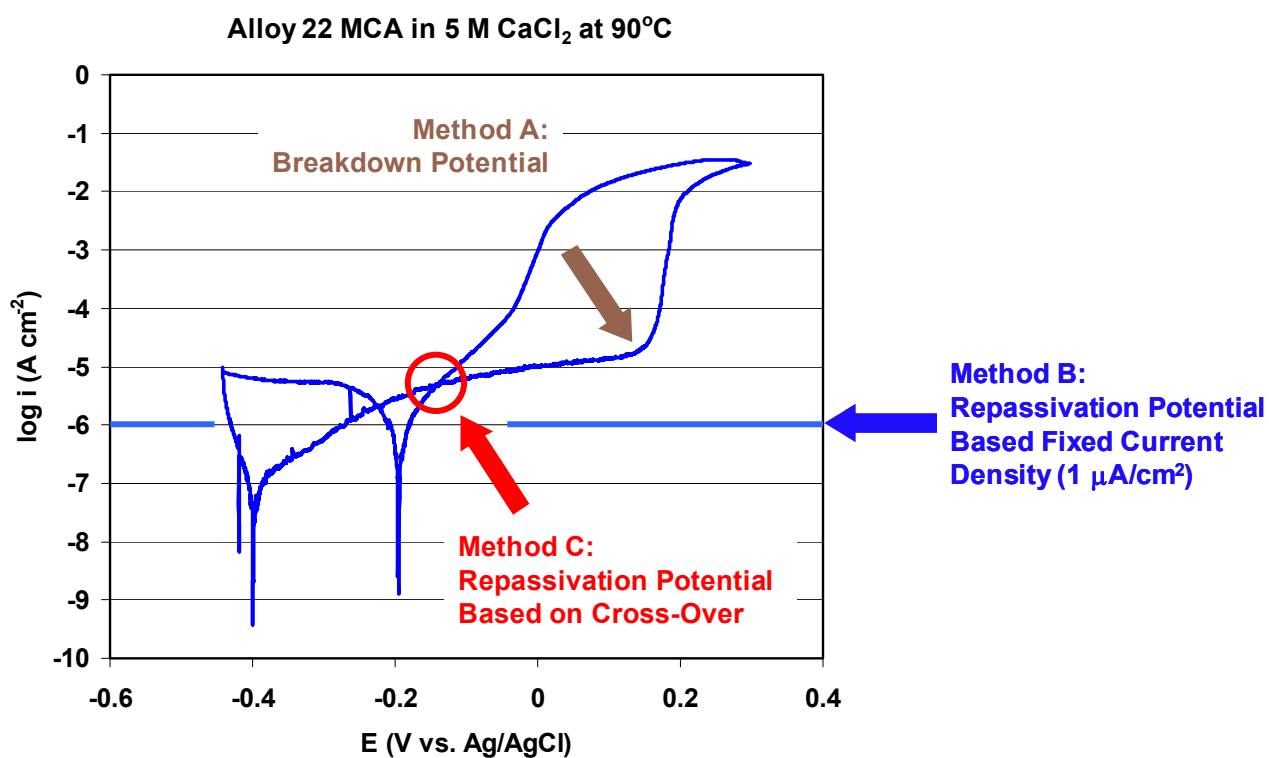


Figure 7-7. CPP data for creviced Alloy 22 in 90°C CaCl₂ brine without NO₃⁻ Inhibitor.

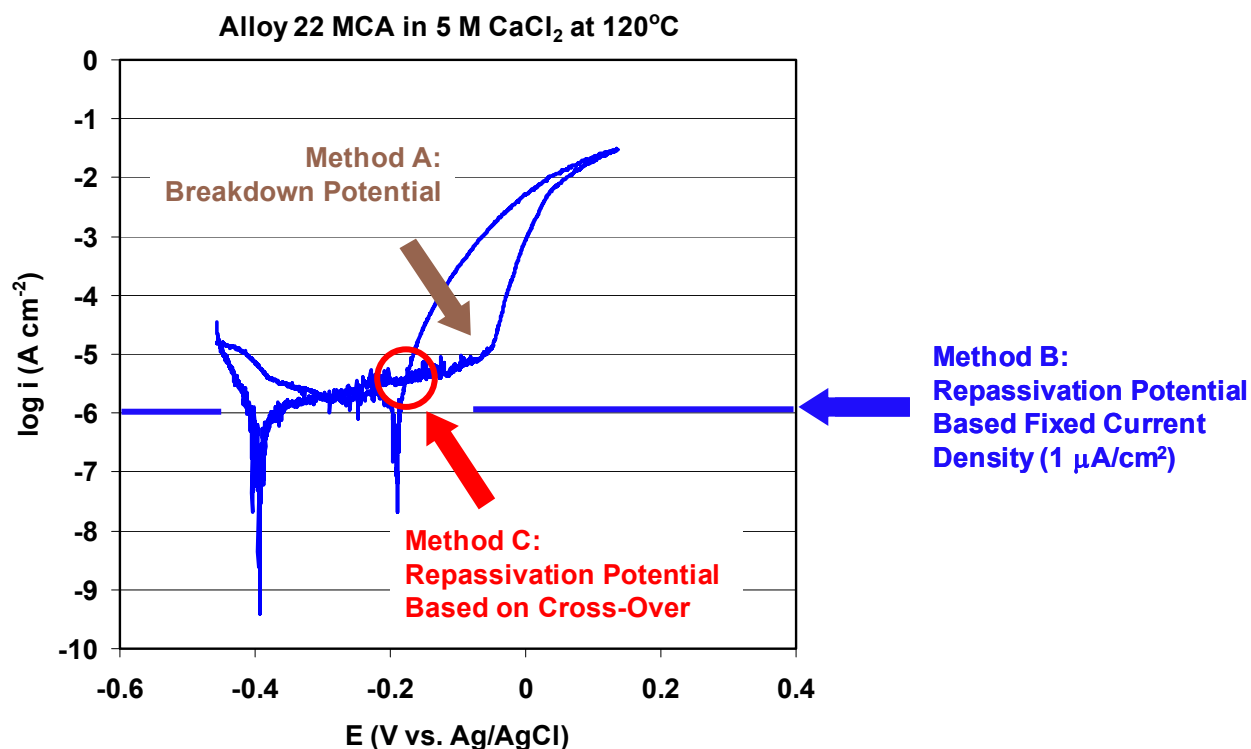


Figure 7-8. CPP data for creviced Alloy 22 in CaCl₂ brine at 120°C without NO₃⁻ Inhibitor.

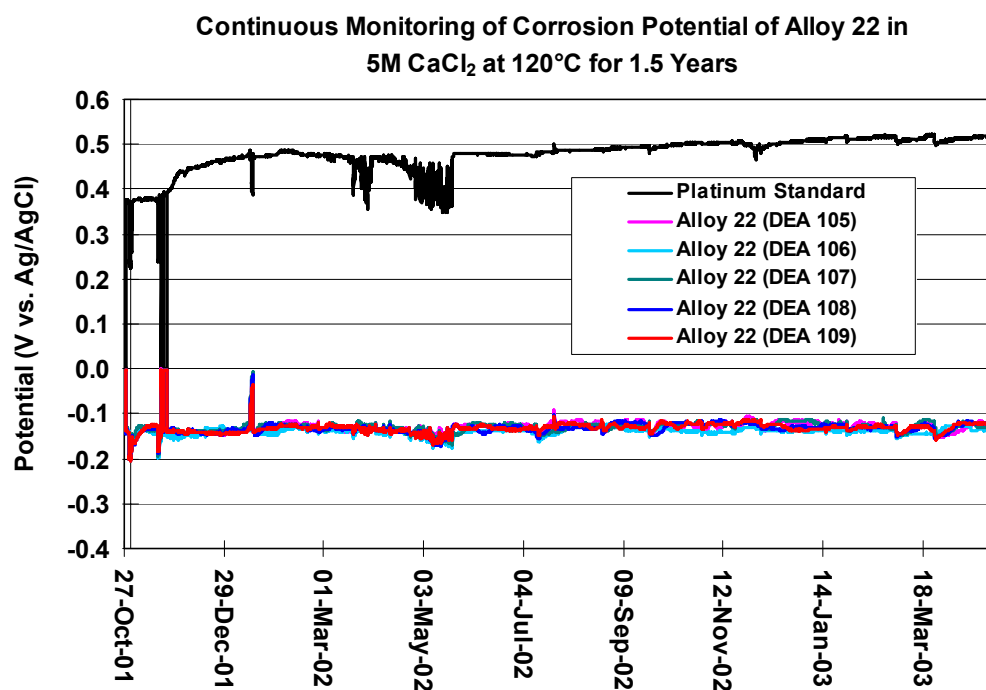


Figure 7-9. Effect of long-term exposure on the open-circuit corrosion potential of Alloy 22 in high-temperature CaCl₂ brine. Note that some of these data are repeated in Figure 7-24, but with lower resolution (fewer data points per unit time), and for a shorter period of time.

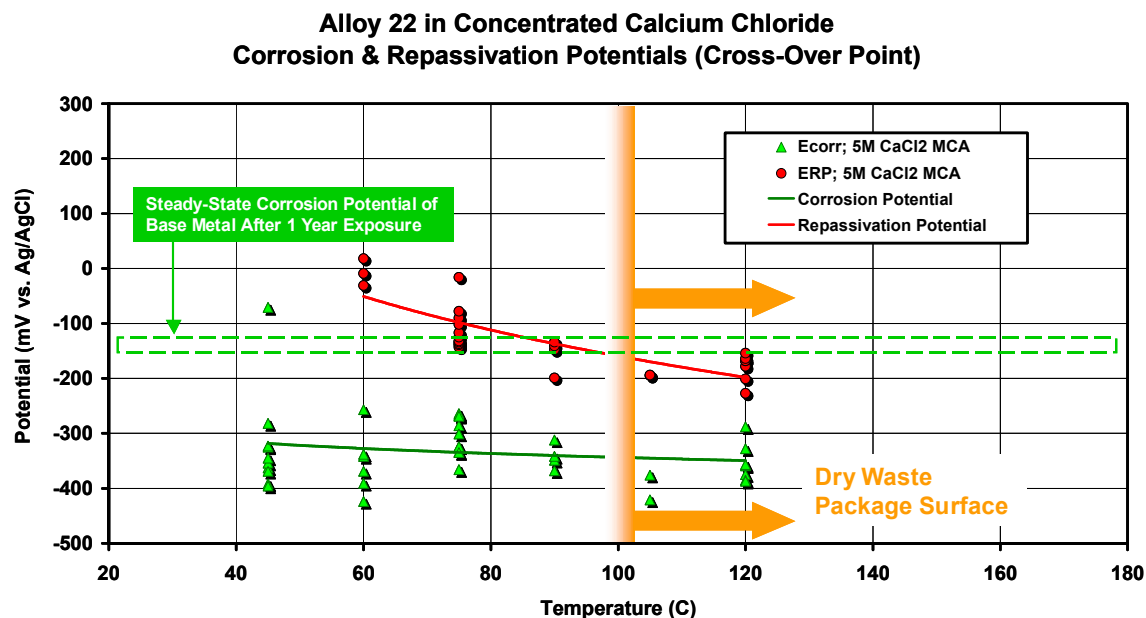


Figure 7-10. Critical potentials of creviced Alloy 22 samples in CaCl₂ brines, without NO₃⁻ inhibitor, and at temperatures ranging from 45-120°C. These data were analyzed by Method C, which uses the cross-over point to establish the repassivation potential. Method C was used in this case to determine the repassivation potential.

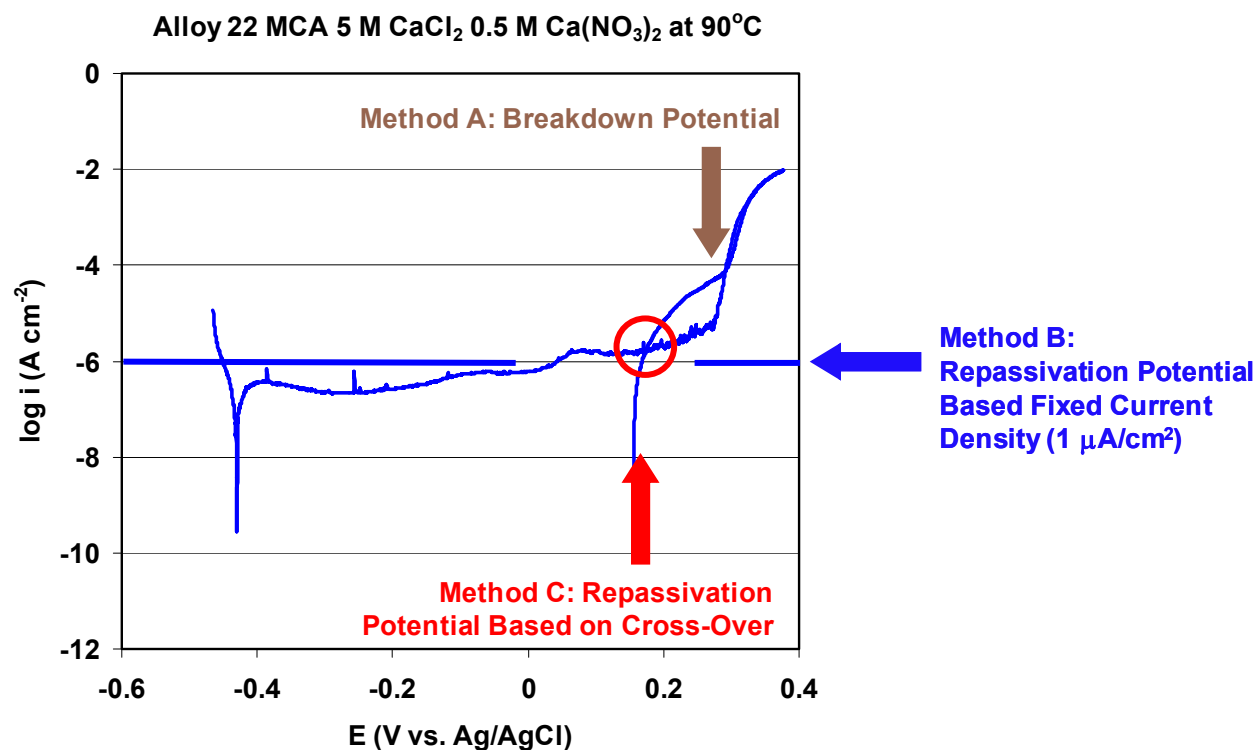


Figure 7-11. CPP data for creviced Alloy 22 in CaCl₂ brine at 90°C with NO₃⁻ Inhibitor.

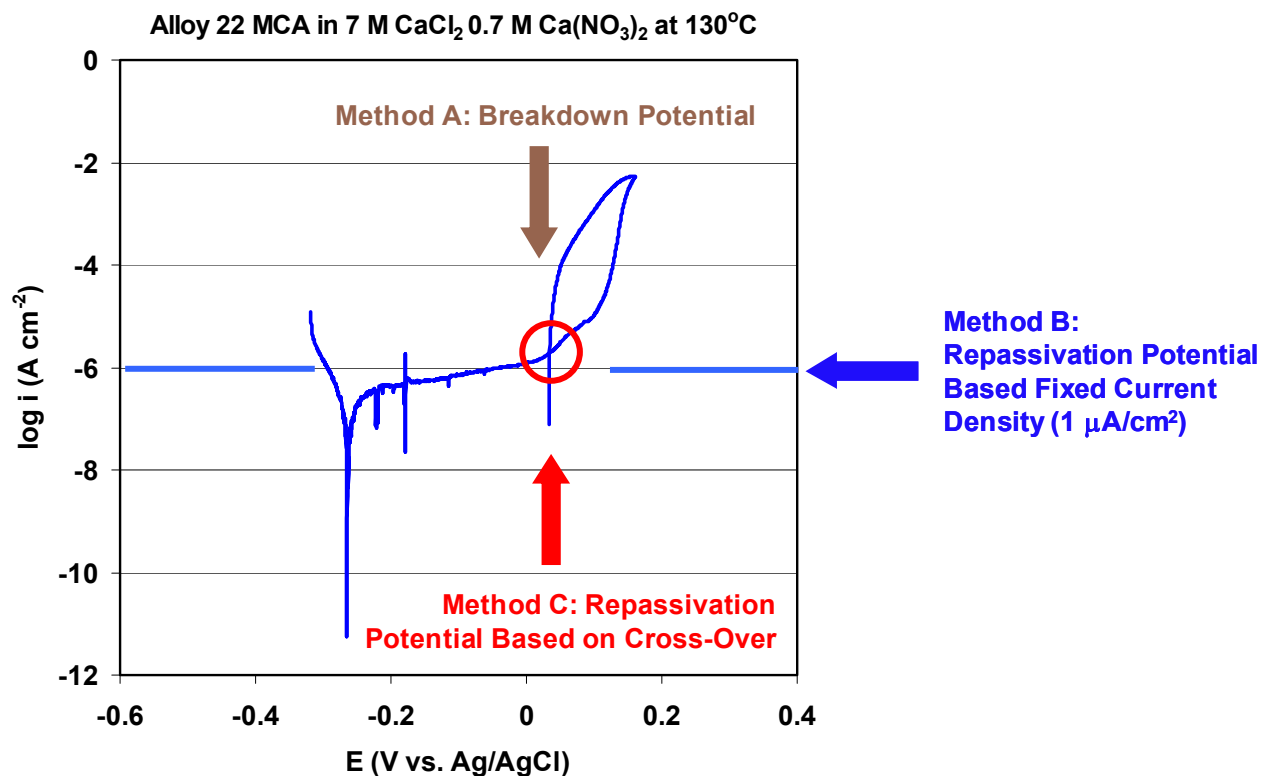


Figure 7-12. CPP data for creviced Alloy 22 in CaCl_2 brine at 130°C with NO_3^- Inhibitor.

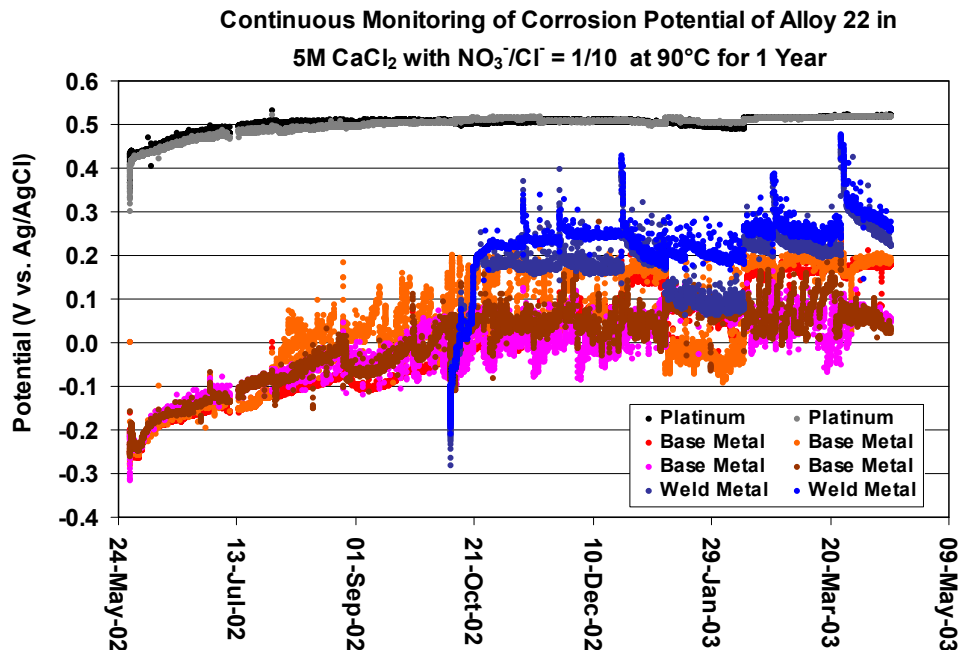


Figure 7-13. Effect of long-term exposure on the open-circuit corrosion potential of Alloy 22 in high-temperature CaCl_2 brine with nitrate inhibitor. Note that these data are repeated in Figure 7-24, but with lower resolution (fewer data points per unit time), and for a shorter period of time.

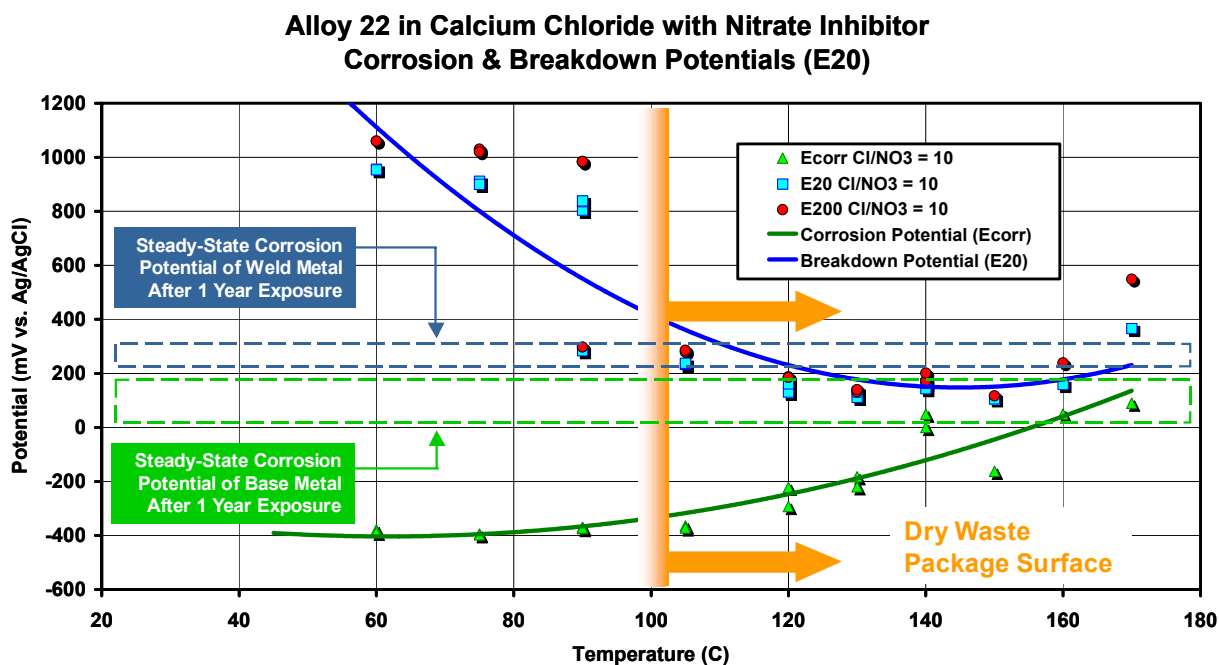


Figure 7-14. Critical potentials of creviced Alloy 22 samples in CaCl₂ brines, with NO₃⁻ inhibitor, and at temperatures ranging from 60-170°C. These data were analyzed by Method A, which is a determination of the breakdown potential.

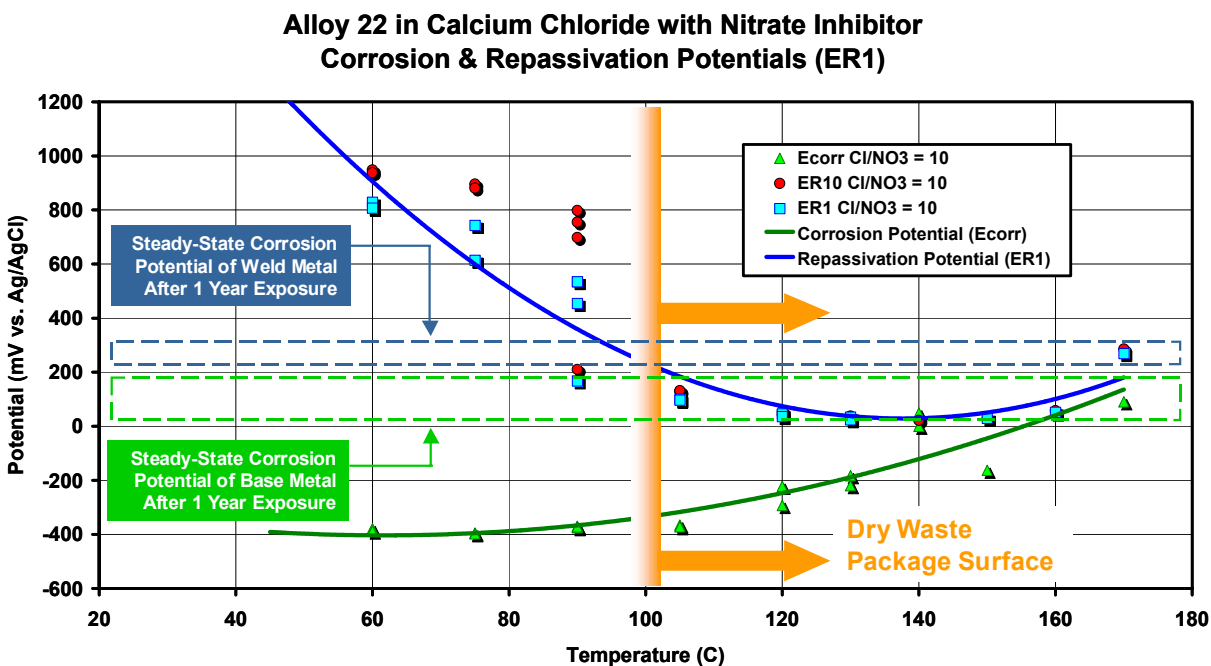


Figure 7-15. Critical potentials of creviced Alloy 22 samples in CaCl₂ brines, with NO₃⁻ inhibitor, and at temperatures ranging from 60-170°C. These data were analyzed by Method B, which is a determination of the repassivation potential.

The strong inhibitory effect of nitrate anion also demonstrated by Figures 7-16 through 7-19. First, consider the shifts in critical potential evident in CPP curves. The localized corrosion during CPP of Alloy 22 MCA in 5M CaCl₂ brine at 105°C, with and without inhibition by NO₃⁻ anion, is shown in Figure 7-16. At a temperature of 105°C, the addition of nitrate ([NO₃⁻]/[Cl⁻] ~ 0.1) shifts the breakdown potential (Method A) by approximately ~200 mV, and the repassivation potential (Method C) by ~300 mV. The localized corrosion of during CPP of Alloy 22 disk in 9M CaCl₂ brine at 150°C, with and without inhibition by NO₃⁻ anion, is shown in Figure 7-17. At a temperature of 150°C, the addition of nitrate ([NO₃⁻]/[Cl⁻] ~ 0.1) shifts the breakdown potential (Method A) by approximately ~200 mV, and the repassivation potential (Method C) by ~300 mV.

Crevice corrosion of an Alloy 22 prismatic sample during CPP in 5M CaCl₂ brine at 75°C, with and without inhibition by NO₃⁻ anion, is shown in Figure 7-18. The sample without nitrate shows clear evidence of crevice corrosion, on a part of the sample that was underneath an o-ring, while the sample with nitrate shows no such attack. The crevice corrosion of an Alloy 22 prismatic sample during CPP in 5M CaCl₂ brine at 90°C, with and without inhibition by NO₃⁻ anion, is shown in Figure 7-19. Here too, the sample without nitrate shows clear evidence of crevice corrosion, on a part of the sample that was underneath an o-ring, while the sample with nitrate shows no such attack. In all electrochemical testing of creviced Alloy 22 samples, nitrate has been shown to inhibit localized attack, and appears to elevate the threshold temperature for crevice corrosion.

While seepage waters that evolve into CaCl₂-type brines are predicted with a frequency of less than 1%, significant electrochemical testing has now been done, and significant insight has been developed to establish the threshold temperature for crevice corrosion in these harsh environments. There appears to be a 25°C range of vulnerability in the absence of nitrate. In the presence of nitrate, there is only a 10°C range of vulnerability, extending from 100 to 90°C during cool-down.

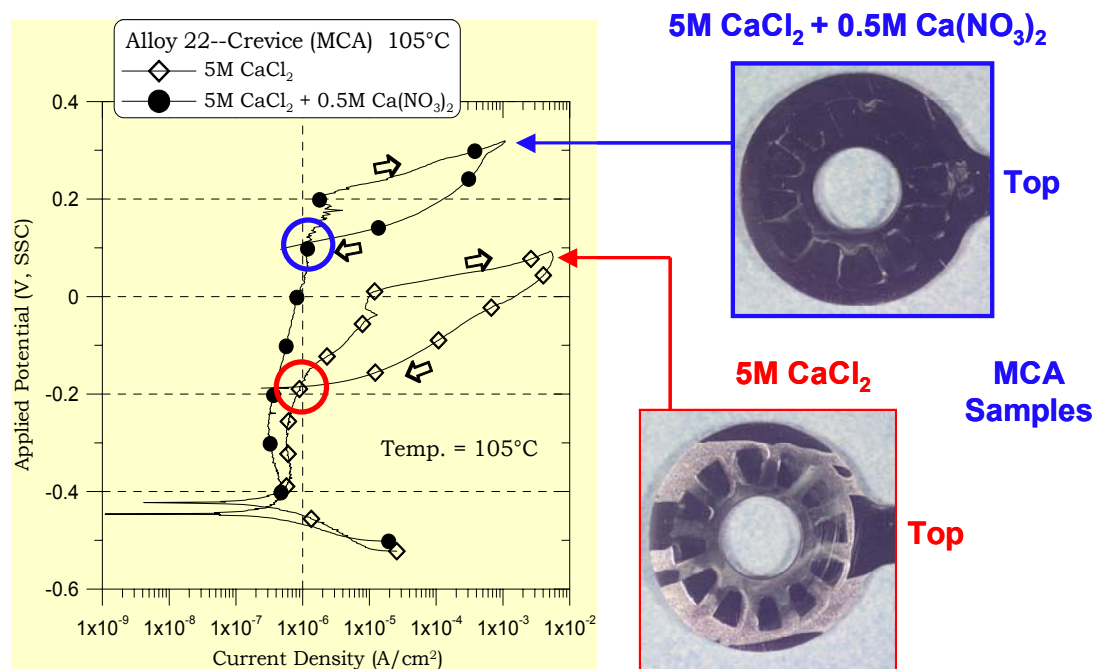


Figure 7-16. Localized corrosion during CPP of Alloy 22 MCA in 5M CaCl_2 brine at 105°C, with and without inhibition by NO_3^- anion.

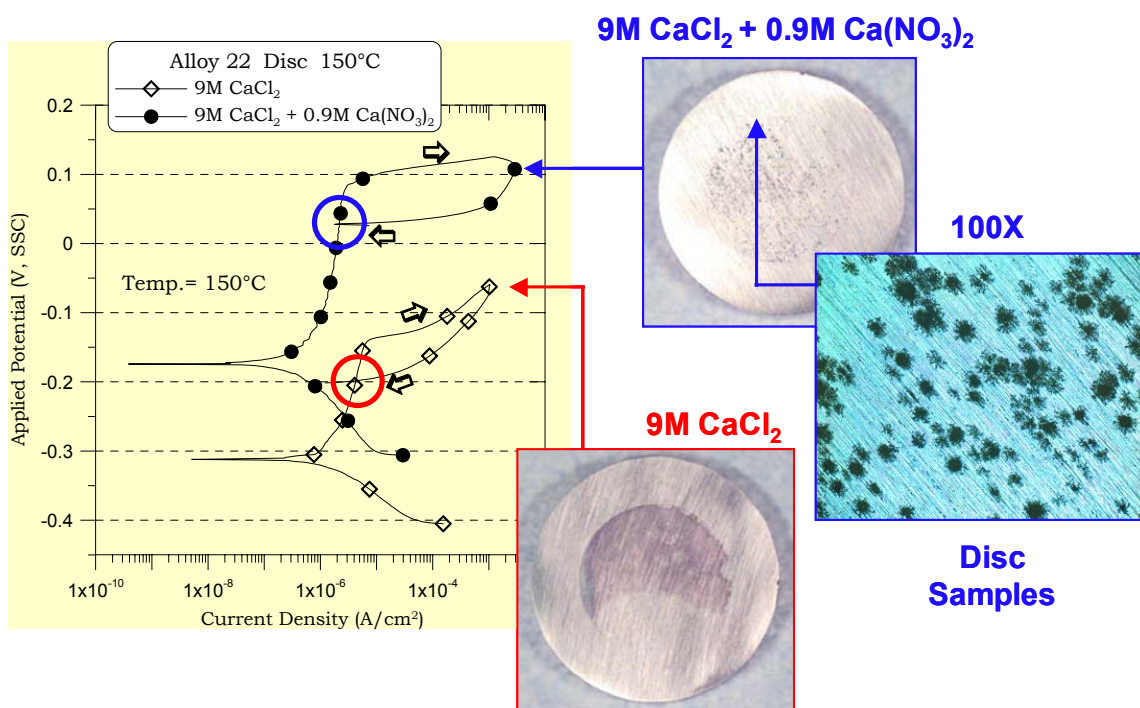
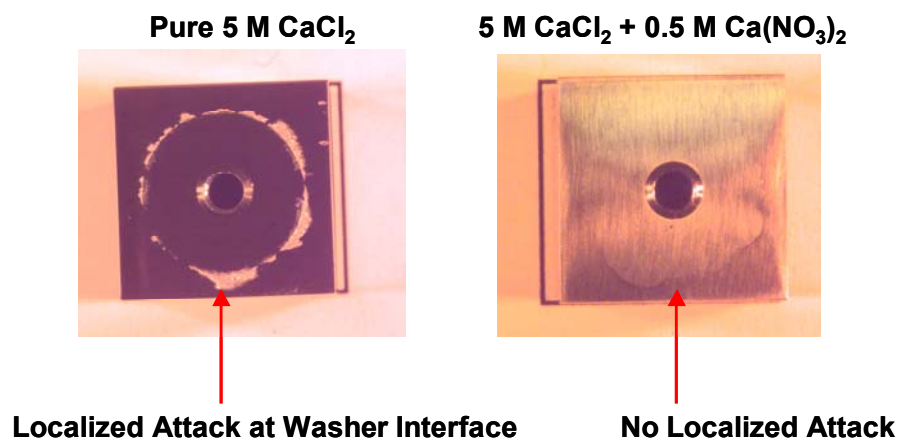
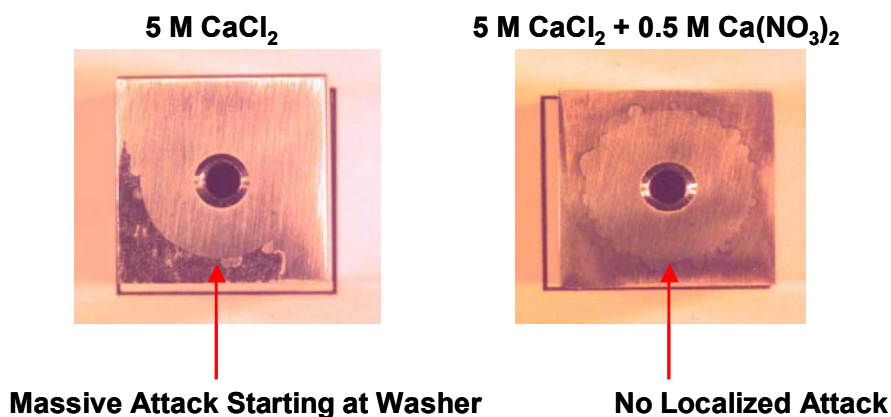


Figure 7-17. Localized corrosion of Alloy 22 disk in 9M CaCl_2 brine at 150°C, with and without inhibition by NO_3^- anion.



**Cyclic Polarization with Prismatic Samples:
Effect of NO_3^- on Alloy 22 Crevice Corrosion at 75°C**

Figure 7-18. Localized corrosion during CPP of Alloy 22 prismatic sample in 5 M CaCl_2 brine at 75°C, with and without inhibition by NO_3^- anion. The crevice attack shown here occurs at the reversal potential experienced during CPP, and did not occur spontaneously at the open-circuit corrosion potential.



**Cyclic Polarization with Prismatic Samples:
Effect of NO_3^- on Alloy 22 Crevice Corrosion at 90°C**

Figure 7-19. Localized corrosion during CPP of Alloy 22 prismatic sample in 5 M CaCl_2 brine at 90°C, with and without inhibition by NO_3^- anion. The crevice attack shown here occurs at the reversal potential experienced during CPP, and did not occur spontaneously at the open-circuit corrosion potential.

Localized Corrosion Initiation Model

The localized corrosion model for the Alloy 22 WPOB has two components: the initiation model, and the propagation model. The initiation model assumes that localized corrosion of the WPOB occurs when the steady-state corrosion potential (E_{corr}) is equal to or greater than the critical potential ($E_{critical}$). This is expressed mathematically as: ($\Delta E \leq 0$) where ($\Delta E = E_{critical} - E_{corr}$). Conservatively, the critical potential ($E_{critical}$) is defined as the crevice repassivation potential (E_{rcrev}), the potential at which the Alloy 22 surface undergoes spontaneous repassivation. All potentials are expressed in the units of mV, relative to the standard Ag/AgCl reference electrode (also referred to as SSC).

The crevice repassivation potential (E_{rcrev}) is defined in terms of the crevice repassivation potential in the absence of inhibitive nitrate ions, and the change in crevice repassivation potential due to inhibiting nitrate anion, (E_{rcrev}^o) and ($\Delta E_{rcrev}^{NO_3^-}$) respectively, by Equation 7-2.

$$E_{rcrev} = E_{rcrev}^o + \Delta E_{rcrev}^{NO_3^-} \quad (\text{Eqn. 7-2})$$

The crevice repassivation potential in the absence of inhibitive nitrate ions (E_{rcrev}^o) is predicted with Equation 7-3.

$$E_{rcrev}^o = a_o + a_1 T + a_2 pH + a_3 \log([Cl^-]) + a_4 T \times \log([Cl^-]) \quad (\text{Eqn. 7-3})$$

The adjustable model parameters in this equation are a_o , a_1 , a_2 , a_3 , and a_4 ; the temperature is represented by T , given in the units of °C, and the chloride concentration is represented by $[Cl^-]$, given in the units of moles per kilogram of water (molal). The value of the adjustable parameters (regression coefficients) and their uncertainty (± 1 standard deviation) are: $a_o = 214.089 \pm 46.880$, $a_1 = -3.696 \pm 0.476$, $a_2 = 25.284 \pm 5.641$, $a_3 = -252.181 \pm 53.912$, and $a_4 = 1.414 \pm 0.547$.

The effect of nitrate on the crevice repassivation potential is accounted for with Equation 7-4.

$$\Delta E_{rcrev}^{NO_3^-} = b_o + b_1 [NO_3^-] + b_2 \frac{[NO_3^-]}{[Cl^-]} \quad (\text{Eqn. 7-4})$$

The adjustable model parameters in this equation are b_o , b_1 and b_2 ; the nitrate concentration is represented by $[NO_3^-]$, given in the units of moles per kilogram of water (molal); and the nitrate-chloride ratio is represented by $[NO_3^-]/[Cl^-]$, and limited to unity (1.0) by the available data set. This correlation accounts for the competing effects of the aggressive chloride anion and the inhibiting nitrate anion through the nitrate-chloride ratio. The adjustable model parameters and their uncertainty (± 1 standard deviation) are: $b_o = -50.959 \pm 78.168$, $b_1 = 115.867 \pm 64.714$, and $b_2 = 1045 \pm 1320.076$.

An empirical model for the long-term steady-state corrosion potential of the Alloy 22 WPOB has been developed, and is applicable over a broad range of exposure conditions related to the proposed repository. This model is expressed as follows:

$$E_{corr} = c_o + c_1T + c_2pH + c_3[Cl^-] + c_4 \log\left(\frac{[NO_3^-]}{[Cl^-]}\right) \quad (\text{Eqn. 7-5})$$

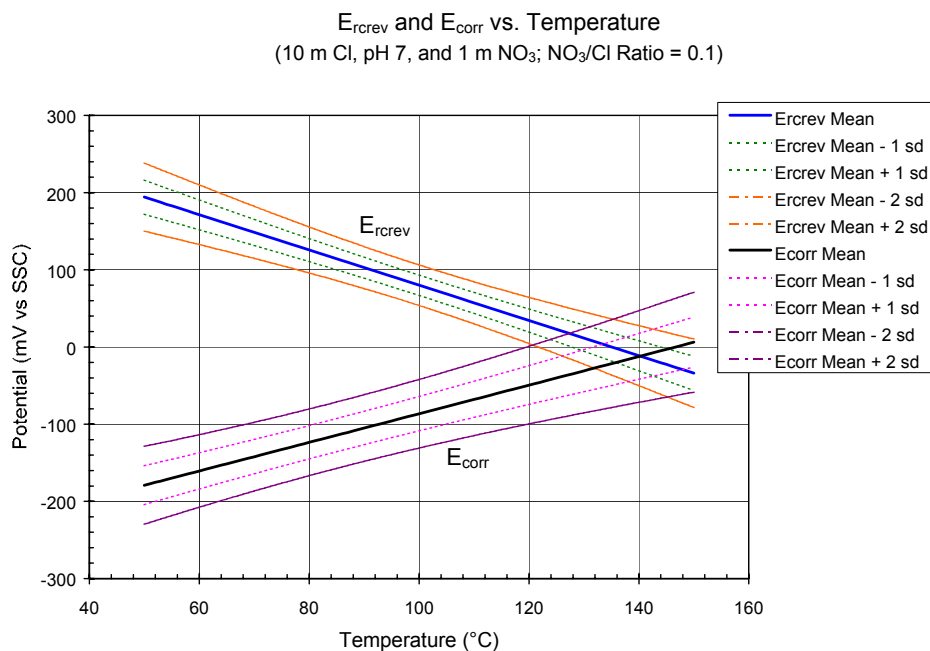
The predicted value of E_{corr} and is expressed in the units of mV, relative to the standard Ag/AgCl reference electrode; adjustable model parameters are c_o , c_1 , c_2 , c_3 , and c_4 and were determined by fitting Equation 7-5 to the long-term corrosion potential data. These estimated regression coefficients and their uncertainty (± 1 standard deviation) are: $c_o = 365.511 \pm 32.901$, $c_1 = 1.853 \pm 0.374$, $c_2 = -48.091 \pm 2.528$, $c_3 = -29.641 \pm 1.931$, and $c_4 = -4.263 \pm 4.326$.

As seen from the dependence of the corrosion potential on the logarithm of the nitrate-to-chloride ion concentration ratio, the model requires the nitrate concentration be greater than zero. Therefore, for a condition with no nitrate ion present, it is recommended that a small value (such as 0.01 M) be used for the nitrate ion concentration.

Because only nitrate ions are accounted for in the crevice corrosion initiation model for the inhibitive effect, the model results for solutions with significant amounts of other potentially inhibitive ions such as carbonate and sulfate (in addition to nitrate ions) are believed to be conservative. The model results for the beneficial effects of the inhibitive nitrate anion, combined with the alkaline pH conditions of the typical carbonate waters in the repository, are consistent with the experimental observations of no localized corrosion susceptibility of Alloy 22 in similar waters.

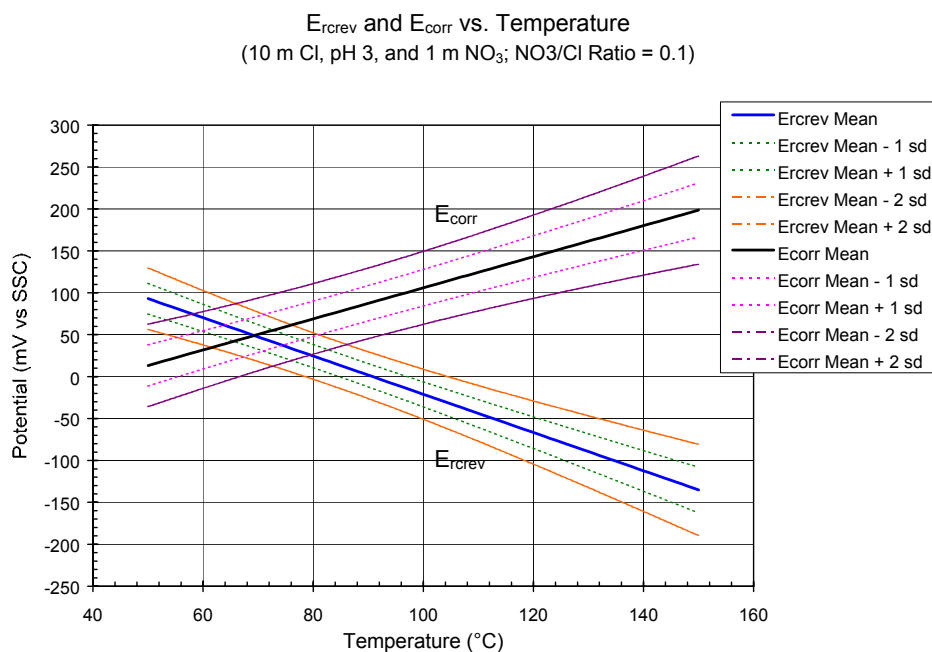
The localized corrosion model for the Alloy 22 WPOB predicts a minimum threshold temperature for crevice corrosion of $\sim 120^\circ\text{C}$ in 10-molal chloride solutions with 1-molal nitrate additions ($[NO_3^-]/[Cl^-] = 0.1$), at near-neutral pH ($\text{pH} \sim 7$). The mean threshold temperature is predicted to be $\sim 140^\circ\text{C}$. Values of the threshold temperature are determined from the intersection of the E_{corr} versus T regression curve(s) with the E_{rev} versus T regression curve(s), as shown in Figure 7-20. At lower pH, the threshold temperature for crevice corrosion is predicted to be lower. For example, the localized corrosion model predicts a minimum threshold temperature of $\sim 50^\circ\text{C}$ in 10-molal chloride solutions with 1-molal chloride solutions with 1-molal nitrate additions ($[NO_3^-]/[Cl^-] = 0.1$), at mildly acidic conditions ($\text{pH} \sim 3$), as shown in Figure 7-21. While such mildly acidic conditions can develop inside crevices, it must be emphasized that the empirical localized corrosion model is highly conservative. The beneficial effects of other dominant anions, such as carbonate, bicarbonate, and sulfate, are not accounted for. Specifically, the carbonate anion is polyprotic, and serves as an effective buffer in crevices. Furthermore, five-year exposures of Alloy 22 crevice samples in SAW ($\text{pH} \sim 2.7$) at the LTCTF, no crevice attack has been observed, contrary to the conservative predictions of the empirical model.

Clearly, the long-term stability of the nitrate inhibitor on the surface of the waste package is important. Removal through electrochemical reduction, or microbial action, should be considered if waste package performance is found to be critically reliant upon this inhibitor.



Output DTN: SN0306T0506303.001

Figure 7-20. Model results for crevice corrosion susceptibility of the WPOB as a function of temperature for 10 m chloride, pH 7, and 1 m nitrate (NO_3/Cl ratio = 0.1).



Output DTN: SN0306T0506303.001

Figure 7-21. Model results for crevice corrosion susceptibility of the WPOB as a function of temperature for 10 m chloride, pH 3, and 1 m nitrate (NO_3/Cl ratio = 0.1).

Application of the Localized Corrosion Model to 11 Bins of EBS Chemistry Model

As discussed in Chapter 1, the EBS Chemistry Model is used to predict the range of expected water chemistry inside the drifts at Yucca Mountain. The EQ3/6 code is a component of the EBS Chemistry Model, as is used to simulate the evaporative concentration of any seepage water that might possibly enter the drift after the temperature drops below the boiling point ($\sim 100^{\circ}\text{C}$). The range of water compositions attained after evaporation to near dryness (corresponding to the lowest predicted RH value) are summarized in Table 7-1. Results are given for eleven characteristic seepage waters (11 bins), each with three (3) levels of temperature and three (3) levels of carbon-dioxide partial pressure (refer to [DTN: MO0304SPACSALT.000]). Since the localized corrosion initiation model (Equations 7-2 through 7-5) requires temperature, pH, chloride concentration and nitrate concentration as input parameters, those specific parameters are included in Table 7-1. By using the data from the EBS Chemistry Model as input for the Localized Corrosion Initiation Model, the corrosion and crevice repassivation potentials (mean values) for the WPOB can be calculated for the entire range of in-drift environments, accounting for evaporative concentration on the hot waste package surface. Differences between the corrosion and crevice repassivation potentials ($\Delta E = E_{rcrev} - E_{corr}$) predicted with Equations 7-2 through 7-5 are used to predict the initiation of localized corrosion in specified environments. If the crevice repassivation potential (E_{rcrev}) is greater than the long-term open-circuit corrosion potential (E_{corr}), the potential difference (ΔE) is positive, and no initiation of localized corrosion is predicted. However, if the crevice repassivation potential (E_{rcrev}) drops below the long-term open-circuit corrosion potential (E_{corr}), the potential difference (ΔE) becomes negative, and the initiation of localized corrosion is predicted. The potential differences (mean values) have been calculated for the eleven characteristic bins of water chemistry, and are tabulated in Table 7-1. Since these values are positive, no localized corrosion is predicted.

While this simple analysis is encouraging, it is important to point out that the uncertainty in the parameters in Equations 7-2 through 7-5 is not accounted for in Table 7-1. The Total System Performance Assessment (TSPA) being done for License Application (LA) does account for such uncertainty, and should be viewed as the ultimate source of information on waste package performance in the Yucca Mountain repository.

Table 7-1. Corrosion and Crevice Repassivation Potentials for Binned Water Chemistries

Bins	Temperature (°C)	P _{CO2} (atm)	RH (%)	pH	Ionic Strength (molal)	[Cl ⁻] (molal)	[NO ₃ ⁻] (molal)	E _{rrev} (mV vs. SSC)	ΔE _{rrev} (mV)	E _{corr} (mV vs. SSC)	ΔE (mV)
1	100	0.01	20.04%	3.82	39.85	25.13	1.99	-214	262	-373	421
1	40	0.01	18.12%	3.57	37.36	24.06	1.31	-114	158	-440	484
1	70	0.01	18.69%	3.65	38.64	24.31	1.94	-165	257	-396	488
1	100	0.001	20.04%	4.32	39.85	25.12	1.99	-201	262	-397	458
1	40	0.001	18.06%	4.02	35.56	22.66	1.49	-97	190	-420	513
1	70	0.001	18.70%	4.15	38.66	24.32	1.94	-152	257	-420	525
1	100	0.0001	20.01%	4.82	39.84	25.11	1.99	-189	262	-420	494
1	40	0.0001	18.25%	4.49	34.41	21.74	1.61	-82	212	-416	547
1	70	0.0001	18.69%	4.65	38.64	24.30	1.94	-139	257	-444	561
2	100	0.01	24.00%	4.42	36.24	21.26	4.69	-191	723	-289	822
2	40	0.01	23.14%	4.60	37.63	21.92	4.90	-80	751	-428	1100
2	70	0.01	23.41%	4.38	35.40	20.66	4.62	-135	718	-325	908
2	100	0.001	24.00%	4.92	36.20	21.23	4.68	-178	722	-312	857
2	40	0.001	23.14%	5.10	37.62	21.91	4.91	-67	751	-452	1136
2	70	0.001	24.00%	4.81	33.58	19.59	4.38	-121	691	-314	883
2	100	0.0001	24.00%	5.42	36.18	21.22	4.68	-165	722	-336	893
2	40	0.0001	23.14%	5.60	37.63	21.91	4.90	-55	751	-476	1172
2	70	0.0001	24.00%	5.31	33.58	19.58	4.38	-108	691	-338	920
3	100	0.01	43.95%	4.91	20.38	13.17	3.62	-155	656	-73	573
3	40	0.01	38.94%	4.44	20.00	12.21	2.38	-34	429	-133	528
3	70	0.01	42.26%	4.74	20.24	11.66	4.31	-88	835	-76	823
3	100	0.001	44.00%	5.42	20.39	13.23	3.60	-143	650	-99	606
3	40	0.001	39.78%	4.97	19.75	12.08	2.37	-20	429	-155	564
3	70	0.001	42.47%	5.27	20.24	11.80	4.24	-76	815	-106	845
3	100	0.0001	44.02%	5.92	20.39	13.23	3.60	-130	650	-123	643
3	40	0.0001	39.95%	5.49	19.73	12.09	2.37	-7	429	-180	602
3	70	0.0001	42.49%	5.77	20.24	11.81	4.23	-63	813	-130	881
4	100	0.01	47.41%	6.47	22.39	3.94	15.23	-58	5757	120	5579
4	40	0.01	65.01%	6.33	13.46	3.99	8.10	109	3007	16	3100
4	70	0.01	52.86%	6.05	20.29	1.90	17.05	65	11282	144	11204
4	100	0.001	47.41%	6.97	22.39	3.94	15.23	-45	5756	96	5615
4	40	0.001	65.01%	6.83	13.46	3.99	8.10	121	3007	-8	3137

4	70	0.001	52.86%	6.55	20.29	1.90	17.05	78	11292	120	11251
4	100	0.0001	47.41%	7.47	22.39	3.94	15.23	-32	5757	72	5652
4	40	0.0001	65.01%	7.33	13.46	3.99	8.10	134	3007	-32	3173
4	70	0.0001	52.86%	7.05	20.29	1.90	17.05	91	11302	96	11297
5	100	0.01	60.13%	7.27	17.27	8.19	1.80	-73	388	-39	354
5	40	0.01	69.13%	7.12	10.01	6.00	1.32	94	332	-78	504
5	70	0.01	62.05%	7.14	16.60	6.38	3.73	13	992	-36	1041
5	100	0.001	60.13%	7.77	17.28	8.19	1.80	-60	388	-63	390
5	40	0.001	69.94%	7.64	9.37	6.27	0.70	103	148	-109	360
5	70	0.001	62.07%	7.64	16.58	6.38	3.73	25	992	-60	1077
5	100	0.0001	60.13%	8.27	17.27	8.18	1.80	-48	388	-87	427
5	40	0.0001	62.35%	7.88	19.96	3.41	8.53	161	3555	-42	3759
5	70	0.0001	62.06%	8.14	16.59	6.38	3.73	38	991	-84	1113
6	100	0.01	59.12%	9.00	17.19	7.21	2.52	-23	606	-94	676
6	40	0.01	62.98%	8.30	19.79	4.30	6.09	152	2133	-88	2372
6	70	0.01	60.50%	8.91	17.82	5.75	4.43	64	1267	-103	1435
6	100	0.001	59.12%	9.50	17.17	7.27	2.44	-11	583	-120	691
6	40	0.001	61.75%	9.27	20.55	3.93	6.92	184	2590	-124	2898
6	70	0.001	59.70%	9.51	18.54	5.46	5.02	83	1491	-124	1698
6	100	0.0001	58.89%	10.00	17.30	7.20	2.21	2	525	-141	669
6	40	0.0001	64.07%	10.10	14.04	5.03	2.57	184	779	-194	1158
6	70	0.0001	59.63%	10.01	18.56	5.46	4.90	96	1454	-148	1697
7	100	0.01	59.11%	9.00	17.20	7.22	2.52	-23	606	-94	677
7	40	0.01	62.98%	8.30	19.79	4.30	6.09	152	2133	-88	2372
7	70	0.01	60.50%	8.91	17.81	5.75	4.43	64	1267	-103	1435
7	100	0.001	59.12%	9.50	17.17	7.27	2.44	-11	583	-120	691
7	40	0.001	61.75%	9.27	20.54	3.93	6.92	184	2590	-124	2898
7	70	0.001	59.70%	9.51	18.54	5.46	5.02	83	1491	-124	1698
7	100	0.0001	60.00%	9.99	16.07	7.12	1.84	3	431	-138	572
7	40	0.0001	66.23%	10.13	12.37	5.61	0.70	176	161	-210	546
7	70	0.0001	59.63%	10.01	18.55	5.46	4.90	96	1454	-148	1697
8	100	0.01	59.11%	9.00	17.20	7.21	2.52	-23	606	-94	676
8	40	0.01	62.98%	8.30	19.78	4.30	6.09	152	2133	-88	2372
8	70	0.01	60.50%	8.91	17.82	5.75	4.43	64	1267	-103	1435
8	100	0.001	59.12%	9.50	17.18	7.27	2.44	-11	583	-120	692
8	40	0.001	61.74%	9.27	20.55	3.93	6.92	184	2590	-124	2898
8	70	0.001	59.70%	9.51	18.54	5.46	5.02	83	1492	-124	1698
8	100	0.0001	58.88%	10.00	17.30	7.20	2.21	2	525	-141	669
8	40	0.0001	62.16%	10.06	15.94	4.49	4.61	193	1556	-177	1926
8	70	0.0001	59.62%	10.01	18.57	5.46	4.90	96	1454	-148	1697
9	100	0.01	50.94%	9.16	30.12	9.90	8.99	-34	1940	-183	2088
9	40	0.01	62.01%	8.33	19.23	4.53	6.77	148	2296	-96	2540
9	70	0.01	50.02%	9.19	32.84	9.34	10.75	39	2397	-224	2660

9	100	0.001	50.91%	9.66	30.17	9.98	8.95	-22	1923	-209	2110
9	40	0.001	61.33%	9.27	20.41	3.93	7.18	184	2687	-124	2996
9	70	0.001	57.51%	9.53	21.68	5.66	6.71	81	1966	-131	2178
9	100	0.0001	52.31%	10.06	27.94	8.01	8.53	-1	2050	-171	2219
9	40	0.0001	62.12%	10.06	15.93	4.48	4.59	193	1552	-177	1922
9	70	0.0001	49.78%	10.27	33.07	9.40	10.70	66	2378	-278	2722
10	100	0.01	58.99%	9.00	17.24	7.18	2.56	-23	617	-93	687
10	40	0.01	66.11%	8.40	12.47	5.58	2.56	133	725	-128	985
10	70	0.01	60.35%	8.91	17.87	5.70	4.49	65	1290	-102	1457
10	100	0.001	59.01%	9.50	17.21	7.23	2.48	-10	594	-118	702
10	40	0.001	61.53%	9.26	20.61	3.88	7.01	185	2650	-122	2957
10	70	0.001	59.60%	9.51	18.57	5.43	5.06	83	1508	-123	1714
10	100	0.0001	58.84%	10.00	17.25	7.15	2.24	3	535	-140	677
10	40	0.0001	62.12%	10.06	15.93	4.48	4.59	193	1551	-177	1921
10	70	0.0001	59.54%	10.01	18.56	5.42	4.93	96	1471	-147	1713
11	100	0.01	59.00%	9.00	17.23	7.17	2.56	-23	617	-93	687
11	40	0.01	62.68%	8.29	19.95	4.23	6.21	153	2205	-85	2443
11	70	0.01	60.35%	8.91	17.86	5.70	4.48	65	1290	-102	1457
11	100	0.001	59.00%	9.50	17.21	7.23	2.48	-10	594	-118	702
11	40	0.001	61.52%	9.26	20.62	3.88	7.01	185	2650	-122	2957
11	70	0.001	59.60%	9.51	18.58	5.43	5.06	83	1508	-123	1714
11	100	0.0001	58.77%	10.00	17.34	7.16	2.25	3	537	-140	679
11	40	0.0001	62.12%	10.06	15.93	4.48	4.59	193	1554	-177	1924
11	70	0.01	59.51%	10.01	18.62	5.43	4.94	96	1471	-147	1714
CK	100			3.00		10.00	1.00	-190	169	114	-135
CK	100			7.00		10.00	1.00	-89	169	-78	158

Long-Term Open-Circuit Corrosion Potential Data Analysis

Because the corrosion potential of Alloy 22 may change over time, it is important to know the most probable value of long-term corrosion potential (E_{corr}) for Alloy 22 under different environmental conditions to evaluate the localized corrosion susceptibility of the WPOB in the proposed repository. As discussed above, the localized corrosion initiation model of the WPOB assumes that localized corrosion will only occur when E_{corr} is equal or greater than a critical potential (crevice repassivation potential (E_{rcrev}) in the current model analysis). That is, if $E_{corr} < E_{rcrev}$, general or passive corrosion will occur. Passive corrosion rates are expected to be exceptionally low.

The specimens used to evaluate E_{corr} of Alloy 22 as a function of immersion time were machined from sheet and bar stock. There were two main groups of specimens, (1) Welded U-bend specimens and (2) Untested rod specimens. Approximately half of the U-bend specimens tested for long-term corrosion potential were from the Long Term Corrosion Test Facility (LTCTF), and other half of the U-bend specimens were not previously exposed to any electrochemical test condition. The U-bend specimens from the LTCTF already had the passive film and other surface alterations from the exposure in the LTCTF. The U-bend specimens were tested in the as-received (AR) or as-machined conditions, which corresponded to a root mean square roughness of 32 μ -inch. The U-bend specimens were fabricated from $\frac{3}{4}$ -inch wide and 1/16-inch thick metal strips according to ASTM G 30 (ASTM G 30-94 1994). The specimens were degreased in acetone and alcohol before testing. During the long-term open-circuit corrosion potential monitoring, the U-bend specimens were fully immersed in the electrolyte of interest. The rod specimens were all previously untested. Rod specimens were $\frac{1}{4}$ -inch in diameter and 12-inch long. They were polished with 600-grit paper and degreased with acetone and alcohol before testing. Although not shown in this AMR, in all the environments, the E_{corr} of pure platinum rods was also monitored. The platinum rods were 1/8-inch in diameter and 12-inch long. The rods (both Alloy 22 and platinum) were immersed to a depth of 1 inch into the electrolyte solution. The platinum data are reported in the input source DTN LL020711612251.017. The data and test details reported in the source DTN LL020711612251.017 are summarized in Attachment V.

Ten different electrolyte solutions were used in the tests (see Attachment V for the type of solutions tested). This included four multi-ionic solutions and six simpler salt solutions. The solutions from the LTCTF tanks (i.e., SDW, SAW and SCW) are referred to as “aged” solution (approximately 4.5-year old). The solutions that were freshly prepared (not from the LTCTF tanks) are referred to as “fresh” solution. In some solutions, more than one temperature was used for testing. The combination of tests totaled sixteen different conditions or cells (see Attachment V).

The volume of the electrolyte solution in each cell was 2 liters. The electrolyte solutions were naturally aerated; that is, the solutions were not purged, but a stream of air was circulated above the level of the solution. This stream of air exited the vessel through a condenser to avoid evaporation of the electrolyte. The electrochemical potentials are reported in the saturated silver chloride scale (SSC). At ambient temperature, the SSC scale with the reference electrode in a saturated KCl solution is 199 mV more positive than the standard hydrogen electrode (SHE) (Sawyer and Roberts 1974, Pages 39 to 45, Table 2-4).

Long-term corrosion potential behaviors of some selected Alloy 22 samples in the SDW, SAW and SCW solutions from the LTCTF tanks are shown in Figure 7-22. The figure shows that after initial changes, the corrosion potentials of the Alloy 22 samples become stable after about 100 days of testing. It is shown that the results of the welded U-bend samples (Samples DUB052 and DUB159) and (non-welded) rod samples (Samples DEA2850, DEA2851 and DEA2852) in aged SAW at 90 °C show no significant differences in their long-term open-circuit corrosion potential behaviors.

The values of E_{corr} of Alloy 22 in SAW are higher than those in other aged LTCTF solutions. The apparent steady state E_{corr} values of Alloy 22 in SAW (an acidic solution) at 60 and 90°C are in the order of 300 to 400 mV vs. SSC. Figure 7-23 compares the long-term corrosion potential evolution of freshly polished Alloy 22 rods in freshly prepared SAW at 90 °C with the corrosion potential evolution of the welded U-bend and rod samples in aged SAW at 90 °C. Because of the long-term nature of the tests, the reference electrodes had to be replaced regularly during the tests due to their operations outside the specified accuracy range. The reference electrode replacements are indicated in the figure. Initially the Alloy 22 rods in the fresh SAW solution had the corrosion potential in the order of about -150 mV vs. SSC. However, over approximately 100 days of testing, the corrosion potential increased rapidly to an oxidizing potential value of approximately 330 mV vs. SSC. This apparent stable corrosion potential was maintained over the balance of the approximately 300-day test, slowly reaching a maximum oxidizing value near 400 mV vs. SSC. This high value of E_{corr} is probably due to the formation of a protective chromium rich oxide film on the surface of the Alloy 22 electrodes. The test results show is that, regardless of the initial condition of the metal surface or the age of the electrolyte solution, eventually Alloy 22 undergoes ennoblement in SAW. This ennoblement is probably promoted by both the pH value and the presence of nitrate in the solution (Estill et al 2003). Such an ennoblement of Alloy 22 with time has also been reported recently, and the ennoblement was significant in acidic solutions (Jayaweera et al 2003, Figures 9.12 and 9.13; Dunn et al 2003, Figures 8 and 9).

In addition, the results in Figure 7-23 show that the E_{corr} values of Alloy 22 rods in SAW at 25 °C are lower than the values at 90 °C by about 150 mV. A similar trend is also observed for the welded U-bend samples in the SDW solutions. This effect could be attributed to kinetic mechanisms either in the behavior of the oxide film or on the redox reactions in solution. The temperature effect in the SCW solution was not evaluated because the tests at 60 °C were terminated early.

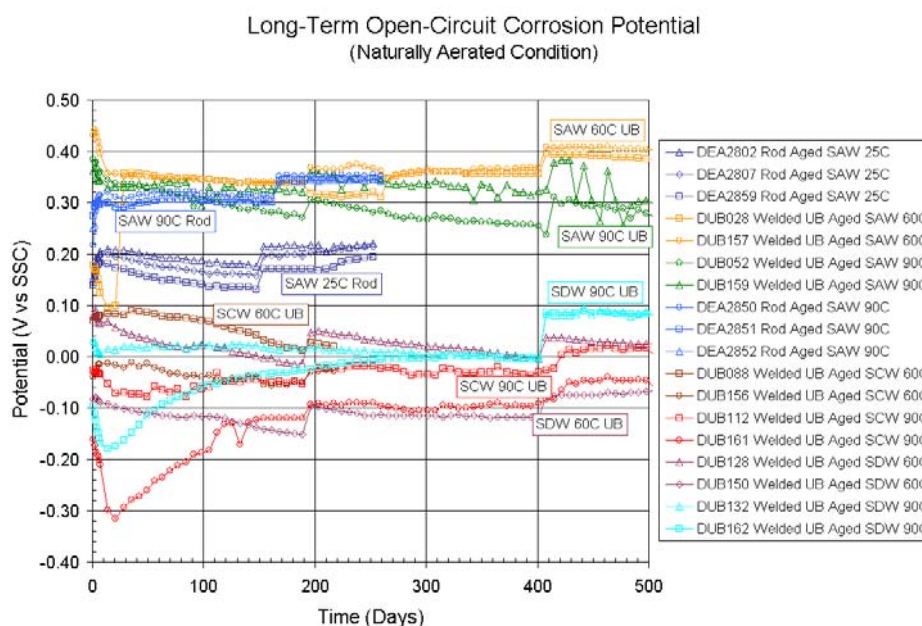
Figure 7-24 shows the test results for the E_{corr} behavior of Alloy 22 in CaCl_2 solutions with varying chloride concentrations and the effect of the addition of nitrate. The data show that E_{corr} of Alloy 22 in the CaCl_2 solutions is affected mostly by the chloride concentration, and addition of nitrate ions slows down the process to attain steady state. E_{corr} for Alloy 22 in 5 M CaCl_2 solution at 120 °C reached steady state in less than 50 days. The average values of E_{corr} after more than 300 days of testing were -129 mV vs. SSC (see Attachment V of the AMR on general and localized corrosion of the WPOB for the numerical values of the data).

After approximately 100 days of testing, the E_{corr} values for Alloy 22 in 5 M CaCl_2 solutions with nitrate added seemed to be approaching a steady state value. The average value of E_{corr} for Alloy 22 in 5 M CaCl_2 + 0.05 M $\text{Ca}(\text{NO}_3)_2$ solution at 90 °C was -39 mV vs. SSC after 100 days

of testing. This solution represents a nitrate to chloride ratio of 0.01. A similar behavior was observed for Alloy 22 tested in 5 M $\text{CaCl}_2 + 0.5 \text{ M Ca(NO}_3)_2$ solution (nitrate to chloride ratio of 0.1) at 90 °C, and the average E_{corr} value was -46 mV vs. SSC. For Alloy 22 electrodes immersed in 1 M $\text{CaCl}_2 + 1 \text{ M Ca(NO}_3)_2$ solution (nitrate to chloride ratio of 1) at 90°C, it appears that, after 120 days of testing, the E_{corr} values had approached a steady state value, and the average E_{corr} value was 168 mV vs. SSC.

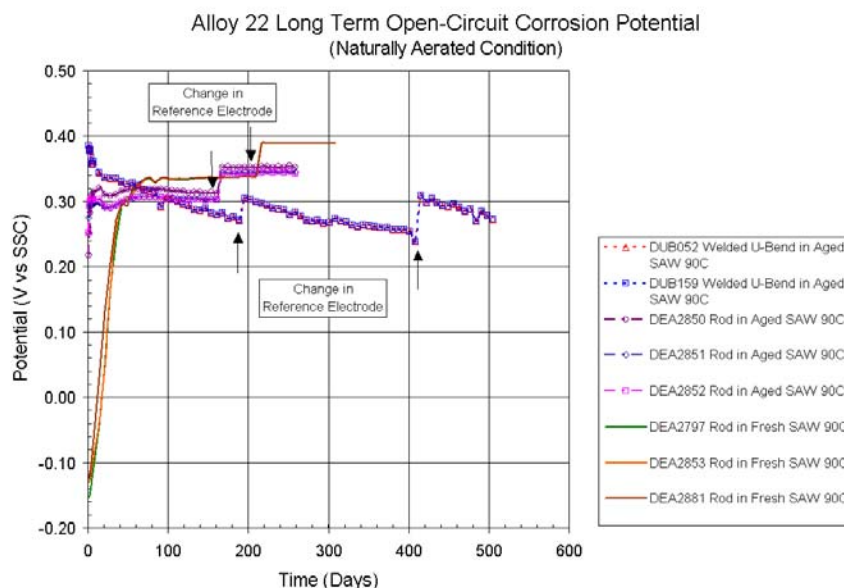
Figure 7-25 shows the steady state open-circuit potentials (or corrosion potentials) of all the Alloy 22 samples (those shown in the previous figures plus the rest of the data in the input DTN LL020711612251.017), as a function of chloride concentration. The figure shows that the sample geometry or configuration and the metallurgical condition have negligible effect on the long-term steady-state corrosion potential of Alloy 22. It is shown that the steady state corrosion potential decreases with chloride concentration, which is consistent with the fact that higher chloride concentration makes the metal more active. Also, part of the potential decrease with chloride concentration may be due to the ‘salting out effect’ because the dissolved oxygen decreases with increasing salt concentration.

As discussed later in the model analysis section, the steady-state corrosion potential is affected significantly by the solution pH.



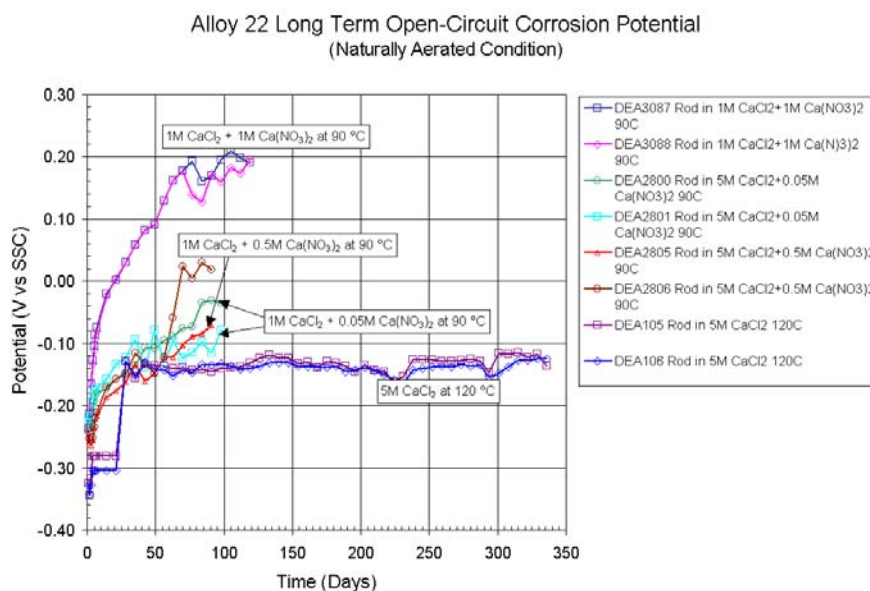
Output DTN: SN0306T0506303.001

Figure 7-22. Open-circuit corrosion potential measurements for samples of Alloy 22 in three types of LTCTF solutions (SDW, SAW and SCW), as a function of time.



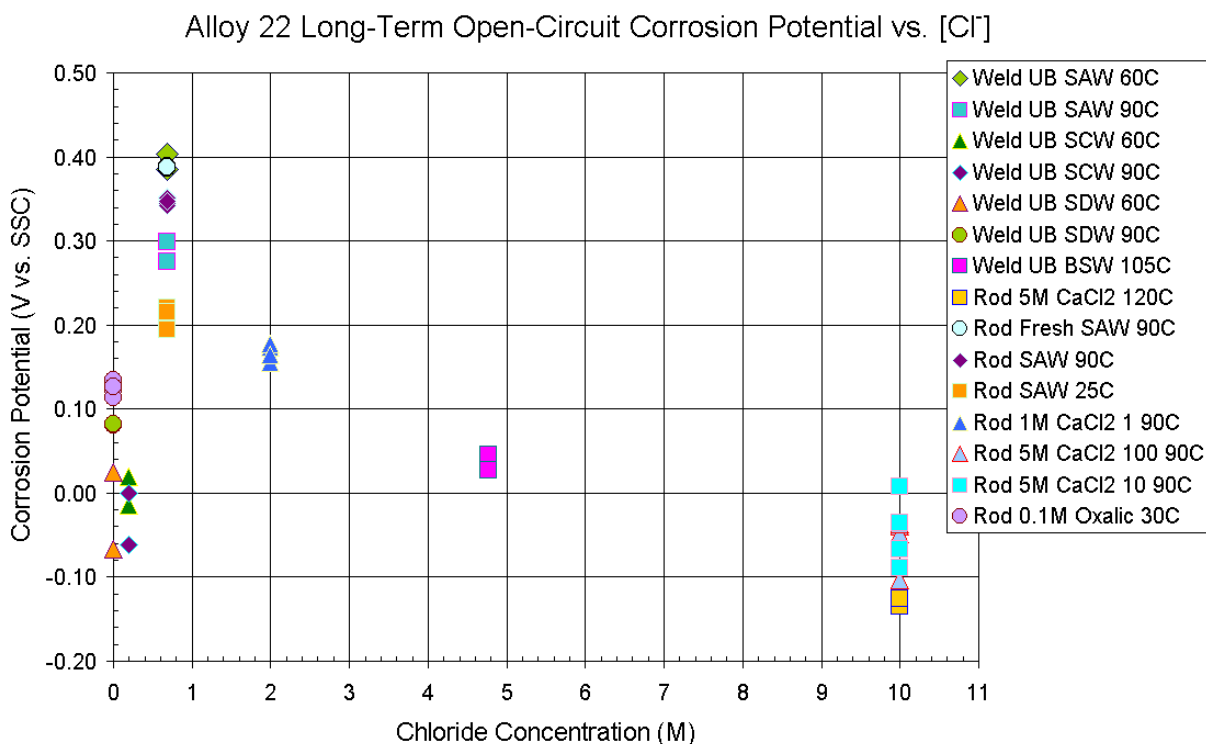
Output DTN: SN0306T0506303.001

Figure 7-23. Open-circuit corrosion potential measurements for samples of Alloy 22 in SAW, at different conditions, and as a function of time.



Output DTN: SN0306T0506303.001

Figure 7-24. Open-circuit corrosion potential measurements for samples of Alloy 22 in CaCl_2 solutions, with various concentrations and inhibitor levels, and as a function of time. Higher resolution and longer duration data are shown in Figure 7-9 for DEA 105 and DEA 106, and in Figure 7-13 for DEA 2800 and DEA 2801.



Output DTN: SN0306T0506303.001

Figure 7-25. Open-circuit corrosion potential for Alloy 22, with various sample configurations, metallurgical conditions, and chloride concentration, after exposure for extended periods of time.

Localized Corrosion Penetration Rate Model

If the corrosion potential of the WPOB exceeds the critical potential, the WPOB is assumed to be subject to localized corrosion, and penetration of the barrier by localized corrosion is modeled. Due to the outstanding corrosion resistance of Alloy 22, very little data exists for such localized corrosion under the conditions expected in the proposed repository. Work originally published by Haynes International (1997b, Page 8) and later reviewed by Gdowski (1991, Table 22) indicates that the corrosion rate of Alloy 22 in 10 weight percent FeCl_3 at 75°C might be as high as $12.7 \mu\text{m}/\text{year}$. This rate is significantly higher than those measured by weight loss of the crevice specimens in the LTCTF and may be representative of the types of rates expected for localized corrosion, including crevice corrosion. In a solution composed of 7 volume percent H_2SO_4 , 3 volume percent HCl , 1 weight percent FeCl_3 , and 1 weight percent CuCl_2 , a penetration rate of $610 \mu\text{m}/\text{year}$ was observed at 102°C . The corrosion rate of Alloy C-276 in dilute HCl at the boiling point is somewhere between 5 and 50 mils per year (127 and $1270 \mu\text{m}/\text{year}$) (Sedriks 1996, Figure 9.12; Haynes International 1997b, Page 13). Comparable rates would be expected for Alloy 22.

For the time being, the localized corrosion penetration rates for the WPOB were assumed to range from 12.7 to $1270 \mu\text{m}/\text{year}$ with the median value of $127 \mu\text{m}/\text{year}$, as shown in Table 7-2. A log-uniform distribution between the bounds was assumed for the penetration rate. The basis for this assumption is that the penetration rate values from the literature span three orders of magnitude, and the percentiles provided are consistent with a log-uniform distribution. This distribution is based on data that bounds those extreme penetration rates found in the literature and are a highly conservative representation of localized corrosion rates of Alloy 22 for the exposure conditions expected in the post-closure repository. The entire variance in the penetration rate is assumed to be due to uncertainty.

However, although localized corrosion can very conservatively be upper bounded by this distribution, the expected case is that once initiated, the crevice corrosion propagation rate would be expected to decrease with increasing depth if it were to initiate under realistic environmental conditions". More details of the time-dependent localized corrosion growth behavior is discussed in Section 0.

Table 7-2. Bounding Rates for Localized Corrosion for Alloy 22 (Distribution).

Percentile	Localized Corrosion Rate ($\mu\text{m}/\text{year}$)
0 th	12.7
50 th	127
100 th	1270

Output DTN: SN0306T0506303.001

Time-Dependent Growth Law for Localized Corrosion

The base case model assumes that, when localized corrosion of the WPOB occurs, it propagates at a (time-independent) constant rate. This assumption is highly conservative because it is known that the localized corrosion rate decreases with time and this is particularly more likely under a thin water film condition that is expected to form on the waste package surface in the post-closure repository. Also, in general, localized corrosion tends to arrest or die shortly after initiation.

An alternative conceptual model for the localized corrosion penetration is a time-dependent growth law. The growth law model can be developed based on a combination of electrochemical and corrosion exposure measurements. A simple pitting model based on hemispherical pit growth yields a penetration law of the form (CRWMS M&O 1998, Table 3-2; Hunkeler and Boehni 1983; McGuire et al 1998, Section 5.3.1)

$$D = k \cdot t^n \quad (\text{Eqn. 7-5})$$

where D is the depth of penetration, t is time, and k is a growth constant. The growth constant will be dependent on the properties of the material, particularly its susceptibility to anodic dissolution in the acidic environment prevailing in a propagating localized corrosion site. The time exponent, n , would be about 0.5 for both diffusion-controlled (i.e., diffusion of metal ions out of the pit) and ohmically-controlled (i.e., rate determined by the ohmic potential drop which develops in the electrolyte in the pit) pit growth (McGuire et al 1998, Section 5.3.1; Vetter and Strehblow 1974). The above model was used in a separate analysis for the proposed repository by the Electric Power Research Institute (EPRI) (Vlasity et al 2002, Section 5.3.1).

The significance of this pit penetration law has been discussed by Frankel (1998) and leads to a pit growth current density (i) proportional to the inverse square root of time (i.e., $i \propto t^{1/2}$) in potentiostatic electrochemical experiments. Hunkeler and Boehni (1983) have shown that this growth law is obeyed for both the pitting and crevice corrosion of stainless steels. Newman and Franz (1984) have also observed a similar relationship on stainless steel.

When trying to adapt such a law for practical applications, two main problems arise: (1) insufficient penetration rate data are available, especially for relatively new materials such as Alloy 22, to determine values of k and n ; and (2) the factors that control the form of this apparently simple growth law are complex and, at best, only qualitatively understood. In order to determine values of k and n , it is necessary to employ short term experiments in which the pit growth process is accelerated electrochemically. In these experiments those features of the propagation process which enhance growth (the development of critical chemistry; the evolution of pit geometry) are dominant. However, it is necessary to predict penetration behavior after long periods of exposure, when those factors that limit growth (IR drop, loss of critical chemistry, evolution of metallurgical factors, polarization of cathodic processes) are more important.

The literature data available for less corrosion resistant materials (Hunkeler and Bohni 1983; Marsh et al 1991; Mughabghab and Sullivan 1989; Sharland et al 1991; Ishikawa et al 1991; and King 2000, Section 4.2) clearly show that a penetration growth law of the form of Equation (7-5)

is appropriate, and that a value of $n = 0.5$, the theoretically predicted value, is justifiable. A key point with the materials discussed above (e.g., iron, carbon steel, copper and Titanium Grade 2) is that they are materials which would be expected to undergo rapid propagation. Providing it is not stifled by the accumulation of corrosion product deposits or slow cathodic kinetics, propagation would be limited only by diffusive or ohmic effects, leading to a value of n approaching 0.5.

By contrast, for highly corrosion resistant materials such as Alloy 22 that are designed and fabricated to resist localized corrosion, additional metallurgical features will be important in determining the value of n . One example of such a metallurgical influence that is pertinent to the case of Alloy 22 is the ability of Mo to decrease the pitting current densities in stainless steels, possibly by reducing the active dissolution rate within the pit (Frankel 1998; and Newman 1985). This prevents the maintenance of the critical pit or crevice chemistry to sustain propagation, leading to repassivation. Again, the n value in the growth law in Equation (7-5) would effectively tend to zero. Evidence to support such a claim has been published by Kehler et al. (2001), who showed that the depth of crevice penetration for Alloy 22 electrochemically driven in extremely saline (5 mol/L LiCl) solutions at 85 °C was limited to less than 100 μm . The adoption of such a value assumes that metallurgical features, such as the influence of Mo on pit/crevice propagation will suppress penetration.

Localized corrosion rate data is needed to obtain a value for k . The only presently available source of crevice corrosion rate data is that published by Haynes (1997b) and summarized in Table 22 of Gdowski (1991). This data was recorded in 10 weight percent FeCl_3 , i.e. under extremely aggressive oxidizing conditions.

The localized corrosion growth law model of the form of Equation (7-5) is not used in the TSPA because of lack of data to obtain the values of the model parameters, n and k for Alloy 22 for the exposure conditions relevant to the proposed repository. The base-case model (time-independent constant penetration rate model) is much more conservative than the growth law model. The base-case model should bound the penetration rate range by localized corrosion of the WPOB when it occurs.

Effect of Microbially Activities on Corrosion

Microbial-influenced corrosion (MIC) is the change in the corrosion rate of an industrial alloy by the presence or activity, or both, of microorganisms. MIC most often occurs due to the increase in anodic or cathodic reactions due to the direct impact of microorganisms on the alloy, or by indirect chemical effects on the surrounding solution. Microorganisms can affect the corrosion behavior of an alloy either by acting directly on the metal or through their metabolic products. For example, some types of aerobic bacteria may produce sulfuric acid by oxidizing reduced forms of sulfur (elemental, sulfide, sulfite), and certain fungi transform organic matter into organic acids (Fontana 1986, Section 8-10).

It has been observed that nickel-based alloys such as Alloy 22 are relatively resistant to microbially influenced corrosion (Lian et al. 1999). Furthermore, it is believed that microbial growth in the repository will be limited by the availability of nutrients (CRWMS M&O 2000c, ANL-EBS-MD-000038 REV 00 ICN 01, Section 6.6.2). For example, H^+ is known to be generated by bacterial isolates from Yucca Mountain. Furthermore, *thiobacillus ferro-oxidans* oxidize Fe^{2+} , while *geobacter metallireducens* reduce Fe^{3+} . Other microbes can reduce SO_4^{2-} and produce S^{2-} .

There are no standard tests designed specifically to investigate the susceptibility of an engineering alloy to MIC (Stoecker 1987). One commonly used type of evaluation to determine the MIC factor is to test the alloy of interest in-situ (field) using the same variables as for the intended application. However, testing in the laboratory with live organisms can provide more controlled conditions of various environmental variables, and sterile controls can be incorporated to better assess MIC-specific effects (Horn, and Jones 2002). This approach was used to evaluate the microbiological processes on general corrosion of the WPOB. For general corrosion of the WPOB, the effect of MIC can be described as follows;

$$CR_{MIC} = CR_{st} \cdot f_{MIC} \quad (\text{Eqn. 7-6})$$

where CR_{MIC} is the general corrosion rate in presence of microorganisms, CR_{st} is the general corrosion rate of the alloy in absence of MIC, and (f_{MIC}) is the MIC factor. If (f_{MIC}) is greater than one, there is an enhancement of the corrosion rate of the alloy as a consequence of the presence or activity of microorganisms.

Lian et al. (1999) has shown that MIC can enhance corrosion rates of Alloy 22 by a factor of at least two. Measurements for Alloy 22 and other similar materials are shown in Table 7-3. The MIC factor (f_{MIC}) is calculated as the ratio of corrosion rates (microbes to sterile) from the table. The value of (f_{MIC}) for Alloy 22 in sterile media is approximately one ($f_{MIC} \approx 1$), whereas the value of (f_{MIC}) for Alloy 22 in inoculated media is larger ($f_{MIC} \approx 2$). It is assumed that the MIC factor (f_{MIC}) is uniformly distributed between 1 and 2, and that this distribution is all due to uncertainty. The MIC factor is applied to the WPOB general corrosion rate when the relative humidity at the WPOB surface is above 90 %. This MIC initiation threshold RH is based on the analysis documented in the AMR entitled "In-Drift Microbial Communities" (CRWMS M&O 2000c, ANL-EBS-MD-000038 REV 00 ICN 01, Sections 6.3.1.6 and 6.5.2, Table 23).

MIC is defined as a local area effect; thus, not all areas are equivalent on any given waste package with respect to bacterial colonization. It is well documented that bacteria preferentially colonize on welds, and heat-affected zones (Borenstein and White 1989; Walsh 1999; Enos and Taylor 1996). However, the current model is based on data collected using un-welded specimens. In order to account for preferential areas of colonization in the model, it might be assumed that the MIC factor (f_{MIC}) is uniformly distributed with respect to area distribution.

The principal nutrient-limiting factor to microbial growth *in situ* at Yucca Mountain has been determined to be low levels of phosphate (CRWMS M&O 2000c, ANL-EBS-MD-000038 REV 00 ICN 01, Section 6.6.2). There is virtually no phosphate contained in J-13 groundwater. Yucca Mountain bacteria grown in the presence of Yucca Mountain tuff are apparently able to solubilize phosphate contained in the tuff to support growth to levels of 10^6 cells/ml of groundwater. When exogenous phosphate is added (10 mM), the levels of bacterial growth increase to 10^7 to 10^8 cells/ml (CRWMS M&O 2000c, ANL-EBS-MD-000038 REV 00 ICN 01, Figures 20 and 21). The one to two orders-of-magnitude difference in bacterial growth with and without the presence of exogenous phosphate is almost certainly not significant with respect to effects on corrosion rates. Therefore, nutrient limitation, at least at a first approximation, was not factored into the overall MIC model. It may be noted, however, that the maximum two-fold f_{MIC} included in the model was in the presence of sufficient phosphate to sustain higher levels of bacterial growth (in an effort to achieve accelerated conditions).

Other environmental factors that could affect levels of bacterial growth include temperature and radiation. These factors, however, are closely coupled to RH; as temperature and radiation decrease in the repository, RH is predicted to increase. At the same time, while there are some types of microorganisms that can survive elevated temperatures (≤ 120 °C) and high radiation doses if there is no available water, then bacterial activity is completely prevented. Thus, because water availability is the primary limiting factor and this factor is coupled to other less critical limiting factors, water availability (as expressed by RH) was used as the primary gauge of microbial activity.

Determination of a critical mass of *total* bacteria required to cause MIC is not an issue that needs to be addressed in the MIC model. Bacterial densities in Yucca Mountain rock have been determined to be on the order of 10^4 to 10^5 cells/gm of rock (CRWMS M&O 2000c, ANL-EBS-MD-000038 REV 00 ICN 01, Figures 20 and 21). In absolute terms, this is almost certainly above the threshold required to cause MIC. Further, bacterial densities were shown to increase one to two orders-of-magnitude when water is available (above). A more germane concern is the *types* of bacteria present, their abundance, and how their relative numbers are affected when water is available for growth. Corrosion rates will be affected (at least on some WP materials) for example, if organic acid producers out-compete sulfate reducers or inorganic acid producers for available nutrients when water is sufficient to support growth. No data is currently available regarding the composition of the bacterial community over the changing environmental conditions anticipated during repository evolution. Instead, this issue has been addressed in the current model by determining overall corrosion rates under a standardized set of conditions, in the presence and absence of a defined set of characterized Yucca Mountain bacteria.

Table 7-3. Alterations in Corrosion Potentials Associated with Microbial Degradation

Tested Sample Initial Condition	Average Corrosion Rate ($\mu\text{m}/\text{year}$)	Corrosion Potential E_{corr} (V vs. SCE)	
		Initial	Endpoint
CS1020 + YM Microbes	8.80	-0.660	-0.685
Sterile CS 1020	1.40	-0.500	-0.550
M400 + YM Microbes	1.02	-0.415	-0.315
Sterile M400	0.005	-0.135	-0.070
C-22 + YM Microbes	0.022	-0.440	-0.252
Sterile C-22	0.011	-0.260	-0.200
I625 + YM Microbes	0.013	-0.440	-0.285
Sterile I625	0.003	-0.160	-0.130
304SS + YM Microbes	0.035	-0.540	-0.280
Sterile 304SS	0.003	-0.145	-0.065

Input DTN: LL991203505924.094

Effect of Aging and Phase Stability on Corrosion

As specified in the waste package design and fabrication specification (Plinski 2001, Section 8.1), the WPOB base metal and all fabrication welds (not including the welds for the closure lids) are fully annealed before the waste packages are loaded with waste. In addition, for a range of thermal loading designs of the proposed repository, the waste package surface temperature will be always kept below 200 °C (BSC 2001b, TDR-MGR-MD-000007 REV 00 ICN 01, Section 5.4.1, Figures 5.4.1-2 and 5.4.1-6). With this constraint, the impact of aging and phase instability on the corrosion of Alloy 22 will be insignificant. The analysis documented in the companion AMR titled *Aging and Phase Stability of Waste Package Outer Barrier* (BSC 2003c, ANL-EBS-MD-000002 REV 01 ICN 00) has shown that an extrapolation of the curves given in the companion AMR on aging and phase stability does not indicate that the phase stability of Alloy 22 base metal and weld metal will be a problem at temperatures near 300°C (BSC 2003b, Section 8.0).

Comparison of the anodic passive current densities of the as-welded Alloy 22 samples to those of the base metal samples showed no significant effect of the welds on the passive corrosion behavior of the alloy (Brossia et al 2001, Section 3.2.1.3, Figure 3-13). Rebak et al. (2002) have investigated the effects of high-temperature aging on the corrosion resistance of Alloy 22 in concentrated hydrochloric acid. However, due to the temperature used to age the samples (922-1033 K) and the extreme test media used (boiling 2.5% HCl and 1 M HCl at 339 K), these data are not considered relevant to performance assessment for the repository.

The fabrication welds including the closure welds of the WPOB can be subject to long-term thermal aging and phase instability under the repository thermal conditions. For the analysis of the thermal aging effect on corrosion of Alloy 22, three metallurgical conditions of Alloy 22 were studied using the multiple crevice assembly (MCA) samples: mill annealed, as-welded, and as-welded plus thermally aged (at 700 °C for 173 hours). The samples were tested in 5 M CaCl₂ solutions with the test temperatures varying from 45 to 120 °C. As described in Attachment I, after being immersed in the test solution in an open circuit condition for 24 hours, the polarization resistance of the samples was measured.

A comparison of calculated corrosion rates for mill annealed, as welded, and as welded plus and thermally aged samples are shown in the AMR. The corrosion rate data are listed in Attachment IV of this document. The mill annealed MCA samples in 5 M CaCl₂ solutions at differing temperatures were considered as the baseline condition for the analysis. The baseline condition rates were compared with those of the as-welded and as-welded plus thermally aged MCA samples tested in the same electrolyte solution condition. A data trend-line was drawn for the baseline condition data for an easier comparison with the as-welded and thermally aged as-welded sample data. The data clearly show that there is no apparent enhancement of the corrosion rate due to welding or thermal aging of the welded samples for the tested conditions. This is consistent with the results by Rebak et al. (2002).

Chapter 8. Electrochemical Determination of the Threshold for Localized Corrosion of Alloy 22 in Benign Brines Expected in the Transition- and Low-Temperature Regions (Frequency $\geq 99\%$)

Chapter 8 focuses attention on testing in a variety of brines that are believed to be more representative of those that might evolve due to evaporative concentration, brines predicted with a frequency of greater than 99%. Such brines include Basic Saturated Water (BSW), Simulated Acidic Water (SAW), and Simulated Concentrated Water (SCW). These test environments have been categorized in terms of the eleven (11) representative water-chemistry bins given in Table 8-1, in the Section entitled "Transition Region: EBS Chemistry Model." SSW and SAW are similar to the waters that evolve from Bins 4 through 7, with a combined frequency of twenty-seven (27%). SCW and BSW are similar to the waters that evolve from Bins 8 through 11, with a combined frequency of seventy-two percent (72%) (CRWMS M&O 2000d, ANL-EBS-MD-000003 REV 00 ICN 00).

Samples of Alloy 22 were aged at 700°C for either 10 or 173 hours. The corrosion resistance of these aged samples is compared to that of base metal in various standardized test media. Figure 8-1 shows a comparison of CPP curves for base metal and thermally aged material in SAW at 90°C. Both curves exhibit generic Type 1 behavior. In this case, aging appears to shift the short-term open-circuit corrosion potential to less noble values from -176 to -239 mV versus a standard Ag/AgCl reference electrode. The passive current density may be increased slightly, which would be indicative of a slight increase in corrosion rate. The highest non-equilibrium passive current observed for the base metal is approximately $4 \mu\text{A cm}^{-2}$ compared to approximately $10 \mu\text{A cm}^{-2}$ for fully aged material. Figure 8-2 shows a comparison of CPP curves for base metal and thermally aged material in SCW at 90°C. In this case, aging also appears to shift the short-term open-circuit corrosion potential to less noble values from -237 to somewhere between -328 and -346 mV versus a standard Ag/AgCl reference electrode. In all three cases, the anodic oxidation peak that is characteristic of generic Type 2 behavior is observed.

CPP curves for base metal and thermally aged material in Basic Saturated Water (BSW-13) at 110°C are also compared. In tests with BSW-13 (Figure 8-3), aging also appears to shift the corrosion potential to less noble values. A sample aged for only 10 hours has a corrosion potential of only -227 mV versus a standard Ag/AgCl reference electrode, whereas a sample aged for 173 hours has a short-term open-circuit corrosion potential of -372 mV relative to the same reference. The difference $E_{\text{CRIT}} - E_{\text{CORR}}$ is about 800 mV for an aged sample in either SAW or BSW. The non-equilibrium current densities (corrosion rates) at 0 mV are also similar. However, more quantitative test are required for any definitive statements regarding corrosion rate.

To further illustrate the corrosion resistance of Alloy 22 in BSW test media, photographic evidence is presented to augment the electrochemical data. The crevice corrosion of the Alloy 22 MCA in 4M NaCl at 100°C, with polarization at 350 mV vs. Ag/AgCl for 2 hours, is shown in Figure 8-4. No such localized attack was observed with the Alloy 22 MCA in BSW at 110°C, during CPP with reversal potential of 800 mV. The resistance to Alloy 22 in this environment is very good.

From data presented in the previous section for CaCl₂-type media, there is an expectation that ennoblement (anodic shift on the open-circuit corrosion potential towards the critical potential) might also be encountered in the more predominant environments discussed in this section. Figures 8-5 and 8-6 show that the criterion for crevice corrosion is not met in BSW at 100-105°C, accounting for ennoblement over two years. Similar findings for SAW and SCW electrolytes are also presented.

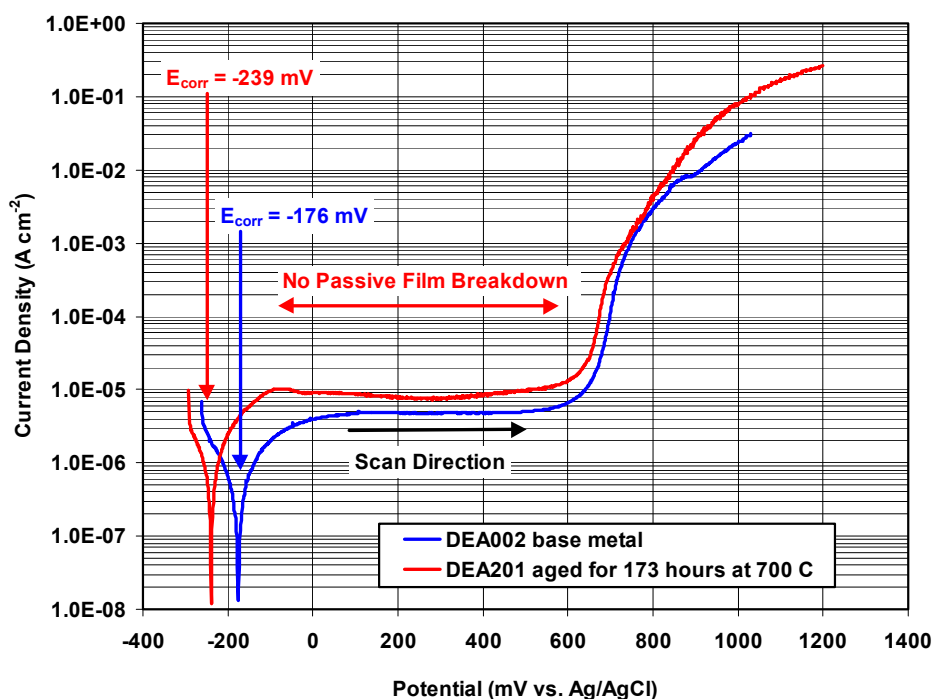


Figure 8-1. Cyclic potentiodynamic polarization (CPP) data for Alloy 22 disks in 90°C SAW, with and without extreme thermal aging at 700°C for 173 hours. Type 1 behavior is exhibited.

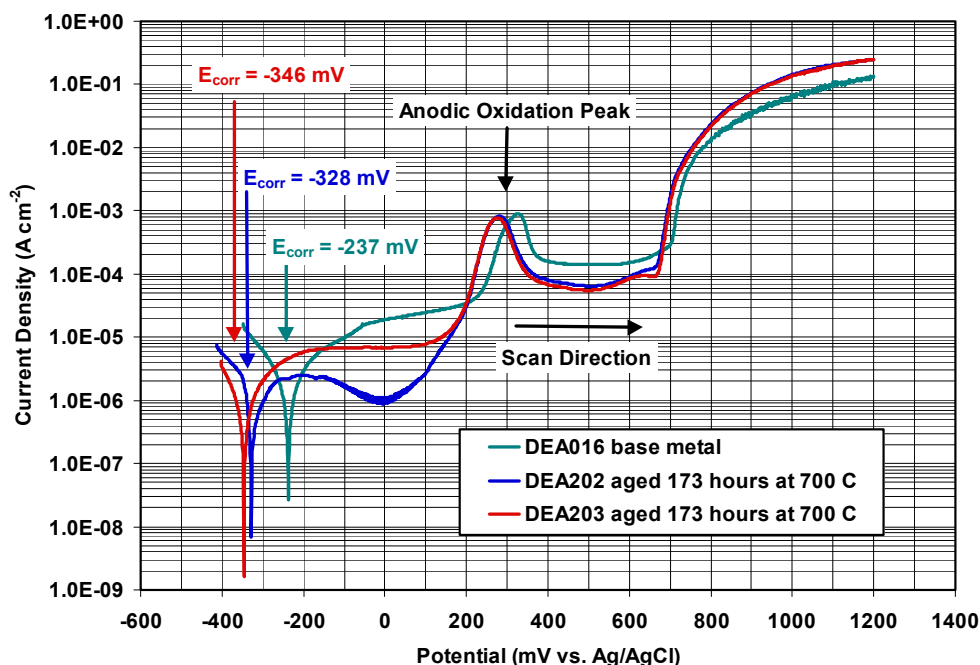


Figure 8-2. Cyclic potentiodynamic polarization (CPP) data for Alloy 22 disks in 90°C SCW, with and without extreme thermal aging at 700°C for 173 hours. Type 2 behavior is exhibited.

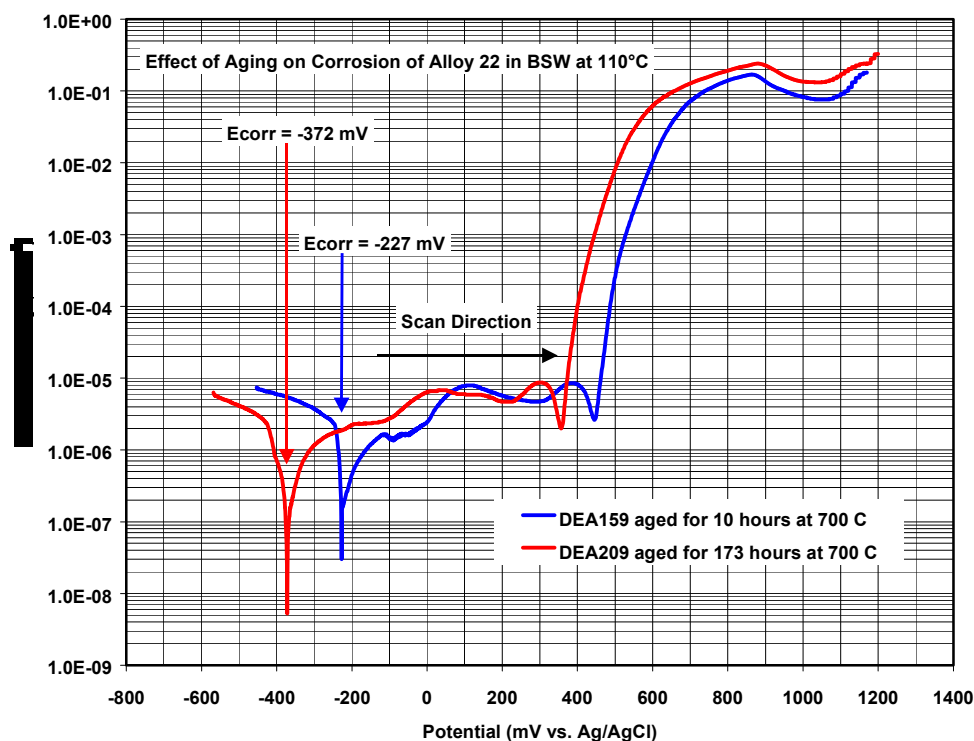


Figure 8-3. CPP data for Alloy 22 disks in BSW-13 at 110°C, with thermal aging at 700°C for 20 and 173 hours.

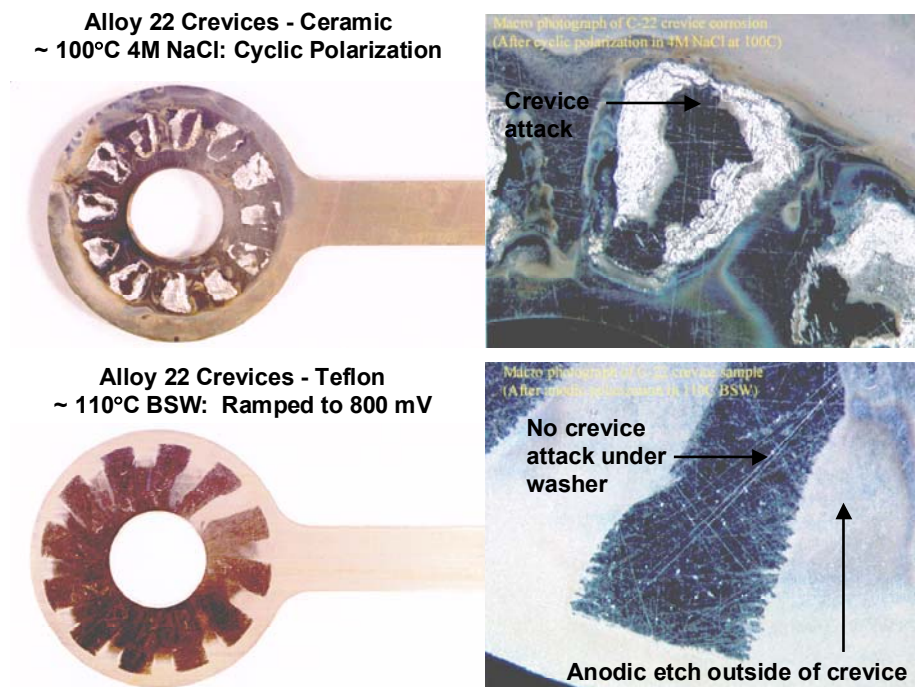
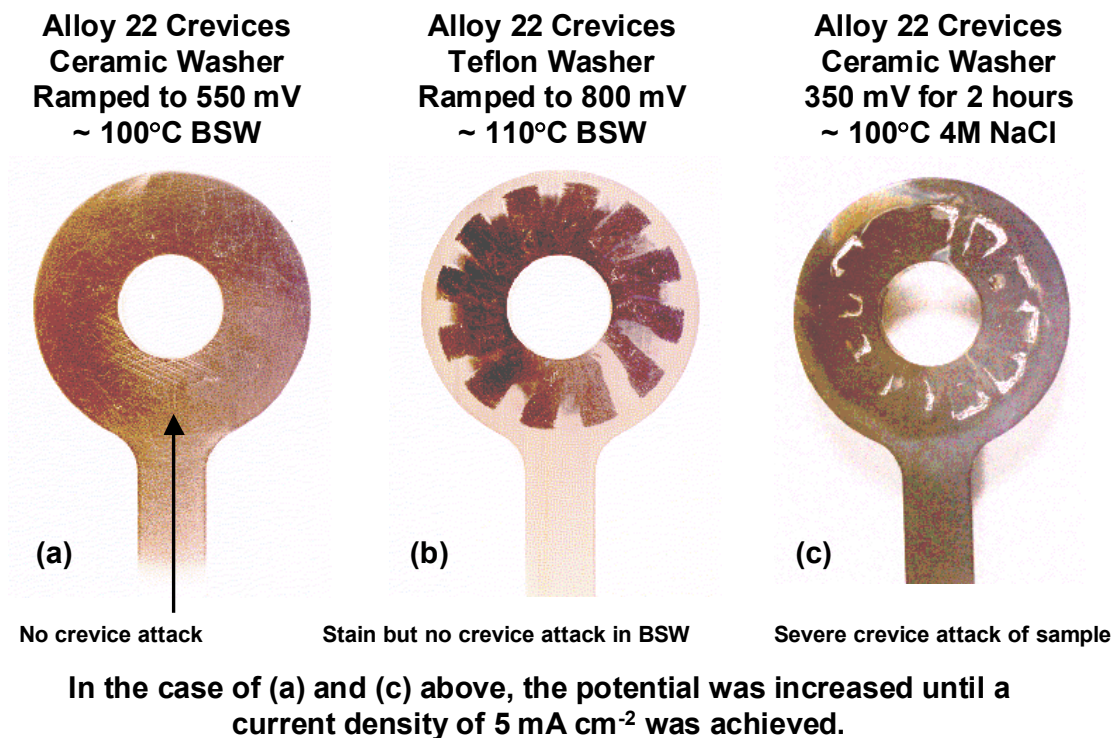


Figure 8-4. Crevice corrosion of Alloy 22 MCA in 4M NaCl solution at 100°C, with polarization at 350 mV vs. Ag/AgCl for 2 hours. No crevice corrosion of Alloy 22 MCA in BSW at 110°C, during CPP with reversal potential of 800 mV.

A cyclic potentiodynamic polarization curve for Alloy 22 in BSW at 100°C is shown in Figure 8-5, and exhibits a 550 mV margin between the short-term open-circuit corrosion potential and the anodic oxidation peak (appearing more as a shoulder in this particular curve). The long-term open-circuit corrosion potential for Alloy 22 in BSW at 105°C is shown in Figure 8-6, and demonstrates that the corrosion potential reaches a stable, constant value of below 150 mV vs. Ag/AgCl after more than two years. Since this value is well below the anodic oxidation peak, destabilization of the passive film is not expected.

A cyclic potentiodynamic polarization curve for Alloy 22 in SAW at 90°C is shown in Figure 8-7, and exhibits a 650 mV margin between the short-term open-circuit corrosion potential and the anodic oxidation peak (appearing more as a shoulder in this particular curve). The long-term open-circuit corrosion potential for Alloy 22 in SAW at 90°C is shown in Figure 8-8, and demonstrates that the corrosion potential reaches a stable, constant value of below 400 mV vs. Ag/AgCl after more than two years. Since this value is well below the anodic oxidation peak, destabilization of the passive film is not expected.

A cyclic potentiodynamic polarization for Alloy 22 in SCW at 90°C is shown in Figure 8-9, and exhibits a 500 mV margin between the short-term open-circuit corrosion potential and the anodic oxidation peak (appearing more as a shoulder in this particular curve). Long-term open-circuit corrosion potential for Alloy 22 in SCW at 90°C is shown in Figure 8-10, and demonstrates that the corrosion potential reaches a stable, constant value of below 0 mV vs. Ag/AgCl after more than two years. Since this value is well below the anodic oxidation peak, destabilization of the passive film is not expected.

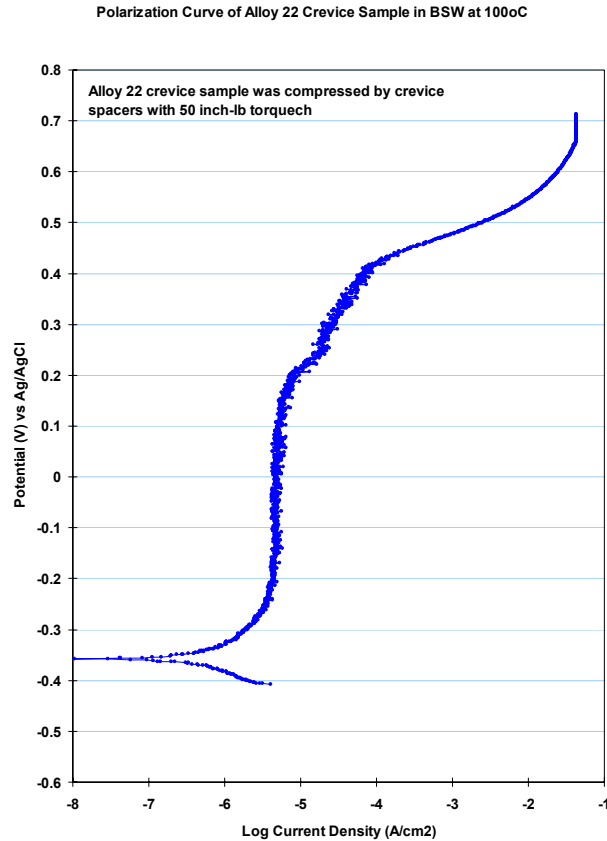


Figure 8-5. Cyclic potentiodynamic polarization of Alloy 22 in BSW at 100°C, showing a 550 mV margin between the short-term open-circuit corrosion potential and the anodic oxidation peak (appearing more as a shoulder in this particular curve).

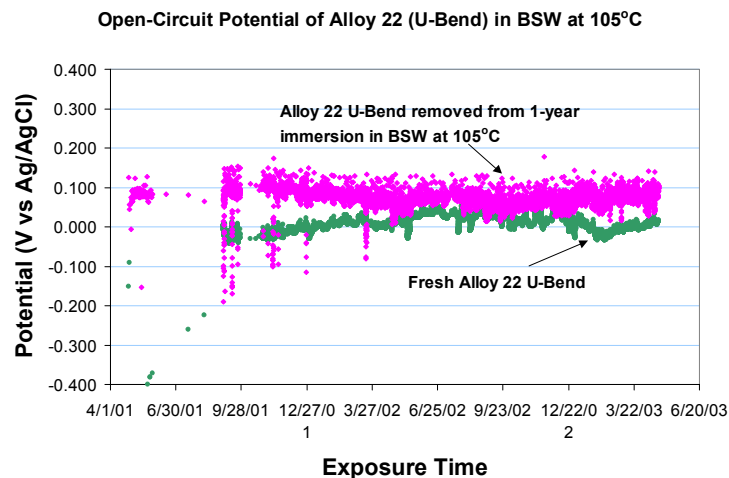


Figure 8-6. Long-term open-circuit corrosion potential for Alloy 22 in BSW at 105°C, showing that the corrosion potential reaches a stable, constant value of below 150 mV after more than two years. Since this value is well below the anodic oxidation peak (shoulder), destabilization of the passive film is not expected, even with ennoblement.

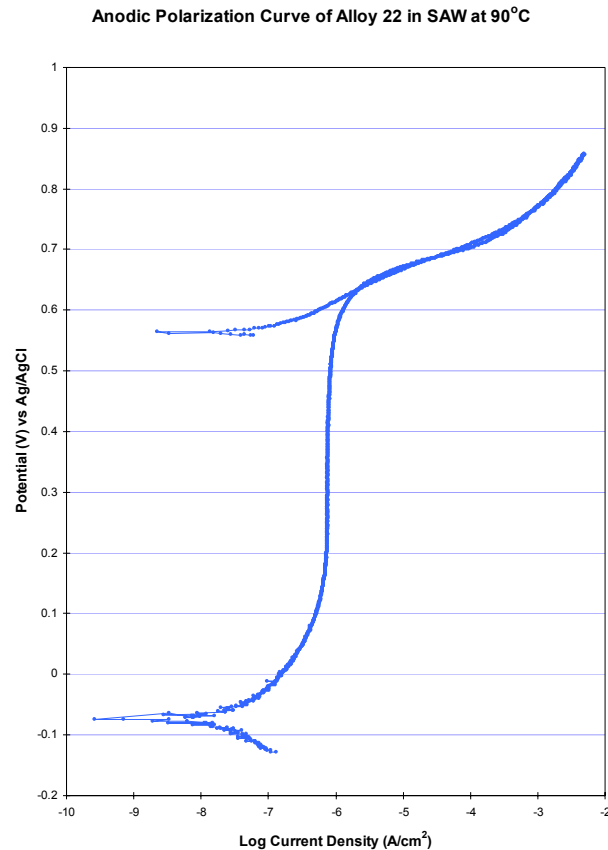


Figure 8-7. Cyclic potentiodynamic polarization of Alloy 22 in SAW at 90°C, showing a 650 mV margin between the short-term open-circuit corrosion potential and the anodic oxidation peak (appearing more as a shoulder in this particular curve).

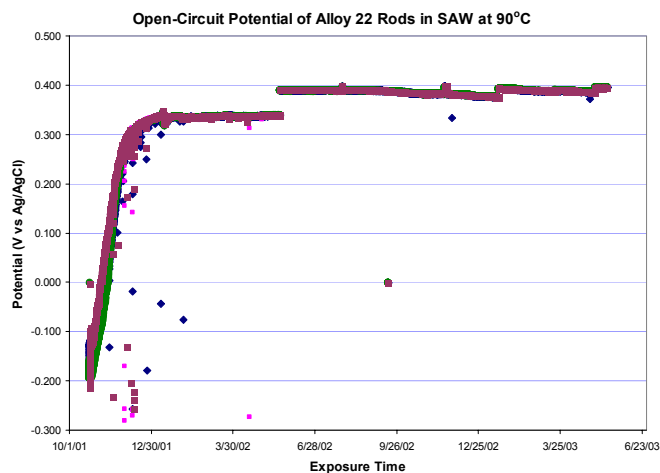


Figure 8-8. Long-term open-circuit corrosion potential for Alloy 22 in SAW at 90°C, showing that the corrosion potential reaches a stable, constant value of below 400 mV after more than two years. Since this value is well below the anodic oxidation peak, destabilization of the passive film is not expected, even with ennoblement.

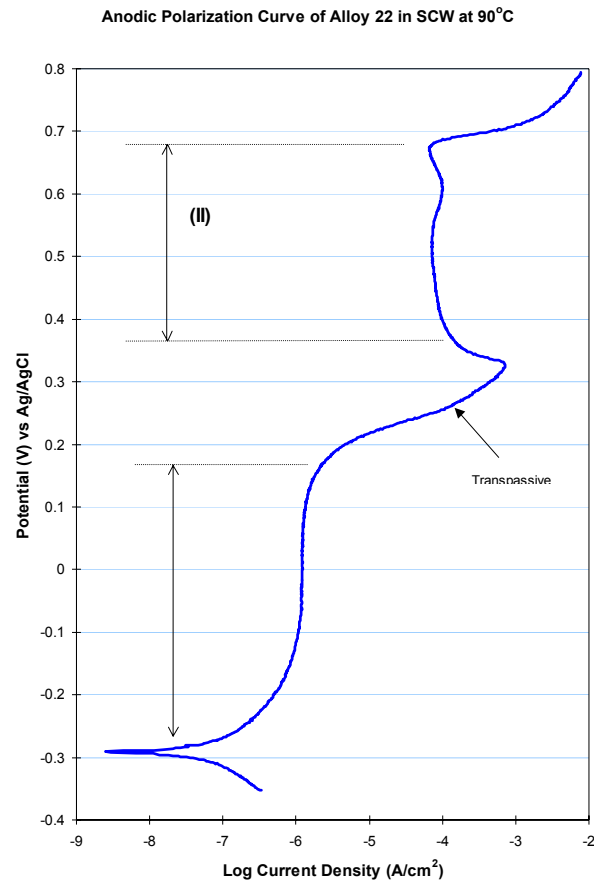


Figure 8-9. Cyclic potentiodynamic polarization of Alloy 22 in SCW at 90°C, showing a 500 mV margin between the short-term open-circuit corrosion potential and the anodic oxidation peak (appearing more as a shoulder in this particular curve).

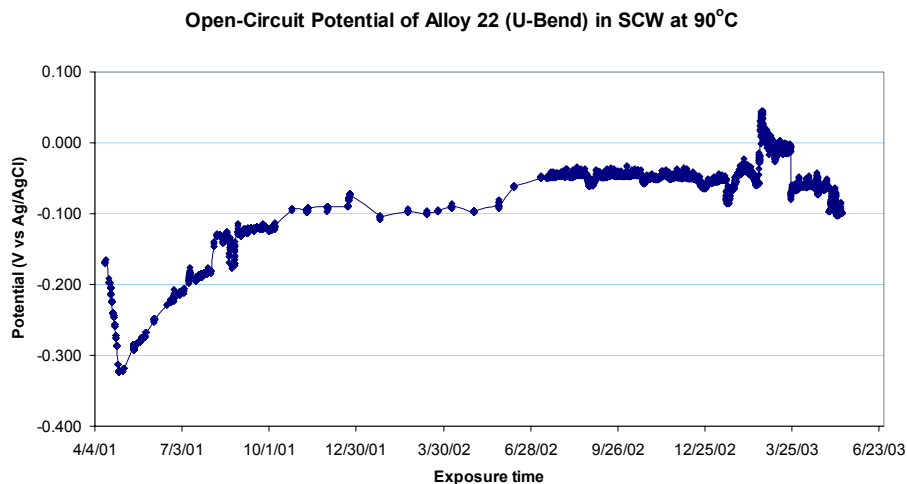


Figure 8-10. Long-term open-circuit corrosion potential for Alloy 22 in SCW at 90°C, showing that the corrosion potential reaches a stable, constant value of below 0 mV vs. Ag/AgCl after more than two years. Since this value is well below the anodic oxidation peak, destabilization of the passive film is not expected, even with ennoblement.

Chapter 9. Transition and Low-Temperature Regions – The Effects of Gamma Radiolysis

Anodic shifts in the open circuit corrosion potential of stainless steel have been experimentally observed (Glass et al. 1986; Kim 1987, 1988, 1999a, 1999b). It is believed that this observation is due to the generation of hydrogen peroxide. Glass et al. performed ambient-temperature CPP of 316L samples in 0.018 M NaCl solution during exposure to 3.5 Mrad h⁻¹ gamma radiation (1986). They found that the corrosion current shifted in the anodic direction by approximately 200 mV. From inspection of the graphical data in this article, it is concluded that there is very little increase in the corresponding corrosion current density. However, the separation between the corrosion potential and the threshold for localized attack decreased slightly. This shift in corrosion potential was shown to be due to the formation of hydrogen peroxide. This finding was subsequently confirmed by Kim (1988). In this case, ambient-temperature CPP of 316 stainless steel in acidic (pH~2) 1.5 M NaCl during exposure to 0.15 Mrad h⁻¹ gamma radiation showed a 100 mV anodic shift in the corrosion potential, with very little effect on the corrosion current. Note that Glass et al. (1986) and Kim (1988) worked on stainless steels, not Alloy 22.

Additional studies of the corrosion and threshold potentials of Alloy 22 in the presence of gamma radiation, as done by Glass et al. in the early 1980's, is beyond the YMP's current work scope. To determine the maximum impact that gamma radiolysis could have on the corrosion potential, hydrogen peroxide was added to electrolytes used for testing Alloy 22, as shown in Figure 9-1. As the concentration of hydrogen peroxide in SAW approaches 72 ppm (calculated from number of added drops of H₂O₂), the corrosion potential asymptotically approaches 150 mV versus Ag/AgCl, well below any threshold where localized attack would be expected in SAW. Similarly, as the concentration of hydrogen peroxide in SCW approaches 72 ppm, the corrosion potential asymptotically approaches -25 mV versus Ag/AgCl, well below any threshold where localized attack would be expected in SCW. This change in corrosion potential is also below any level where a change in oxidation state would be expected. Since extremely high radiation levels would be required to achieve such shifts in corrosion potential and since even the maximum shifts in potential would be less than those required for breakdown of the passive film, it seems unlikely that gamma radiolysis will lead to catastrophic failure of Alloy 22 due to localized corrosion. However, as more resources become available, actual tests with a gamma source should be performed.

Dry-out is expected to help mitigate the impact of gamma radiolysis on the open-circuit corrosion potential. Decay heat is expected to prevent seepage water from contracting the waste package until the gamma dose is low. The time-dependent dose for a standard 21 PWR waste package is predicted to be approximately 700 rad/h at emplacement, approximately 20 rad/h at 90 years, and less than 0.1 rad/h at 375 years. Though seepage may be possible at 1000 years, the corresponding gamma dose is expected to be too low to cause much effect on the corrosion potential.

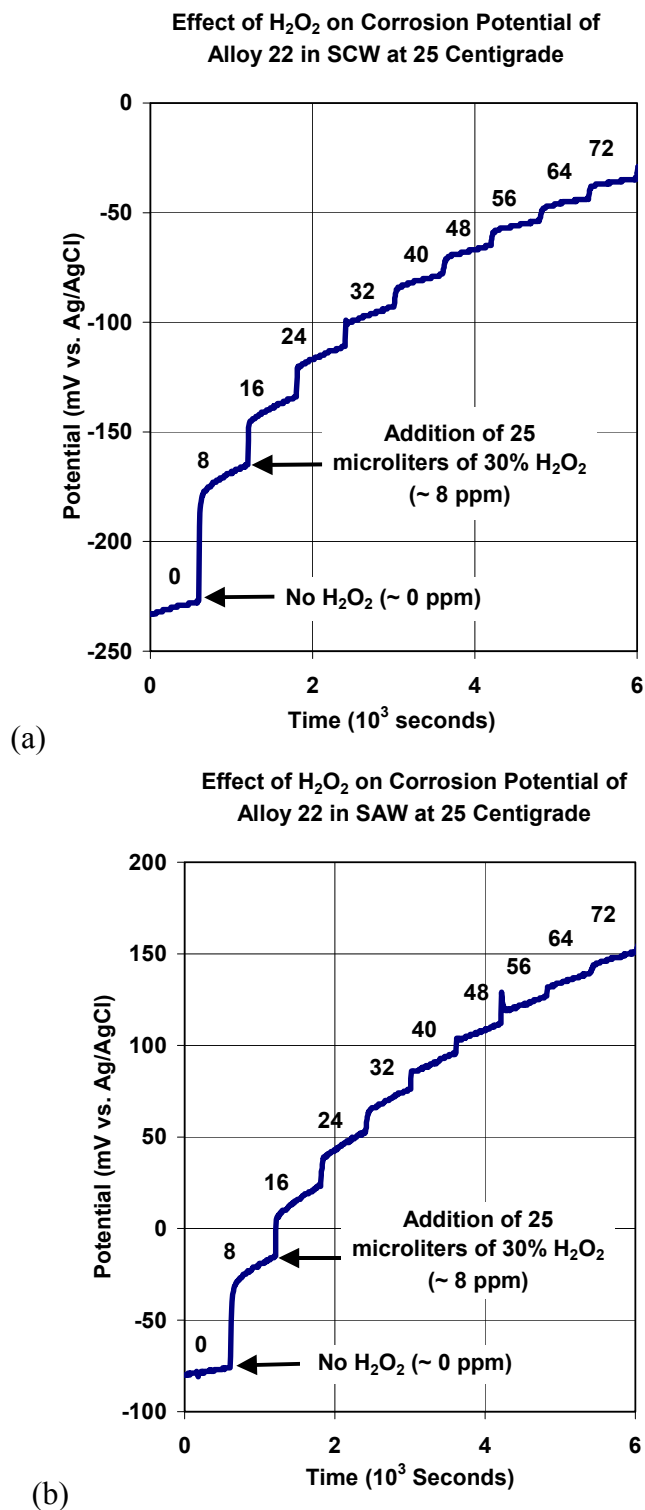


Figure 9-1. Increase of open circuit corrosion potential induced by hydrogen peroxide, a product that is expected to form during gamma radiolysis. The maximum effect of about (a) 275 mV in SCW or (b) 200 mV in SAW is achieved at a H_2O_2 concentration of about 72 ppm.

Chapter 10. Environmental Fracture and Prevention Through Stress Mitigation

There are several modes of failure that could lead to premature breach of the waste package. One of the most threatening is stress corrosion cracking (SCC). Initiation and propagation of SCC can occur at relatively low stress intensity factors (K_I). After initiation, through-wall penetration is essentially instantaneous when compared to the 10,000-year time scale of importance to the high-level waste repository at Yucca Mountain. Three criteria have to be met for SCC to occur: metallurgical susceptibility; a corrosive environment; and static tensile stresses. Environments that cause SCC are usually aqueous and can be condensed layers of moisture or bulk solutions. The SCC of a particular alloy is usually caused by the presence of a specific chemical species in the environment. For example, the SCC of copper alloys is virtually always due to the presence of ammonia in the environment. Chloride ions cause SCC in stainless steels and aluminum-based alloys. Reduced sulfate is known to promote SCC in nickel-based alloys. Changes in the environmental conditions, which include temperature, dissolved oxygen, and ionic concentrations, will normally influence the SCC process. Radionuclide release is possible if SCC causes breach of the WPOB and underlying structural support. Adequate models to account for SCC must therefore be employed (BSC 2003f, ANL-EBS-MD-000005 REV 01 ICN 00; Farmer et al. 2000b).

SCC in Aggressive CaCl₂-Type Brines in the Transition Region

Given the impact of the aggressive CaCl₂-type brines on localized corrosion, it is important to assess the impact of these types of evolved environments on SCC. Thus, a series of slow strain rate tests (SSRTs) were performed on Alloy 22 at 73-120°C, and at a strain rate of 1.6×10^{-6} per second. Although SSRT does not give a direct measure of the threshold stress or threshold stress intensity factor for SCC initiation, the absence of SCC in tests in which specimens are pulled to failure at a low strain rate corroborates the high threshold stress used in the model (90% TS).

These tests are summarized in Table 10-1, and cover a broad range of relevant and bounding environments, with/without lead additions, and with/without applied potential. Examination of the tabulated results indicates a high degree of SCC resistance at open circuit potentials in all environments evaluated: ~8.5M (saturated) CaCl₂-type brines at pH~4 and 120°C; and in the presence of dissolved lead at pH~3. The only environment evaluated in which incipient SCC initiation may have been observed was simulated concentrated water (SCW) with an applied potential between 300 to 400 mV versus SSC, with a corresponding open-circuit corrosion potential between -94 to -241 mV versus SSC. Clearly, these results are entirely consistent with the high threshold stress used in the model.

Table 10-1. SSRT Results for Annealed Alloy 22 (Strain Rate = 1.66×10^{-6} per second)

Specimen ID	Test Environment	Temperature (°C)	E_{corr} (mV vs. SSC)	E_{Applied} (mV vs. SSC)	Time to Failure (hours)	Max. Stress (MPa)	Reduction in Area (%)	Observation
012	Air	22	N/A	N/A	124	786	74	Inert
123	4M NaCl at pH ~ 6	98	-323	+350	127	758	80	No SCC
004	8.5M CaCl ₂ at pH ~ 6	120	-140 to -180	E_{corr}	127	752	71	No SCC
013	1% PbCl ₂ at pH ~ 4 Aerated	---		E_{corr}	126	765	72	No SCC
015	SAW at pH ~ 3	63	-7 to +360	E_{corr}	118	758	79	No SCC
016	SAW at pH ~ 3 + 0.005% Pb(NO ₃) ₂	76	-6 to +370	E_{corr}	124	772	74	No SCC
017	SAW at pH ~ 3 + 0.005% Pb(NO ₃) ₂	76	0 to +350	E_{corr}	125	772	74	No SCC
003	SAW at pH ~ 3 + 0.005% Pb(NO ₃) ₂	95	-90 to +400	E_{corr}	118	752	85	No SCC
127	BSW at pH ~ 13 With [NO ₃ + SO ₄]	98	-240 to -220	E_{corr}	123	745	72	No SCC
124	BSW at pH ~ 13 With [NO ₃ + SO ₄]	105	-330	+100	100	745	78	No SCC
122	BSW at pH ~ 13 With [NO ₃ + SO ₄]	98	-245	+200	122	752	72	No SCC
120	BSW at pH ~ 13	105	-323	+400	99	745	74	No SCC
119	BSW at pH ~ 13	105	-301	+400	118	745	75	No SCC
115	BSW at pH ~ 13 With [NO ₃]	105	-335	+400	115	752	77	No SCC
129	BSW at pH ~ 13 With [NO ₃]	105	-314	+400	119	731	82	No SCC
020	SCW	22	-109	+400	116	800	85	No SCC
125	SSW at pH ~ 6	100	-154	+400	113	717	71	No SCC
112	SCW at pH ~ 9	73	-94	+400	91	696	71	SCC
021	SCW at pH ~ 9	73	-171	+400	90	662	64	SCC
030	SCW at pH ~ 9	73	-182	+300	98	NA	65	SCC
026	SCW at pH ~ 9	73	-241	+100	120	111	79	No SCC

DTN:LL020603612251.015

Predictive Models for SCC – Initiation and Propagation

Andresen and Ford (1994) have applied the slip-dissolution film-rupture (SDFR) model to the SCC of stainless steels, low-alloy and carbon steel, ductile nickel alloys, and irradiated stainless steel. Specific applications include Types 304 and 316L stainless steel, A533B and A508 low-alloy steels, and nickel-based alloys such as Inconel 600. Therefore, there is ample reason to hypothesize that SCC of nickel-based Alloy 22 occurs by the same fundamental mechanism characterized by the SDFR model for SCC propagation.

In regard to stress corrosion cracking of the waste package performance, one model is needed for initiation, and second for propagation. The first is the threshold stress or threshold stress intensity factor model for SCC initiation, while the second is a variation of the slip-dissolution film-rupture (SDFR) model for SCC propagation. In the second model, SCC is assumed to initiate if the tensile stress at the smooth surface exceeds a threshold stress.

SCC Initiation – Threshold Stress Intensity Factor and Threshold Stress

The most common initiation model assumes that SCC initiates at pre-existing surface flaws if the stress intensity factor at that flaw (K_I) exceeds the threshold stress intensity factor (K_{ISCC}) for stress corrosion cracking. If this criterion is not met, no crack will initiate and grow. The criterion is represented by Eqn. 10-1 (Farmer et al. 2000b).

$$K_I \geq K_{ISCC} \quad (\text{Eqn. 10-1})$$

The threshold (K_{ISCC}) is a material and environment dependent property; which can be obtained through fracture mechanics testing of the materials in the specified environment. The K_{ISCC} concept has been widely used by engineers to assess the susceptibility of various materials to SCC. Descriptions of this concept can be found in Jones and Ricker (1987) and Sprowls (1987). The (K_{ISCC}) concept has been widely used by engineers to assess the susceptibility of various materials to SCC. Typical values of (K_{ISCC}) are 20-30 MPa m^{1/2}.

For a given alloy, metallurgical condition, environment, and in the absence of cyclic stresses, initiation of SCC will not occur on a smooth surface (without sharp defects such as weld flaws) if the surface stress is below a threshold value defined as the threshold stress (ASM International 1987, Vol. 13, p. 276). Constant-load crack-initiation tests were performed on one hundred and twenty (120) Alloy 22 samples by exposing them to BSW (pH ~ 10.3) at 105°C for 9,600 hours. The time-to-failure (total exposure time without failure) was determined at various applied stress ratios (applied stress to yield strength). Testing was done at applied stress ratios up to 2.1 times the yield stress of the as-received material ($2.1 \times YS$), and up to 2.0 times the yield strength of the welded material ($2.0 \times YS$). These high stress ratios correspond to an applied stress of 89 to 96% of the ultimate tensile strength (UTS). It is therefore concluded that Alloy 22 exhibited excellent resistance to SCC, since no failure was observed in any of the 120 samples, including those in the as-welded state. The outstanding SCC resistance of Alloy 22 is corroborated by results of high-magnification visual examination of numerous U-bend specimens, exposed for five years to relevant LTCTF environments (SDW, SCW, SAW) at 60 and 90°C. These Alloy 22 U-bends showed no evidence of SCC initiation ([DTN: LL021105312251.023] and [DTN: LL021105312251.023]).

SCC Propagation – Slip-Dissolution Film-Rupture (SDFR) Model

The propagation model relates crack propagation (advance) to the periodic rupture and repassivation of the passive film at the crack tip. This approach has been successfully applied to assess SCC crack propagation in light-water nuclear reactors. This model has now been adopted to assess the SCC susceptibility of the materials to be used for the DS and WP. Parameters in this particular model are being quantified through in situ measurements of crack velocity at known stress intensities. Calculated values of K_I indicate eventual penetration of the WPOB closure weld by through-wall radial cracks (which are driven by circumferential tensile forces).

The theory of slip dissolution (or film rupture) has been successfully applied to assess the SCC crack propagation for light-water nuclear reactors operating at relatively high temperature (~316°C) (Andresen et al. 1994). The slip-dissolution or film-rupture model is discussed in detail in other publications. This model has been adopted to assess the SCC susceptibility of the materials to be used for construction of the DS and WP (Farmer et al. 1991). The ultimate validity of this model and the associated model parameters will be demonstrated and determined through experimental testing at LLNL and elsewhere. It is desirable to separate the SCC mechanism into initiation and propagation phases, though the distinction between these two phases is blurred in experiments. Practical detection of SCC initiation usually requires a crack length of at least a few millimeters (significant metallurgical dimension). The actual initiation step may occur prior to any such detection.

Initiation of embryonic cracks may occur at microscopic surface flaws or sites of localized corrosion (pitting and inter-granular attack). The coalescence of the embryonic cracks to form larger cracks must also be understood. It has been observed that the crack growth rate increases as small cracks coalesce, and approaches a steady-state value when the mean crack length (depth) is about 20 to 50 microns. Thereafter, the crack propagation rate may be analyzed in terms of linear elastic fracture mechanics, normally applicable to long (deep) cracks.

The slip dissolution model has been successfully employed to predict crack extension in boiling-water nuclear reactors (Andresen et al. 1980's through 1990's). The slip dissolution is represented by Equation 10-2, which shows the dependence of crack propagation rate (V_t) on the crack tip strain rate ($\dot{\epsilon}_{ct}$) (BSC 2003f, ANL-EBS-MD-000005 REV 01 ICN 00, Eqn. 5; Farmer et al. 2000b):

$$V_t = A \left(\dot{\epsilon}_{ct} \right)^n \quad (\text{Eqn. 10-2})$$

The parameters A and n depend upon the material and environment at the crack tip. These two parameters can be determined from the measured rate of repassivation. Such measurements are made by rapidly straining wires that are fabricated from the material of interest. The initial application of the slip-dissolution or film-rupture model was on the quantitative prediction of cracking in type 304 or 316 stainless steels in high-purity water at 288°C (boiling-water reactor environment). These investigations led to a quantification of parameters in the model. The value of A is determined with Equation 10-3 (BSC 2003f, ANL-EBS-MD-000005 REV 01 ICN 00, Eqn. 11; Farmer et al. 2000b):

$$A = 7.8 \times 10^{-3} (n)^{3.6} \quad (\text{Eqn. 10-3})$$

Equations 10-2 and 10-3 have been combined to yield Equation 10-4 (BSC 2003f, ANL-EBS-MD-000005 REV 01 ICN 00, Eqn. 12; Farmer et al. 2000b):

$$V_t = 7.8 \times 10^{-3} (n)^{3.6} \left(\dot{\varepsilon}_{ct} \right)^n \quad (\text{Eqn. 10-4})$$

where V_t has the unit of cm s^{-1} and ε_{ct} has the units of s^{-1} . The exponent n (~ 0.75) is fundamentally related to the crack tip environment (pH, potential, anionic activity) and material properties. In the case of constant load, the crack-tip strain rate in Equation 10-4 is related to the engineering stress or the stress intensity factor through Equation 10-5 (BSC 2003f, ANL-EBS-MD-000005 REV 01 ICN 00, Eqn. 13; Farmer et al. 2000b):

$$\dot{\varepsilon}_{ct} = 4.1 \times 10^{-14} K_I^4 \quad (\text{Eqn. 10-5})$$

where K_I is in the units of $\text{MPa m}^{1/2}$. Substitution of Equation 10-5 for constant load into Equation 10-4 yields the following alternative expression for SCC propagation rate (BSC 2003f, ANL-EBS-MD-000005 REV 01 ICN 00, Eqn. 14; Farmer et al. 2000b):

$$V_t = \bar{A} (K_I)^{\bar{n}} \quad (\text{Eqn. 10-6})$$

where (BSC 2003f, ANL-EBS-MD-000005 REV 01 ICN 00, Eqn. 16; Farmer et al. 2000b)

$$\bar{A} = A (4.1 \times 10^{-14})^n \quad (\text{Eqn. 10-7})$$

and

$$\bar{n} = 4n \quad (\text{Eqn. 10-8})$$

Integration of this crack velocity algorithm is straightforward and leads to an appropriate equation for crack length (depth) as a function time. This approach involves the implicit assumption of an intrinsic initiating defect that exists at time zero. The size of this defect is estimated to be approximately 51 microns (0.002 inches) and would exist on an otherwise smooth surface.

The repassivation slope (n) is a key parameter in the SDFR model for SCC propagation. This parameter can be determined from a variety of experiments. An electrochemical determination consists of plotting the decaying repassivation current (i/i_0) against time (t/t_0), with log-log scales. The slope of the resultant straight line is the repassivation slope (n), hence the name. An alternative determination consists of plotting the crack growth rates measured under constant load (da/dt) against the stress intensity factor (K_I), with log-log scales. In this case, the slope of the resultant straight line is four-times the repassivation slope ($4n$). The later method was employed by Andresen et al. at the General Electric Global Research Center (GEGRC) to determine this parameter for Alloy 22 in BSW (pH ~ 13.4) at 110°C . The composition of this test medium has been documented [DTN: LL021105312251.023]. Four compact-tension (CT) specimens (c144, c152, c153, and c200) were subjected to cyclic loading in order to initiate crack growth, and then subjected to constant-load conditions with various hold times. The set of crack propagation rate data used to establish the repassivation parameter (n) are summarized in

Table 10-2 [DTN: LL021105312251.023]. As pointed out in the SCC AMR, caution should be exercised in using relatively few data for the determination of such model parameters.

The mean value of the repassivation parameter (n) and the standard deviation are 1.304 and 0.160, respectively. By assuming that the parameter (n) was normally distributed, the mean and standard deviation could be used to construct the distribution given in Table 10-3. The lower and upper bounds of n , based upon two standard deviations ($\pm 2\sigma$), are 0.984 to 1.624, respectively.

The threshold stress intensity factor is applied to both incipient flaws (once the threshold stress for initiation is exceeded) and for weld flaws. At each time step, the stress intensity factor, K_I , at a growing crack tip or defect tip will be compared with the K_{ISCC} value. At the point that the K_I value drops below K_{ISCC} , the crack will arrest. The distribution for K_{ISCC} , based on the flaw size distribution, is given in Table 10-4.

Figure 10-1 shows predictions of the crack-growth during the SCC of Alloy 22 in BSW at 110°C, as a function of stress intensity factor, and for bounding values of the repassivation parameter. Several crack-growth curves are shown in the figure: the lower bound ($n = 0.984$), the mean ($n = 1.304$), the upper bound ($n = 1.624$) for Alloy 22; It also has a crack-growth for the mean for stainless steel ($n = 0.54$). In comparison to stainless steel, Alloy 22 has exceptional resistance to SCC.

Table 10-2. Determination of the SDFR Model Parameters for Alloy 22 in BSW at 110°C

Specimen	Hold Time (hours)	Tested Stress Intensity Factor (MPa m ^{1/2})	Measured Crack Growth Rate (mm/s)	DTN: LL021105312251.023 (page number)	Calculated Repassivation Parameter (n) Note 3
C153	CL ^{Note 1}	30	2.50E-10	p. 11	1.168
C153	CL ^{Note 1}	30	5.00E-10	p. 11	1.119
C144	1	30	1.00E-11 ^{Note 2}	p. 7	1.391
C152	24	45	1.00E-11 ^{Note 2}	p. 10	1.563
C152	24	45	4.00E-10	p. 10	1.281

Notes: (1) CL denotes constant load; (2) cracking was assumed to cease at a crack growth rate of 10⁻¹¹ millimeters per second; (3) all values of the repassivation parameter were deduced from crack growth rate data as a function of stress intensity factor.

Table 10-3. Normal Distribution for Repassivation Slope (n)

Value of n	Percentile
0.984 (-2 σ)	2.28
1.041	5.00
1.099	10.00
1.139	15.00
1.145 (-1 σ)	15.87
1.170	20.00
1.221	30.00
1.264	40.00
1.304 (Mean)	50.00
1.345	60.00
1.388	70.00
1.439	80.00
1.464 (+1 σ)	84.13
1.470	85.00
1.509	90.00
1.568	95.00
1.624 (+2 σ)	97.72

Table 10-4. Threshold Stress Intensity Factor (K_{ISCC}) Distribution for Alloy 22 in 110 °C BSW

Value of n	Value of K_{ISCC} (MPa \sqrt{m})
0.984 (-2 σ)	2.65
1.041	3.65
1.099	4.90
1.139	5.90
1.145 (-1 σ)	6.06
1.170	6.76
1.221	8.35
1.264	9.85
1.304 (Mean)	11.38
1.345	13.10
1.388	15.04
1.439	17.56
1.464 (+1 σ)	18.87
1.470	19.19
1.509	21.36
1.568	24.89
1.624 (+2 σ)	28.50

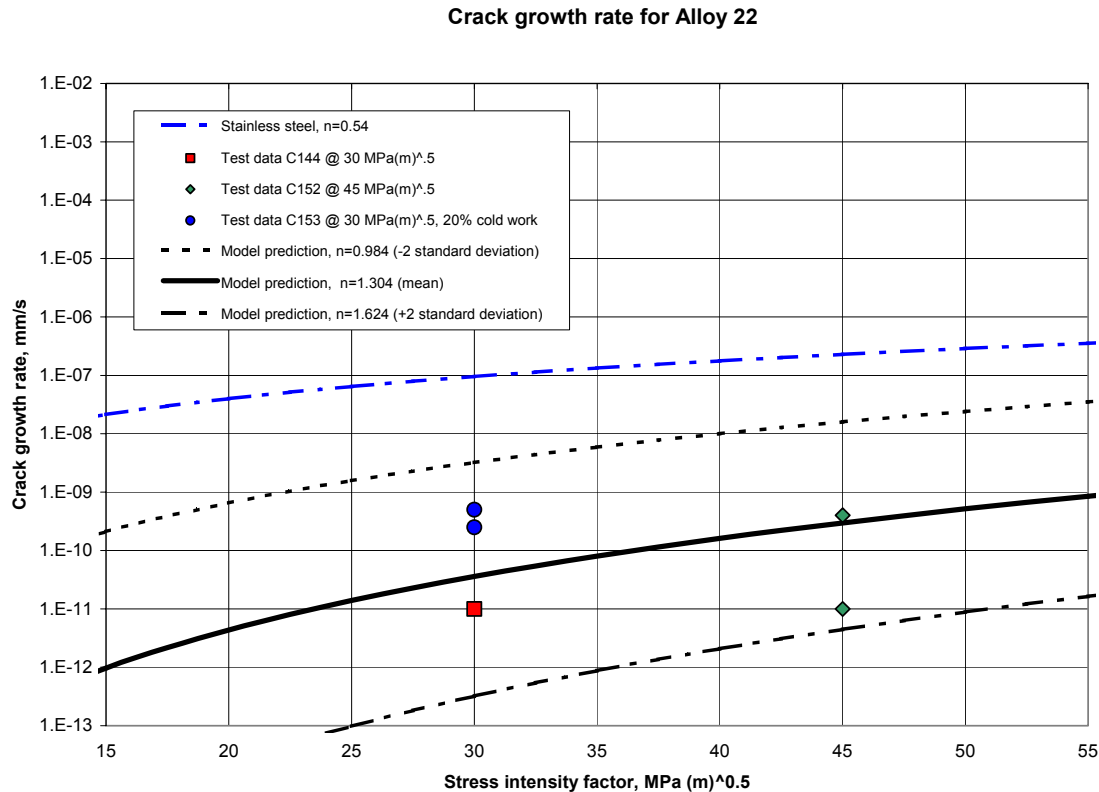


Figure 10-1. Predicted crack-growth rate for the SCC of Alloy 22 in BSW at 110°C as a function of stress intensity factor, and for bounding values of the repassivation parameter (n).

The Driving Force for SCC – Residual Weld Stress

Stress corrosion cracking (SCC) requires tensile stress as a driving force. The highest stress in the WPOB (and the highest probability of SCC) will be in the final closure weld. Post-weld processing such as peening can also be used to mitigate residual weld stress. Such stress mitigation must also be accounted for in the SCC model. Significant stress can be introduced into Alloy 22 during welding operations. In evaluating weld-induced stress, the effect of each weld pass is determined by simulating the heat being deposited by the welding process through heat generation rate that is deposited over a prescribed time interval. Typical parameters for weld application include the rate of electrical energy input, the speed of welding, and the assumed efficiency of heating (dependent upon heat transfer). Such information was used to determine the heat generation rate for the elements that represent each weld bead. A finite element model (FEM) is used to calculate weld-induced residual stress, shrink-fit stresses, and the corresponding stress intensity factors in the waste package materials. Determining the weld-induced residual stress and the shrink-fit stress is a problem that can best be solved using finite element models.

Stress Intensity Factor Calculation

Both SCC models (initiation and propagation) require knowledge of the stress intensity factor (K_I) as a function of crack depth. The calculation of this quantity from the stress distribution in the final closure weld is discussed in this section. Two orientations of the crack (or flaw) relative to the circular closure weld are accounted for: parallel to the weld (circumferential) and perpendicular to the weld (radial). A flaw with radial orientation is driven by hoop stress, while a flaw with circumferential orientation is driven by radial stress. In either case, the stress intensity factor K_I is defined as a function of stress (σ) and crack depth (a) (BSC 2003f, ANL-EBS-MD-000005 REV 01 ICN 00, Eqn. 21; Farmer et al. 2000b):

$$K_I(a, \sigma) = \beta \sigma \sqrt{\pi a} \quad (\text{Eqn. 10-9})$$

where β is a factor dependent on the shape (geometry) of the crack and the configuration of the structural component, and σ is the tensile stress. In most cases of practical importance, closed-form solutions are not available for evaluating K_I since the stress σ may be non-uniformly distributed, and since the geometry factor β is a function of crack size. Closed-form solutions are possible in some ideal cases involving uniform tensile stress and simple geometry, such as the classical problem of a single-edge cracked plate with thickness h . In this case, it has been shown that β can be expressed by the following approximate formula (Ewalds & Wanhill 1984) (BSC 2003f, ANL-EBS-MD-000005 REV 01 ICN 00; Farmer et al. 2000b):

$$\beta = 1.12 - 0.231\left(\frac{a}{h}\right) + 10.55\left(\frac{a}{h}\right)^2 - 21.72\left(\frac{a}{h}\right)^3 + 30.95\left(\frac{a}{h}\right)^4 \quad (\text{Eqn. 10-10})$$

Since stresses are non-uniformly distributed in most practical problems, the stress intensity factor has to be calculated through application of numerical algorithms (finite element model). The true value of K_I must be calculated from the idealized single-edge cracked plate (SECP) solution through application of a geometry correction factor G . The geometry correction factor is not a constant, but a function of the crack size. The true value of K_I is estimated with Equation 10-11 (BSC 2003f, ANL-EBS-MD-000005 REV 01 ICN 00, Eqn. 22; Farmer et al. 2000b):

$$K_I = G(K_I)_{SECP} \quad (\text{Eqn. 10-11})$$

where $(K_I)_{SECP}$ is the stress intensity factor for a single-edge cracked plate (SECP). The stress-intensity factor for a SECP with an infinitely long flaw is estimated with Equation 10-12 (Buchalet & Bamford 1976) (BSC 2003f, ANL-EBS-MD-000005 REV 01 ICN 00, Eqn. 24; Farmer et al. 2000b).

$$(K_I)_{SECP} = \sqrt{\pi a} \left[A_0 F_1 + \left(\frac{2a}{\pi}\right) A_1 F_2 + \left(\frac{a^2}{2}\right) A_2 F_3 + \frac{4a^3}{3\pi} A_3 F_4 \right] \quad (\text{Eqn. 10-12})$$

where F_0 , F_1 , F_2 and F_3 are magnification factors. These magnification factors are functions of crack aspect ratio (a/h), where (a) is the crack depth and (h) is the crack thickness (Buchalet & Bamford 1976). The parameters A_0 , A_1 , A_2 and A_3 are coefficients of a third-order polynomial, fit

to the through-wall stress distribution. This polynomial is given below (BSC 2003f, ANL-EBS-MD-000005 REV 01 ICN 00, Eqn. 23; Farmer et al. 2000b):

$$\sigma = A_0 + A_1 x + A_2 x^2 + A_3 x^3 \quad (\text{Eqn. 10-13})$$

where x is the distance from the outer surface of the closure lid. Values of the coefficients (A_i 's) for welds without stress mitigation are found in the SCC AMR (BSC 2003f, ANL-EBS-MD-000005 REV 01 ICN 00, Tables 4.1-2, 6-4 and 6.5). Values of the coefficients are also found in the WAPDEG AMR (BSC 2003h, ANL-EBS-PA-000001 REV 01 ICN 00, Table 13). The coefficients (A_0 , A_1 , A_2 and A_3) are obtained from [DTN: LL000316205924.142] for radial and hoop stresses (units of ksi) in the 25-mm outer lid of the CRM-21 PWR WP design; coefficients are converted to metric units in Table 10-5. Similarly, the coefficients (A_0 , A_1 , A_2 and A_3) are obtained from [DTN: LL000316205924.142] for radial and hoop stresses (units of ksi) in the 10-mm lid of the modified CRM-21 PWR WP design; coefficients are converted to metric units in Table 10-6.

Table 10-5. Stress Coefficients for the As-Welded Waste Package Outer Lid.

Stress Coefficient	Unit	Radial Stress	Hoop Stress
A_0	MPa	116.321	382.136
A_1	MPa/mm	9.107	8.096
A_2	MPa/mm ²	-3.146	-1.991
A_3	MPa/mm ³	0.111	0.060

DTN: LL000316205924.142

Table 10-6. Stress Coefficients for the As-Welded Waste Package Middle Lid.

Stress Coefficient	Unit	Radial Stress	Hoop Stress
A_0	MPa	181.636	219.908
A_1	MPa/mm	-177.592	56.494
A_2	MPa/mm ²	23.385	-20.848
A_3	MPa/mm ³	-0.900	1.083

DTN: LL000316205924.142

The integrity of components subjected to multi-axial stresses can be assessed with uniaxial stress information. This is an acceptable approach, and is consistent with standard industrial practice. The prediction of stress-strain behavior in sophisticated elastic-plastic analyses typically uses the equivalent (von Mises) stress-strain approach, and uniaxial material stress-strain behavior. The American Society of Mechanical Engineers (ASME) Boiler and Pressure Vessel Code specify the use of uniaxial materials-strength data for the assessment of materials performance under multi-axial stress conditions. In order to apply the uniaxial stress-strain information to multi-axial conditions, principal stresses are used. This approach recognizes that a combination of stresses can be validly represented by an equivalent, uniaxial stress. Even in a uniaxial stress-strain test (where failure typically occurs along the 45-degree plane – in pure shear), the cross-sections that are not perpendicular to the load line are in a biaxial stress condition that is equivalent to a uniaxial condition. These biaxial stress states can be observed using Mohr's circle.

Prevention of SCC Through Mitigation of Residual Tensile Stress in Closure Weld

Post-weld stress-mitigation processes at the final closure weld to lower the probability of SCC. Two options are currently being considered, laser-shock peening (LSP) and controlled-plasticity burnishing (CPB). LSP is the baseline process for License Application (LA), and utilizes a high-power pulsed laser beam to introduce shock waves into the weld surface. These pulses produce compressive stress that counter balances the tensile stress caused by welding (due to shrinkage during cooling). Single-pass LSP has been successfully demonstrated on prototypical Alloy 22 welds. Multiple-pass LSP can be used to increase the depth of the compressive stress layer. As discussed in a subsequent section, compressive stress can be produced at depths of 2 to 3 mm.

The waste package design for the license application (LA) consists of the following changes from the Site Recommendation (SR) design:

- Replacing the full penetration stainless steel lid weld with a spread ring and seal weld;
 - Eliminating the outer lid extension;
 - Changing the outer lid mitigation method from induction annealing to LSP;
 - Changing the inner lid weld configuration from a full penetration weld to a seal weld; and
 - Eliminating LSP of the inner lid.
- Sketches of the Site Recommendation design and the current recommended LA design of the waste package are shown in Figure 10-1 (Arthur 2003, Attachment 1, Figure 1).

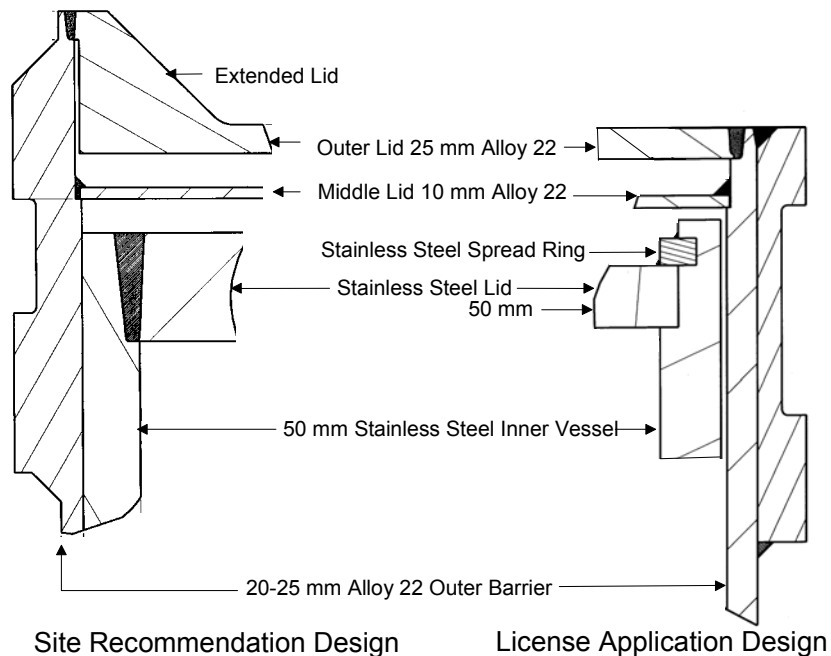
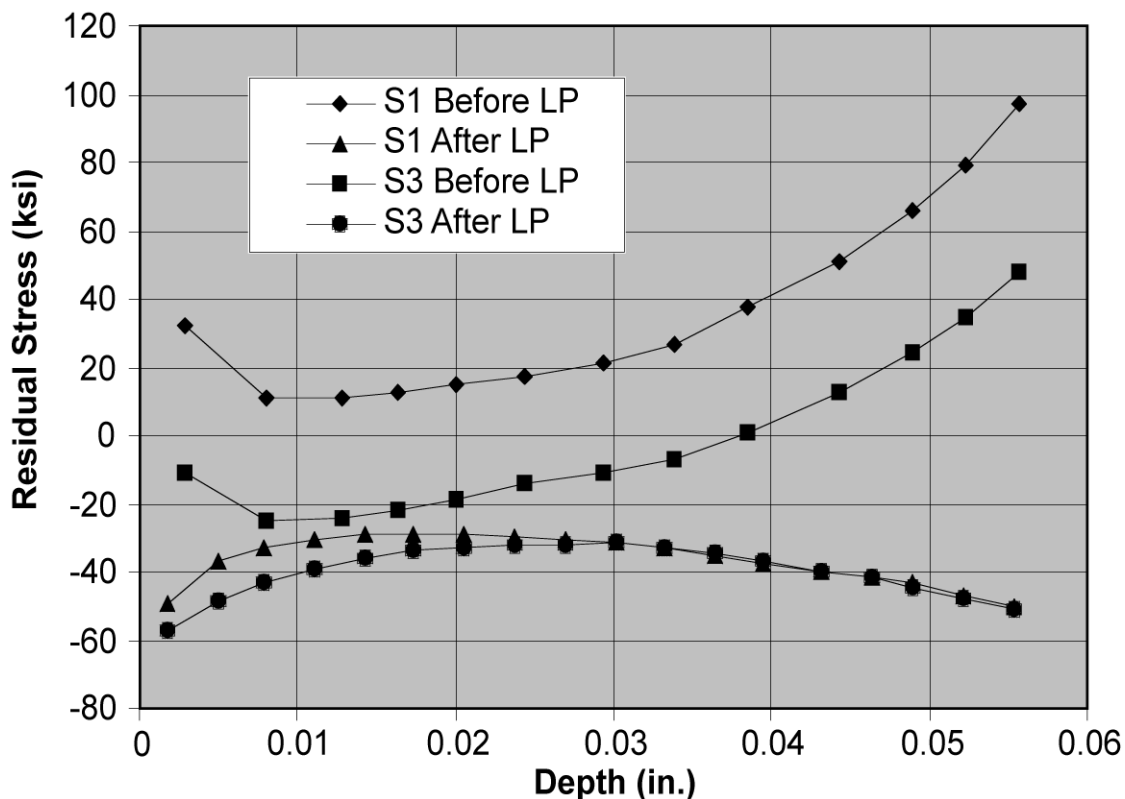


Figure 10-2. Waste package designs with two Alloy 22 lids: site recommendation (SR) and license application (LA) versions.

One can see in Figure 10-1 that there is a physical separation between the two lids. Thus, any SCC cracks initiated in the outer closure-lid stop after penetrating it, and then the middle closure-lid welds are subject to the external environment and the potential for SCC crack initiation and growth.

Based on the modification of the WP outer lid closure weld configuration as indicated in Figure 10-1, induction annealing is no longer being considered as a residual stress mitigation process for outer lid closure weld. Instead, the current plan is to implement one of two potential mechanical residual stress mitigation processes, i.e. either LSP or CPB. The final decision has not yet been made on which process to adopt. This decision will be based on cost and practicality of implementation in the YMP site welding and stress mitigation hot cell and will be made as part of the hot cell design effort planned for the near future. Currently, for the performance assessment of the waste package subjected to stress corrosion cracking, through-wall stress and stress intensity factor profiles due to weld residual stress in the WP closure welds are based on ANSYS finite element model calculations for a 25-mm thick Alloy 22 outer lid that is subjected to LSP and an as-welded 10 mm thick middle Alloy 22 closure lid. The near surface residual stress distribution before and after LSP the one inch welded Alloy 22 plate is shown in Figure 10-3.



DTN: LL000320005924.145

Figure 10-3. Mitigation of residual tensile stress in Alloy 22 weld with LSP.

The analyses of the through-wall stress and stress intensity factor distributions are documented in the current AMR on SCC (BSC 2003f, ANL-EBS-MD-000005 REV 01 ICN 00 [DIRS 161234] Section 6.). The results of these stress analyses, including the associated uncertainty, are included in the current WAPDEG analysis (BSC 2003e, ANL-EBS-MD-000004 REV 01 ICN 00, BSC 61317).

In the current SCC AMR, it was concluded that the dominant component of stress in the WPOB closure weld is the hoop stress, which promotes the growth of cracks oriented in the radial direction (BSC 2003f, ANL-EBS-MD-000005 REV 01 ICN 00, Section 6.2.2.3). As a direct result of this conclusion, it was only necessary to account for the hoop stress in the current WAPDEG analysis (BSC 2003e, ANL-EBS-MD-000004 REV 01 ICN 00).

The hoop stress (σ) as a function of depth (x) within the WPOB closure weld is given by the third-order polynomial, given here as Equation 10-14 (BSC 2003f, ANL-EBS-MD-000005 REV 01 ICN 00, Equation 23):

$$\sigma(x, 0) = A_0 + A_1 \cdot x + A_2 \cdot x^2 + A_3 \cdot x^3 \quad (\text{Eqn. 10-14})$$

Values of the coefficients (A_i 's) for stress-mitigated welds are found in the SCC AMR (BSC 2003f, ANL-EBS-MD-000005 REV 01 ICN 00, Tables 4.1-2 and 6-8), and are repeated in the table below.

Table 10-7. Stress Coefficients for the Laser Shock Peened (LSP) Waste Package Outer Lid.

Stress Coefficient	Unit	Radial Stress	Hoop Stress
A_0	MPa	-265.920	-292.607
A_1	MPa/mm	103.987	178.277
A_2	MPa/mm ²	-9.857	-14.135
A_3	MPa/mm ³	0.254	0.320

The second term in Equation 10-14 is to represent angular variation ($\theta = 0$ arbitrarily chosen) around the circumference of the WPOB closure weld. The angular variation is included using the following functional form (BSC 2003f, ANL-EBS-MD-000005 REV 01 ICN 00, Section 6.4.5, Equation 25a):

$$\sigma(x, \theta) = \sigma(x, 0) - (17.236893) \cdot (1 - \cos(\theta)) \quad (\text{Eqn. 10-15})$$

The expression for $\sigma(x, \theta)$ is given as Equation 10-15, and requires knowledge of the stress coefficients (A_i 's). Note that the original reference uses $S_\theta(x)$, $S_\theta(X)$, and ∇S to represent $\sigma(x, \theta)$, $\sigma(x, 0)$ and the 17.236893-MPa value, respectively.

The angular variation of the stress intensity factor is given as Equation 10-16 (BSC 2003f, ANL-EBS-MD-000005 REV 01 ICN 00, Section 6.4.5, Equation 25b):

$$K(x, \theta) = K(x, 0) \cdot \left(\frac{\sigma(Thck, \theta)}{\sigma(Thck, 0)} \right) \quad (\text{Eqn. 10-16})$$

The angular-dependent stress intensity factor is $K(x, \theta)$, the reference-value ($\theta = 0$) of the stress intensity factor is $K(x, 0)$, and the thickness of the WPOB closure lid is $Thck$. Note that the original reference uses $K_\theta(x)$, $K_0(x)$, $S_\theta(h)$, $S_0(h)$ and h to represent $K(x, \theta)$, $K(x, 0)$, $\sigma(Thck, \theta)$, $\sigma(Thck, 0)$ and $Thck$, respectively.

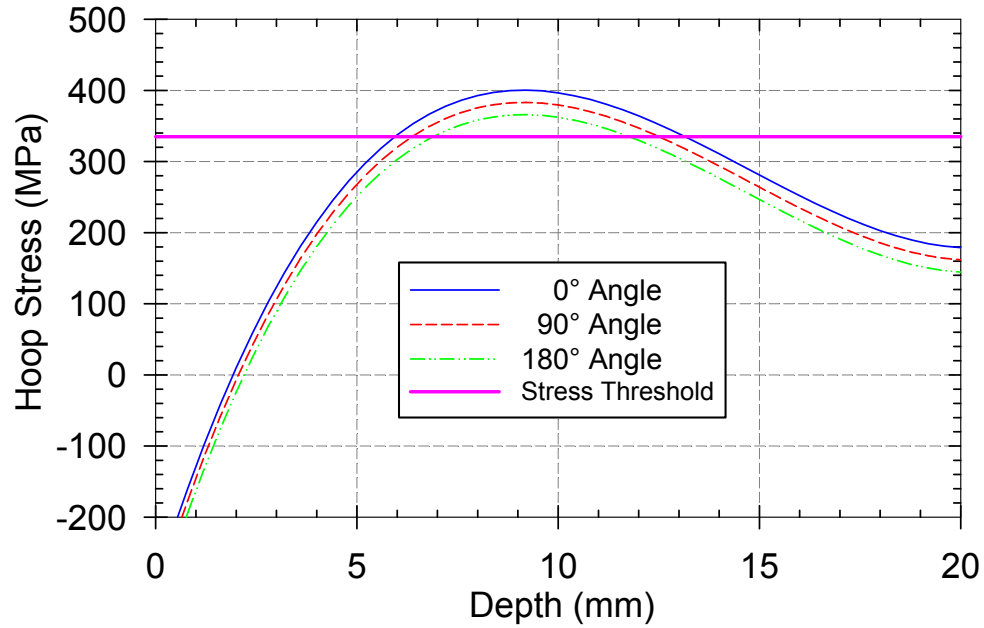
In the current waste package design, stress mitigation with LSP is used as a means of introducing compressive stress in the closure weld, and thereby preventing SCC. Thus, the stress distributions of welds processed with LSP (or another mitigation process such as CPB) should be used in the model. The predicted depth-dependent hoop stress (σ) for a stress-mitigated weld, at three representative angular positions (0° , 90° , and 180°), is shown in Figure 10-3. The predicted hoop stress in the stress-mitigated weld is compressive at a depth of 2 mm, and rises to the threshold stress at a depth of 6 mm. The threshold stress is approximately ninety percent of the yield stress (90% YS) and is discussed in the SCC AMR (BSC 2003f, ANL-EBS-MD-000005 REV 01 ICN 00, Section 6.2.1). These predictions are based on experimental measurements of the stress distribution in an Alloy 22 weld with LSP stress mitigation. The depth-dependent stress intensity factor (K_I) for a stress-mitigated weld, at three representative angular positions (0° , 90° , and 180°), can be predicted by combining the results shown in Figure 10-4 with the size distribution for weld flaws. The resultant stress intensity factor profile is shown in Figure 10-5.

Uncertainty in the stress and stress intensity factor profiles is accounted for with a scaling factor (sz). The scaling factor (sz) is sampled from a normal distribution, with a mean of zero, and a standard deviation of five percent of the yield strength (5% YS), an upper bound of fifteen percent of the yield strength (15% YS), and a lower bound of minus fifteen percent of the yield strength (-15% YS) (BSC 2003h [DIRS 161234], Section 6.4.5). Equation 10-17 is used to predict the stress profile and the associated uncertainty shown in Figure 10-6.

$$\sigma_u(x, \theta, z) = \sigma(x, \theta) \cdot \left(\frac{\sigma(Thck, \theta) + sz}{\sigma(Thck, \theta)} \right) \quad (\text{Eqn. 10-17})$$

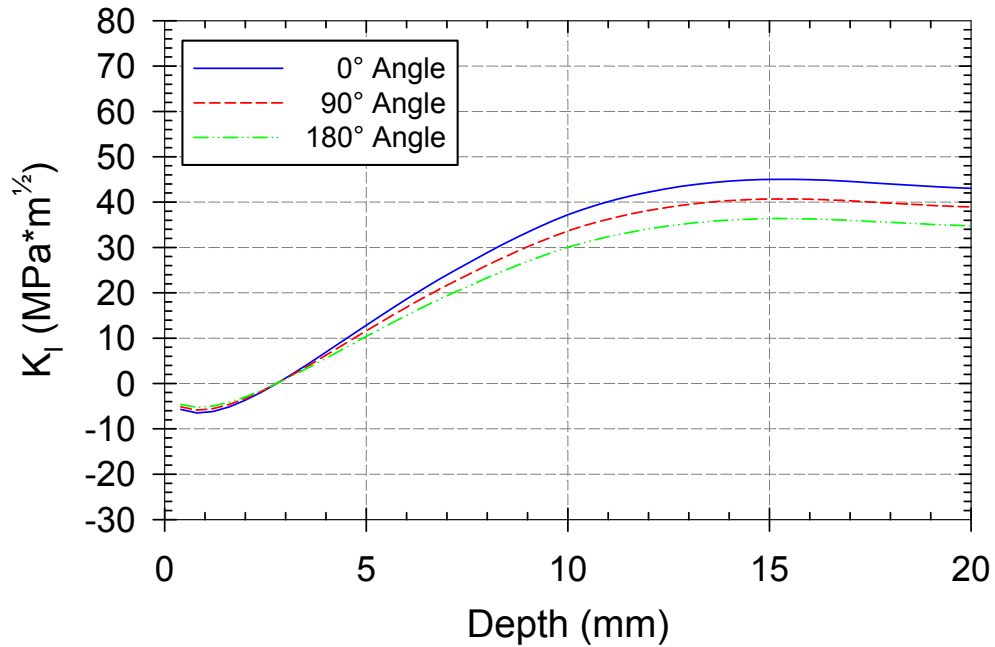
Equation 10-18 is the corresponding relationship for the stress intensity factor:

$$K_u(x, \theta, z) = K(x, \theta) \cdot \left(\frac{\sigma(Thck, \theta) + sz}{\sigma(Thck, \theta)} \right) = K(x, 0) \cdot \left(\frac{\sigma(Thck, \theta) + sz}{\sigma(Thck, 0)} \right) \quad (\text{Eqn. 10-18})$$



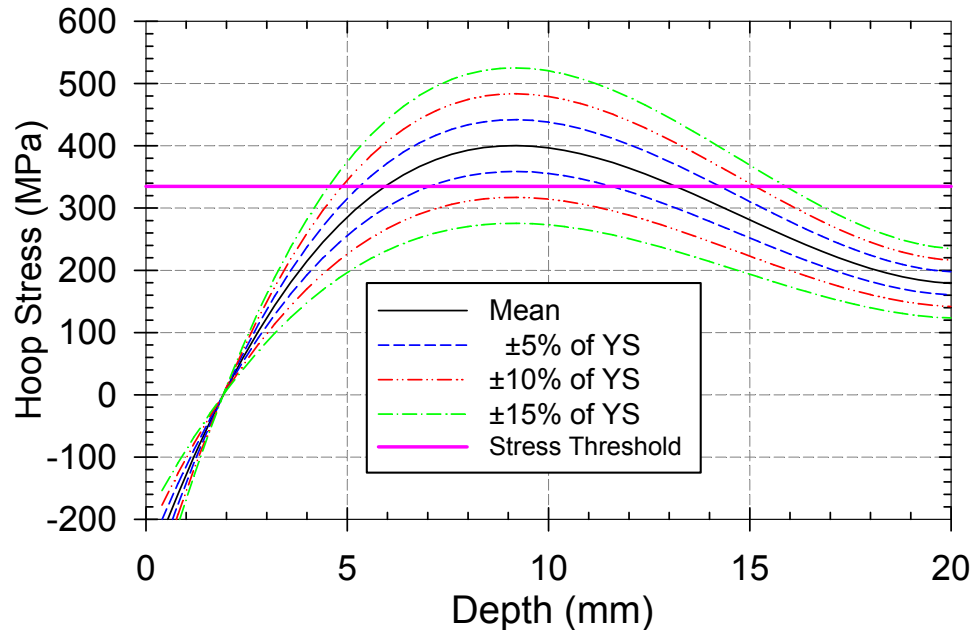
Source DTN: LL030607012251.065

Figure 10-4. Hoop stress verses depth for the outer lid of the WPOB (see Fig. 10-2).



Source DTN: LL030607012251.065 [DIRS 163968]

Figure 10-5. Stress intensity factor verses depth for the outer lid of the WPOB (see Fig. 10-2).



Source DTN: LL030607012251.065 [DIRS 163968]

Figure 10-6. Predictions of the hoop stress ($\theta = 0$) as a function of depth in the stress-mitigated outer weld of the WPOB. The various curves represent various scaling factors that range from 5 to 15% of YS.

The current stress-distribution model for LSP-processed welded plate of Alloy 22 predicts that the threshold stress (90% YS) will be reached at a depth of six millimeters (6 mm), based upon mean values. More conservatively, the model predicts that the threshold stress will be reached at a depth of only five millimeters (4.7 mm), based upon the upper bound of uncertainty. Corroborative measurements of the through-wall residual stress have been made on Alloy 22 GTAW welds (one-inch thick) that were processed with LSP and CPB, and are shown in Figures 10-7 and 10-8. These corroborative measurements show that the predicted values are very conservative estimate of the depth of compression (thickness protected from SCC) achieved through stress mitigation. The depth of the compressive layer for both stress-mitigation processes (LSP and CPB) is much greater than the predicted value of 2 mm. These corroborative measurements were measured with the one-inch ring-core technique and are reported in “X-Ray Diffraction and Ring-Core Determination of the Subsurface Residual Stress Distributions in Two Alloy 22 Welded Plates” (Lambda Research Report No. 1181-10952, January 2003 [DTN: MO0301SPAXRA52.001]). Note that stresses parallel to the weld centerline are referred as being in the “parallel direction.”

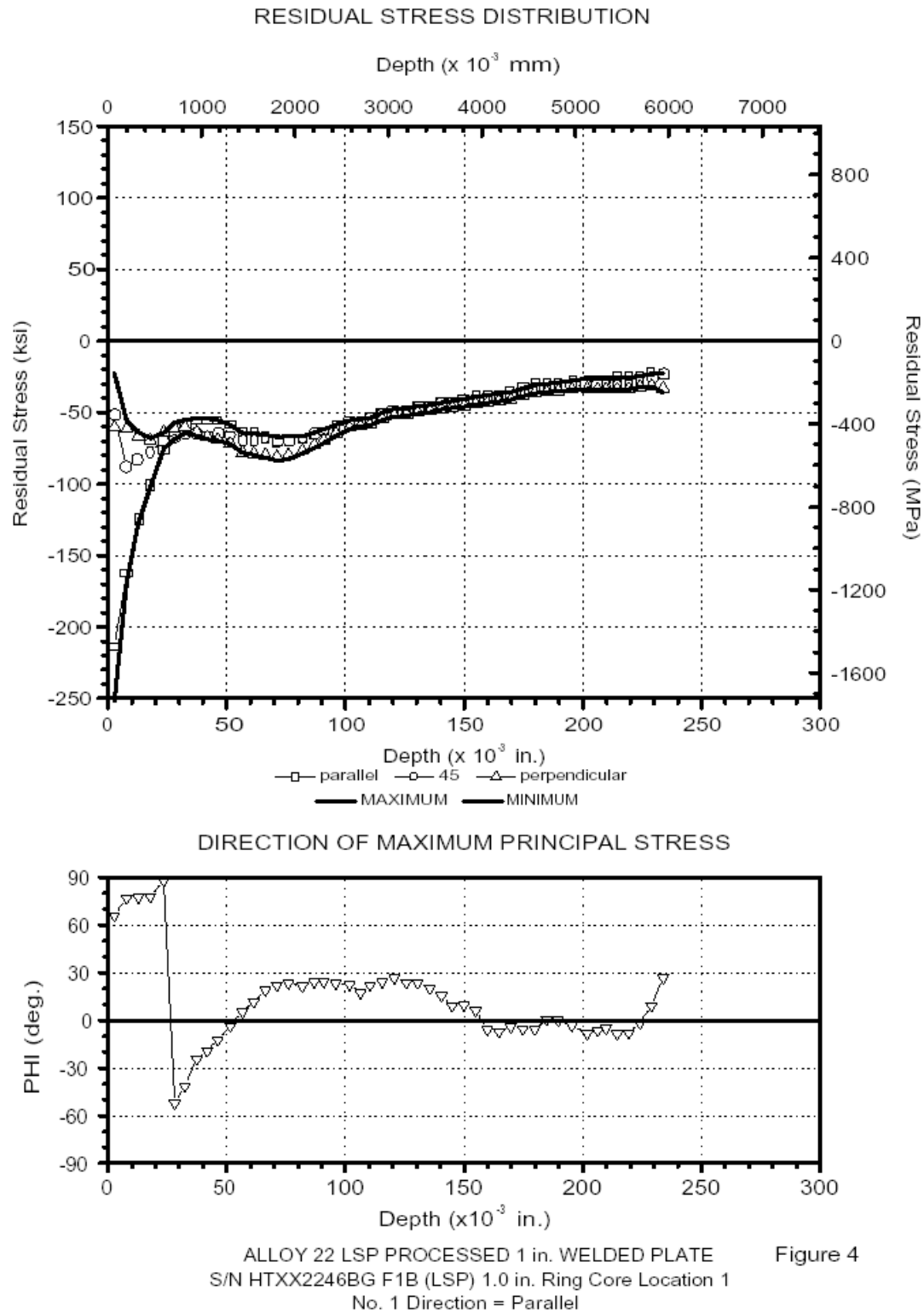


Figure 10-7. Residual stress distribution in welded Alloy 22 plates with LSP stress mitigation.

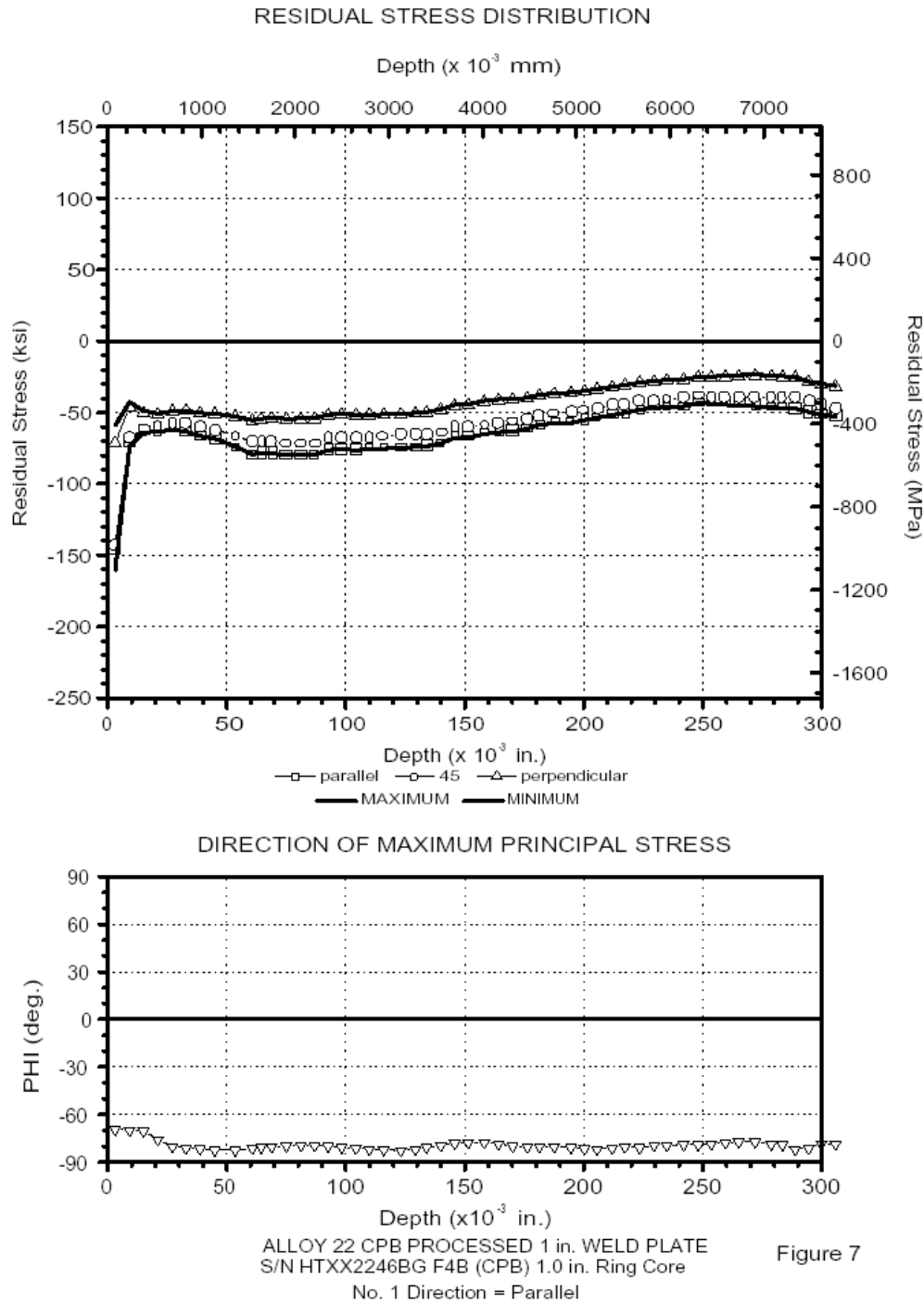


Figure 10-8. Residual stress distribution in welded Alloy 22 plates with CPB stress mitigation.

Impact of Corrosion on Stress-Mitigated Weld (Compressive Layer)

The time-to-failure due to SCC at the stress-mitigated closure weld will be determined by the time required for the compressive layer to be removed by corrosion, or by the time required for the surface layer to relax into a tensile stress state. The rate of SCC propagation is assumed to be fast enough to penetrate the waste package in one (WAPDEG) simulation time step. The scenario for removal of the compressive layer by corrosion is relatively easy to assess. From Figures 6-3 through 6-13, and the associated statistical analyses, the general corrosion rate for Alloy 22 is $\sim 7.24 \pm 4.95$ (1 σ) nanometers per year for crevice samples, and $\sim 2.75 \pm 2.74$ (1 σ) nanometers per year for weight-loss samples. The wall thickness of the Alloy 22 WPOB is approximately 2 centimeters, and the thickness of the compressive layer at the laser-peened or burnished weld is approximately 5 millimeters. Estimates of the times-to-failure (t_f) are summarized in Table 10-7. The stress-mitigated layer is deep enough to extend the service life of the WPOB well beyond the 10,000-year performance period specified in 10CFR63.

Table 10-8. Estimates of the Time-to-Failure (t_f) for Stress-Mitigated Closure Weld

		Crevice Sample	Wt. Loss Sample	Crevice Sample	Wt. Loss Sample
		Corrosion Rate (+1 σ) = 12.19×10^{-9} meters/year	Corrosion Rate (+1 σ) = 5.49×10^{-9} meters/year	Corrosion Rate (+2 σ) = 17.14×10^{-9} meters/year	Corrosion Rate (+2 σ) = 8.23×10^{-9} meters/year
	Meters	Years	Years	Years	Years
WPOB Wall Thickness	2×10^{-2}	1.64×10^6	3.64×10^6	1.17×10^6	1.43×10^6
Compressive Layer Thickness	5×10^{-3}	4.10×10^5	9.11×10^5	2.92×10^5	6.08×10^5

Chapter 11. Protection of the Alloy 22 WPOB by the Ti Drip Shield – Defense in Depth

Stress Corrosion Cracking of Titanium Grade 7 Drip Shield

Titanium Grade 7 appears to be more susceptible to SCC initiation, as indicated by the failure of constant-load specimens at applied stress ratios of 1.1 to 1.4 times the yield strength. Some specimens failed relatively early (≤ 168 hours), at an applied stress greater than 110% of the yield stress. However, the results were mixed at 110% of the yield stress: some failed after an exposure of ~ 200 hours; others showed no failure after an exposure of ~ 7000 hours. A threshold stress for SCC close to the yield stress is also consistent with the results of U-bend tests in the LTCTF. No SCC initiation was detected in a number of fixed-deflection Ti Grade 7 U-bend specimens after several years of exposure in the LTCTF at 60 and 90°C. These U-bend specimens were bent ~ 180 degrees and then the legs were restrained to give an apex strain (cold work level) of greater than about 10% which resulted in sustained stress levels at or over yield stress.

Conclusions

The waste package and drip shield will experience a wide range of interactive environmental conditions and degradation modes that will determine the overall performance of the waste package and repository. The operable modes of degradation are determined by the temperature regime of operation (region), and are summarized here.

Dry-Out Region ($T \geq 120^\circ\text{C}$; 50 to 400 Years)

During the pre-closure period, the waste package will be kept dry by ventilation air. During the thermal pulse, heat generated by radioactive decay will eventually increase the temperature of the waste package, drip shield and drift wall to a level above the boiling point, where the probability of seepage into drifts will become insignificant. Further heating will push the waste package surface temperature above the deliquescence point of expected salt mixtures, thereby preventing the formation of deliquescence brines from dust deposits and humid air. Phase and time-temperature-transformation diagrams predicted for Alloy 22, and validated with experimental data, indicates no significant phase instabilities (LRO and TCP precipitation) at temperatures below 300°C for 10,000 years. Neither will dry oxidation at these elevated temperatures limit waste package life. After the peak temperature is reached, the waste package will begin to cool, eventually reaching a point where deliquescence brine formation may occur. While the formation of deliquescence brines may be possible at temperatures that lie between the boiling and deliquescence points, no corrosion of Alloy 22 has been observed beneath films of CaCl_2 deliquescence brines at 150°C (close to deliquescence point).

Transition Region ($120^\circ\text{C} \geq T \geq 100^\circ\text{C}$; 400 to 1,000 Years)

During continued cooling, the temperature of the drift wall will drop to a level close to the boiling point of the seepage brine, thus permitting the onset of seepage. Corrosion in a concentrated, possibly aggressive, liquid-phase brine, evolved through evaporative concentration, is possible while in this region. However, based upon chemical divide theory, most ($\geq 99\%$) of the seepage water entering the drift is predicted to evolve as benign chloride-sulfate or bicarbonate brines. Less than one percent will evolve to aggressive calcium chloride brines, and these brines will have significant levels of nitrate inhibitor present. Application of the Localized Corrosion Initiation Model (Chapter 7) to the range of water chemistries predicted with the EBS Chemistry Model (Chapter 1) indicates that the initiation of localized corrosion is unlikely (based upon mean values). Thus, waste package life will not be limited by localized corrosion while in this region of operation. Rates of uniform general corrosion are relatively insignificant, and Alloy 22 has been shown to be very resistant to stress corrosion cracking in a broad range of expected environments, even after five-year exposures. The possibility of stress corrosion cracking is further diminished by the application of stress mitigation processes, such as laser-shock peening (LSP) or controlled plasticity burnishing (CPB), and physical isolation of welded regions from corrosive environments.

Low Temperature Region ($100^{\circ}\text{C} \leq T$; 1,000-10,000 Years)

Continued cooling will eventually lower the temperature below the boiling point of the seepage brine, thus minimizing the extent of evaporative concentration. Once the waste package temperature drops below the critical temperature for crevice corrosion, corrosion will no longer limit waste package performance.

Long-Term High-Temperature Phase Stability of Alloy 22

Alloy 22 is a metastable austenitic alloy, where intermetallic phases can be precipitated at high temperature. These intermetallic phases (P, σ and μ) are rich in those elements responsible for the exceptional corrosion resistance of Alloy 22, and can therefore cause depletion of the passivating elements in close proximity to the precipitates. Such depleted, localized areas may be more susceptible to corrosion than areas where no precipitation has occurred. Furthermore, these precipitates may cause degradation of the mechanical properties. Predictions of multi-component phase diagrams have enabled the Project to predict the phases that are possible, as a function of elemental composition and temperature. Time-temperature-transformation (TTT) diagrams have been predicted, and are used to calculate the rate at which allowable phases (precipitates and long range ordering) can occur. As will be discussed in a subsequent section, such predictions indicate insignificant precipitation and long-range ordering (LRO) during the 10,000-year service life of the repository, as long as the temperature is kept below 300°C .

Significance of High-Temperature Oxidation Processes

Dry oxidation is another high-temperature degradation mode. The reaction of oxygen with Alloy 22, or Ti Grade 7, can cause a uniform thickening of the oxide layer on the surface. The surface oxide can consist of any of the alloying elements/constituents, through a chromium oxide layer has been assumed as the basis of approximate calculations. The rate of dry oxidation at the highest temperature in the repository is insignificant compared to other modes of attack.

Aqueous Phase Corrosion Processes

As the temperature begins to decrease during cooling, the possibility of aqueous phase electrolytes exists, first through the formation of deliquescence brines, and then through the evaporative concentration of seepage brines. Modes of attack experienced in aqueous electrolytes include general uniform corrosion, localized corrosion, and environmental fracture. In the case of general corrosion, the rate of dissolution is uniform over all surfaces, and is due to the transport of cations from the metal-oxide interface to the oxide-electrolyte interface, where the formation of soluble metal-containing corrosion products can occur. The transport of cations and/or anions through the passive oxide film is controlled by the diffusion and electric field-driven electromigration.

Localized Corrosion

Localized corrosion is any type of distributed, non-uniform corrosive attack of the surface, and is due to the localized failure of the passive film. Such localized failure may be due to surface

inclusions of relatively soluble species, the precipitation of small soluble halide crystallites on the passive film, destabilization of the passive film within occluded areas such as crevices, due to the lowering of pH, which results from the combined effects of differential aeration, the hydrolysis of dissolved metal cations within the crevice, and the electric field-driven electromigration of aggressive halide anions into the crevice. Localized attack may also occur at sites where intermetallic precipitation has occurred, which includes exposed grain boundaries.

Crevices may be formed between the waste package and supports, beneath mineral precipitates, corrosion products, dust, rocks, cement, and bio-films, and between layers of the containers. In the absence of inhibitor and buffer ions, the hydrolysis of dissolved metal can lead to the accumulation of H^+ and a corresponding decrease in pH. Electromigration of Cl^- (and other anions) into the crevice must occur to balance cationic charge associated with H^+ ions. These exacerbated conditions can set the stage for subsequent attack of the corrosion resistant material by passive corrosion, pitting (initiation and propagation), stress corrosion cracking (SCC), or other mechanisms. Gamma radiolysis may produce hydrogen peroxide, thereby increasing the open circuit corrosion potential.

Stress Corrosion Cracking

There are several modes of failure that could lead to premature breach of the waste package. One of the most threatening is stress corrosion cracking (SCC). Initiation and propagation of SCC can occur at relatively low stress intensity factors (K_I). After initiation, through-wall penetration is essentially instantaneous when compared to the 10,000-year time scale of importance to the high-level waste repository at Yucca Mountain. Three criteria have to be met for SCC to occur: metallurgical susceptibility; a corrosive environment; and static tensile stresses. Environments that cause SCC are usually aqueous and can be condensed layers of moisture or bulk solutions. The SCC of a particular alloy is usually caused by the presence of a specific chemical species in the environment. For example, the SCC of copper alloys is virtually always due to the presence of ammonia in the environment. Chloride ions cause SCC in stainless steels and aluminum-based alloys. Reduced sulfate is known to promote SCC in nickel-based alloys. Changes in the environmental conditions, which include temperature, dissolved oxygen, and ionic concentrations, will normally influence the SCC process. Radionuclide release is possible if SCC causes breach of the WPOB and underlying structural support.

Stress corrosion cracking (SCC) requires tensile stress as a driving force. The highest stress in the WPOB (and the highest probability of SCC) will be in the final closure weld. Post-weld processing such as LSP or CPB can be used to mitigate residual weld stress.

Since analyses based on either SCC model (Method A or B) indicate that through-wall radial cracking is a likely threat to the WP, it is necessary to implement post-weld stress mitigation processes at the final closure weld to lower the probability of SCC. Two options are currently being considered, LSP and high-plasticity burnishing. LSP is the baseline process for License Application (LA), and utilizes a high-power pulsed laser beam to introduce shock waves into the weld surface. These pulses produce compressive stress that counter balances the tensile stress caused by welding (due to shrinkage during cooling). Single-pass LP has been successfully

demonstrated on prototypical Alloy 22 welds. Multiple-pass LP can be used to increase the depth of the compressive stress layer.

The depth of laser-peened weld-metal with stresses less than the threshold stress (90% of the yield stress) has been shown to be about 4.7 mm at the upper uncertainty bound, and about 6 mm for the mean stress value. More recently, stresses have been measured using a 1-inch ring core technique, showing that the depth of the compressive layer achieved with LSP or CPB is greater than 5 millimeters.

The time-to-failure due to SCC at the stress-mitigated closure weld will be determined by the time required for the compressive layer to be removed by corrosion, or by the time required for the surface layer to relax into a tensile stress state. The rate of SCC propagation is assumed to be fast enough to penetrate the waste package in one (WAPDEG) simulation time step. The scenario for removal of the compressive layer by corrosion is relatively easy to assess. From Figures 6-3 through 6-13, and the associated statistical analyses, the general corrosion rate for Alloy 22 is $\sim 7.24 \pm 4.95$ (1 σ) nanometers per year for crevice samples, and $\sim 2.75 \pm 2.74$ (1 σ) nanometers per year for weight-loss samples. The wall thickness of the Alloy 22 WPOB is approximately 2 centimeters, and the thickness of the compressive layer at the laser-peened or burnished weld is approximately 5 millimeters. Estimates of the times-to-failure (t_f) are summarized in Table 10-1. The stress-mitigated layer is deep enough to extend the service life of the WPOB well beyond the 10,000-year performance period specified in 10CFR63. Based upon 5-year corrosion rates from the LTCTF, more than 10,000 years will be required to remove the compressive layer by general corrosion (30,000 to 90,000 years). It is also possible to use thermally-sprayed protective-coatings of ceramics to isolate these welds from the repository environment, thereby preventing SCC.

Summary

This TBR documents the analyses and models for general and localized corrosion of the waste package outer barrier (WPOB). The general and localized corrosion models have been used to analyze the degradation of the Alloy 22 outer barrier of the waste package by general and localized corrosion, under the expected repository exposure condition, and over the repository performance period. The general and localized corrosion models include several sub-models, which account for dry oxidation (DOX), aqueous general corrosion (GC), localized corrosion (LC), which includes crevice corrosion initiation and propagation, and microbial-influenced corrosion (MIC).

References

- Agarwal, D.C. 2000. "Nickel and Nickel Alloys." Chapter 45 of *Uhlig's Corrosion Handbook*. 2nd Edition. Revie, R.W., ed. New York, New York: John Wiley & Sons. TIC: 248360.
- Akashi, M.; Nakayama, G.; and Fukuda, T. 1998. "Initiation Criteria for Crevice Corrosion of Titanium Alloys Used for HLW Disposal Overpack." *CORROSION/98*. Paper No. 158. Houston, Texas: NACE International.
- Andresen, P. L.; Ford, F. P. 1994. *Intl. J. Pressure Vessels and Piping* **59**, 61-70.
- Andresen, P.L.; Young, L.M.; Kim, Y.J.; Emigh, P.W.; Catlin, G.M.; and Martiniano, P.J. 2002. *Stress Corrosion Crack Initiation & Growth Measurements in Environments Relevant to High Level Nuclear Waste Packages*. [Schenectady, New York]: GE Global Research Center. ACC: MOL.20020614.0298.
- Baker, E.A. 1988. "Long-Term Corrosion Behavior of Materials in the Marine Atmosphere." Degradation of Metals in the Atmosphere, [Proceedings of the Symposium on Corrosion of Metals, Philadelphia, Pennsylvania, 12-13 May 1986]. Dean, S.W. and Lee, T.S., eds. ASTM STP 965. Pages 125-144. Philadelphia, Pennsylvania: American Society for Testing and Materials. TIC: 224019.
- Beavers, J.A.; Devine, T.M., Jr.; Frankel, G.S.; Jones, R.H.; Kelly, R.G.; Latanision, R.M.; and Payer, J.H. 2002. *Final Report, Waste Package Materials Performance Peer Review Panel, February 28, 2002*. [Las Vegas, Nevada]: Waste Package Materials Performance Peer Review Panel. ACC: MOL.20020614.0035.
- Bohni, H. 2000. "Localized Corrosion of Passive Metals." Chapter 10 of *Uhlig's Corrosion Handbook*. 2nd Edition. Revie, R.W., ed. New York, New York: John Wiley & Sons. TIC: xxxxxx.
- Bojinov, M.; Fabricius, G.; Laitinen, T.; Makela, K.; Saario, T.; and Sundholm, G. 2001. "Influence of Molybdenum on the Conduction Mechanism in Passive Films on Iron–Chromium Alloys in Sulfuric Acid Solution." *Electrochimica Acta*, **46**, ([9]), 1339-1358. New York, New York: Pergamon. TIC: 249796.
- Borenstein, S.W. and White, D.C. 1989. "Influence of Welding Variables on Microbiologically Influenced Corrosion of Austenitic Stainless Steel Weldments." *Corrosion 89 April-17-21, 1989 New Orleans Convention Center, New Orleans, Louisiana, Paper Number 183*, 183/1 - 183/13. Houston, Texas: National Association of Corrosion Engineers. TIC: 246583.
- Brossia, C.S.; Browning, L.; Dunn, D.S.; Moghissi, O.C.; Pensado, O.; and Yang, L. 2001. Effect of Environment on the Corrosion of Waste Package and Drip Shield Materials. CNWRA 2001-03. Center for Nuclear Waste Regulatory Analyses, San Antonio, Texas.
- BSC (Bechtel SAIC Company) 2001a. *Environment on the Surfaces of the Drip Shield and Waste Package Outer Barrier*. ANL-EBS-MD-000001 REV 00 ICN 02. ACC: MOL.20010724.0082.

BSC (Bechtel SAIC Company) 2001b. *FY 01 Supplemental Science and Performance Analyses, Volume 1: Scientific Bases and Analyses*. TDR-MGR-MD-000007 REV 00 ICN 01. ACC: MOL.20010801.0404; MOL.20010712.0062; MOL.20010815.0001.

BSC (Bechtel SAIC Company) 2002a. *Technical Work Plan for: Waste Package Materials Data Analyses and Modeling*. TWP-EBS-MD-000005 REV 05. ACC: MOL.20021218.0029.

BSC (Bechtel SAIC Company) 2002b. *The Enhanced Plan for Features, Events, and Processes (FEPs) at Yucca Mountain*. TDR-WIS-PA-000005 REV 00. ACC: MOL.20020417.0385.

BSC (Bechtel SAIC Company) 2003a. *Engineered Barrier System, Physical and Chemical Environment (Darren Jolly)*. ANL-EBS-MD-000033 REV 02 ICN 00.

BSC (Bechtel SAIC Company) 2003b. *Waste Package & Drip Shield Surface Environment (Tom Wolery)*. ANL-EBS-MD-000001 REV 01 ICN 00.

BSC (Bechtel SAIC Company) 2003c. *Aging and Phase Stability of Waste Package Outer Barrier (Frank Wong)*. ANL-EBS-MD-000002 REV 01 ICN 00.

BSC (Bechtel SAIC Company) 2003d. *General Corrosion and Localized Corrosion of Waste Package Outer Barrier (Joon Lee)*. ANL-EBS-MD-000003 REV 01 ICN 00.

BSC (Bechtel SAIC Company) 2003e. *General Corrosion and Localized Corrosion of the Drip Shield (Fred Hua, Kevin Mon)*. ANL-EBS-MD-000004 REV 01 ICN 00.

BSC (Bechtel SAIC Company) 2003f. *Stress Corrosion Cracking of the Drip Shield, the Waste Package Outer Barrier, and the Stainless Steel Structural Material (Stephen Lu)*. ANL-EBS-MD-000005 REV 01 ICN 00.

BSC (Bechtel SAIC Company) 2003g. *Hydrogen Induced Cracking of Drip Shield (Gopal De)*. ANL-EBS-MD-000006 REV 01 ICN 00.

BSC (Bechtel SAIC Company) 2003h. *WAPDEG Analysis of Waste Package and Drip Shield Degradation (Kevin Mon, Bryan Bullard, Alda Behie)*. ANL-EBS-PA-000001 REV 01 ICN 00.

Buchalet, C. B.; Bamford, W. H. 1976. *Mechanics of Crack Growth*, ASTM Special Publication STP 590, pp. 385-402.

Canori, G.F. and Leitner, M.M. 2003. *Project Requirements Document*. TER-MGR-MD-000001 REV 01. Las Vegas, Nevada: Bechtel SAIC Company. ACC: DOC.20030404.0003.

Castrup, H.: *Distributions for Uncertainty Analysis*, Proceedings of the International Dimensional Workshop, Knoxville, TN, May 2001. (12 pgs).

Cieslak, M.J.; Headley, T.J.; and Romig, A.D., Jr. 1986. "The Welding Metallurgy of Hastelloy Alloys C-4, C-22, and C-276." *Metallurgical Transactions A*, 17A, (11), 2035-2047. Warrendale, Pennsylvania: Metallurgical Society of AIME. TIC: [233952](#).

Cleveland, W.S. 1993. *Visualizing Data*. Murray Hill, New Jersey: AT&T Bell Laboratories.

CRWMS M&O 1998. *Waste Package Degradation Expert Elicitation Project*. Rev. 1. ACC: MOL.19980727.0002.

CRWMS M&O 1999a. *Waste Package Material Properties*. BBA000000-01717-0210-00017 REV 00. ACC: MOL.19990407.0172.

CRWMS M&O 1999b. *Classification of the MGR Uncanistered Spent Nuclear Fuel Disposal Container System*. ANL-UDC-SE-000001 REV 00. ACC: MOL.19990928.0216.

CRWMS M&O 1999c. *License Application Design Selection (LADS) Report*. B00000000-01717-4606-00123 REV 01 ICN 01.

CRWMS M&O 2000a. *WAPDEG Analysis of Waste Package and Drip Shield Degradation*. ANL-EBS-PA-000001 REV 00 ICN 01. ACC: MOL.20001208.0063.

CRWMS M&O 2000b. *Total System Performance Assessment for the Site Recommendation*. TDR-WIS-PA-000001 REV 00 ICN 01. ACC: MOL.20001220.0045.

CRWMS M&O 2000c. *In-Drift Microbial Communities*. ANL-EBS-MD-000038 REV 00 ICN 01. ACC: MOL.20001213.0066.

CRWMS M&O 2000d. *General and Localized Corrosion of Waste Package Outer Barrier*. ANL-EBS-MD-000003 REV 00 ICN 00. UCRL-ID-134993. ACC: MOL.20000202.0172.

CRWMS M&O 2000e. *General and Localized Corrosion of the Drip Shield*. ANL-EBS-MD-000004 REV 00 ICN 00.

CRWMS M&O 2000f. *Degradation of Stainless Steel Structural Support for Waste Package*. ANL-EBS-MD-000007 REV 00 ICN 00.

CRWMS M&O 2000g. *Stress Corrosion Cracking*. ANL-EBS-MD-000005 REV 00 ICN 00.

CRWMS M&O 2000h. *Aging and Phase Stability of Waste Package Outer Barrier*. ANL-EBS-MD-000002 REV 00 ICN 00.

CRWMS M&O 2000i. *Environment on the Surfaces of the Drip Shield and Waste Package Outer Barrier*. ANL-EBS-MD-000001 REV 00 ICN 00.

DOE (U.S. Department of Energy) 2002. *Yucca Mountain Science and Engineering Report*. DOE/RW-0539, Rev. 1. Washington, D.C.: U.S. Department of Energy, Office of Civilian Radioactive Waste Management. ACC: MOL.20020404.0042.

DOE (U.S. Department of Energy) 2003. *Quality Assurance Requirements and Description*. DOE/RW-0333P, Rev. 13. Washington, D.C.: U.S. Department of Energy, Office of Civilian Radioactive Waste Management. ACC: DOC.20030422.0003.

Dunn, D.S.; Cragnolino, G.A.; and Sridhar, N. 2000. "An Electrochemical Approach to Predicting Long-Term Localized Corrosion of Corrosion-Resistant High-Level Waste Container Materials." *Corrosion*, 56, (1), 90-104. Houston, Texas: National Association of Corrosion Engineers International. TIC: xxxxxx.

Dunn, D.S.; and Brossia, C.S. 2002. "Assessment of Passive and Localized Corrosion Processes for Alloy 22 As a High-Level Nuclear Waste Container Material." *Corrosion* 2002. Paper No. 02548. Houston, Texas: NACE International. TIC: xxxxxx.

Dunn, D.S.; Yang, L.; Pan, Y.-M.; and Cragnolino, G.A. 2003. "Localized Corrosion Susceptibility of Alloy 22." *Corrosion* 2003. Paper No. 03697. Houston, Texas: NACE International. TIC: xxxxxx.

Enos, D.G. and Taylor, S.R. 1996. "Influence of Sulfate-Reducing Bacteria on Alloy 625 and Austenitic Stainless Steel Weldments." *Corrosion Science*, 52, (11), 831-843. Houston, Texas: National Association of Corrosion Engineers International. TIC: 246554.

Estill, J.C.; Hust, G.A.; and Rebak, R.B. 2003. "Long Term Corrosion Potential Behavior of Alloy 22." *CORROSION* 2003. Paper No. 03688. Houston, Texas: NACE International

Estill, J.C. 1998. "Long-Term Corrosion Studies." *Engineered Materials Characterization Report*. UCRL-ID-119564. Vol. 3. Livermore, California: Lawrence Livermore National Laboratory. ACC: MOL.19981222.0137.

Evans, M.; Hastings, N.; and Peacock, B. 1993. *Statistical Distributions*. 2nd Edition. New York, New York: John Wiley & Sons. TIC: 246114.

Farmer, J. C.; Gdowski, G. E.; McCright, R. D.; Ahluwalia, H. S. 1991. "Corrosion Models for Performance Assessment of High-Level Radioactive Waste Containers." *Nuclear Engineering Design*, 129, 57-88.

Farmer, J. C.; McCright, R. D. 1998. "Crevice Corrosion and Pitting of High-Level Waste Containers: Integration of Deterministic and Probabilistic Models." Paper No. 98160, Symposium 98-T-2A, Annual Meeting of the National Association of Corrosion Engineers (NACE), Corrosion 98, San Diego, CA March 22-27, 1998.

Farmer, J.; Lu, S.; McCright, D.; Gdowski, G.; Wang, F.; Summers, T.; Bedrossian, P.; Horn, J.; Lian, T.; Estill, J.; Lingenfelter, A.; Halsey, W. 2000a. "General and Localized Corrosion of High-Level Waste Container in Yucca Mountain." *The 2000 ASME Pressure Vessel and Piping Conference*. Seattle, Washington. July 23-27, 2000. Transportation, Storage, and Disposal of Radioactive Materials, PVP Vol. 408, pp. 53-70.

Farmer, J.; Lu, S.; Summers, T.; McCright, D.; Lingenfelter, A.; Wang, F.; Estill, J.; Hackel, L.; Chen, H-L.; Gordon, G.; Pasupathi, V.; Andresen, P.; Tang, S.; Herrera, M. 2000b. "Modeling and Mitigation of Stress Corrosion Cracking in Closure Welds of High-Level Waste Containers for Yucca Mountain." *The 2000 ASME Pressure Vessel and Piping Conference*. Seattle, Washington. July 23-27, 2000. Transportation, Storage, and Disposal of Radioactive Materials, PVP, Vol. 408, pp. 71-81.

Fontana, M. G. 1986. Corrosion Engineering, McGraw Hill, New York, NY.

Frankel, G.S. 1998. "Pitting Corrosion of Metals. A Review of Critical Factors." *Journal of Electrochemical Society*, 145, 2186-2198.

Frankel, G.S. 2002a. "Localized Corrosion Phenomenology and Controlling Parameters." Chapter 8 of *A Compilation of Special Topic Reports, Waste Package Materials Performance Peer Review*. Wong, F.M.G. and Payer, J.H., eds. Las Vegas, Nevada: Waste Package Materials Performance Peer Review Panel. ACC: MOL.xxxxxxxx.xxx.

Frankel, G.S. 2002b. "Passivity-Induced Ennoblement." Chapter 11 of *A Compilation of Special Topic Reports, Waste Package Materials Performance Peer Review*. Wong, F.M.G. and Payer, J.H., eds. Las Vegas, Nevada: Waste Package Materials Performance Peer Review Panel. ACC: MOL.xxxxxxxx.xxx.

Freeze, G.A.; Brodsky, N.S.; Swift, P.N 2001. *The Development of Information Catalogued in REV00 of the YMP FEP Database*. TDR-WIS-MD-000003 REV 00 ICN 01. Las Vegas, Nevada: Bechtel SAIC Company. ACC: MOL.20010301.0237.

Gartland, P.O. 1997. "A Simple Model of Crevice Corrosion Propagation for Stainless Steels in Seawater." *Corrosion* 97, 417/1 to 417/17. Houston, Texas: NACE International. TIC: 245216.

Gdowski, GE 1991. *Survey of Degradation Modes of Four Nickel-Chromium-Molybdenum Alloys*. UCRL-ID-108330. Livermore, California: Lawrence Livermore National Laboratory. ACC: NNA.19910521.0010.

Gruss, K.A.; Cragnolino, G.A.; Dunn, D.S.; and Sridhar, N. 1998. "Repasivation Potential for Localized Corrosion of Alloys 625 and C22 in Simulated Repository Environments." *Proceedings of Corrosion 98, March 22-27, 1998, San Diego, California*, 149/1 to 149/15. Houston, Texas: NACE International. TIC: 237149.

Glass, R.S.; Overturf, G.E.; Van Konynenburg, R.A.; and McCright, R.D. 1986. *Corrosion Science* 26 8, 577-590.

Hack, H.P. 1983. "Crevice Corrosion Behavior of Molybdenum-Containing Stainless Steels in Seawater." *Materials Performance*, 22, (6), 24-30. Houston, Texas: NACE International. TIC: 245826.

Harrar, J.E.; Carley, J.F.; Isherwood, W.F.; and Raber, E. 1990. UCID-21867, 111 p.

Haynes International. 1997a. *Hastelloy C-22 Alloy*. Kokomo, Indiana: Haynes International. TIC: 238121.

Haynes International 1997b. *Hastelloy Alloy C-276. Haynes International Product Brochure*. Kokomo, Indiana: Haynes International. TIC: 238832.

Hilliard, J.E. and Cahn, J.W. 1961. "An Evaluation of Procedures in Quantitative Metallography for Volume-Fraction Analysis." *Transactions of the Metallurgical Society of AIME*, 221, (2),

344-352. New York, New York: American Institute of Mining, Metallurgical, and Petroleum Engineers. TIC: [253830](#).

Horn, J.; and Jones, D. 2002. "Microbiologically Influenced Corrosion: Perspectives and Approaches," in *Manual of Environmental Microbiology*, Second Edition, C.J. Hurst et al., ed., American Society of Microbiology Press, Washington DC, 2002, pp.1072-1083.

Horn, J.M.; Rivera, A.; Lian, T.; and Jones, D. 1998. "MIC Evaluation and Testing for the Yucca Mountain Repository." *Proceedings of Corrosion 98, National Association of Corrosion Engineers, March 22-27, San Diego, California*, 152/2 to 152/14. Houston, Texas: NACE International. TIC: 237146.

Hua, F.H. 2002. Testing of Candidate Container Materials to Resolve Post-VA Waste Package Materials Issues. RDD:02:43761-301-000:02. Alliance, Ohio: McDermott Technology, Inc. ACC: [MOL.2002xxxx.xxxx](#).

Hunkeler, F.; and Bohni, H. 1983. *Pit Growth Measurements on Stainless Steels*. In *Passivity of Metals and Semiconductors*, (edited by M. Froment) Elsevier, Amsterdam, 655-660.

Ishikawa, H.; Honda, A.; and Sasaki, N. 1991. "Long Life Prediction of Carbon Steel Overpacks for Geological Isolation of High-Level Radioactive Waste." In *Life Prediction of Corrodible Structures* (edited by R.N. Parkins), NACE International, Houston, TX, 454-484.

Jain, V.; Dunn, D.; Sridhar, N.; and Yang, L., 2003. "Effect of Measurement Methods and Solution Chemistry on the Evaluation of the Localized Corrosion of Candidate High-Level Waste Container Materials." Paper 03690, *CORROSION/03*, NACE International, Houston, Texas.

Jayaweera, P.; Macdonald, D.D.; Engelhard, G.; and Davydov, A., 2003. Deterministic Prediction of Localized Corrosion Damage to Alloy C-22 HLNW Canisters. SRI International Report, Menlo Park, CA. TIC: 253900.

Jones, R. H.; Ricker, R. E. 1987. *ASM Metals Handbook*, 9th Ed., Vol. 13, pp. 145-163.

Karmazin, L. 1982. "Lattice Parameter Studies of Structure Changes of Ni-Cr Alloys in the Region of Ni₂Cr." *Materials Science and Engineering*, 54, 247-256. [Lausanne, Switzerland]: Elsevier. TIC: [249655](#).

Karmazin, L.; Krejčí, J.; and Zeman, J. 1994. "γ Phase and Ni₂Cr-Type Long-Range Order in Ni-rich Ni-Cr-Mo Alloys." *Materials Science and Engineering A. Structural Materials: Properties, Microstructure and Processing*, A183, (1-2), 103-109. Lausanne, Switzerland: Elsevier. TIC: [253803](#).

Kehler, B.A.; Ilevbare, G.O.; and Scully, J.R., 1999. "Comparison of the Crevice Corrosion Resistance of Alloy 625 and C-22." In *Passivity and Localized Corrosion*, Volume 99-27. The Electrochemical Society. Pennington, NJ. Pp. 644-.

- Kehler, B.A.; Ilevbare, G.O.; and Scully J.R. 2001. "Crevice Corrosion Stabilization and Repassivation Behavior of Alloys 625 and 22." *Corrosion*, 57, (12), 1042-1065. Houston, Texas: NACE International.
- Kim, Y-K. 1987. *Journal of the Corrosion Science Society of Korea* **16** 1, 25–30.
- Kim, Y-K. 1988. *Journal of the Corrosion Science Society of Korea* **17** 1, 20–26.
- Kim, Y-K. 1999a. *Corrosion* **55** 1, 81–88.
- Kim, Y-K. 1999b. Paper 437, *Corrosion 99*, NACE, Houston, TX.
- King, F.; and Kolar, M. 2000. *The Copper Container Corrosion Model Used in AECL's Second Case Study*. 06819-REP-01200-10041-R00. Toronto, Ontario, Canada: Ontario Power Generation.
- Lian, T.; Martin, S.; Jones, D.; Rivera, A.; and Horn, J. 1999. "Corrosion of Candidate Container Materials by Yucca Mountain Bacteria." *Corrosion 99, Paper No. 476*, Houston, Texas: NACE International. TIC: 245833.
- Lide, D.R., ed. 1991. *CRC Handbook of Chemistry and Physics*. 72nd Edition. Boca Raton, Florida: CRC Press. TIC: 3595.
- Lloyd, A.C.; Shoesmith, D.W.; McIntyre, N.S.; and Noël, J.J. 2001. "Investigating the Localized Corrosion Properties of Ni-Cr-Mo Alloys for Their Use in Nuclear Waste Disposal Systems." *Stainless Steel World*, 13, (4), 29-30, 33. [Zutphen, The Netherlands]: KCI Publishing. TIC: 249982.
- Lorang, G.; Jallerat, N.; Quang, K.V.; and Langeron, J.-P. 1990. "AES Depth Profiling of Passive Overlayers Formed on Nickel Alloys." *Surface and Interface Analysis*, 16, 325-330. [New York, New York]: John Wiley & Sons. TIC: 249830.
- Macdonald, D.D. 1992. "The Point Defect Model for the Passive State." *Journal of the Electrochemical Society*, 139, (12), 3434-3449. Manchester, New Hampshire: Electrochemical Society. TIC: 249804.
- Macdonald, D.D. 1999. "Passivity—the Key to Our Metals-Based Civilization." *Pure and Applied Chemistry*, 71, (6), 951-978. Oxford, England: Blackwell Scientific Publishers. TIC: 249795.
- Manahan, M.P.; Macdonald, D.D.; and Peterson, A.J. 1995. "Determination of the Fate of the Current in the Stress Corrosion Cracking of Sensitized Type 304SS in High Temperature Aqueous Systems." *Corrosion Science*, 37, (1), 189-208. Elsevier Science Ltd. TIC: xxxxxx.
- Marcus, P. and Maurice, V. 2000. "Passivity of Metals and Alloys." Chapter 3 of *Corrosion and Environmental Degradation Vol. I*. Schutze, M., Volume Editor. Materials Science and Technology, A Comprehensive Treatment. New York, New York: Wiley-VCH. TIC: 249831.

Marsh, G.P., Taylor, K.J.; and Harker, A.H. 1991. *The Kinetics of Pitting Corrosion of Carbon Steel Applied to Evaluating Containers for Nuclear Waste Disposal*. Swedish Nuclear Fuel and Waste Management Company, Stockholm, Technical Report 91-61.

McCright, R.D. 1998. *Corrosion Data and Modeling Update for Viability Assessment*. Volume 3 of *Engineered Materials Characterization Report*. UCRL-ID-119564, Rev. 1.1. Livermore, California: Lawrence Livermore National Laboratory. ACC: MOL.19981222.0137.

McGuire, R.; Vlasity, J.; Kessler, J.; Long, A.; Childs, S.; Ross, B.; Schwartz, F.; Shoesmith, D.; Kolar, M.; Apted, M.; Zhou, W.; Sudicky, E.; Smith, G.; Kozak, M.; Salter, P.; Klos, R.; Venter, A.; Stenhouse, M.; Watkins, B.; and Little, R. 1998. *Alternative Approaches to Assessing the Performance and Suitability of Yucca Mountain for Spent Fuel Disposal*. EPRI TR-108732. Palo Alto, California: Electric Power Research Institute. TIC: 248813.

Mughabghab, S.F.; and Sullivan, T.M. 1989. "Evaluation of the Pitting Corrosion of Carbon Steels and Other Ferrous Metals in Soil Systems." *Waste Management*, 9, 239-251.

Newman, R.C.; and Franz, E.M. 1984. "Growth and Repassivation of Single Corrosion Pits in Stainless Steel." *Corrosion*, 40, 325.

Newman, R.C. 1985. "The Dissolution and Passivation Kinetics of Stainless Alloys Containing Molybdenum." *Corrosion Science*. 25, 331.

NRC (U.S. Nuclear Regulatory Commission) 2003. *Yucca Mountain Review Plan*. NUREG-1804, Rev. 3. Washington, D.C.: U.S. Nuclear Regulatory Commission, Office of Nuclear Material Safety and Safeguards.

Papoulis, Athanasios; Second Edition 1965. *Probability, Random Variables, and Stochastic Processes*. McGraw-Hill Book Company.

Plinski, M.J. 2001. *Waste Package Operations Fabrication Process Report*. TDR-EBS-ND-000003 REV 02. Las Vegas, Nevada: Bechtel SAIC Company. ACC: MOL.20011003.0025.

Pourbaix, M. 1974. "Atlas of Electrochemical Equilibria in Aqueous Solutions," NACE, Houston, Texas: National Association of Corrosion Engineers. TIC: xxxxxx.

Rebak, R.B.; Summers, T.S.E.; Lian, T.; Carranza, R.M.; Dillman, J.R.; Corbin, T.; and Crook, P. 2002. "Effect of Thermal Aging on the Corrosion Behavior of Wrought and Welded Alloy 22." *Corrosion 2002*. Paper No. 02542. Houston, Texas: NACE International.

Reed-Hill, R. 1973. *Physical Metallurgy Principles*. Second Edition. Boston, Massachusetts: PWS-KENT Publishing Co.

Sawyer, D.T.; and Roberts, Jr., J.L., 1974. *Experimental Electrochemistry for Chemists*. A Wiley-Interscience Publication, John Wiley & Sons, Inc.

Scully, J.R.; Hudson, J.L.; Lunt, T.; Ilevbare, G.; and Kehler, B. 1999. *Localized Corrosion Initiation and Transition to Stabilization in Alloys 625 and C-22*. 1-27. Charlottesville, Virginia: University of Virginia. TIC: 246630.

Scully, J.R.; Ilevbare, G.; and Marks, C. 2001. *Passivity and Passive Corrosion of Alloys 625 and 22*. SEAS Report No. UVA/527653/MSE01/103. Charlottesville, Virginia: University of Virginia, School of Engineering & Applied Science. TIC: 248056.

Sedriks, A.J. 1996. *Corrosion of Stainless Steels*. 2nd Edition. 179, 377. New York, New York: John Wiley & Sons. TIC: 245121.

Sharland, S.M.; Naish, C.C.; Taylor, K.J.; and Marsh, G.P. 1991. "An Experimental and Modelling Study of the Localized Corrosion of Carbon Steel Overpacks for the Geological Disposal of Radioactive Waste." *In Life Prediction of Corrodible Structures* (edited by R.N. Parkins), NACE International, Houston, TX, 402-408.

Smailos, E. and Köster, R. 1987. "Corrosion Studies on Selected Packaging Materials for Disposal of High Level Wastes." *Materials Reliability in the Back End of the Nuclear Fuel Cycle*, Proceedings of a Technical Committee Meeting, Vienna, 2-5 September 1986. IAEA TECHDOC-421, 7-24. Vienna, Austria: International Atomic Energy Agency. TIC: 252877.

Sprowls, D. O. 1987. *ASM Metal Handbooks*, 9th Ed., Vol. 13, pp. 245-282.

Stedinger, J.R.; Vogel, R.M.; and Foufoula-Georgiou, E. 1993. "Frequency Analysis of Extreme Events." Chapter 18 of *Handbook of Hydrology*. Maidment, D.R., ed. New York, New York: McGraw-Hill. TIC: 236568.

Stoecker, J. G. 1987. "Evaluation of Microbiological Corrosion" in *Metals Handbook*, Volume 13, ASM International, Metals Park, OH.

Summers, T. and Turchi, P. 1999. Aging and Phase Stability of Waste Package Outer Barrier. UCRL-ID-134582. Livermore, California: Lawrence Livermore National Laboratory. TIC: [246033](#).

Summers, T.S.E.; Rebak, R.B.; and Seeley, R.R. 2000. Influence of Thermal Aging on the Mechanical and Corrosion Properties of C-22 Alloy Welds. UCRL-JC-137727. Livermore, California: Lawrence Livermore National Laboratory. ACC: [MOL.20010517.0257](#).

Summers, T.S.E.; Wall, M.A.; Kumar, M.; Matthews, S.J.; and Rebak, R.B. 1999. "Phase Stability and Mechanical Properties of C-22 Alloy Aged in the Temperature Range 590 to 760°C for 16,000 Hours." *Scientific Basis for Nuclear Waste Management XXII*, Symposium held November 30-December 4, 1998, Boston, Massachusetts. Wronkiewicz, D.J. and Lee, J.H., eds. 556, 919-926. Warrendale, Pennsylvania: Materials Research Society. TIC: [246426](#).

Tada, H.; Paris, P.; Irwin, G. 1973. *The Stress Analysis Handbook*, 2nd Ed., Del Research Corporation.

Tawancy, H.M.; Herchenroeder, R.B.; and Asphahani, A.I. 1983. "High-Performance Ni-Cr-Mo-W Alloys." *Journal of Metals*, 35, (6), 37-43. Warrendale, Pennsylvania: The Minerals, Metals & Materials Society. TIC: [245100](#).

Taylor, Barry, N.; and Kuyatt, Chris, E. NIST Technical Note 1297 1994 Edition. *Guidelines for Evaluating and Expressing the Uncertainty of NIST Measurement Results*. United States Department of Commerce, Technology Administration, National Institute of Standards and Technology.

Thermo-Calc Software 1998. DICTRA User's Guide, Version: 20. Stockholm, Sweden: Thermo-Calc Software.

Treseder, R.S.; Baboian, R.; and Munger, C.G. 1991. *NACE Corrosion Engineer's Reference Book*. 156-181. Houston, Texas: NACE International. TIC: 245834.

Turchi, P.E.A. 2001. "Delivery of Property Diagram (Phase Fraction Versus Temperature) of Alloy 22 at Its Nominal Composition." Memorandum from P.E.A. Turchi (BSC) to RPC = 3, May 21, 2001, PROJ.05/01.051, with enclosure. ACC: [MOL.20010522.0158](#).

Turchi, P.E.A. April 2003. Modeling of Stability and Aging of Candidate Alloys for Use In Waste Disposal Canisters. SN-LLNL-SCI-477-V1.

Turchi, P.E.A., Kaufman, L., Liu, Z.K. 2003. "Stability and Aging of Candidate Alloys for the Yucca Mountain Project: CALPHAD Results." Scientific Basis for Nuclear Waste Management XXVI. Finch, R.J. and Bullen, D.B.. 757, Warrendale, Pennsylvania: Materials Research Society.

Urquidi, M. and Macdonald, D.D. 1985. "Solute-Vacancy Interaction Model and the Effect of Minor Alloying Elements on the Initiation of Pitting Corrosion." *Journal of the Electrochemical Society*, 132, (3), 555-558. [New York, New York]: Electrochemical Society. TIC: 249843.

Vander Voort, G.F. 2000. "Volume Fraction." *Metallography, Principles and Practice*. Pages 425-435. Materials Park, Ohio: ASM International. TIC: [254149](#).

Vetter, K.J.; and Strehblow, H.H. 1974. *Pitting Corrosion in an Early Stage and its Theoretical Implications*. In *Localized Corrosion* (edited by R.W. Staehle, B.F. Brown, J. Kruger and A. Agrawal), NACE International, Houston, TX.

Vlasity, J.; McGuire, R.; Kessler, J.; Long, A.; Childs, S.; Ross, B.; Schwartz, F.; Shoesmith, D.; Massari, J.; Zhou, W.; Arthur, R.; Apted, M.; and Sudicky, E. 2002. *Evaluation of the Proposed High-Level Radioactive Waste Repository at Yucca Mountain Using Total System Performance Assessment Phase 6*. EPRI TR-1003031. Palo Alto, California: Electric Power Research Institute. TIC: xxxxxx.

Walsh, D.W. 1999. "The Effects of Microstructure on MIC Susceptibility in High Strength Aluminum Alloys." *Corrosion 99, Paper 187*, 1-13. Houston, Texas: National Association of Corrosion Engineers. TIC: 246549.

Walton, J.C.; Cragnolino, G.; and Kalandros, S.K. 1996. "A Numerical Model of Crevice Corrosion for Passive and Active Metals." *Corrosion Science*, 38, (1), 1-18. Amsterdam, The Netherlands: Pergamon. TIC: 233439.

Wang, F. 1999. Memorandum, Summary on the Modification of BSW Solutions for SCC Tests, Lawrence Livermore National Laboratory.

Welsch, G.; Smialek, J.L.; Doychak, J.; Waldman, J.; and Jacobson, N.S. 1996. "High Temperature Oxidation and Properties." Chapter 2 of *Oxidation and Corrosion of Intermetallic Alloys*. Welsch, G. and Desai, P.D.; eds. West Lafayette, Indiana: Purdue University. TIC: 245280.

Wilfinger, K. R.; Farmer, J. C.; Hopper, R. W.; Shell, T. E. 1999. "Corrosion Protection of Metallic Waste Packages Using Thermal Sprayed Ceramic Coatings." *Proceedings of the Symposium on the Scientific Basis for Nuclear Waste Management XXII*. Wronkiewicz, D. J.; Lee, J. H., eds. Materials Research Society Symposium Series, Vol. 556, pp. 927-934. Warrendale, PA.

Zhang, L. and Macdonald, D.D. 1998a. "Segregation of Alloying Elements in Passive Systems—I. XPS Studies on the Ni–W System." *Electrochimica Acta*, 43, (18), 2661-2671. [New York, New York]: Pergamon Press. TIC: 249845.

Zhang, L. and Macdonald, D.D. 1998b. "Segregation of Alloying Elements in Passive Systems—II. Numerical Simulation." *Electrochimica Acta*, 43, (18), 2673-2685. [New York, New York]: Pergamon Press. TIC: 249846.

Zhou, X.; Balachov, I.; and Macdonald, D.D. 1998. "The Effect of Dielectric Coatings on IGSCC in Sensitized Type 304 SS in High Temperature Dilute Sodium Sulfate Solution." *Corrosion Science*, 37, (1), 189-208. Elsevier Science Ltd. TIC: xxxxxx.

Codes, Standards and Regulations

10 CFR 63. Energy: Disposal of High-Level Radioactive Wastes in a Geologic Repository at Yucca Mountain, Nevada. Readily available.

AP-2.14Q, Rev. 2, ICN 2. *Review of Technical Products and Data*. Washington, D.C.: U.S. Department of Energy, Office of Civilian Radioactive Waste Management. ACC: DOC.20030206.0001.

AP-2.27Q, Rev. 0, ICN 0. *Planning for Science Activities*. Washington, D.C.: U.S. Department of Energy, Office of Civilian Radioactive Waste Management. ACC: MOL.20020701.0184.

AP-SIII.2Q, Rev. 1, ICN 1. *Qualification of Unqualified Data*. Washington, D.C.: Office of Civilian Radioactive Waste Management. ACC: DOC.20030422.0008.

AP-SIII.10Q, Rev. 1, ICN 0. *Models*. Washington, D.C.: U.S. Department of Energy, Office of Civilian Radioactive Waste Management. ACC: DOC.20030312.0039.

AP-SV.1Q, Rev. 0, ICN 3. *Control of the Electronic Management of Information*. Washington, D.C.: U.S. Department of Energy, Office of Civilian Radioactive Waste Management. ACC: MOL.20020917.0133.

AP-SI.1Q, Rev. 5, ICN 0. *Software Management*. Washington, D.C.: U.S. Department of Energy, Office of Civilian Radioactive Waste Management. ACC: DOC.20030422.0012.

ASTM B 575-94. 1994. *Standard Specification for Low-Carbon Nickel-Molybdenum-Chromium and Low-Carbon Nickel-Chromium-Molybdenum Steel Alloy Plate, Sheet, and Strip*. Philadelphia, Pennsylvania: American Society for Testing and Materials. TIC: 237683.

ASTM 1987. Designation G 1-81, 1987 Annual Book of ASTM Standards, Section 3, Vol. 3.02, pp. 89–94.

ASTM 1989. Designation G 5-87, 1989 Annual Book of ASTM Standards, Section 3, Vol. 3.02, pp. 79–85.

ASTM 1997a. Designation B 575-94, 1997 Annual Book of ASTM Standards, Section 2, Vol. 2.04, pp. 409–410, Subsection 7.1.

ASTM 1997c. Designation G 61-86, 1997 Annual Book of ASTM Standards, Section 3, Vol. 3.02, pp. 231–235.

ASTM 1997e. Designation G 1-90, 1997 Annual Book of ASTM Standards, Section 3, Vol. 3.02, pp. 15–21.

ASTM C 1174-97. 1998. *Standard Practice for Prediction of the Long-Term Behavior of Materials, Including Waste Forms, Used in Engineered Barrier Systems (EBS) for Geological Disposal of High-Level Radioactive Waste*. West Conshohocken, Pennsylvania: American Society for Testing and Materials. TIC: 246015.

ASTM G 1-90 (Reapproved 1999). 1990. *Standard Practice for Preparing, Cleaning, and Evaluating Corrosion Test Specimens*. West Conshohocken, Pennsylvania: American Society for Testing and Materials. TIC: 238771.

ASTM G 3-89 (Reapproved 1999). 1989. *Standard Practice for Conventions Applicable to Electrochemical Measurements in Corrosion Testing*. West Conshohocken, Pennsylvania: American Society for Testing and Materials. TIC: 247076.

ASTM G 5 - 94. *Standard Reference Test Method for Making Potentiostatic and Potentiodynamic Anodic Polarization Measurements*. Philadelphia, Pennsylvania: American Society for Testing and Materials. TIC: 231902.

ASTM G 30-94. 1994. *Standard Practice for Making and Using U-Bend Stress-Corrosion Test Specimens*. Philadelphia, Pennsylvania: American Society for Testing and Materials. TIC: 246890.

ASTM G 59-97. 1997. *Standard Test Method for Conducting Potentiodynamic Polarization Resistance Measurements*. West Conshohocken, Pennsylvania: American Society for Testing and Materials.

ASTM G 61-86 (Reapproved 1998). 1987. *Standard Test Method for Conducting Cyclic Potentiodynamic Polarization Measurements for Localized Corrosion Susceptibility of Iron-, Nickel-, or Cobalt-Based Alloys*. West Conshohocken, Pennsylvania: American Society for Testing and Materials. TIC: 246716.

ASTM G 102-89 (Reapproved 1999). 1989. *Standard Practice for Calculation of Corrosion Rates and Related Information from Electrochemical Measurements*. West Conshohocken, Pennsylvania: American Society for Testing and Materials.

Input Source Data

Brossia, C.S.; Browning, L.; Dunn, D.S.; Moghissi, O.C.; Pensado, O.; and Yang, L. 2001. Effect of Environment on the Corrosion of Waste Package and Drip Shield Materials. CNWRA 2001-03. Table A-1. Center for Nuclear Waste Regulatory Analyses, San Antonio, Texas.

LL991203505924.094. Approach and Supporting Data for MIC Modeling. Submittal date: 12/13/1999. ACC: MOL.20000128.0142.

LL000320405924.146. Target Compositions of Aqueous Solutions Used for Corrosion Testing. Submittal date: 03/22/2000.

LL020506212251.013. Electrochemical Behavior of Alloy 22 in CaCl₂ Solutions. Submittal date: 08/30/2002.

LL020711612251.017. Open Circuit Potential Tests. Submittal date: 10/11/2002.

LL021105112251.022. Electrochemical Behavior of Alloy 22 in Simulated Acidic Concentrated Water (SAW), Simulated Concentrated Water (SCW) and 5 M CaCl₂ Solutions. Submittal date: 12/11/2002.

LL021105312251.023. Stress Corrosion Crack Growth and Initiation Measurements for C-22 and Ti-7, General Electric Global Research Center (GEGRC) 121202. Submittal date: 01/08/2003.

LL030201212251.033. Chemical Analysis and Thermodynamic Calculations of Solutions Used to Monitor Corrosion Potentials of Alloy C22. Submittal date: 02/25/2003.

LL030309512251.042. Low Temperature Operating Mode Electrochemical Test Data: Corrosion Potential, Linear Polarization, and Cyclic (Potentiodynamic) Polarization Tests of Alloy 22 in Oxalic Acid, NaF, NaCl, NaF+NaCl, and CaCl₂ Solutions Recorded at 30, 45, 60, 75, 90 and 105°C. Submittal date: 05/22/2003.

LL030400112251.043. Electrochemical Behavior of Multiple Crevice Assembly (MCA) Alloy 22 Specimens in 5M CaCl₂. Submittal date: 04/07/2003.

LL030406212251.044. Alloy 22 in 5M CaCl₂ at 75C - Supplemental. Submittal date: 04/08/2003.

LL030406412251.045. Transmission Electron Microscopy (TEM) Images of Oxide Film on Air-Oxidized Alloy22 (UNS N06022) Samples Aged at 550C. Submittal date: 04/11/2003.

LL030409512251.051. Electrochemical Analysis of Alloy 22 - CaCl₂ Data at Various Temperatures, Surface Conditions, and Electrolyte Solutions.. Submittal date: 05/23/2003.

LL030409812251.054. Electrochemical Data of Alloy 22 in CaCl₂ Solutions-Effect of Nitrate.. Submittal date: 06/26/2003.

LL030412512251.057. LTCTF Corrosion Rate Calculations for Five-Year Exposed Alloy C22 Specimens Cleaned under TIP-CM-51.. Submittal date: 05/28/2003.

LL030502212251.063. Corrosion Potential, Polarization Resistance, and Cyclic (Potentiodynamic) Polarization in Several Environments at Several Temperatures for Alloy 22.. Submittal date: 05/20/2003.

LL030703723121.031. Conversion of Corrosion Testing Solutions from Molar to Molal Concentration Units.. Submittal date: 07/10/2003.

LL030706223121.032. Conversion of Corrosion Testing Solutions from Molar to Molal Concentration Units (II). Submittal date: 07/17/2003.

LL030709812251.067. Basic Saturated Water (BSW) Test Solution Composition.. Submittal date: 07/25/2003.

MO0301SEPFEPS1.000. LA FEP List. Submittal date: 01/21/2003.

MO0003RIB00071.000. Physical and Chemical Characteristics of Alloy 22. Submittal date: 03/13/2000.

Output Data

SN0306T0506303.001. Localized Corrosion Model and Analyses of Waste Package Outer Barrier. Submittal date: 06/03/2003.

SN0306T0506303.002. General Corrosion Model and Analyses of Waste Package Outer Barrier. Submittal date: 06/10/2003.

Attachments. Relationship of NRC Key Technical Issues to TBR Strategy

[CLST 1.01] Provide documentation for Alloy 22 and titanium for the path forward items on Slide 8. DOE will provide the documentation in a revision to AMR “Environment on the Surfaces of the Drip Shield and Waste Package Outer Barrier by License Application. Gordon Slide 8: establish credible range of brine water chemistry, evaluate effect of introduced materials on water chemistry, determine likely concentrations and chemical form of minor constituents in Yucca Mountain waters, characterize Yucca Mountain waters with respect to the parameters which define the type of brine which would evolve; and evolve periodic water-drip evaporation [Due: DOE March 2003 & NRC April 2004]. **Response – Credible ranges of brine water chemistry are discussed in Chapter 1 and illustrated in Figures 1-8, 1-9, and 1-11, as well as in Chapter 7, Table 7-1.**

[CLST 1.02] Provide documentation for the path forward items on Slide 12. Gordon Slide 12: Surface elemental analysis of alloy test specimens is necessary for determination of selective dissolution; surface analysis of welded specimens for evidence of dealloying; and continue testing including simulated saturated repository environment to confirm enhancement factor. DOE will provide the documentation in a revision to AMR “General and Localized Corrosion of Waste Package Outer Barrier” by License Application [Due: DOE March 2004 & NRC April 2004]. **Response – Additional work is needed.**

[CLST 1.03] Provide documentation that confirms the linear polarization resistance measurements with corrosion rate measurements using other techniques. The documentation will be provided in a revision of the AMR (ANL-EBS-MD-000003) entitled “General and Localized Corrosion of Waste Package Outer Barrier by License Application [Due: DOE April 2003 & NRC May 2004]. **Response – Additional work is needed.**

[CLST 1.04] Provide the documentation for Alloy 22 and titanium for the path forward items listed on slide 14. Gordon Slide 14: continue testing in the Long Term Corrosion Test Facility (LTCTF); add new bounding water test environments to LTCTF (SSW and BSW); install thinner coupons in LTCTF with larger surface area to volume ratios (e.g. 10 cm × 10 cm instead of current 5 cm × 5 cm × 2.5 cm) and thereby decrease measurement error; install high-sensitivity probes of Alloy 22 in some of the LTCTF vessels (permits on-line measurements and monitoring of changes in corrosion rates); and materials testing continues during performance confirmation. DOE will provide the documentation in a revision to AMRs (ANL-EBS-MD-000003 and ANL-EBS-MD-000004) by License Application [Due: DOE July 2005 & NRC August 2005]. Paraphrase. **Response – while new high sensitivity probes have not yet been installed, the collection of additional data from the LTCTF, with exposures of five years, have increased confidence in the corrosion rate measurements. The additional measurements and associated statistical analysis are discussed in Chapter 6, and shown in Figures 6-1 through 6-15. It should also be noted that high-sensitivity measurements of corrosion rate underneath deliquescence brines are in fact being made with the Project’s Environmental TGA, as Discussed in Chapter 5. Data are shown in Figures 5-1 through 5-3.**

[CLST 1.06] Provide the documentation on testing showing corrosion rates in the absence of silica deposition. DOE will document the results of testing in the absence of silica deposits in the revision of Alloy 22 AMR (ANL-EBS-MD-000003) prior to License Application [Due: DOE December 2003; January 2004].

[CLST 1.07] Provide documentation for the alternative methods to measure corrosion rates of the waste package materials (e.g., ASTM G-102 testing) or provide justification for the current approach. DOE will document the alternative methods of corrosion measurement in the revision of Alloy 22 AMR (ANL-EBS-MD-000003) prior to License Application [Due: DOE December 2003; January 2004]. **Response – Weight-loss and dimensional-change measurements of samples exposed to concentrated brines in the LTCTF for five years have increased confidence in the corrosion rate measurements. These data have undergone detailed statistical analysis, and provide very good insight into the corrosion rates of Alloy 22 under realistic environments. These measurements are discussed Chapter 6, and shown in Figures 6-1 through 6-15.**

[CLST 1.08] Provide documentation for Alloy 22 and titanium for the path forward items listed on Slide 16 and 17. DOE will provide the documentation in the revision to the AMRs (ANL-EBS-000003 and ANL-EBS-MD-000004) prior to License Application. Gordon Slide 16: Calculate potential-pH (Pourbaix) diagrams for multi-component Alloy 22; grow oxide films at higher temperatures (90-175°C) in autoclaves, air, and/or electrochemically (anodic polarization) to accelerate film growth for compositional and structural studies below; resolve kinetics of film growth: parabolic or higher order, whether film growth becomes linear, and if, as film grows it becomes mechanically brittle and spalls off; and determine chemical, structural and mechanical properties of films, including thickened films. Gordon Slide 17: correlate changes in E_{corr} measured in LTCTF with compositional changes in passive film over time; perform analyses on cold-worked materials to determine changes in film structural properties; and perform examination of films formed on naturally-occurring Josephinite (which some consider to be a natural analogue of nickel-based alloys) [Due: DOE April 2004; May 2004]. **Response – Dr. Larry Kaufman has predicted Pourbaix diagrams for Alloy 22, assuming relevant brine chemistry, with the ThermoCalc model. Dr. Chris Orme has performed microstructural analysis of surface films, which include both oxides formed at high temperature, and passive films formed in aqueous solution. The surface layer formed on Josephinite has also been studied.**

[CLST 1.09] Provide the data that characterizes the passive film stability, including the welded and thermally aged specimens. DOE will provide the documentation in a revision of AMRs (ANL-EBS-MD-000003 and ANL-EBS-MD-000004) prior to License Application. [Due: DOE April 2004; May 2004]. **Response – The open-circuit corrosion potential is indicative of the nature of the passive film on the surface. Thus, the long-term open-circuit corrosion potential measurements on mill-annealed and as-welded samples serve as a means of characterizing passive film stability. These measurements are discussed in Chapter 7, and are shown in Figures 7-9 through 7-13. Chapter 8 discusses CPP measurements of mill-annealed and thermally aged samples. These data are shown in Figures 8-1 through 8-3. The electrochemical responses show no dramatic change with aging.**

[CLST 1.10] Provide the documentation for Alloy 22 and titanium for the path forward items listed on Slides 21 and 22. Gordon Slide 21: measure corrosion potentials in the LTCTF to determine any shift of potential with time toward the critical potentials for localized corrosion; and determine critical potentials on welded, and welded and aged coupons of Alloy 22 verses those for base metal, particularly important if precipitation or severe segregation of alloying elements occurs in the welds. Gordon Slide 22: Separate effects of ionic mix of species in Yucca Mountain waters on critical potentials, damaging species (chloride, fluoride, possibly sulfate) from potentially beneficial species (nitrate, carbonate, and silicate), noting that pore water, perched water, and groundwater have somewhat different ionic ratios; and determine critical potentials in environments containing heavy metal concentrations (e.g., Pb, As, Hg). DOE will provide the documentation in a revision to AMRs (ANL-EBS-MD-000003 and ANL-EBS-MD-000004) prior to License Application [Due: DOE April 2004; May 2004]. **Response – Long-term corrosion potential data for mill-annealed and welded samples are discussed in Chapter 7, and shown in Figures 7-9 through 7-13. Chapter 8 discusses CPP measurements of mill-annealed and thermally aged samples. These data are shown in Figures 8-1 through 8-3. The electrochemical responses show no dramatic change with aging.**

[CLST 1.11] Provide the technical basis for the selection of the critical potentials as bounding parameters for localized corrosion, taking into account microbial influenced corrosion (MIC). DOE will provide the documentation in a revision of AMRs (ANL-EBS-MD-000003 and ANL-EBS-MD-000004) prior to License Application [Due: DOE April 2004 & NRC May 2004]. **Response – The technical basis for selecting the critical potential as a bounding parameter for localized corrosion is discussed in Chapter 7, and illustrated in Figures 7-16 through 7-19. Clearly, crevice attack is induced at imposed electrochemical potentials above the critical value. The impact of microbial growth on corrosion is summarized in Table 2.**

[CLST 1.12] Provide the documentation for Alloy 22 and titanium for the path forward items listed on slides 34 and 35. Gordon Slide 34: quantify and optimize mitigation processes; generate SCC data for mitigated material over full range of metallurgical conditions (base metal, as-welded, welded and aged, cold worked); new vessels for LTCTF will house many of the SCC specimens; continue slow strain rate testing (SSRT) in same types of environments as above, specimens in the same range of metallurgical conditions. Gordon Slide 35: Determine repassivation constants needed for film rupture SCC model to obtain value for the model parameter (n); continue reversing direct current potential drop crack propagation rate determinations in same types of environments and same metallurgical conditions as for SSRT and LTCTF tests; evaluate SCC resistance of welded and laser-peened material verses non-welded unpeened material; evaluate SCC resistance of induction annealed material; evaluate SCC resistance of full thickness material (with welds) obtained from the demonstration prototype cylinder of Alloy 22 (mock-up of SR design). DOE will provide the documentation in a revision to AMRs (ANL-EBS-MD-000005 and ANL-EBS-MD-000006) prior to License Application [Due: DOE September 2003 & NRC October 2003]. **Response – SSRT has been conducted with a variety of environments, and have indicated excellent resistance to SCC. These data are discussed in Chapter 10 and are summarized in Table 10-1. The repassivation parameter (n) for the slip-dissolution film-rupture (SDFR) model has been determined, with the results summarized in Tables 10-2 through 10-1. Predictions based upon the measured value of (n) are shown in Figure 10-1.**

[CLST 1.13] Provide the data that characterizes the distribution of stresses due to LSP and induction annealing of Alloy 22. DOE will provide the documentation in a revision to AMR (ANL-EBS-MD-000005) prior to License Application [Due: DOE September 2003 & NRC October 2003]. **Response – Stress mitigation with laser-shock peening (LSP) and controlled-plasticity burnishing is discussed in Chapter 10. Results for stress mitigation with these processes are summarized by the coefficients given in Table 10-7, and by the stress profiles shown in Figures 10-4 through 10-8.**

[CLST 1.14] Provide the justification for not including the rock-fall effect and dead-load from drift collapse on SCC of the waste package and drip shield. DOE will provide the documentation for the rockfall and dead-weight effects in the next revision of the SCC AMR (ANL-EBS-MD-000005) prior to License Application [Due: DOE September 2003 & NRC October 2003]. Paraphrase. **Response – Requires additional work.**

[CLST 1.15] Provide the documentation for Alloy 22 and titanium for the path forward items listed on slide 39. Gordon Slide 39: install specimens cut from welds of SR design mock-up in LTCTF and in other SCC test environments, and determine which specimen geometry is most feasible to complement SCC evaluation; evaluate scaling and weld process factors between thin coupons and dimensions in actual welded waste package containers, including thermal/metallurgical structural effects of multi-pass weld processes; provide representative weld-test specimens for MIC work, thermal aging, and localized corrosion evaluations. DOE will provide documentation for Alloy 22 and Ti path forward items on slide 39 in a revision to the SCC and general and localized corrosion AMRs (ANL-EBS-MD-000003, ANL-EBS-MD-000004, ANL-EBS-MD-000005) by License Application [Due: DOE September 2003 & NRC October 2003]. **Response – Requires additional work.**

[CLST 1.16] Provide the documentation on the measured thermal profile of the waste package material due to induction annealing. DOE stated that the thermal profiles will be measured during induction annealing, and the results will be reported in the next SCC AMR (ANL-EBS-MD-000005) prior to License Application [Due: DOE September 2003 & NRC October 2003]. Paraphrase. [Note: since localized induction annealing is no longer included in the License Application Baseline Design, this KTI is no longer relevant]. **Response – Stress mitigation processes are discussed in Chapter 10. Localized induction annealing has been abandoned, so any associated data has become irrelevant.**

[CLST 2.04] Provide information on the effect of the entire fabrication sequence on phase instability of Alloy 22, including the effect of welding thick sections using multiple weld passes and the proposed induction annealing process. DOE stated that the aging studies will be expanded to include solution annealed and induction annealed Alloy 22 weld and base metal samples from the mock-ups as well as laser-peened, thick, multi-pass welds. This information will be included in revisions of the AMR (ANL-EBS-MD-000002) entitled Aging and Phase Stability of the Waste Package Outer Barrier before License Application (Due: DOE March 2005 & NRC April 2005). **Response – TTT diagrams can be used to assess the impact of metallurgical processing on a material. The phase stability of Alloy 22 is discussed in Chapter 2, with the results summarized in the TTT diagrams shown in Figures 4-4 through 4.6. Phase stability data specific to welds is shown in Figure 4-10.**

[CLST 2.05] Provide the AMR entitled "Aging and Phase Stability of Waste Package Outer Barrier," including the documentation of the path forward items listed in the "Sub-Issue 2: Effects of Phase Instability of Materials and Initial Defects on the Mechanical Failure and Lifetime of the Containers" presentation, Slides 5 & 6. DOE stated that the "Aging and Phase Stability of the Waste Package Outer Barrier" AMR, ANL-EBS-MD-000002, Rev. 00 was issued 3/20/00. This AMR will be revised to include the results of the path forward items before License Application [Due: DOE March 2005 & NRC April 2005]. **Response – phase stability is discussed in Chapter 4. The initiation of SCC depends upon the stress intensity factor at incipient flaws in the surface, and at flaws in the welds. The role of these flaws is discussed in Chapter 10.**

[CLST 6.01] Provide documentation for the path forward items in the "Sub-Issue 6: Alternate EBS Design Features – Effect on Container Lifetime" presentation, Slides 7 & 8. DOE stated that the documentation of the path forward items will be completed and as results become available, they will be documented in the revisions of AMRs (ANL-EBS-MD-000005, Stress Corrosion Cracking of the Drip Shield, the Waste Package Outer Barrier and the Stainless Structural Material, and ANL-EBS-MD-000004, General Corrosion and Localized Corrosion of the Drip Shield), to be completed by License Application [Due: DOE September 2003 & NRC October 2003]. **Response – Additional work needed.**

[CLST 6.02] Provide additional justification for the use of a 400 ppm hydrogen criterion or perform a sensitivity analysis using a lower value. DOE stated that additional justification will be found in the AMR entitled "Review of Expected Behavior of Alpha Titanium Alloys under Yucca Mountain Condition" TDR-EBS-MD-000015, which is in preparation and will be available in January 2001 [Due: DOE June 2004 & NRC July 2004]. **Response – Hydrogen induced cracking of the titanium drip shield is discussed in the July 2003 KTI Letter Report for Agreement CLST 6.02 and 6.03 by Fred Hua.**

[CLST 6.03] Provide the technical basis for the assumed fraction of hydrogen absorbed into titanium as a result of corrosion. DOE stated that additional justification will be found in the AMR entitled "Review of Expected Behavior of Alpha Titanium Alloys under Yucca Mountain Condition" TDR-EBS-MD-000015, which is in preparation and will be available in January 2001. [Due: DOE June 2004 & NRC July 2004]. **Response – Hydrogen induced cracking of the titanium drip shield is discussed in the July 2003 KTI Letter Report for Agreement CLST 6.02 and 6.03 by Fred Hua.**

[TSPAI 3.01] Propagate significant sources of uncertainty into projections of waste package and drip shield performance included in future performance assessments. Specific sources of uncertainty that should be propagated (or strong technical basis provided as to why it is insignificant) include: (1) the uncertainty from measured crevice and weight-loss samples general corrosion rates and the statistical differences between the populations, (2) the uncertainty from alternative explanations for the decrease in corrosion rates with time (such as silica coatings that alter the reactive surface area), (3) the uncertainty from utilizing a limited number of samples to define the correction for silica precipitation, (4) the confidence in the upper limit of corrosion rates resulting from the limited sample size, and (5) the uncertainty from alternative statistical representations of the population of empirical general corrosion rates. The technical

basis for sources of uncertainty will be established upon completion of existing agreement items CLST 1.4, 1.5, 1.6, and 1.7. DOE will then propagate significant sources of uncertainty into projections of waste package and drip shield performance included in future performance assessments. This technical basis will be documented in a future revision of the General and Localized Corrosion of Waste Package Outer Barrier AMR (ANL-EBS-MD-000003) expected to be available consistent with the scope and schedules for the specified CLST agreements. The results of the AMR analyses will be propagated into future TSPA analyses for any potential License Application [Due: DOE February 2004 & NRC March 2004]. **Response – most aspects of this KTI are addressed in Chapter 6, in the section entitled “Uncertainty Analysis of General Corrosion Rate Data.” Uncertainty in the measurements is illustrated in Figures 6-1, 6-2, 6.14, and 6.16.**

[TSPAI 3.02] Provide the technical basis for re-sampling the general corrosion rates and the quantification of the impact of re-sampling of general corrosion rates in revised documentation (ENG1.1.1). DOE will provide the technical basis for re-sampling the general corrosion rates and the quantification of the impact of re-sampling of general corrosion rates in an update to the WAPDEG Analysis of Waste Package and Drip Shield Degradation AMR (ANL-EBS-PA-000001). This AMR is expected to be available to NRC in FY03. [Not Scheduled]. **Response – Additional work is required.**

[TSPAI 3.03] Provide the technical basis for crack arrest and plugging of crack openings (including the impact of oxide wedging and stress redistribution) in assessing the impact of SCC of the drip shield and waste package in revised documentation (ENG1.1.2 and ENG1.4.1). DOE will provide the technical basis for crack arrest and plugging of crack openings (including the impact of oxide wedging and stress redistribution) in assessing the stress corrosion cracking of the drip shield and waste package in an update to the Stress Corrosion Cracking of the Drip Shield, Waste Package Outer Barrier, and the Stainless Steel Structural Material AMR (ANL-EBS-MD-000005) in accordance with the scope and schedule for existing agreement item CLST 1.12. [Due: DOE December 2003 & NRC January 2004]. **Response – SCC is discussed in detail in Chapter 10, and in the corresponding AMR. Additional work is required.**

[TSPAI 3.04] Provide the technical basis that the representation of the variation of general corrosion rates (if a significant portion is a lack of knowledge of uncertainty) does not result in risk dilution of projected dose responses (ENG1.3.3). DOE will provide the technical basis that the representation of the variation of general corrosion rates results in reasonably conservative projected dose rates. The technical basis will be documented in an update to the WAPDEG Analysis of Waste Package and Drip Shield Degradation AMR (ANL-EBS-PA-000001). This AMR is expected to be available to NRC in FY03. These results will be incorporated into future TSPA documentation for any potential license application. [Due: DOE February 2004 & NRC March 2004]. **Response – Additional work is required.**

[TSPAI 3.05] Provide the technical basis for the representation of uncertainty/variability in the general corrosion rates in revised documentation. This technical basis should provide a detailed discussion and analyses to allow independent reviewers the ability to interpret the representations of 100% uncertainty, 100% variability, and any intermediate representations in the DOE model (ENG1.3.6). DOE will provide the technical basis for the representation of uncertainty/variability in the general corrosion rates. This technical basis will include the results of 100% uncertainty,

100% variability, and selected intermediate representations used in the DOE model. These results will be documented in an update to the WAPDEG Analysis of Waste Package and Drip Shield Degradation AMR (ANL-EBS-PA-000001) or other document. This AMR is expected to be available to NRC in FY03 [Due: DOE February 2004 & NRC March 2004]. **Response – The uncertainty and variability of general corrosion rate measurements is discussed in detail in Chapter 6, and in the AMR on general and localized corrosion of the WPOB. From the empirical cumulative distribution functions (CDFs) shown in Figures 6-3 through 6.15, the separation of uncertainty from variability is clear. Each CDF reflects the uncertainty in general corrosion rate measurements, while differences between CDFs reflects variability.**

[PRE 7.02] Provide the waste package finite element analysis based numerical simulations that represent a significant contribution to DOE's safety case. Provide documentation demonstrating that a sufficient finite element model mesh discretization has been used and the failure criterion adequately bounds the uncertainties associated with effects not explicitly considered in the analysis. These uncertainties include but are not limited to: (1) residual and differential thermal expansion stresses, (2) strain rate effects, (3) dimensional and material variability, (4) seismic effects on ground motion, (5) initial tip-over velocities, and (6) sliding and inertial effects of the waste package contents, etc. In addition, document the loads and boundary conditions used in the models and provide the technical bases and or rationale for them. DOE agreed to provide the information. The information will be available in FY03 and documented in Waste Package Design Methodology Report. [Due: DOE September 2003 & NRC October 2003]. **Response – See the individual KTI response.**

[RDTME 3.18] Provide a technical basis for a stress measure that can be used as the equivalent uniaxial stress for assessing the susceptibility of the various engineered barrier system materials to stress corrosion cracking (SCC). The proposed stress measure must be consistent and compatible with the methods proposed by the DOE to assess SCC of the containers in WAPDEG and in accordance with the agreements reached at the CLST Technical Exchange. DOE will include a detailed discussion of the stress measure used to determine nucleation of stress corrosion cracks in the calculations performed to evaluate waste package barriers and the drip shield against stress corrosion cracking criterion. DOE will include these descriptions in future revisions of the following: Design Analysis for UCF Waste Packages, ANL-UDC-MD-000001, Design Analysis for the Defense High-Level Waste Disposal Container, ANL-DDC-ME-000001, Design Analysis for the Naval SNF Waste Package, ANL-UDC-ME-000001, and Design Analysis for the Ex-Container Components, ANL-XCS-ME-000001. The stresses reported in these documents will be used in WAPDEG and will be consistent with the agreements and associated schedule made at the Container Life and Source Term Technical Exchange (Subissue 1, Agreement 14, Subissue 6, Agreement 1). [Due: DOE September 2003 & NRC October 2003]. **See the last paragraph in the section entitled "Stress Intensity Factor Calculation" in Chapter 10. The use of uniaxial stress data to analyze components under multi-axial stress is a valid industrial practice, and is discussed in the American Society of Mechanical Engineers (ASME) Boiler and Pressure Vessel Code.**